TRANSIENT WAVE BEHAVIOR IN WATER PIPES WITH NON-UNIFORM BLOCKAGES

TONGCHUAN CHE

PhD

The Hong Kong Polytechnic University

2019

The Hong Kong Polytechnic University

Department of Civil and Environmental Engineering

Transient Wave Behavior in Water Pipes with Non-Uniform Blockages

Tongchuan CHE

A thesis submitted in partial fulfilment of the requirements for the degree of

Doctor of Philosophy

May 2019

CERTIFICATE OF ORIGINALITY

I hereby declare that this thesis is my own work and that, to the best of my knowledge and belief, it reproduces no material previously published or written, nor material that has been accepted for the award of any other degree or diploma, except where due acknowledgement has been made in the text.

_____ (Signed)

Tongchuan CHE

***To my family**,*

for their unconditional love and support.

ABSTRACT

In urban water supply systems, partial *blockages* are commonly formed in *water pipes* from various complicated physical, chemical, and biological processes (e.g., sediment deposition, corrosion, and biofilm accumulation); thus, their cross-sectional areas usually constrict randomly and non-uniformly along their lengths (termed as *non-uniform blockages*). In recent years, the transient-based method, which utilizes the physical information collected by transient waves, has been developed and applied for blockage detection in water pipes. However, the current transient-based method for blockage detection is largely based on blockages with idealized uniform constriction along their lengths (termed as *uniform blockages*), which are equivalent to multiple pipes with different diameters connected in series. As a result, inaccuracy and invalidity of the current transient-based method have been widely observed in the applications for non-uniform blockage detection. This is mainly due to the incapability of the current transient-based theory for describing the interaction between transient waves and non-uniform blockages. Therefore, a physical understanding of *transient wave behavior in water pipes with non-uniform blockages* is necessary to enhance the theoretical development and practical applications of the transient-based method for real blockage detection.

In this thesis, the transient wave behavior in water pipes with non-uniform blockages is investigated in both the time and frequency domains by a combined methodology of theoretical analysis and numerical simulation. First, the transfer matrix method is adopted to understand and analyze the effect of properties of a non-uniform blockage in water pipes on the system frequency responses. Second, the physical mechanisms of the interaction between transient waves and non-uniform blockages are explained from an energy perspective. Afterwards, the frequency range of validity of the developed theory is investigated and quantified numerically by a full two-dimensional (2D) water hammer

model. Finally, the developed theory and gained findings are validated through advanced numerical investigations with the aid of the computational fluid dynamics (CFD) model coupled with user-defined functions (UDFs).

The obtained results indicate that the resonant frequency shifts induced by non-uniform blockages have very different patterns from that of uniform blockages presented in the literature. Specifically, the frequency shifts induced by non-uniform blockages become less evident for higher harmonics of the incident waves. This is because the impedance of non-uniform blockages is highly frequency dependent, which becomes smaller for higher frequency incident waves. That means non-uniform blockages have a less blocking effect on the propagation of higher frequency incident waves; thus, the frequency shifts induced by non-uniform blockages become less evident. This understanding and theory is developed based on the 1D wave equation, where the plane wave assumption is imposed. Therefore, to satisfy the developed theory, the incident wave frequency (i.e., the frequency range of validity) must be lower than the cut-off frequency of the radial mode 1 (M1). This result has been confirmed by preliminary experiments in the literature as well as numerical results from the full 2D model and CFD tools.

The physical understanding gained in this thesis may contribute to narrow the gap between transient-based theory and practical applications of non-uniform blockage detection, which is crucial and necessary for developing smart urban water supply systems. Based on the results and achievements of this thesis, essential and useful recommendations are also made for future work.

PUBLICATION LIST

(A) Journal Papers:

1. **Che, T.C.**, Duan, H.F.*, Lee, P.J., Pan, B., and Ghidaoui, M.S. (2018). "Transient frequency responses for pressurized water pipelines containing blockages with linearly varying diameters." ***Journal of Hydraulic Engineering - ASCE***, 144(8), 04018054.
DOI: 10.1061/(ASCE)HY.1943-7900.0001499

2. **Che, T.C.**, Duan, H.F.*, Lee, P.J., Meniconi, S., Pan, B., and Brunone, B. (2018). "Radial pressure wave behavior in transient laminar pipe flows under different flow perturbations." ***Journal of Fluids Engineering - ASME***, 140(10), 101203.
DOI: 10.1115/1.4039711

3. **Che, T.C.**, Duan, H.F.*, Pan, B., Lee, P.J., and Ghidaoui, M.S. (2019). "Energy analysis of the resonant frequency shift pattern induced by non-uniform blockages in pressurized water pipes." ***Journal of Hydraulic Engineering - ASCE***, 145(7), 04019027.
DOI: 10.1061/(ASCE)HY.1943-7900.0001607

4. **Che, T.C.***, Duan, H.F., *et al*. (2019). "2D numerical study of the non-uniform blockage effect on transient waves in pressurized water pipes." ***Computers & Fluids***, to be submitted.

5. **Che, T.C.**, Duan, H.F.*, *et al*. (2019). "Transient-based methods for anomaly detection in pressurized water pipes: a review." ***Applied Mechanics Reviews - ASME***, to be submitted.

6. Duan, H.F.*, **Che, T.C.**, Lee, P.J., and Ghidaoui, M.S. (2018). "Influence of nonlinear turbulent friction on the system frequency response in transient pipe flow modelling and analysis." ***Journal of Hydraulic Research***, 56(4), 451-463.
DOI: 10.1080/00221686.2017.1399936

7. Duan, H.F.*, Lee, P.J., **Che**, **T.C.**, Ghidaoui, M.S., Karney, B.W., and Kolyshkin, A.A. (2017). "The influence of non-uniform blockages on transient wave behavior and blockage detection in pressurized water pipelines." ***Journal of Hydro-environment Research***, 17(2017), 1-7.

DOI:10.1016/j.jher.2017.08.002

8. Pan, B., Duan, H.F.*, Meniconi, S., Urbanowicz, K., **Che, T.C.**, and Brunone, B. (2019). "Multistage frequency-domain transient-based method for the analysis of viscoelastic parameters of plastic pipes." ***Journal of Hydraulic Engineering - ASCE***, accepted.
DOI: 10.1061/(ASCE)HY.1943-7900.0001700

(B) Conference Papers:

1. **Che, T.C.***, Duan, H.F., Pan, B., Lee, P.J., and Ghidaoui, M.S. (2018). "Explanation of the transient frequency shift pattern of non-uniform blocked pipeline systems from an energy perspective." *Proceedings of the 13th International Conference on Pressure Surges* (*PS 2018*), 14-16 November 2018, Bordeaux, France.

2. **Che, T.C.**, Duan, H.F.*, Zheng, F., Pan, B., and Lee, P.J. (2018). "Energy analysis of transient frequency shift pattern induced by non-uniform blockages in water pipelines." *Proceedings of the 1st International WDSA/CCWI Joint Conference* (*WDSA/CCWI 2018*), 23-25 July 2018, Kingston, Ontario, Canada.

3. **Che, T.C.***, Duan, H.F., Pan, B., Lee, P.J., and Ghidaoui, M.S. (2018). "Transient-based method for non-uniform blockage detection in water pipelines." *Proceedings of the 8th International Symposium on Environmental Hydraulics* (*ISEH 2018*), 4-6 June 2018, University of Notre Dame, Indiana, USA.

4. **Che, T.C.***, Duan, H.F., Lee, P.J., and Ghidaoui, M.S. (2017). "Theoretical analysis of the influence of blockage irregularities on transient waves in water supply pipelines." *Proceedings of the 37th IAHR World Congress* (*IAHR 2017*), 13-18 August 2017, Kuala Lumpur, Malaysia.

5. **Che, T.C.***, and Duan, H.F. (2016). "Evaluation of plane wave assumption in transient laminar pipe flow modeling and utilization." *Proceedings of the 12th International Conference on Hydroinformatics* (*HIC 2016*), 21-26 August 2016, Inchon, South Korea.

6. Pan, B., Duan, H.F.*, **Che, T.C.**, Meniconi, S., and Brunone, B. (2018). "A frequency-domain transient-based method for the analysis of viscoelastic parameters of plastic pipes." *Proceedings of the 13th International Conference on Pressure Surges* (*PS 2018*), 14-16 November 2018, Bordeaux, France.

7. Pan, B.*, Duan, H.F., **Che, T.C.**, Zheng, F.F., Meniconi, S., and Brunone, B. (2018). "Inverse analysis of pipe viscoelastic parameters using frequency-domain transient-based method." *Proceedings of the 1st International WDSA/CCWI Joint Conference* (*WDSA/CCWI 2018*), 23-25 July 2018, Kingston, Ontario, Canada.

ACKNOWLEDGEMENTS

I am lucky enough to have such a caring supervisor, *Dr. Huan-Feng Duan*, who always has his door open when I need any support, especially during my early days at PolyU. I have already begun to miss our efficient discussions in regular group meetings, which keep my research on the right track and result in this thesis work. Over the years, *Dr. Duan* is not only an inspiring mentor, who shares his wisdom based on things he has experienced, but also a close friend, who has some common interests with us outside of research.

Sincere thanks also go to my co-supervisors *Prof. Pedro J. Lee* of the University of Canterbury and *Prof. Mohamed S. Ghidaoui* of the Hong Kong University of Science and Technology for their continual input and support during my PhD study. Among them, the most impressive ones are the detailed hand-written comments and revisions given by *Prof. Lee* on PDF files of all our co-authored papers, from which I benefited a lot.

I would like to thank *Dr. Silvia Meniconi* and *Prof. Bruno Brunone* of the University of Perugia for their insightful suggestions for the journal paper that we co-authored.

Special thanks to *Dr. Hexiang Yan* of Tongji University for his patient instructions in numerical schemes at the beginning of my academic career.

Mr. Chunying Huang, a software engineer of Xiamen Airlines, also contributed some preliminary work of the 2D NS numerical simulation at the end of my PhD study.

I would like to express my special appreciation to members of the Board of Examiners *Prof. Helena M. Ramos* of the University of Lisbon, *Prof. Shuming Liu* of Tsinghua University, and *Prof. Kwok-Wing Chau* of the Hong Kong Polytechnic University for finding their precious time to review this thesis.

This thesis study is supported by the project *Smart Urban Water Supply Systems* (T21-602/15R) under the Theme-based Research Scheme of the Hong Kong Research Grants Council.

Last but not least, I would like to thank my parents (*Zun-Jin Che* and *Dian-Zhen Chen*) and wife (*Ruby Li*) for their unconditional love and support over the years. Thank you for making me feel better about my life and setting me on the right path.

TABLE OF CONTENTS

LIST OF FIGURES

LIST OF TABLES

LIST OF ABBREVIATIONS

CCTV - closed-circuit television;

CFD - computational fluid dynamics;

CFL - Courant-Friedrichs-Lewy;

CFO - central force optimization;

FFT - fast Fourier transform;

FOSM - first-order second-moment;

FRF - frequency response function;

FVM - finite volume method;

GA - genetic algorithm;

HDPE - high-density polyethylene;

HHT - Hilbert-Huang transform;

IMFs - intrinsic mode functions;

IRF - impulse response function;

ITA - inverse transient analysis;

LM - Levenberg–Marquardt;

M0 - plane wave mode;

M1 - radial mode 1;

M2 - radial mode 2;

M3 - radial mode 3;

M4 - radial mode 4;

MFP - matched-field processing method;

MOC - method of characteristics;

ODE - ordinary differential equation;

PDEs - partial differential equations;

PPWM - portable pressure wave-maker;

PRBS - pseudorandom binary sequence;

PVC - polyvinyl chloride;

RPV - reservoir-pipe-valve;

SIMPLE - semi-implicit method for pressure linked equations;

SNR - signal-to-noise ratio;

SQP - sequential quadratic programming;

TFR - transient wave reflection;

TWD - transient wave damping;

TWR - transient frequency response;

UDFs - user-defined functions;

1D - one-dimensional;

2D - two-dimensional;

3D - three-dimensional.

NOTATION

Chapter 2

Roman Letters

A = pipe cross-sectional area;

a = transient wave speed;

D = pipe diameter;

E = Young's modulus of elasticity of the pipe wall;

$FRF(\omega)$ = frequency response function;

f = Darcy-Weisbach friction factor;

g = gravitational acceleration;

H = piezometric pressure head;

H_0 = mean pressure head;

h = pressure head perturbation in the frequency domain;

h^* = pressure head perturbation from the mean;

h_D^* = dimensionless pressure head $(H - H_0)/(au_0/g)$;

$i = (-1)^{1/2}$;

K = bulk modulus of elasticity of the water;

L = total pipe length;

l_n = length of the n-th pipe;

n = n-th pipe (subscript);

n = upstream end of the n-th pipe (superscript);

n+1 = downstream end of the n-th pipe (superscript);

P = piezometric pressure;

Q = pipe discharge;

Q_0 = mean discharge;

q = discharge perturbation in the frequency domain;

q^* = discharge perturbation from the mean;

R = frictional resistance;

$S_{xx}(\omega)$ = Fourier transform of the autocorrelation of the input;

$S_{xy}(\omega)$ = Fourier transform of the cross-correlation between the input (x) and the output (y);

T_{th} = theoretical period of the pipe system;

t = time;

t_D^* = dimensionless time t/T_{th};

u_0 = initial average axial velocity in the pipe;

x = distance along the pipe;

Z = characteristic impedance;

Greek Symbols

α = a nondimensional parameter that is determined by the elastic properties of the pipe and its external constraints;

ρ = fluid (water) density;

τ_w = pipe wall shear stress;

τ_{ws} = quasi-steady component of τ_w;

τ_{wu} = unsteady component of τ_w;

ω = frequency;

ω_D^* = dimensionless frequency ω/ω_{th};

ω_{th} = theoretical frequency of the pipe system $1/T_{th}$.

Chapter 3

Roman Letters

A = pipe cross-sectional area;

a_0 = transient wave speed;

D/Dt = material derivative in cylindrical coordinates;

f_x = body force along x;

f_r = body force along r;

f_r = body force along θ;

g = gravitational acceleration;

H = pressure head;

k = bulk modulus;

M = Mach number;

p = pressure;

Q = discharge;

r = radial distance from the pipe axis;

t = time;

u = axial velocity;

v = radial velocity;

w = azimuthal velocity;

x = axial distance along the pipe axis;

Greek Symbols

θ = azimuth;

κ = volume viscosity of the fluid;

μ = dynamic viscosity of the fluid;

ρ = density of the fluid;

ρ_0 = reference density of the fluid;

τ_w = wall shear stress;

τ_{ws} = quasi-steady component of τ_w;

τ_{wu} = unsteady component of τ_w.

Chapter 4

Roman Letters

$A = A(x)$ = pipe cross-sectional area;

$a = a(x)$ = wave speed;

a_0 = wave speed in intact pipelines;

$a_b = a_b(x)$ = wave speed within non-uniform blockages;

$\bar{a}_b$ = average wave speed within non-uniform blockages;

c_m = sensitivity coefficient;

g = gravitational acceleration;

h = pressure head deviation in the frequency domain;

$k = k(x) = \omega/a(x)$ = wave number;

k_b = wave number for the non-uniform blockage;

k_0 = wave number for the uniform blockage;

L = total length of pipeline systems;

l_n = length of the n-th non-uniform blockage;

m = peak number;

n = pipeline number;

P = instantaneous pressure in the time domain;

P_0 = mean pressure in the time domain;

p^* = pressure deviation from the P_0;

p = pressure in the frequency domain;

q = discharge deviation in the frequency domain;

R = intact pipe radius;

R_{Ln} = pipe radius at the left boundary of the n-th non-uniform blockage;

r_n = pipe radius of the n-th non-uniform blockage;

$S = (R–R_{L3})/R$ = blockage severity;

$s_n = (R–R_{Ln})/l_n$ = slope of the n-th non-uniform blockage;

t = time;

U_{ij} = elements of transfer matrix;

U_{ij}^* = elements of the overall transfer matrix for the four-pipeline system;

x = axial coordinate along the pipeline;

Greek Symbols

$\delta\omega^*_m$ = blockage induced frequency shift for the m-th resonant peak;

$\delta h_{B,m}$ = blockage induced resonant peak amplitude change for the m-th resonant peak;

ω = angular frequency;

ω_{th} = fundamental frequency of the pipeline system;

ω^* = non-dimensional frequency;

ω^*_{mb} = frequency of m-th resonant peak for the blocked pipeline system;

ω^*_{mi} = frequency of m-th resonant peak for the intact pipeline system.

Chapter 5

Roman Letters

$A = A(x)$ = pipe cross-sectional area;

a_0 = wave speed;

"exp" = is short for "exponential";

g = gravitational acceleration;

h = pressure head deviation in the frequency domain;

I = power intensity;

"Im" = imaginary part;

i = imaginary number;

k = wave number;

k_0 = wave number in intact pipe sections;

k' = group wave number in the exponential non-uniform blockage;

l_n = length of the n-th non-uniform blockage (or pipe);

M, N = constants;

P = pressure in the time domain;

P^* = dimensionless pressure in the time domain;

P_{in} = the incident wave pressure at the generator;

P_0 = the initial pressure in the pipeline;

p^* = pressure deviation from the mean in the time domain;

p = pressure deviation from the mean in the frequency domain;

q = discharge deviation in the frequency domain;

R = radius of an intact pipe;

"Re" = real part;

R_C = pipe radius at Junction C;

$r = r(x)$ = pipe radius;

S_0 = pipe cross-sectional area of intact junctions;

S_n = pipe cross-sectional area at Junction n;

s = a coefficient that determines the radius changing rate of non-uniform blockages;

T_C = energy transmission coefficient;

t = time;

U_{ij} = transfer matrix elements;

U_{ij}^* = system overall transfer matrix elements;

V_{ij}^* = system overall transfer matrix elements (in terms of u and p);

u^* = axial velocity deviation from the mean in the time domain;

u = axial velocity deviation from the mean in the frequency domain;

W = energy flow;

x = distance along the pipeline;

Z = impedance;

Greek Symbols

$\delta\omega^*$ = normalized resonant frequency shift induced by blockages;

ρ_0 = fluid density;

ω = angular frequency;

ω^* = dimensionless angular frequency;

ω_c = angular central frequency of the incident wave;

ω_{cut} = cutoff frequency of the exponential non-uniform blockage.

Chapter 6

Roman Letters

a_0 = wave speed;

f_{in} = valve oscillation frequency;

f_r = radial wave frequency;

F_r = body force along r;

F_x = body force along x;

I = total number of spatial grids in the ξ-direction;

i = i-th spatial step in the ξ-direction;

J = total number of spatial grids in the η-direction;

j = j-th spatial step in the η-direction;

$\mathbf{K}$ = $\mu/R\rho_0 a_0$;

k = bulk modulus;

k_{rm} = radial wave number of the m-th radial mode;

L = total length of the pipe;

$\mathbf{M}$ = Mach number u_0/a_0;

N_r = grid number along the pipe radius;

n = n-th time step;

p' = pressure;

p = dimensionless pressure $(p' - p_e')/\rho_0 u_0 a_0$;

p_{avg} = area-averaged pressure;

p_{axis} = pressure at the pipe axis;

p_{wall} = pressure at the pipe wall;

p_e' = pressure at $x = 0$;

R = pipe radius;

r = radial coordinate from pipe centerline;

Re = Reynolds number;

T_{th} = system theoretical period $4L/a0$;

t = time;

u_0 = the initial average axial velocity;

u' = axial velocity;

u = dimensionless axial velocity u'/u_0;

V_{gm} = group velocity of m-th radial mode;

v' = radial velocity;

v = dimensionless radial velocity v'/u_0;

x = axial coordinate along pipe centerline;

Greek Symbols

$\Delta\eta$ = spatial step in the η-direction;

$\Delta\xi$ = spatial step in the ξ-direction;

$\Delta\tau$ = size of time step;

η = dimensionless radial coordinate r/R;

κ = volume viscosity;

μ = dynamic viscosity;

ξ = dimensionless axial coordinate x/R;

ρ = fluid density;

ρ_0 = mean density of the fluid (water);

τ = dimensionless time a_0t/R;

τ_0 = time duration of the valve oscillation;

ω = frequency in radius per second.

Chapter 7

Roman Letters

a = transient wave speed;

a_0 = transient wave speed in intact pipes;

a_{th} = theoretical transient wave speed in elastic pipes;

$\bar{a}_b$ = average wave speed within the blockage section;

D = pipe diameter;

E = Young's modulus of elasticity of the pipe wall;

e = pipe wall thickness;

F_r = body force along r;

F_x = body force along x;

$FRF(\omega)$ = frequency response function;

g = gravitational acceleration;

h = pressure head deviation in the frequency domain;

K = bulk modulus of elasticity of water;

K' = modified bulk modulus of water;

L = total length of the pipe;

l_n = pipe length of the n-th pipe;

M_{in} = amplitude of the incident wave in the frequency domain;

M_{tr} = amplitude of the transmitted wave in the frequency domain;

m = m-th resonant peak in the frequency domain;

n = n-th pipe;

N_r = number of mesh in the radial direction;

p = pressure;

p^* = dimensionless pressure $(p - p_0)/(\rho a_0 u_0)$;

p_{in} = incident wave pressure at the generator;

q = discharge deviation in the frequency domain;

R = inner radius of the pipe;

R_C = pipe radius at Junction C;

Re = Reynolds number;

r = radial coordinate from the pipe axis;

r^* = dimensionless radial coordinate r/R;

S = pipe cross-sectional area;

S_0 = intact pipe cross-sectional area;

$S_{xx}(\omega)$ = Fourier transform of the autocorrelation of the input;

$S_{xy}(\omega)$ = Fourier transform of the cross-correlation between the input (x) and the output (y);

T_C = energy transmission coefficient;

t = time;

t^* = dimensionless time $t/(4L/a_0)$;

U_{ij}^* = elements of the system overall transfer matrix;

u = axial velocity;

u_0 = initial average axial velocity;

u^* = dimensionless axial velocity u/u_0;

v = radial velocity;

W_{in} = energy flow incident on the non-uniform blockages;

W_{tr} = energy flow (i.e., power) transmitted through the non-uniform blockages;

x = axial coordinate along the pipe axis;

Greek Symbols

α = a coefficient that determines the amplitude of the incident wave;

β = a coefficient that determines the frequency bandwidth of the incident wave;

Δr = mesh size along the radial direction;

Δt = time step;

Δx = mesh size along the axial direction;

$\Delta\omega_m^*$ = dimensionless frequency shift of the m-th resonant peak;

μ = dynamic viscosity;

v = Poisson ratio;

ρ = density of water;

ω_c = central frequency of the incident wave;

ω^* = dimensionless frequency of the wave, which is normalized by the fundamental frequency of the non-uniform blockage;

ω_{mb}^* = frequency of the m-th resonant peak in the blocked pipe system;

ω_{mi}^* = frequency of the m-th resonant peak in the intact pipe system.

CHAPTER 1 INTRODUCTION[1]

1.1 Research Background and Problem Statement

1.1.1 Aging Urban Water Supply Systems

Urban water supply systems, comprised of thousands of kilometers of underground pipes, are the backbone of the public health and economic welfare of modern cities. Most of these vast networks were accumulatively laid down and paid for by previous generations, especially after World War II (i.e., 1945), to meet the needs of population growth and urban expansion (AWWA, 2001). Due to aging without timely repairs, a substantial portion of these pipes are reaching or have reached the end of their service lives, which are riddled with anomalies (e.g., leaks, blockages, illegal branches, and corrosion in Fig. 1.1) and inefficiencies. It was estimated that the volume of drinking water annually lost by water facilities worldwide is around 126 billion m^3 (i.e., nearly 77 liters per capita per day) in 2016, mostly from unseen leaks, which costs US$ 39 billion (Liemberger & Wyatt, 2019). As shown in Fig. 1.2, the percentage of water lost through leaks during its transmission varies significantly among cities around the world, from 3-5% in well maintained cities like Tokyo (Japan), Amsterdam (Netherlands), and Los Angeles (USA) to 40-60% in cities like Dublin (Ireland), Lusaka (Zambia), and Kolkata (India) (Cao & Ruan, 2017). The level of services to consumers has been deteriorating during the last couple of decades due to the continuous emergence of leaks, blockages, and other pipe anomalies.

Over the past decades, these anomalies in pipe networks were thought to be insignificant and largely ignored by the younger generation (Ferrante & Brunone, 2003a) because (i)

[1] This chapter is an excerpt from the review paper of the author and his co-authors (Che et al., 2019a).

these problems happen underground, out of sight and out of mind; (ii) most of these pipes are inherited from, and initially paid for by, earlier generations; and (iii) the supply of tap water is sufficient and cheap due to the abundance of water and energy resources. For these reasons, the younger generation has enjoyed the honeymoon period with the relatively young pipe networks for several decades.

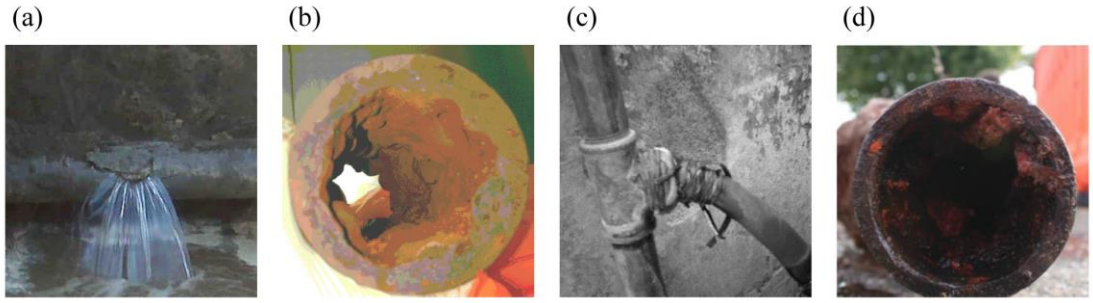

Fig. 1.1. Different types of pipe anomalies in real urban water supply systems: (a) leak; (b) blockage (James & Shahzad, 2003); (c) illegal branches (Meniconi et al., 2011d); and (d) corrosion (internal view) (Lee et al., 2017).

However, the repair, or even replacement, of these pipes is needed as they reach the end of their service lives. The Hong Kong Government has investigated US$ 3 billion to its 15-year (i.e., 2000 to 2015) Replacement and Rehabilitation of Water Mains Programme. This program involves the replacement and rehabilitation of 3000 km of aged water mains (i.e., more than 50%) out of its total 5700 km water mains in 15 years to rejuvenate the water supply network. Despite such a comprehensive and systemic program, around 16% of the supplied water and energy is still lost, at an annual cost of US$ 200 million (HK-WSD, 2019). In fact, a massive upgrade of the ageing pipe networks around the world exerts growing financial pressure on governments that will continually increase in the coming decades. For example, to maintain a reasonable level of services to consumers, the American Water Works Association (AWWA) estimated that the total costs needed nationally to restore its aged water pipes are around US$ 500 billion and US$ 1 trillion in the next 25 and 40 years, respectively (AWWA, 2012). Therefore, these programs result in huge expenses most of which will be borne by customers in the younger generation, mainly through higher water bills. It was estimated that these investments could triple the

usual water bills of a typical American family (AWWA, 2012). In addition, the worldwide water and energy shortages in recent years also enable water utility managers to give priority and allocate expenditure to pipe anomaly detection and pipe condition assessment, which is regarded as “a money- saving expense” (AWWA, 1979).

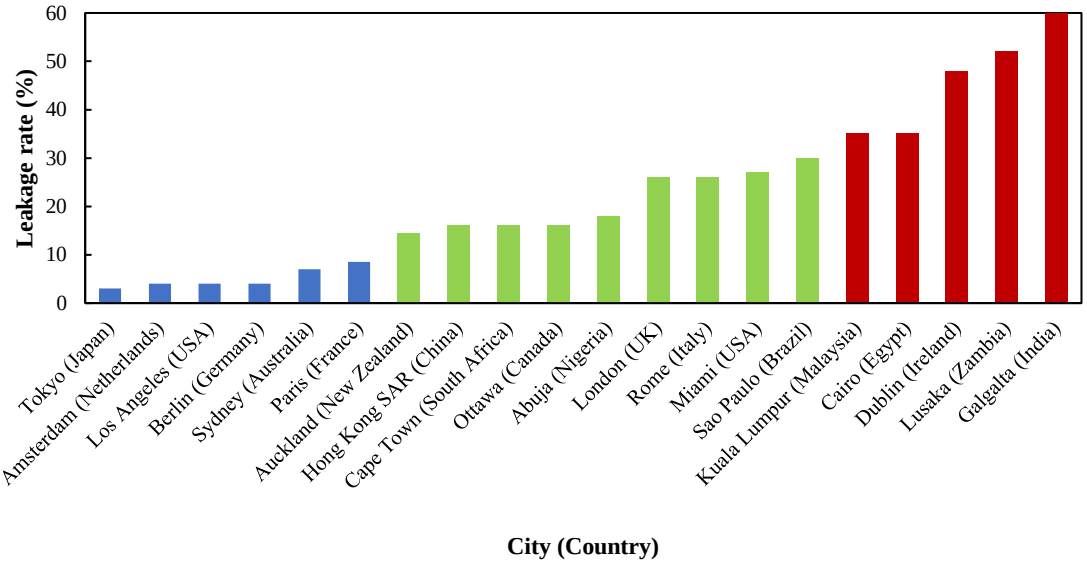

Fig. 1.2. Percentage of water losses through leaks in 20 cities worldwide.

These deteriorating situations and growing market demands have stimulated the development of various techniques for pipe anomaly detection and overall pipe condition assessment (Datta & Sarkar, 2016; Hamilton & Charalambous, 2013; Liu & Kleiner, 2013).

1.1.2 Existing Methods for Pipe Anomaly Detection

Based on the obtained information used for pipe anomaly detection, existing methods can be generally classified into two categories: acoustic and non-acoustic techniques. A detailed review of existing methods for anomaly detection is beyond the scope of the present chapter; thus, only several typical acoustic and non-acoustic techniques are briefly summarized as follows:

Acoustic Techniques

A leak induces a hissing noise (i.e., vibrate the pipe wall and the surrounding soil at high frequency) when the water jets out from the pipe (Lee, 2005). A listening stick with an earpiece is placed in contact with the ground surface to listen to the leak-induced noise. The leak location can be estimated by shifting the stick along the pipe until the maximum leak-induced noise is detected. In practical applications, the leak-induced noise can be further enhanced by some electronic amplified listening devices (e.g., an electronic acoustic microphone) (Hamilton & Charalambous, 2013; Lee, 2005). A leak noise correlator is a more advanced acoustic technique used as a leak locator to find leaks in pressurized water pipes. Usually, accelerometers or hydrophones are placed in contact with the outside of the pipe wall or the water inside the pipe, at two points, to measure the noise induced by a potential leak between these two points. The cross-correlation (see Section 2.3.1) between these two measured signals is used to determine the time lag between two sensors for receiving the same noise emitted by the leak. Based on this time lag, along with the known acoustic wave speed and locations of measurement points, the location of the leak can be determined (Hamilton & Charalambous, 2013; Lee, 2005). More detailed information about these acoustic techniques for leak detection can refer to (Hamilton & Charalambous, 2013; Lee, 2005; Li et al., 2014; Liu & Kleiner, 2013, 2014).

Small leaks induce high frequency noises (while big leaks do not), but the amplitude of these noises is relatively small. In addition, these leak-induced noises may attenuate rapidly in elastic pipes within 200 m (Lee, 2005). This attenuation becomes even more rapid in plastic pipes because of the more significant energy absorption into the pipe wall and the surrounding soil (Hamilton & Charalambous, 2013). Therefore, acoustic techniques have evident limitations in terms of the detection range and the application diversity of pipes. Moreover, due to the lack of external evidence (i.e., a hissing noise), acoustic techniques are even more difficult to apply for the detection of other pipe anomalies, such as blockages.

Non-acoustic Techniques

Besides hissing noises, the presence of a leak (or other pipe anomalies) also changes the appearance of the pipe wall and physical properties (i.e., porosity and conductivity) of surrounding soils, which forms the basis of non-acoustic techniques for pipe anomaly detection. The current commercially available non-acoustic techniques can be classified into two groups: (i) intrusive techniques, such as the closed-circuit television (CCTV) cameras and gas injection method; and (ii) non-intrusive techniques, such as the ground penetrating radar and thermal infrared imagers.

At present, internal real-time inspection of pipe wall conditions by inserted CCTV cameras (or smart balls) is a common approach for pipe anomaly detection (Henry & Luxmoore, 1996). This technique is more appropriate for single or simple pipe systems, because internal inspection by CCTV cameras is a slow, tedious, and costly process, which needs to be operated by relatively experienced personnel. In addition, it may need the target pipe systems to be off-line, and the caused service interruption would disturb the normal life of water users. The ground penetrating radar, which is a non-intrusive technique, allows leaks to be detected without a device intrusion into the pipe. A radar pulse is injected into the ground, and the reflected signals from subsurface structures are collected by receivers on the surface. The general conditions (i.e., porosity and conductivity) of surrounding soils can be determined based on the reflected signals, which are indicators of potential leaks (Hamilton & Charalambous, 2013; Lee, 2005). However, the relatively high energy consumption of this technique limits its extensive field applications. Besides, considerable expertise is needed to effectively conduct the surveys and interpret the obtained results.

The above mentioned acoustic and non-acoustic techniques (Datta & Sarkar, 2016; Hamilton & Charalambous, 2013; Liu & Kleiner, 2013) have played important roles in the pipe condition assessment of urban water supply systems. But none of them is a panacea that could be used in all pipe systems with different scales and configurations,

and the current severe situation of water and related energy losses (see Section 1.1.1) has evidenced the inadequacy and inefficiency of these existing techniques for improving the current situation. Therefore, it is practically urgent and necessary to develop a more comprehensive and effective method for pipe anomaly detection.

1.1.3 Transient-based Methods for Pipe Anomaly Detection

Ideally, a pipe anomaly detection technique should be accurate, efficient, and cheap to use. In addition, it should not disturb the normal operations of the pipe system (Ferrante et al., 2014; Taghvaei et al., 2006). The transient-based method, which detects pipe anomalies based on the data collected by transient waves with high propagation speeds, meets these requirements.

As an attractive alternative to existing methods, in the past two decades, *transient waves* (also termed as transient pressure waves, hydraulic transients, or water hammer waves) have been widely used for the detection of various pipe anomalies and general pipe wall condition assessment (Brunone, 1999; Duan et al., 2012a; Gong et al., 2013b; Lee et al., 2006a; Lee et al., 2008b; Liggett & Chen, 1994; X. J. Wang et al., 2005; X. J. Wang et al., 2002) (more detailed information is summarized in Chapter 2). This transient-based method is regarded as a promising way for diagnosis pipe anomalies since it has the desirable merits of high efficiency, low cost, and non-destructive applications. As shown in Fig. 1.3, the tenet of this transient-based method is that a transient wave, with a high propagation speed around 1000 m/s, is injected into the target pipe system at an accessible point (e.g., a fire hydrant), and the pressure response of the pipe system is measured at specified location(s), which is modified by, and thus contains information on, properties and states of the pipe system. Compared with the leak-induced acoustic signals, the transient waves have a high tolerance to background noise and can propagate longer distances with less attenuation, which are suitable for remote surveillance (X. J. Wang et al., 2005).

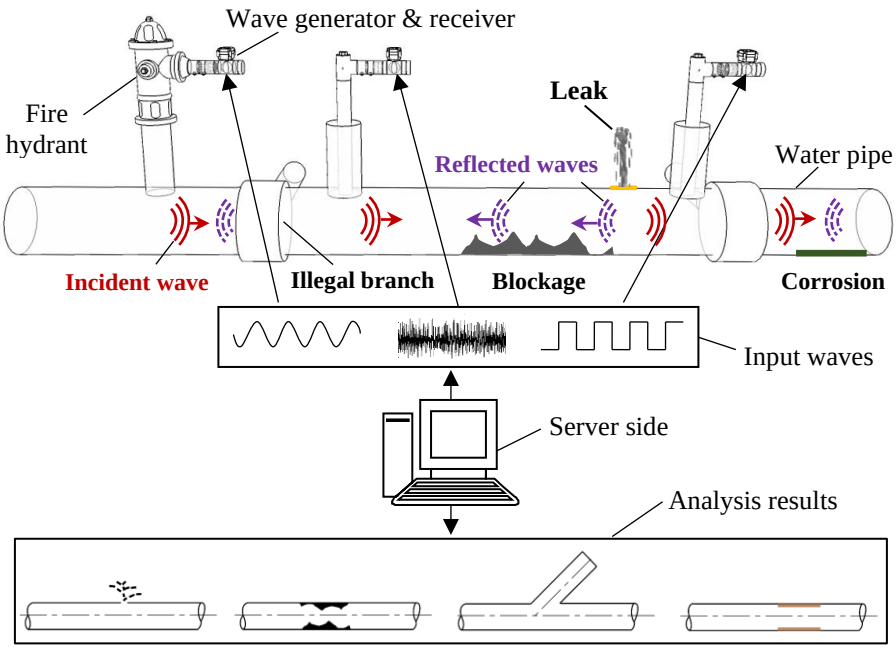

Fig. 1.3. Illustration of the tenet of the transient-based method for pipe anomaly detection.

1.1.4 Problems of the Transient-based Method for Blockage Detection

In urban water supply systems, partial and extended *blockages* are commonly formed in pipes from various complicated physical, chemical, and biological processes (e.g., sediment deposition, corrosion, and biofilm accumulation). These blockages reduce pipe diameters and increase pipe wall roughness, resulting in lower water-carrying capacity, additional energy loss, and deterioration of water quality. In addition, blockages may significantly change the maximum and minimum pressure heads during hydraulic transients, which may exceed the original transient design capacity; thus, potentially increase the failure rate of pipe systems. Unlike leaks, blockages are easily masked in the inaccessible buried pipe network since they lack external evidence (e.g., a hissing noise) needed for detection, and the lost pressure and flow across blockages can be compensated by other branch pipes in the network. For these reasons, detection techniques are in urgent need to diagnose these blockages in the early stages so as to minimize the resultant problems and wastage.

Despite the successful applications of the transient-based method for extended blockage detection in many numerical and laboratory tests (Duan et al., 2014; Duan et al., 2012a; Duan et al., 2013; Meniconi et al., 2013a), this method in these previous studies is based on blockages of uniform constriction along their lengths (termed as *uniform blockages*), which is equivalent to multiple pipes with different diameters connected in series as shown in Fig. 1.4(c). However, real world blockages are commonly formed from various complicated sources and processes; thus, as shown in Figs. 1.4(a) and 1.4(b), they usually constrict randomly and non-uniformly along their lengths (termed as *non-uniform blockages*). Inaccuracy and invalidity of the current transient-based method have been observed in laboratories for non-uniform blockage detection. This is mainly because the current transient-based theory is incapable of describing the interaction between transient waves and non-uniform blockages. Therefore, a physical understanding of the ***transient wave behavior in water pipes with non-uniform blockages*** is necessary to enhance the practical applications of the transient-based method for real world blockage detection, which is the main research motivation of this thesis.

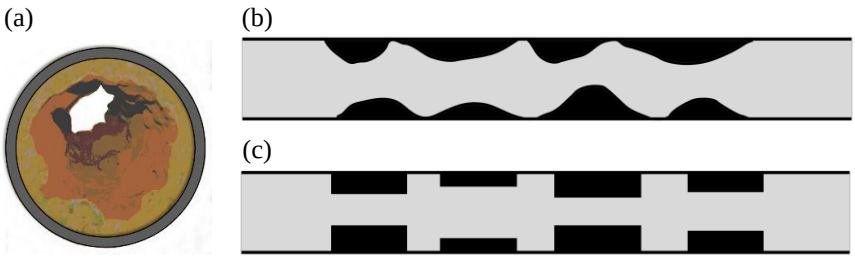

Fig. 1.4. (a) Random and non-uniform blockages in real water pipes (Che et al., 2018b); (b) sketch of a real pipe with random and non-uniform blockages; and (c) sketch of a pipe with simplified uniform blockages used in previous studies.

1.2 Research Aims

The overall aim of this thesis is to investigate *transient wave behavior in water pipes with non-uniform blockages*. It is expected that the physical understanding gained in this thesis would narrow the gap between transient-based theory and practical applications of non-uniform blockage detection. The overall aim is decomposed into four specific aims, as follows. The relationships between these aims are illustrated in Fig. 1.5.

Aim 1: To quantify the effect of properties of a non-uniform blockage in water pipes on the system response in the *frequency* domain.

Aim 2: To understand the physical mechanism of the interaction between transient waves and non-uniform blockages and observe the transient wave behavior in the *time* domain.

Aim 3: To determine the *frequency range of validity* of the developed theory (i.e., Aims 1 & 2) and observe the behavior of radial pressure waves in water pipes.

Aim 4: To validate the developed theory by numerical computational fluid dynamics (CFD) experiments under more realistic and complex conditions.

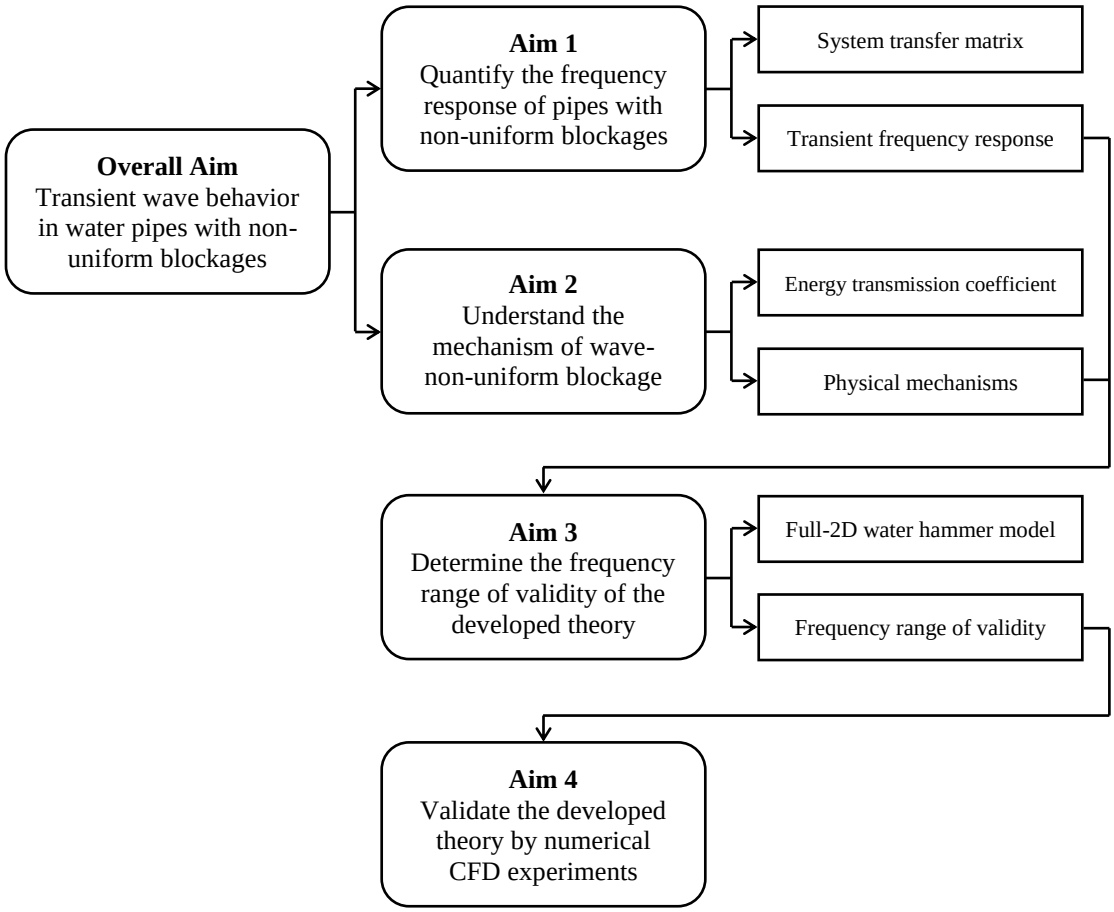

Fig. 1.5. Research aims and their relationships.

1.3 Thesis Outline

Besides **Chapter 1** Introduction, this thesis consists of seven additional chapters, which are organized as follows. The relationships of these chapters are illustrated in Fig. 1.6.

Chapter 2 conducts an extensive literature review on the application of transient waves for pipe anomaly detection. This chapter first introduces the fundamentals of transient theory and applications (e.g., the basic properties of transient waves, the excitation and measurement of transient waves, and the techniques for signal processing and feature extraction). On these bases, the state-of-the-art review of four transient-based methods (i.e., ITA, TWR, TWD, and TFR) for pipe anomaly detection since 1990s is conducted, followed by a brief description of the transient-based method for extended blockage detection in water pipes.

Chapter 3 presents the fundamental models and governing equations of transient pipe flows used in this thesis. The derivation procedure of various forms of one-dimensional (1D) and 2D water hammer models from the 3D Navier-Stokes equations for a compressible fluid is given, during which the assumptions inherent in these models are illuminated.

Chapter 4 investigates the transient frequency responses of water pipes with a non-uniform blockage. To understand the fundamental physics and mechanism of wave-non-blockage interaction, the transient wave behavior in a linear non-uniform blockage is obtained by analytically solving the 1D wave equation under specific initial and boundary conditions. The obtained wave solutions are incorporated into the overall transfer matrix of a reservoir-pipe-valve (RPV) system with a non-uniform blockage, which is used to systematically quantify the effect of properties of a non-uniform blockage on the transient frequency responses.

Chapter 5 explains the physical mechanism of the resonant frequency shift pattern induced by a non-uniform blockage in water pipes (observed in Chapter 4) from an energy

perspective. For this purpose, the energy transmission coefficient of transient waves in an unbounded water pipe with various blockages is analytically derived based on the system overall transfer matrix. Afterwards, the influence of non-uniform blockage properties on the energy transmission of transient waves is investigated systematically based on the derived result.

Chapter 6 studies the frequency range of validity of the developed theory (in Chapters 4 and 5) and observes the behavior of radial pressure waves in water pipes. The inefficiency of the current numerical scheme for solving the full-2D water hammer model is firstly addressed. The modified efficient scheme is used to study the generation mechanism and components of radial pressure waves induced by different valve operations.

Chapter 7 validates the developed theory (in Chapters 4 and 5) by numerical CFD experiments under more realistic and complex conditions. The full-2D axisymmetric Navier-Stokes equations are solved by the Semi-Implicit Method for Pressure Linked Equations (SIMPLE) algorithm in a cylindrical coordinate system. Various boundary conditions (e.g., pipe wall elasticity and transient excitation operations) are included into the full-2D model by user-defined functions (UDFs).

Chapter 8 summarizes major conclusions of this thesis and gives recommendations for potential future work.

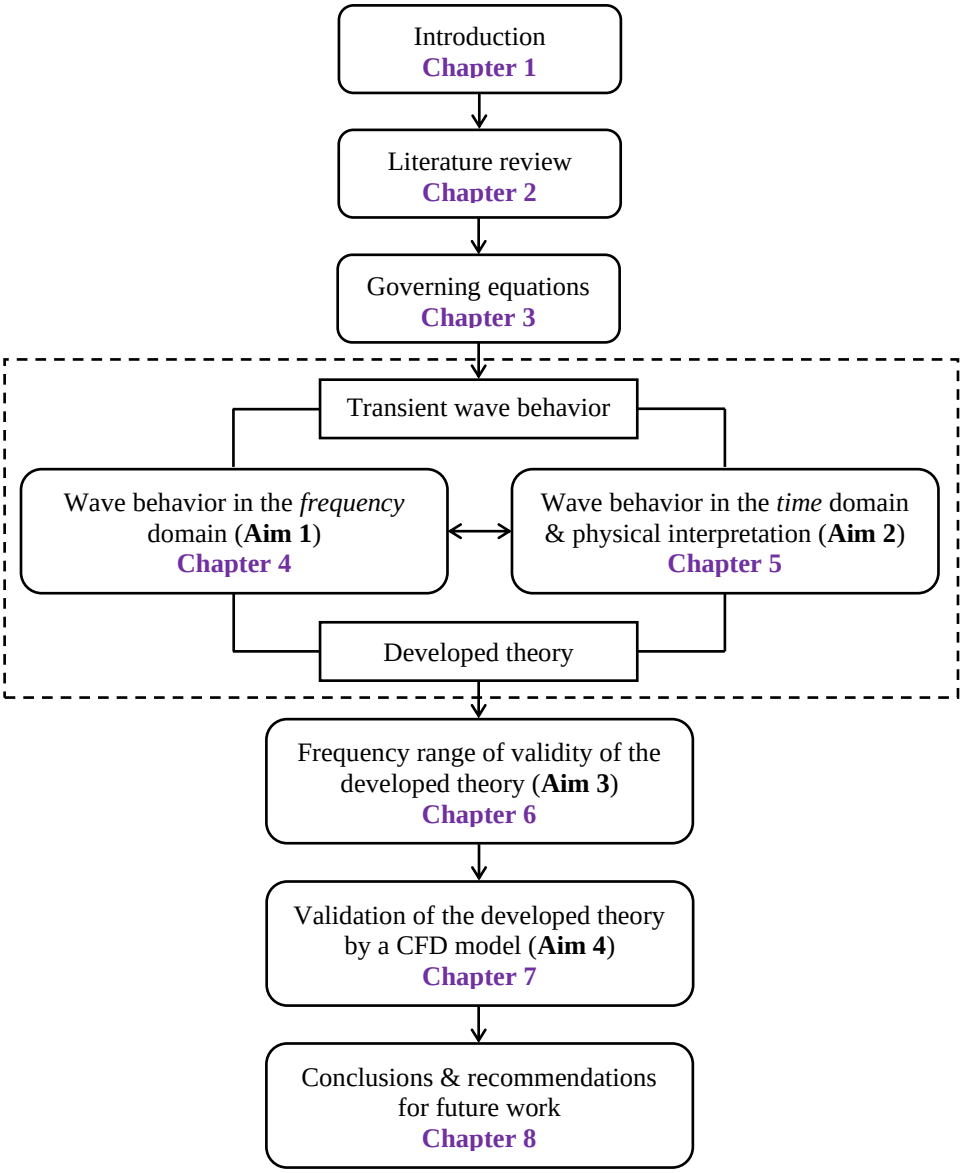

Fig. 1.6. Structure of this thesis.

1.4 Contributions to the Field

The main contributions of this thesis to the field are:

1. This research is one of the first to investigate the interaction between transient waves and non-uniform blockages, which provides a general framework for the analysis of real pipes with non-uniform blockages.

2. The quantification of properties of a non-uniform blockage on the transient frequency response of a pipe system is fundamental to extend the current transient-based method for non-uniform blockage detection in future work.

3. The development of a procedure for deriving the energy transmission coefficient of transient waves through various non-uniform blockages in water pipes. In practical non-uniform blockage detection, this coefficient allows to select the appropriate frequency and bandwidth of the incident wave to ensure that the reflected wave contains enough energy for pressure transducers to measure.

4. The modification of a numerical scheme for solving the full-2D water hammer model provides a useful tool for: (i) determining the frequency range of validity of the plane wave assumption; and (ii) observing the behavior of radial pressure waves in water pipes.

The physical understanding gained in this thesis may contribute to narrow the gap between transient-based theory and practical applications of non-uniform blockage detection, which is crucial and necessary for developing smart urban water supply systems.

The key results and findings of this thesis research have been or are to be published in the top professional journals or conference proceedings in this field, which may provide useful information and a scientific basis for future research work.

CHAPTER 2 LITERATURE REVIEW[2]

2.1 Fundamentals of Transient Waves in Pipes

2.1.1 Transient Waves and Transient Wave Speeds

Transient Waves

Transient (or water hammer) waves are a series of positive and negative pressure waves (i.e., unsteady pressure fluctuations) propagating at high wave speeds around 1000 m/s in elastic water pipes. These pressure fluctuations are often caused by sudden flow changes in terminals or boundaries of the pipe system. In urban water supply systems, transient waves are easily and frequently introduced through some accidental or planned changes in operating conditions, such as opening or closing of valves, starting or stopping of pumps, and variations in water supply and customer consumption (Chaudhry, 2014; Wylie et al., 1993).

Transient Wave Speeds

The general expression of the transient wave speed is (Ghidaoui, 2004; Ghidaoui et al., 2005)

$$\frac{1}{a^2} = \frac{d\rho}{dP} + \frac{\rho}{A}\frac{dA}{dP} \tag{2.1}$$

where a = transient wave speed; ρ = fluid (water) density; P = piezometric pressure; A = pipe cross-sectional area.

[2] This chapter is an excerpt from the review paper of the author and his co-authors (Che et al., 2019a).

Eq. (2.1) indicates that the transient wave speed mainly depends on two factors: (i) the first term on the right-hand side represents the effect of water compressibility; and (ii) the second term represents the effect of pipe wall elasticity.

By relating the right-hand side of Eq. (2.1) to the material properties of the water and to the material and geometrical properties of the pipe (the detailed process is reported in Ghidaoui et al. (2005)), Eq. (2.1) becomes (Chaudhry, 2014)

$$a = \sqrt{\frac{K}{\rho\left[1+\left(K/E\right)\alpha\right]}} \tag{2.2}$$

where K = bulk modulus of elasticity of the water (depends on temperature, pressure, and the quantity of entrained air); E = Young's modulus of elasticity of the pipe wall; α = a nondimensional parameter that is determined by the elastic properties of the pipe (depends on its size, wall thickness, and wall material) as well as its external constraints (depends on the type of supports and longitudinal restraints).

In practical urban water supply systems, the actual wave speed may be different from the theoretical value given by Eq. (2.2) due to many factors, such as uncertainties in the age and condition of most buried pipes (Covas et al., 2004; Shucksmith et al., 2012).

2.1.2 Analysis and Simulation of Transient Waves

Governing Equations

The commonly used tool for transient wave simulation in the time domain is the following one-dimensional (1D) water hammer model (see Chapter 3), which consists of mass and momentum equations (Chaudhry, 2014; Ghidaoui et al., 2005; Wylie et al., 1993)

$$\frac{gA}{a^2}\frac{\partial H}{\partial t}+\frac{\partial Q}{\partial x}=0 \tag{2.3}$$

$$\frac{\partial Q}{\partial t}+gA\frac{\partial H}{\partial x}+\frac{\pi D}{\rho}\tau_w=0 \tag{2.4}$$

where H = piezometric pressure head; Q = pipe discharge; t = time; x = distance along the pipe; g = gravitational acceleration; D = pipe diameter; and τ_w = pipe wall shear stress, which can be divided into two parts as

$$\tau_w = \tau_{ws} + \tau_{wu} \tag{2.5}$$

where τ_{ws} = quasi-steady component of τ_w; and τ_{wu} = unsteady component of τ_w.

The method of characteristics (MOC) is the most popular numerical scheme for this 1D model, because it is simple, stable, and efficient for numerical implementation (Chaudhry, 2014; Ghidaoui et al., 2005). In addition, this 1D model can be also solved by other numerical schemes (e.g., finite difference and finite volume methods), which are well summarized in the review paper of Ghidaoui et al. (2005).

Alternatively, the above 1D model can be linearized, transformed, and solved in the frequency domain using the transfer matrix method (Chaudhry, 2014; Wylie et al., 1993). The obtained transfer matrix equations are linearized frequency domain equivalents of the 1D mass and momentum equations in Eqs. (2.3) and (2.4), which describe the transient wave behavior in the frequency domain. It is assumed that the discharge and pressure head in the pipe during a transient event are consisted of two parts: (i) the mean value; and (ii) perturbation from the mean.

$$Q = Q_0 + q^* \tag{2.6}$$

$$H = H_0 + h^* \tag{2.7}$$

where Q_0 = mean discharge; q^* = discharge perturbation from the mean; H_0 = mean pressure head; h^* = pressure head perturbation from the mean.

Substituting Eqs. (2.6) and (2.7) into Eqs. (2.3) and (2.4) and performing a sequence of essential mathematical operations (the detailed process is reported in (Chaudhry, 2014; Wylie et al., 1993)), during which only the quasi-steady part of pipe wall shear stress (i.e., τ_{ws} in Eq. (2.5)) is considered. Finally, the transfer matrix equation is expressed as

$$\begin{Bmatrix} q \\ h \end{Bmatrix}^{n+1} = \begin{bmatrix} \cosh(\mu_n l_n) & -\frac{1}{Z}\sinh(\mu_n l_n) \\ -Z\sinh(\mu_n l_n) & \cosh(\mu_n l_n) \end{bmatrix} \begin{Bmatrix} q \\ h \end{Bmatrix}^{n} \tag{2.8}$$

where q = discharge perturbation in the frequency domain; h = pressure head perturbation in the frequency domain; subscript n = n-th pipe; superscript n, n+1 = upstream and downstream ends of the n-th pipe, respectively; l_n = length of the n-th pipe; $\mu_n = (-\omega^2/a^2 + igA\omega R/a^2)^{1/2}$, in which ω = frequency, $i = (-1)^{1/2}$, $R = (fQ_0)/(gDA^2)$ = frictional resistance, f = Darcy-Weisbach friction factor; and $Z = (\mu_n a^2)/(i\omega gA)$ = characteristic impedance.

Once the magnitude of responses (i.e., discharge and pressure head) at the upstream end is known, the responses at the downstream end can be produced by Eq. (2.8). In other words, the transfer matrix in Eq. (2.8) directly relates the discharge and head perturbations at both ends without discretization of the pipe in space; thus, the transfer matrix method has the advantage of high computational efficiency compared with some time domain methods, such as the MOC.

Common Boundary Conditions

In practical urban water supply systems, pipes are commonly bounded by various hydraulic devices, from simple (e.g., reservoirs and valves) to complex (e.g., pumps and turbines). An injected transient wave can be reflected by these boundaries and their detailed characteristics can refer to (Chaudhry, 2014; Wylie et al., 1993). To simplify the problem, the theoretical development of transient-based methods in previous studies for pipe anomaly detection is mainly conducted in pipe systems with simple boundary conditions (e.g., reservoirs and valves). In this chapter, a simple reservoir-pipe-valve (RPV) system, as shown in Fig. 2.1, is adopted to illustrate the transient wave behavior in intact pipes as well as pipes with various anomalies.

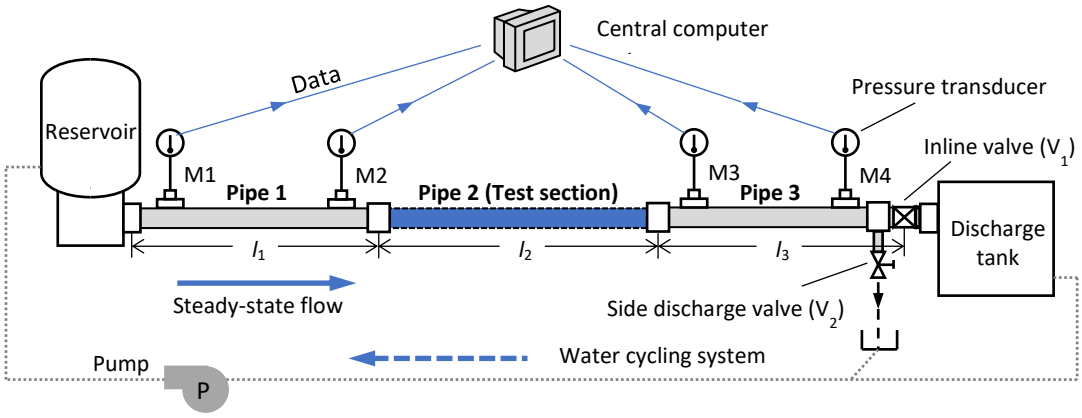

Fig. 2.1. A reservoir-pipe-valve (RPV) system.

As shown in Fig. 2.1, the pipe system consists of three pipe sections (i.e., Pipe 1-3) with flange connections. There is a reservoir at the upstream end of the pipe system, whose pressure head is assumed to remain constant during the transient events (i.e., a large reservoir). The downstream end of the pipe system is bounded by an inline valve (i.e., V_1). The inline valve is initially kept open to form a steady flow in the pipe system. One simple way to generate transient waves is to operate (e.g., close) the inline valve to induce a flow change. The pressure response of the pipe system is measured by one, or multiple, pressure transducer(s) along the pipe with a suitable sampling frequency.

2.1.3 Behavior of Transient Waves in Intact Pipes

Influence Factors of Transient Wave Attenuation

Various factors affect the attenuation of transient waves in intact pipes, such as steady friction, unsteady friction, and pipe wall viscoelasticity. In this section, the influence of these factors is investigated and demonstrated numerically by the 1D water hammer model (i.e., Eqs. (2.3) and (2.4)), which is made in the sequence from the simple frictionless case to the complicated (e.g., including steady friction, unsteady friction, or pipe wall viscoelasticity).

As shown in Fig. 2.1, initially, the inline valve (i.e., V_1) is kept fully open to form a steady flow in the RPV system. Transient waves are introduced into the pipe system through a

sudden and complete closure of the inline valve. The induced transient waves propagate back and forth in the pipe system between the upstream and downstream boundaries. A pressure transducer (i.e., M_4) at just upstream of the inline valve is selected to measure the pressure-time history.

The pressure-time histories of different tests (i.e., including different influence factors) measured by the pressure transducer M_4 are plotted in Fig. 2.2(a). As shown in Fig. 2.2(a), the time in the horizontal axis is normalized by the theoretical period of the RPV system $T_{th} = 4L/a$, where L = total pipe length, and plotted as t_D^*. The pressure head in the vertical axis is normalized as $h_D^* = (H - H_0)/(au_0/g)$, where u_0 = initial average axial velocity in the pipe. In the test with no friction, the amplitude and sharpness of the pressure curve keep constant without any attenuation. The first reflected wave occurs at $t^* = 0.5$, during which the initial induced transient wave originates from the downstream valve, propagates in the pipe, impacts on the upstream reservoir, and returns. To gain an insight into the components of the measured pressure curves in the frequency domain, their corresponding frequency response functions (FRF) (see Section 2.3.2) are calculated and plotted in Fig. 2.2(b). As shown in Fig. 2.2(b), the frequency is normalized by the theoretical frequency of the RPV system $\omega_{th} = 1/T_{th}$, and plotted as ω_D^* in the horizontal axis. Fig. 2.2(b) indicates that hydraulic resonance, which results in an amplification of pressure, occurs at characteristic frequencies of the RPV system. In this frictionless test, the amplitude of resonant peaks can be infinite due to the continuous energy accumulation in each time domain cycle without any attenuation.

Subsequently, the steady friction is included in the 1D water hammer model. As shown in Fig. 2.2(a), the presence of steady friction results in a gradual decrease in the pressure amplitude with time. In addition, the period and sharpness of the pressure curve almost keep the same with the frictionless test. Fig. 2.2(b) shows that the inclusion of steady friction does not change the resonant frequencies of the RPV system. Moreover, the steady friction induces a uniform reduction, which is frequency independent, in the amplitude of the FRF. This reduction of amplitude to a finite value is due to the balance

between the provided energy and the energy attenuated by the steady friction of the RPV system.

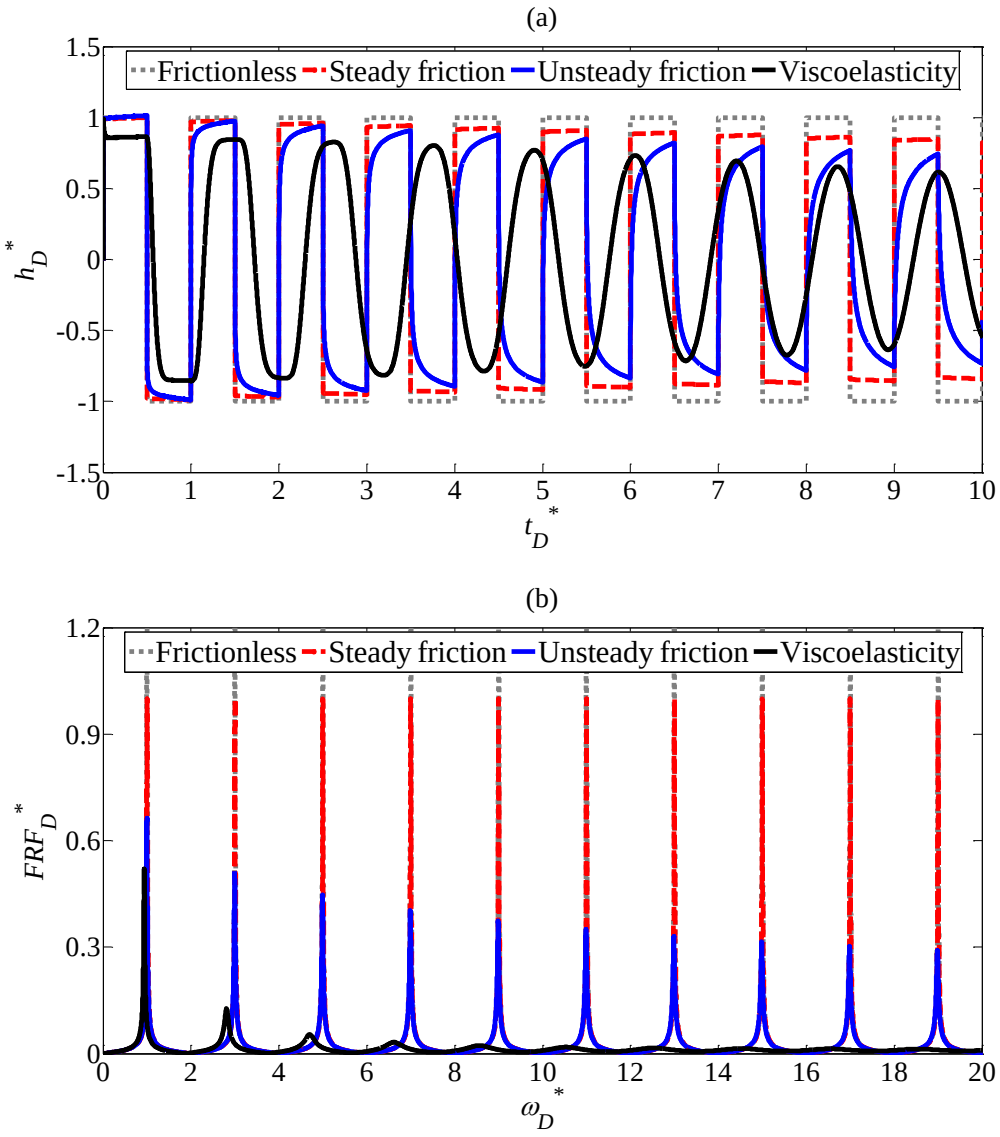

Fig. 2.2. Influence of various factors on transient wave attenuation in intact pipes: (a) time domain; and (b) frequency domain.

Afterwards, the 1D numerical simulation includes the effects of both steady and unsteady friction (Vardy & Brown, 1995; Zielke, 1968). According to Fig. 2.2(a), the presence of unsteady friction dissipates more amplitude of the pressure curve and makes its shape smoother. Fig. 2.2(b) indicates that the unsteady friction causes a further reduction in the amplitude of the FRF. This induced reduction is frequency dependent, which is more evident in higher harmonics.

The last investigated influence factor is the pipe wall viscoelasticity, which is the property of plastic pipes undergoing deformation. It is included in the 1D water hammer model and simulated by the Kelvin-Voigt model (Covas et al., 2005b). Fig. 2.2(a) indicates that the inclusion of pipe wall viscoelasticity induces large amplitude attenuation, significant shape smoothing, and evident period change of the pressure curve. Similar with the unsteady friction, the pipe wall viscoelasticity results in a significant reduction of the amplitude of the FRF, which is also frequency dependent and more evident for higher harmonics. Moreover, the pipe wall viscoelasticity causes the resonant peaks to shift due to the change of oscillation period in the time domain.

Radial Pressure Waves

Note that the behavior of transient waves in pipes demonstrated in this chapter is based on the plane wave theory (Ghidaoui, 2004; Ghidaoui et al., 2005), which means the pressure variation along the pipe radial direction is not considered. However, the pressure along the pipe radius may become curved if the incident wave frequency is higher than the cut-off frequency of the radial mode 1 (M1); thus, radial pressure waves may form and propagate in the pipe system. More detailed information about the behavior of radial pressure waves is reported in (Che et al., 2018a; Louati & Ghidaoui, 2017b, 2017c). This phenomenon is out of the scope of this chapter, because nearly all previous studies on transient-based methods for pipe anomaly detection are based on the plane wave theory.

2.1.4 Behavior of Transient Waves in Pipes with Anomalies

Common Anomalies in Pipes

Various pipe anomalies are commonly existed in urban water supply systems, such as leaks, discrete blockages, extended blockages, and pipe wall corrosion. These anomalies are generally classified into two categories based on their relative length scales: (i) if the relative size of an anomaly is small compared to the total length of the pipe system and

can be considered as a point discontinuity, it is termed a localized pipe anomaly, such as a leak and a discrete blockage; and (ii) if the relative size of an anomaly is large and cannot be represented by a point discontinuity, it is termed an extended pipe anomaly, such as an extended blockage and pipe wall corrosion (Duan et al., 2012a; Lee et al., 2013).

To demonstrate the behavior of transient waves in pipes with anomalies, one localized (i.e., a leak) and one extended anomalies (i.e., an extended blockage) are selected to numerically investigate in a RPV system, as shown in Fig. 2.1. To highlight the interaction between transient waves and pipe anomalies, only the steady friction is considered in this section (i.e., Section 2.1.4).

Pipes with a Localized Anomaly

As shown in Fig. 2.1, a pipe with a leak (i.e., a localized anomaly) is installed as the test section (i.e., Pipe 2) of the RPV system. Transient waves are introduced into the RPV system by a sudden and complete closure of the downstream valve to disturb the initial steady flow. The pressure-time history is measured by a pressure transducer located at just upstream of the downstream valve (i.e., M_4), and plotted in Fig. 2.3(a).

As shown in Fig. 2.3(a), the first partial reflection is a negative wave. The occurrence time of this negative wave is the time duration that the induced transient wave propagates along the pipe, impacts on the leak, and returns to the downstream valve. Such partial reflected waves divert energy away from the main waveform; thus, the pressure amplitude is gradually decreased (Lee et al., 2005b). The FRF of the PRV system, as shown in Fig. 2.3(b), indicates that the resonant frequencies of a pipe with a leak are the same with the intact pipe. In addition, the leak causes a frequency dependent decrease in the amplitude of resonant peaks, which results in a sinusoidal pattern.

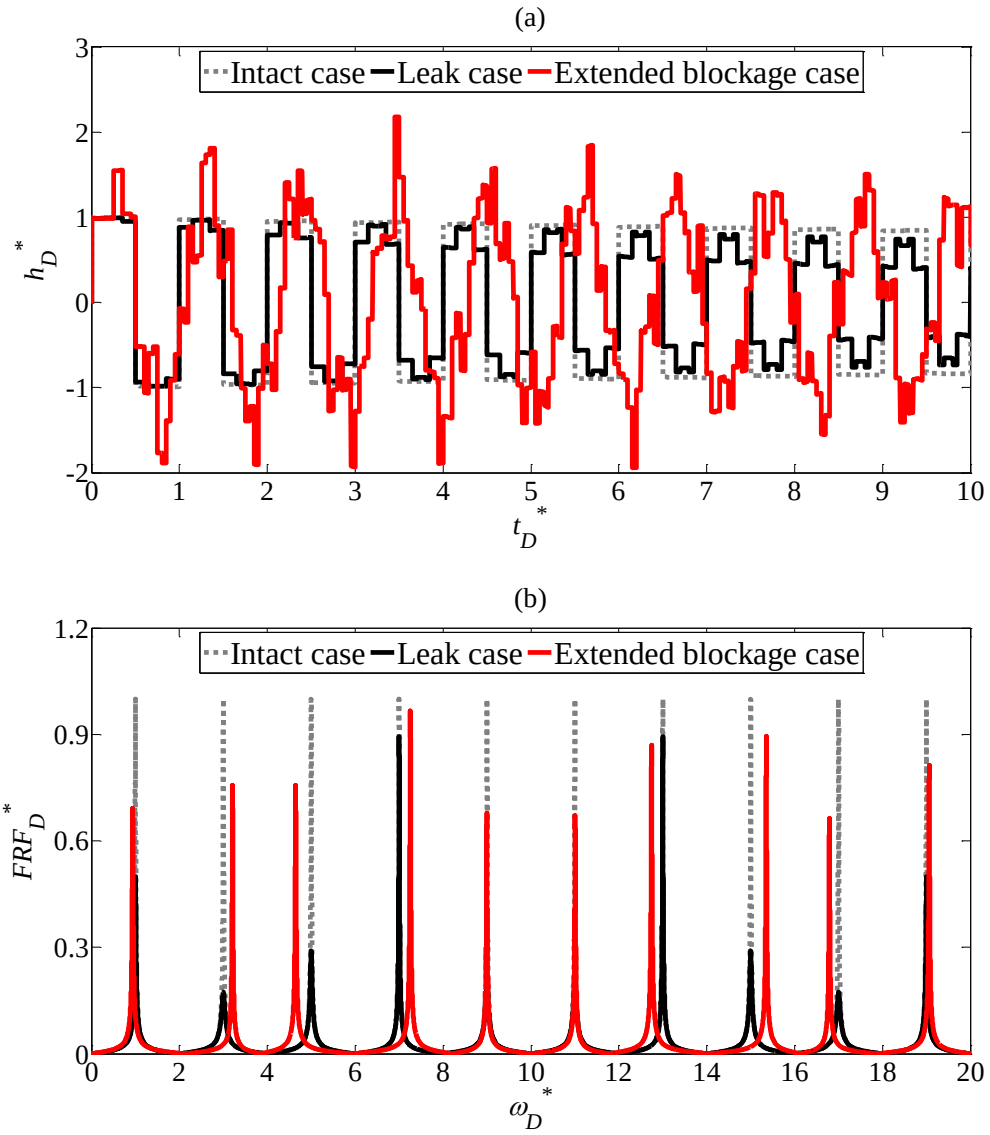

Fig. 2.3. Influence of various pipe anomalies on transient waves: (a) time domain; and (b) frequency domain.

Pipes with an Extended Anomaly

Similarly, a pipe with a smaller diameter (i.e., an extended blockage) is installed as the test section (i.e., Pipe 2) of the RPV system. Unlike the leak case, as shown in Fig. 2.3(a), the first partial reflection from the extended blockage is a positive wave due to the increased impedance of the blocked pipe section. Fig. 2.3(a) also shows that the presence of an extended blockage significantly changes the maximum and minimum pressure heads of the transient waves, and these changed heads may exceed the original transient design capacity; thus, extended blockages potentially increase the failure rate of existing

pipe systems. In addition, it can be observed that the characteristic period of the transient wave becomes longer than the intact test. According to the FRF in Fig. 2.3(b), similar with the leak case, the extended blockage induces a frequency dependent reduction in the amplitude of the FRF. Moreover, the extended blockage results in evident frequency shifts of resonant peaks due to the change of characteristic period in the time domain.

2.2 Excitation and Measurement of Transient Waves

2.2.1 Signal Bandwidth and Anomaly Detection Resolution

The excitation of well controlled transient waves suitable for pipe anomaly detection is a key step for the development and application of this innovative technology (Lee et al., 2015). Lee et al. (2005a) are one of the first to introduce the concept of signal bandwidth of the induced transient waves. The idea is that all the induced transient waves, in any shape or form, have their own frequency spectra. The signal bandwidth is the frequency range (or content), in which most of the energy (e.g., at least 50%) is distributed; thus, transient waves have relatively high signal-to-noise ratios within the signal bandwidth. For the purpose of illustration, several time domain signals and their frequency spectra are plotted in Fig. 2.4. It indicates that the sharper signal (caused by rapider flow changes) in the time domain, the larger bandwidth of this signal in the frequency domain (Lee et al., 2015).

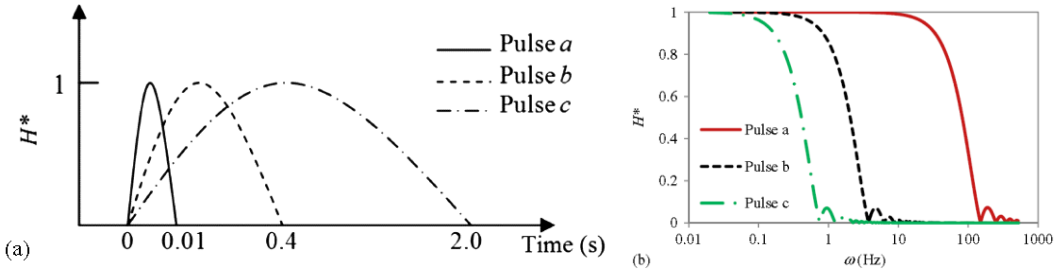

Fig. 2.4. Input transient signals with different bandwidth in the: (a) time domain; and (b) frequency domain (Lee et al., 2013).

The influence of the signal bandwidth of induced transient waves on the spatial resolution, accuracy, and surveillance range of the detection method was investigated systematically by Lee et al. (2015). It was observed that the induced transient wave with higher bandwidth has a higher spatial resolution, which allows pipe anomalies to be detected with higher accuracy. A similar conclusion was drawn by X. Wang and Ghidaoui (2018) that the spatial resolution of a detection method depends on the maximum frequency (or minimum wavelength) of the induced transient wave, which equals to half of the

minimum wavelength. However, the induced transient wave with higher bandwidth suffers from a higher attenuation rate along the pipe, reducing the surveillance range of the detection method. While the induced transient wave with lower bandwidth has opposite features (i.e., lower attenuation, but lower spatial resolution). It was suggested that transient waves with both low and high bandwidth should be applied together in practical cases, where the transient wave with low bandwidth is first used to estimate roughly the potential damaged pipe section, followed by the application of the transient wave with high bandwidth in this pipe section to pinpoint the anomaly (Lee et al., 2015).

2.2.2 Excitation of Transient Waves

Excitation Techniques

(1) Operations on the end valve

(a) *A sudden and complete closure of the end valve*

A sudden valve closure is a common and simple operation to introduce transient waves into the pipe system (Brunone & Ferrante, 2004; Evangelista et al., 2015). In numerical studies, this valve closure process is usually finished within one time step (~ 10^{-3} s). Due to this rapid operation, the wave fronts of induced transient waves are relatively narrow and sharp; thus, their high bandwidth would result in a high spatial resolution of pipe anomaly detection. However, the discharge variation (i.e., the input) during this one time step, which is the necessity for calculating the FRF (see Section 2.3.2) of a pipe system, is relatively difficult to obtain. While in laboratories, the valve closure (manual or electric) cannot be as fast as numerical studies because of the inertia of of these mechanical end valves, and it often takes 10^{-1} ~ 10^{-2} s. Therefore, the induced transient waves have relatively spread and smooth wave fronts, whose limited bandwidth could make the anomaly detection less accurate. One problem of the sudden valve closure is that the triggered high pressure may pose potential damage to practical pipe systems. In addition, transient events generated by this operation on the end valve are usually unrepeatable.

(b) *Closure-open-closure of the end valve*

In numerical and experimental studies, the overall bandwidth properties of transient waves (i.e., a pulse) induced by a "closure-open-closure" operation on the end valve are similar the operation of a sudden closure. One additional feature of this operation is that the discharge variation (i.e., the input) during this valve operation is known; thus, the FRF (see Section 2.3.2) of the pipe system can be obtained following the procedure given by Lee et al. (2006a).

(c) *Oscillations of the end valve*

This operation is commonly used in numerical studies to obtain the frequency response of a pipe system by the frequency sweeping technique (Chaudhry, 2014). This technique needs the end valve to be oscillated in a sinusoidal pattern, at a series of frequencies, to form a steady oscillatory flow in the pipe system. Oscillations of the end valve may encounter several problems in practical applications (Lee et al., 2005a): (i) it is a complex and time-consuming process to form steady oscillatory flows in the pipe system for each input frequency; (ii) the resulted resonant condition may inflict potential damage to the pipe system; and (iii) a specially-made end valve is needed to generate a smooth and well-controlled sinusoidal wave in the pipe system.

(2) Operations on side-discharge valves

Various operations (e.g., sudden closure and closure-open-closure) on a side-discharge valve are often used in numerical and experimental studies to induce transient waves in pipe systems. In general, the operation time of a side-discharge valve is relatively short compared with that of an end valve, which results in a sharp transient wave with high bandwidth. In addition, the amplitude of the induced transient wave is relatively low due to the small initial flow through the side-discharge valve; thus, it is safe for the pipe system. In this way, the pipe system can be regarded as a linear system. Therefore, it is possible to analyze the measured pressure signal in the frequency domain.

(3) Custom-built transient wave generators

(a) *Portable pressure wave-maker (PPWM)*

This PPWM is an easily transported device. It was designed by Brunone et al. (2008b) for leak detection and pipe characterization. The PPWM consists of a steel vessel, with pressurized air (supplied by an air compressor) and water in it, which is connected to the target testing pipe system by a short pipe with an initially closed ball valve at its end. The pressure in the PPWM is fixed at a value that is higher than the pressure of the pipe system; thus, a positive transient wave propagating into the pipe system is triggered once the end ball valve is opened rapidly. One major advantage of this device is that the amplitude of generated transient waves can be controlled and limited to a safe range to the pipe system. In addition, this device can be applied to pipe systems where suitable maneuver valves are not available. More details about this device and its guidelines for application can be found in (Brunone et al., 2008b).

(b) *Pseudorandom binary sequence (PRBS) signal generator*

The PRBS is a continuous perturbation signal. It consists of a series of random spaced transient pulses with equal amplitude (Liou, 1998). The energy of this continuous signal is more widely distributed in the time domain, which allows the amplitude of each pulse to be small (safe to the pipe system) and the bandwidth to be wide (high spatial resolution). The PRBS is generated by repeatedly and rapidly opening and closing a side discharge valve controlled by a solenoid-spring system (Lee et al., 2008a). This device can be applied into any pipe system easily and inexpensively. Moreover, the PRBS has a high tolerance to the random background noise and provides an alternative to various valve operations for extracting the FRF (see Section 2.3.2). Afterwards, Gong et al. (2016) further designed a dual-solenoid side-discharge valve to generate PRBS signals to extract the FRF for leak detection within a single pipe in the laboratory. It was found that one type of the PRBS signal (i.e., inverse repeat signal) has a better performance in the face of significant nonlinearity.

(c) *Underwater electric spark-based generator*

The spark-based method for transient wave excitation was proposed by Mazzocchi et al. (2016) to conduct an overall pipe wall condition assessment. The principle of this method is that the breakdown of water by the high voltage between two discharge electrodes results in high temperature and pressure locally, which is nonequilibrium with the surroundings; thus, the water is vaporized. The formed bubble keeps expanding until it collapses in an extremely short time (~ 10^{-6} s). This collapse induces an extreme sharp transient wave with wide bandwidth (i.e., short wavelength) in the pipe system; thus, it enhances the spatial resolution and improves the accuracy of pipe anomaly detection. One major challenge of this method is that the generated transient wave cannot be well controlled in terms of both amplitude and bandwidth. In addition, the induced transient wave may suffer from relatively high attenuation during propagation due to its high frequency components.

(d) *Piezoelectric wave generation system* (*PIPE SONAR*)

PIPE SONAR (Lee et al., 2017) uses a piezoelectric actuator consisting of a vibrating ceramic element to generate transient waves with small and safe amplitude (< 0.4 m) in pipe systems. The operational frequency range of this PIPE SONAR is 40 to 8000 Hz. The PIPE SONAR can generate well controlled and repeatable transient waves without any loss of water resources from the pipe system. In specific field conditions (e.g., heavy background traffic noise), customized transient waves can be created to distribute most of their energy out of the background noise spectrum. In addition, this PIPE SONAR system is compact and can be easily transported and attached to existing fire hydrants through flange connections by 1 or 2 people.

Bandwidth of Transient Waves Excited by Various Techniques

A list of effective bandwidth of each transient excitation method in laboratory or field tests is provided in Table 2.1 to assist in selecting the appropriate transient excitation technique for a specific application (Gong et al., 2018; Gong et al., 2016; Lee et al., 2017; Lee et al., 2008a; Lee et al., 2007; Mazzocchi et al., 2016; Nguyen et al., 2018).

Table 2.1. Effective bandwidth of various transient excitation techniques in laboratory/field tests.

Excitation method	Manual valve closure	Solenoid side-discharge valve	PRBS signal generator	Spark-based generator	PIPE SONAR
Bandwidth (Hz)	< 60	< 300	45-50	< 2000	40-8000

Optimal Excitation Location of Transient Waves

In general, the optimal location for transient wave excitation largely depends on the boundaries and configurations of the pipe system. Lee et al. (2006a) found that the optimal excitation location of a single pipe system with symmetric boundaries (e.g., a reservoir-pipe-reservoir system) is at the center of the pipe. While this optimal location is at the high impedance boundary (i.e., valve) for a single pipe system with antisymmetric boundaries (e.g., a reservoir-pipe-valve system). In a pipe network, the optimal excitation location should be selected at locations where the generated transient waves are highly sensitive to pipe anomaly unknowns (Haghighi & Shamloo, 2011).

2.2.3 Measurement of Transient Waves

Measurement Parameters and Corresponding Methods

The pressure head and discharge are two key parameters that collect useful information of the pipe system during transient events. Typically, the pressure head is measured and analyzed as the pipe system output, because the pressure head measurement in pipes is more accurate and less expensive than the discharge measurement (X. J. Wang et al.,

2002). Common devices used for measuring the pressure head are pressure transducers with various sapling frequencies.

In some transient-based methods (see Section 2.4.4) for pipe anomaly detection, the input (e.g., the induced discharge change or opening coefficient) to the pipe system is also needed. This input can be determined in two ways: (i) identify the portion of transient directly induced by the motion the excitation device, followed by the calculation of corresponding discharge (Lee et al., 2006a); and (ii) calculate the variation of the opening coefficient of the transient wave excitation device by measuring its movement through a linear voltage displacement transducer (Lee et al., 2008a; Nguyen et al., 2018).

Optimal Measurement Location of Transient Waves

The success of the transient-based pipe anomaly detection method greatly depends on the quantity and location of the collected data. Similar with the optimal location for transient wave excitation, the optimal location for measurement largely depends on the boundaries and configurations of the pipe system.

It was observed by Lee et al. (2006a) that the maximum signal-to-noise ratio occurs for a single pipe system with symmetric boundaries (e.g., a reservoir-pipe-reservoir system), if both the excitation and measurement locations of transient waves are chosen at the mid-length of the pipe. While both the excitation and measurement locations should be at the high impedance boundary (i.e., valve) for a single pipe system with antisymmetric boundaries (e.g., a reservoir-pipe-valve system). Shamloo and Haghighi (2010) suggested that the optimal measurement location in a pipe network should have a high accumulated sensitivity to unknown anomaly parameters (e.g., location and size).

In addition, data measured at different locations can be used to confirm and increase the detection accuracy if necessary (X. J. Wang et al., 2005).

2.3 Signal Processing and Feature Extraction Techniques

2.3.1 Time Domain Techniques

Wavelet Transform

The wavelet transform is a powerful tool for automatic identification of local singularities or discontinuities in the measured transient wave signal caused by reflected waves from pipe anomalies (due to the presence of pipe discontinuities). The wavelet transform improves the identification accuracy of the arriving time of these reflected waves. In this way, pipe anomalies can be localized more accurately (Ferrante & Brunone, 2003b; Meniconi et al., 2011a). In practical applications, one possible problem of the wavelet transform is that the transient wave front may become smeared as it travels along the pipe due to wave dispersion, which makes the accurate arriving time of reflected waves difficult to identify (Taghvaei et al., 2006).

Cross-correlation and Autocorrelation

In general, the time delay estimation (of one signal between two separated pressure transducers) is obtained as the time-lag that maximizes the cross-correlation function between these two measured pressure signals. The cross-correlation has a robust performance in comparing signals even in a relatively noisy environment (Beck et al., 2005).

Impulse Response Function (*IRF*)

The impulse response function (IRF) is defined as the response measured at the output when a unit impulse is injected at the input. It depends on the physical properties (e.g., integrity) of the pipe system, which provides a unique relationship between the introduced discharge perturbation (i.e., input) and the measured pressure signal (i.e., output). All transient responses, in any shape or form (e.g., a PRBS signal), can be compared by their IRFs. This property of IRF allows pipe anomalies to be detected by a specific input

transient signal under a specific condition, such as a PRBS signal with certain effective bandwidth in a noisy environment. The IRF is used to convert the reflected transient waves from pipe anomalies or system components to sharp impulses with well-defined spikes; thus, it improves the identification accuracy of arriving time of these reflected waves. In addition, the IRF allows these reflected waves to be identified without an intact pipe benchmark (Lee et al., 2007).

2.3.2 Frequency Domain Techniques

Fast Fourier Transform (*FFT*)

The measured pressure signals from the pipe system during transient events can be expressed in terms of Fourier series because the transient flow in pipe systems is a quasi-linear problem (X. J. Wang et al., 2002). Fast Fourier transform (FFT) is an efficient algorithm that converts a discrete pressure signal from its original time domain to a representation in the frequency domain and vice versa. It decomposes discrete signals into their Fourier series, which give an overall and insightful description of frequency components of these signals in the entire time domain (Hachem & Schleiss, 2012a).

Cepstrum Analysis

A cepstrum is defined as the Fourier transform of the logarithm of the Fourier transform of a measured signal in the time domain (Shucksmith et al., 2012). The Fourier transform looks for the frequency components of a signal; thus, the Fourier transform of a Fourier transform identifies the repeatability of the frequency components of the original measured signal. The result of cepstrum analysis consists of a series of sharp spike with well-defined peaks. This means that the cepstrum is suited to identifying and locating the presence of discontinuities along the pipe (e.g., pipe anomalies and hydraulic components). In addition, the cepstrum can be applied to identify the time delay between the initial outgoing wave and its later reflections. One main advantage of the cepstrum is

that it performs well even when the induced transient wave suffers from dispersion, because it follows the wave using a moving window technique (Taghvaei et al., 2006).

Frequency Response Function (*FRF*)

In general, pipe systems play the role of frequency filters (Lee et al., 2005a), amplifying and transmitting input signals at particular frequencies (e.g., resonant frequencies) and attenuating and absorbing input signals at other frequencies. The FRF describes the degree of amplification or attenuation of the pipe system on each frequency component of the input signal (Lee et al., 2005b), which is defined as

$$FRF(\omega) = \frac{S_{xy}(\omega)}{S_{xx}(\omega)} \tag{2.9}$$

where $FRF(\omega)$ = frequency response function; $S_{xy}(\omega)$ = Fourier transform of the cross-correlation between the input (x) and the output (y); and $S_{xx}(\omega)$ = Fourier transform of the autocorrelation of the input.

The FRF is the Fourier transform of the IRF (Lee & Vitkovsky, 2008). This means that FRF is a unique relationship between the introduced discharge perturbation (i.e., input) and the measured pressure data (i.e., output), which describes the physical properties of the pipe system. The FRF is an efficient way to determine the response of a pipe system at a large number of frequencies from a single transient wave input of any shape with sufficient bandwidth. The correlation operation before FRF calculation removes certain amount of random background noise from the measured data; thus, it further enhances the practical applicability of the FRF (Lee et al., 2005a, 2005b).

2.3.3 Time-frequency Domain Techniques

Hilbert-Huang transform (HHT) is a technique to decompose and separate a measured signal into a series of simple oscillatory modes (in the time domain), which are termed as intrinsic mode functions (IMFs), and conduct an instantaneous frequency analysis of

different IMF combinations. The obtained IMFs represent different physical behavior of transient waves in the pipe system. The original measured signal can be reconstructed inversely by appropriate combinations of different IMFs. The noise in the original signal can be reduced or filtered by conducting correlation analysis between the original and reconstructed signals. The HHT is well suited for non-stationary and non-linear signal analysis (Sun et al., 2016).

2.3.4 Optimization Techniques

In some transient-based methods for pipe anomaly detection, the number of unknowns is larger than the number of equations; thus, the problem is often underdetermined and optimization techniques are needed (Haghighi et al., 2012). Two main criteria used to select an optimization algorithm are: (i) the ability to find the global optimal solution (i.e., computational accuracy); and (ii) the convergence speed (i.e., computational efficiency).

Levenberg–Marquardt (*LM*) *Algorithm*

The Levenberg–Marquardt (LM) algorithm is a classical gradient-based optimization method used to solve non-linear least squares problems (Liggett & Chen, 1994). It has a fast convergence speed once the initial value is given appropriately. The main drawback of this algorithm is that its solution largely depends on the initial value as well as the shape and complexity of the search space; thus, it easily converges to only a local minimum, which is not necessarily the global minimum (Malekpour & She, 2018; Vítkovský et al., 2000). This may limit the practical applications of this algorithm.

Genetic Algorithm (*GA*)

The genetic algorithm (GA) is often applied to solve global optimization problems. It is inspired by the concept of Darwin's theory of evolution, a process involving selection, crossover and mutation, in which a population of potential solutions of an optimization problem evolve toward improved solutions. Each potential solution has a set of properties

(e.g., chromosomes) (Vítkovský et al., 2000). Compared with LM, GA searches more widely in the solution space and is cable of capturing the global minimum at the expense of the computation speed (i.e., slow convergence) (Kapelan et al., 2004; Malekpour & She, 2018). A fine adjustment of a number of optimization parameters is needed to maximize its performance.

Sequential Quadratic Programming (*SQP*)

Like the LM algorithm, the sequential quadratic programming (SQP) is another gradient-based method, which is fast and simple to apply, but its solutions largely depend on the starting value and may converge to a local minimum (Shamloo & Haghighi, 2010).

Central Force Optimization (*CFO*)

The central force optimization (CFO) algorithm is a deterministic technique based on the metaphor of gravitational kinematics, which tells that objects traveling in the physical universe can be trapped in close orbits around highly gravitating masses (Haghighi & Ramos, 2012). The CFO models "probes" flying in the decision space under the influence of a "mass", which is the user-defined objective function to be maximized. The CFO performs like the hybrid GA-LM model (Kapelan et al., 2003) and has the advantages of both separated LM (i.e., efficiency) and GA (i.e., accuracy) models. In addition, it is much easier to set and implement than the hybrid GA-LM model.

Other optimization algorithms are also adopted in transient-based methods for pipe anomaly detection, such as shuffled complex evolution (SCE) (Lee et al., 2005a), particle swarm optimization (PSO) (Zhang et al., 2018a; Zhang et al., 2018b), shuffled complex evolution-University of Arizona (SCE-UA) (Stephens et al., 2013). More details of these algorithms are reported in corresponding literature.

2.4 Transient-based Methods for Pipe Anomaly Detection

2.4.1 Inverse Transient Analysis (ITA) Method

Principle and Application Procedure

The inverse transient analysis (ITA) method is generally a time domain approach. It stems from the pioneering work of Liggett and Chen (1994) for leak area determination and friction factor identification in a simple pipe network. In this ITA method, potential leaks were assumed to be located at junctions of the pipe network. A sophisticated transient model was selected to simulate the time domain transient pressure response of the pipe network with one or multiple leaks. The leak area of each junction and friction factor of each pipe were varying within a certain bound, until the difference between the simulated transient pressure response and the actual measured pressure response was minimized. This was a non-linear optimization process and an optimization algorithm (see Section 2.3.4) was needed.

The main application procedure of a standard ITA method is that (Kapelan et al., 2004; Sarkamaryan et al., 2018):

(1) Introduce a transient wave into the pipe network by a discharge change at an accessible point (e.g., a fire hydrant);
(2) The resultant transient pressure heads are measured by pressure transducers at some accessible points of the pipe network;
(3) To simulate the transient pressure head at the measurement points, a 1D water hammer model (see Section 3.3.3) with assumed unknown parameters (e.g., anomaly locations, anomaly sizes, and pipe friction factors) is developed for the target pipe network;
(4) The sum of squares of the difference between the simulated and measured transient pressure heads is calculated, which is an objective function of unknown parameters;

(5) A non-linear optimization algorithm (see Section 2.3.4) is selected and applied to minimize the above-mentioned objective function in Step (4), so as to determine unknown parameters.

Advances of the ITA Method

The optimization method used in the pioneering work of Liggett and Chen (1994) was the Levenberg-Marquardt (LM) algorithm (see Section 2.3.4), which is a gradient-based approach with fast computational speeds. As introduced in Section 2.3.4, this LM algorithm may fail to converge or converge to a local optimal solution instead of the global optimal solution if the starting point is not well chosen. To address this problem, Vítkovský et al. (2000) implemented the ITA method using a more robust and comprehensive genetic algorithm (GA) technique (see Section 2.3.4) as an alternative. Compared with the LM algorithm, the GA technique searches more widely in the solution space; thus, it is more effective in finding the global optimal solution at the price of decreased convergence speeds. Afterwards, Kapelan et al. (2003) overcame the convergence problem (i.e., no or slow convergence) of the ITA method in these two previous studies (Liggett & Chen, 1994; Vítkovský et al., 2000) by proposing a hybrid GA-LM method. The GA-LM is a two-staged method, where the GA is applied in the first stage to conduct an effective global search and generate acceptable starting points, based on which the LM is used in the second stage to carry out an efficient local search and finally get the global optimal result. It turns out that the hybrid GA-LM method is more stable and efficient than the LM-based (Liggett & Chen, 1994) and GA-based (Vítkovský et al., 2000) methods, respectively. The successful applications of the ITA method for single and multiple leak detection in a laboratory copper pipe system were firstly presented by Vítkovský et al. (2007). As an alternative to the pressure head optimization used in previous studies, the difference between the simulated and the measured discharge is adopted in the ITA method and is verified by a single copper pipe system in the laboratory (Al-Khomairi, 2008). The above-mentioned ITA studies are mainly confined to elastic pipes, but less applied to plastic pipes, which have totally

different influences on transient waves. Covas and Ramos (2010) and Soares et al. (2010) further extended the ITA method for the simultaneous creep calibration and leak detection in plastic pipe systems (laboratory and quasi-field), where an accurate hydraulic transient solver to describe transient waves in viscoelastic pipes was needed.

Shamloo and Haghighi (2009) used an alternative optimization method, i.e., the Sequential Quadratic Programming (SQP) algorithm (see Section 2.3.4), which is an efficient gradient-based method (like LM), in the ITA method for leak detection in a single pipe system. This study also eliminates the uncertainty of valve operation simulation during the transient modeling by measuring the pressure-time history at the valve after its full closure. Afterwards, this method was further extended to a pipe network to find: (i) the optimal generated transient wave; and (ii) the optimal measurement location of transient waves (Shamloo & Haghighi, 2010). It is suggested that: (i) transient waves should be quickly generated to contain more useful information about the pipe system and consequently result in more accurate leak detection results; and (ii) pressure sensors should be allocated at locations which are most sensitive to ITA unknow parameters. This method was further verified by data of field tests in a single branch iron pipe system (Haghighi et al., 2012). More recently, a new optimization method, i.e., the Central Force Optimization (CFO) algorithm (see Section 2.3.4), was numerically incorporated into the ITA method for leak detection in a pipe network (Haghighi & Ramos, 2012). The CFO algorithm performs like the accurate and efficient hybrid GA-LM method, but it is much easier to implement. One problem of the traditional ITA method is that potential leaks are assumed only at characteristic nodes. To allocate candidate leaks everywhere in the pipe network, Sarkamaryan et al. (2018) used a Gaussian function to simulate the true location of a leak, which significantly increases the accuracy and efficiency of the ITA method.

The ITA method was also applied in the frequency domain to estimate unknown parameters by fitting the simulated FRF (see Section 2.3.2) with the FRF calculated from actual measurement (Lee et al., 2005a). Unlike the time domain ITA method, the ITA

method in the frequency domain does not need to discretize the pipe system; thus, anomalies can be assumed at any location along the pipe system and can be detected more accurately. In addition, the frequency domain ITA method is efficient in terms of unsteady friction computation (Kim, 2005; Lee et al., 2005a). Given these advantages, Kim et al. (2014) proposed an alternative to the direct numerical modeling in the time domain by the MOC, where transient responses are firstly obtained in the frequency domain by the impedance-based method, which are subsequently converted back into the time domain for ITA calibration of pipe characteristics. Capponi et al. (2017) used another frequency domain ITA method based on the network admittance matrix method (NAMM) (Zecchin et al., 2009) for leak detection in a branched high-density polyethylene (HDPE) pipe system. In this study, a two-stage optimization method is applied, where the GA is used in the first stage to generate acceptable starting points, based on which the Nelder-Mead algorithm is used in the second stage to obtain more accurate solutions. One possible disadvantage of the frequency domain ITA method is the linearized error related to the friction term (Duan et al., 2018).

In recent years, the ITA method has been extended to the detection of other pipe anomalies, such as corrosion (Stephens et al., 2013; Tuck & Lee, 2013; Zhang et al., 2018a; Zhang et al., 2018b), air pockets (Malekpour & She, 2018), dead-end side branches (Capponi & Ferrante, 2017), and multiple coexisting anomalies (Kim, 2016), such as a leak, a discrete blockage, and a dead-end side branch.

Characteristics of the ITA Method

One major advantage of the ITA method is that it can be applied to pipe systems with complex topography and configurations.

The heavy computational burden may be a limiting factor of the ITA method when it is applied to a practical large pipe network (Duan et al., 2010a; Vítkovský et al., 2007). Parallel computing is one potential and effective way to speed up the overall calculation of the ITA method (Liggett & Chen, 1994).

Another disadvantage of the ITA method is that all detailed properties and boundaries of the pipe system should be well surveyed and defined before simulating transient events by a sophisticated numerical model (Vítkovský et al., 2007). This is a time consuming and expensive process for the real-life pipe networks especially for old ones. The occurred uncertainties and errors during this process may influence the reliability of the ITA method, which greatly depends on the quality and quantity of the measured data (Gong et al., 2014a; Haghighi & Ramos, 2012).

One key assumption of the ITA method is that the numerical model is accurate enough to represent the transient wave behavior in the pipe system. However, the rigorous verification of the numerical model is rare in field pipes and almost none in field pipe networks. This knowledge gap is one of the key obstacles in the practical filed applications of the ITA method (Vítkovský et al., 2007).

2.4.2 Transient Wave Reflection (TWR) Method

Principle and Application Procedure

The transient wave reflection (TWR) method is another time domain approach. To the author's knowledge, Jönsson and Larson (1992) are one of the first to use the TWR method to detect a leak by measuring and analyzing the transient pressure variation in field tests. Theoretically, an injected transient wave propagates along the pipe and partially reflected waves occur when it encounters any internal pipe anomaly; thus, the locations of these anomalies can be estimated once the arrival time of these reflected waves and the wave speed are determined. In addition, the amplitude of reflected waves is an indicator of the anomaly severity (i.e., size). In practical applications, the reflected waves are easily interfered by background noise, making the arrival time difficult to identify. Therefore, some signal processing techniques may be needed to enhance the arrival time identification.

It seems that the friction losses are not the key factors for the TWR method, because only the first half period of the transient wave is considered (Ferrante et al., 2009a).

The main application procedure of a standard TWR method is as follows:

(1) Inject a transient wave into the target pipe system;
(2) Measure the pressure variation at one or multiple points of the pipe system;
(3) Compare the measured pressure signal with the signal of the corresponding intact (i.e., anomaly-free) pipe system, which is obtained from numerical simulation or measurement of newly built pipes, to identify the arrival time of reflected waves;
(4) Obtain the transient wave speed by theoretical calculations (see Section 2.1.1) or field measurement;
(5) Estimate the relative location of the anomaly to the measurement point by the arrival time and wave speed of reflected waves.

Advances of the TWR Method

Silva et al. (1996) measured the pressure variation of a leaking PVC pipe by four pressure transducers in the laboratory. Leaks along the pipe system are simulated as side outlets controlled by solenoid valves. The transient wave speed is determined by the known distance between two transducers and the detected pulse time delay between them. It is observed that the reflected wave of a leak in the pipe system causes a sudden drop in the pressure curve (as shown in Fig. 2.3(a)), whose arrival time is used to locate the leak. Brunone (1999) systematically investigated the influence of a leak on the behavior of a transient wave and proposed a TWR method for leak detection in outfall pipes. This proposed method is verified in the laboratory by a single polyethylene pipe system. The arrival time of the reflected wave of a leak is determined by comparing the measured pressure curve with the pressure curve of an intact (i.e., leak-free) pipe system.

To enhance the arrival time identification of reflected waves, the wavelet transform technique (see Section 2.3.1) is used to detect the local singularity occurs in the pressure

curve caused by a leak in a polyethylene pipe in the laboratory (Ferrante & Brunone, 2003b). More detailed information about this edge detection technique (i.e., the wavelet transform technique) is reported in (Ferrante et al., 2007, 2009a). Afterwards, this proposed TWR method was further extended to complex branched systems for leak detection in both laboratory (i.e., HDPE pipes) and field (i.e., ductile iron pipes) tests (Ferrante et al., 2009b). It suggests that the number of transient measurement points should increase as the increase of the number of junctions of the pipe network to determine the true location of a leak among multiple potential locations.

Beck et al. (2005) proposed an enhanced cross-correlation technique (see Section 2.3.1) to produce well-defined peaks representing the occurrence of reflected waves. In this study, this technique was applied to detect the leak and identify pipe features (e.g., bends and junctions) of a pipe network with T-shape junctions in the laboratory. This method needs a leak-free benchmark and performs well even in the face of high levels of noise. The cepstrum analysis (see Section 2.3.2) is another powerful tool to identify the time delay between the initial outgoing wave and its corresponding later reflections. The occurrence of a leak in the pipe system induces a new well-defined peak in the output of cepstrum, which is a series of sharp peaks, making the arrival time of reflected waves easy to identify. The cepstrum analysis was used by Taghvaei et al. (2006) to identify features (e.g., leaks, junctions, and pipe ends) of a simple T-shaped pipe network in the laboratory by their reflected waves. One major advantage of the cepstrum method in practical applications is that it performs well even for dispersive waves. Afterwards, this method was successfully applied to detect leaks and features of various practical full-scale pipe networks, which consist of various pipe materials (e.g., PVC, ductile iron, asbestos-cement, and cast-iron) (Shucksmith et al., 2012).

Lee et al. (2007) used the IRF (see Section 2.3.1) to convert all measured reflected waves into sharp pulses with well-defined peaks for more accurate arrival time estimation. Pulses that do not belong to the reflected waves from boundaries indicate the presence of leaks; thus, this method allows leaks to be detected without a leak-free benchmark. This

improved TWR method was validated in a single pipe system in the laboratory. Recently, this method was further extended by Nguyen et al. (2018) to a branched pipe network using a least squares deconvolution approach for IRF estimation and a specific type of PRBS for transient wave excitation, making it more robust to background noise.

The TWR method also utilizes the frequency domain information for pipe anomaly detection. Specifically, the pipe system is forced by an oscillating valve to form a steady-oscillatory flow. A leak induces a continuous periodic effect (i.e., a standing wave) on the measured pressure signal, which creates the resonance phenomenon. The spectral analysis of the measured pressure response enables the identification of the leak-induced resonant frequency, which is used to locate the leak (Covas et al., 2005a). One problem of this method is that the pipe may collapse if the frequency of the oscillating valve is the same with the resonant frequency of the pipe system.

The influence of various pipe anomalies (e.g., leaks, illegal branches, extended blockages, and discrete blockages) on transient waves in the time domain was investigated by Meniconi et al. (2011c). The TWR method has also been applied for the detection of other types of pipe anomalies, such as discrete blockages (Meniconi et al., 2011a; Meniconi et al., 2011b), corrosion (Gong et al., 2018; Gong et al., 2013b; Gong et al., 2015; Hachem & Schleiss, 2012a, 2012b; Mazzocchi et al., 2016; Misiunas et al., 2007; Shi et al., 2017), dead ends (Meniconi et al., 2011d).

Characteristics of the TWR Method

The standard TWR method (Brunone, 1999) needs an intact (i.e., anomaly-free) benchmark to identify the arrival time of reflected waves from pipe anomalies. A benchmark can be obtained from: (i) the measurement of the original anomaly-free pipe system; and (ii) an accurate numerical simulation, where a detailed understanding of the pipe system is needed. One problem of this benchmark-based TWR method is that the induced transient wave may not be perfectly repeatable, making it difficult to determine

directly whether the status of a pipe system has changed or not between different tests (Lee et al., 2007).

In practical applications, the attenuation of transient waves (see Section 2.1.3), especially in plastic pipes, is a key factor that should be taken into account for accurate pipe anomaly detection, which limits the detection range of the TWR method (Silva et al., 1996). Transient waves (e.g., induced and reflected waves) are also dispersive in nature, which means that they spread out and become less sharp as they travel in the pipe system (Taghvaei et al., 2006). This makes the arrival time of reflected waves difficult to be identified accurately (Beck et al., 2005).

The real-life pipe networks contain a great number of features (e.g., pipe junctions, hydraulic devices, and pipe anomalies), which cause a great number of reflected waves (Beck et al., 2005; Wu et al., 2010). The change of the flow demand may induce new transient waves into the pipe system, which will be superposed with the measurement of reflected waves from pipe anomalies. In addition, these networks are consisted of pipes with various diameters and materials, which may change the wave speed along the pipe system (Beck et al., 2005). Therefore, an equivalent wave speed should be determined to locate the anomaly based on the arrival time of reflected waves.

2.4.3 Transient Wave Damping (TWD) Method

Principle and Application Procedure

As shown in Fig. 2.3(a), localized pipe anomalies (e.g., leaks and discrete blockages) significantly contribute to the attenuation of transient waves, which is the basis of the transient wave damping (TWD) method for anomaly detection. Transient pipe flows are weakly nonlinear (i.e., nearly linear); thus, the measured pressure-time history can be decomposed into separate harmonic components in the frequency domain by a Fourier transform. The localized anomaly-induced attenuating rate with time is different for each harmonic component (i.e., frequency dependent). The attenuating rate of one harmonic component indicates the size of a localized anomaly and the ratio of attenuating rates between different harmonic components is useful for finding the location of a localized anomaly.

The main process of localized anomaly detection, location, and quantification is as follows (X. J. Wang et al., 2002):

(1) Introduce a transient wave into the target pipe system;
(2) Measure the transient pressure-time history at one or more accessible points along the pipe system;
(3) Decompose each period of the measured pressure curve into its M separate harmonic components (i.e., 1…m…M) using a Fourier transform and calculate their amplitude;
(4) Plot the variation of its amplitude with the period (normalized by L/a) for each harmonic component m;
(5) Calculate the attenuating rate of each harmonic component m by an exponential fitting function;
(6) Detect the size of a localized anomaly by the attenuating rate of one harmonic component and the location of a localized anomaly by the ratio of attenuating rates between different harmonic components.

Advances of the TWD Method

The TWD method was firstly proposed and verified in the laboratory by X. J. Wang et al. (2002) for leak detection based on the leak-induced attenuating rates of different harmonic components, which is frequency dependent. Afterwards, the validity range of this TWD method was investigated by Nixon et al. (2006). Similar with leaks, discrete blockages also introduce different attenuation on each harmonic component of the measured transient pressure curve; thus, the TWD method was further extended for the detection of discrete blockages in a single pipe system (X. J. Wang et al., 2005).

Characteristics of the TWD Method

The TWD method is efficient and easy to apply, which gives a direct solution of anomaly parameters (e.g., locations and sizes) without any optimization procedure.

To calculate the localized anomaly-induced attenuating rate, the friction-induced attenuating rate should be subtracted from the overall attenuating rate of an intact pipe system. The friction-induced attenuating rate can be estimated in two ways: (i) measured by an experiment, which is more suitable for newly built pipes; and (ii) obtained from an accurate numerical simulation, which includes both steady and unsteady friction (X. J. Wang et al., 2002). In old pipes, the detection error may increase with an increase of uncertainties in the friction-induced attenuation estimation.

The TWD method is mainly limited to simple pipe systems without any internal boundary conditions. In practical applications, various pipe junctions and hydraulic components in pipe networks may also contribute to the attenuation of transient waves, which is relatively difficult to distinguish from the localized anomaly-induced attenuation (X. J. Wang et al., 2002). One possible solution is to isolate individual pipes from the rest of the pipe network by valves so that the analytical solution of each pipe can be determined (Nixon et al., 2006).

In addition, due to the symmetry of sine and cosine squared functions, the relationship between the anomaly location and the attenuating ratio of two harmonic components is not unique (X. J. Wang et al., 2005; X. J. Wang et al., 2002). This means that one attenuating ratio may correspond to two or multiple anomaly locations. To uniquely determine the true location of a pipe anomaly, pressure data measured at different locations can be used (X. J. Wang et al., 2005).

2.4.4 Transient Frequency Response (TFR) Method

Principle and Application Procedure

The transient frequency response (TFR) method uses the frequency domain information to detect pipe anomalies. As shown in Fig. 2.3(b), the FRF (see Section 2.3.2) of an intact pipe system is uniformly distributed in the frequency domain. The presence of a localized anomaly (e.g., a leak) in the pipe system induces a sinusoidal fluctuation pattern on the resonant peaks of the FRF (termed as the leak-induced pattern), whose period and amplitude can be used to detect the location and size of the localized anomaly.

The application procedure of the TFR method for anomaly detection (includes FRF extraction) in a pipe system is as follows (Lee et al., 2006a):

(1) Extract the FRF of the target pipe system by the following sub-steps;

(a) Place excitation and measurement devices of transient waves at the optimal locations in pipe systems with various boundary conditions as suggested in Sections 2.2.2 and 2.2.3;

(b) Introduce a transient wave with enough bandwidth into the pipe system and measure the transient pressure variation at the excitation point until the transient signal is fully attenuated, which is the system output (i.e., y in Eq. (2.9));

(c) Identify the portion of the transient pressure variation directly induced by the motion of excitation devices, which is the input signal. Calculate the discharge corresponding to the input signal, which is the input (i.e., x in Eq. (2.9)) to the system;

(d) Substitute the input and output obtained in Steps (c) and (b) into Eq. (2.9) to calculate the FRF.

(2) Identify the leak-induced pattern on resonant peaks from the FRF;

(3) Find the dominant amplitude and period of the leak-induced pattern by a least squares regression of the analytical result;

(4) Apply the obtained amplitude and period of the leak-induced pattern to detect the location and size of the leak based on the analytical result.

Advances of the TFR Method

Lee et al. (2005a) observed that the presence of a leak at each specific location within a single pipe induces a unique pattern on resonant peaks of the FRF, based on which a resonant peak-sequencing method was proposed to locate the leak. In this method, the location of a leak is detected by comparing the obtained pattern with known patterns in a lookup table generated for leaks at various locations. Only the steady friction is considered in this study. However, in practical applications, the unsteady friction causes greater attenuation at higher harmonics, which distorts the patterns of resonant peaks. This distortion effect can be eliminated by introducing a series of scaling factors between numerical results with steady and unsteady friction for a leak-free case. In the same year, a comprehensive TFR technique based on the FRF was first proposed by Lee et al. (2005b) to detect the location and size of both single and multiple leaks in a single pipe system. It was observed that the occurrence of a leak within the pipe induces a sinusoidal pattern on resonant peaks of the FRF. The shape of this pattern is related to the leak location, whereas the amplitude of this pattern is a function of the leak size. This method allows leaks to be detected without a leak-free benchmark. This study also introduced an efficient alternative way to extract the FRF for a large number of frequencies (see Section 2.3.2). The idea of this alternative is to inject a single transient wave with sufficient bandwidth, as a combination of individual frequencies, into the pipe system and extract the FRF by Eq. (2.9). The correlation process in Eq. (2.9) reduces the random background noise in the measured pressure data, which makes the proposed method more robust. In addition,

the true location of a leak can be uniquely determined based on the phase of the leak-induced sinusoidal pattern from two symmetric potential leak locations. One problem of this method is that two symmetric leaks may be detected as a single leak and the leak located at the mid-length of the pipe may not be detected. The analytical results of this method are based on linearized equations; thus, the induced transient wave perturbation should not be too large to violate this assumption. Afterwards, this FRF-based method for leak detection was validated in the laboratory by Lee et al. (2006a).

Sattar and Chaudhry (2008) utilized the frequency sweeping technique (Chaudhry, 2014) to determine the frequency response of a single pipe system with a leak. It was found that, compared with the intact pipe system, the presence of a leak induces oscillation patterns with increased and decreased amplitude on even and odd harmonics, respectively. The frequency and amplitude of these oscillation patterns are directly related to the location and size of the leak. Moreover, compared with odd harmonics, the leak-induced oscillation pattern on even harmonics has more evident amplitude for the same leak; thus, the induced oscillation pattern on even harmonics was used to detect the leak within the pipe. One problem of this method is that the true leak location cannot be uniquely determined among two symmetric potential leak locations. Afterwards, this TFR method (Sattar & Chaudhry, 2008), which uses the leak-induced pattern on even harmonics, was compared with the TFR method (Lee et al., 2005b) based on the leak-induced pattern on odd harmonics of the FRF by Gong et al. (2014b). It was suggested that the TFR method (Lee et al., 2005b) based on odd harmonics is more robust.

Previous studies of the TFR method for leak detection based on the FRF (Lee et al., 2006a; Lee et al., 2005a, 2005b; Sattar & Chaudhry, 2008) are mainly confined to a single pipe system made of elastic materials. However, the real-life water distribution networks are usually comprised of pipes in various connections (e.g., series, branched, and looped junctions) and materials (e.g., PVC and HDPE), which may affect the validity of the existing TFR method. Afterwards, the TFR method was successfully extended to pipe systems with series junctions to detect single and multiple leaks (Duan et al., 2011a). It

was observed that the series junction in pipe systems modifies the locations of resonant frequencies but has little influence on the leak-induced sinusoidal pattern on resonant peaks of the FRF. More recently, Duan (2016b) further extended the FRF-based TFR method for leak detection to relatively more complex pipe systems with branched and looped junctions. In addition, Duan et al. (2012b) also investigated the influence of pipe wall viscoelasticity on the FRF. It was found that viscoelastic pipes change the amplitude and frequency of resonant peaks, but they have a small effect on the leak-induced pattern on resonant peaks of the FRF; thus, the analytical expression of the FRF originally for elastic pipes was extended for leak detection in viscoelastic pipes.

The FRF-based TFR method may be restricted in practical applications due to its two problems: (i) to detect the leak accurately, a number of resonant peaks are needed to estimate the frequency and amplitude of the leak-induced pattern, which requires the input transient signal with sufficient bandwidth; and (ii) frequency dependent factors (e.g., unsteady friction) may distort the leak-induced pattern. To address these problems, Gong et al. (2013a) proposed a new FRF-based TFR method that only uses the first three resonant peaks of the FRF to detect a leak in a single pipe system. It turns out that the unsteady friction has little influence on the amplitude of the first three harmonics and the required bandwidth for input signals is only five times that of the fundamental frequency of the pipe system, which is much less than that needed for traditional FRF-based TFR methods. This proposed method was validated in a single copper pipe in the laboratory.

The implementation of the TFR method for leak detection is robust in previous literature because of the environments with a high signal-to-noise ratio (SNR). However, the real-life pipe networks are exposed to various noise sources, such as traffic, turbulence, and some accidental or planned changes in operating conditions. X. Wang and Ghidaoui (2018) developed an efficient matched-field processing method (MFP) to detect the leak location and size separately in noisy environments. Unlike the previous FRF methods, which only use information at resonant peaks, this method uses all available frequencies;

thus, further improves the accuracy and robustness of the TFR method. The true leak location can be uniquely determined by two measurement points.

Discrete blockages in pipes were found to have a similar influence on the resonant peaks to leaks (Lee et al., 2008b; Sattar et al., 2008), therefore the size and location of discrete blockage can be diagnosed using a similar approach (Lee & Vitkovsky, 2008; Lee et al., 2008b; Mohapatra & Chaudhry, 2011; Mohapatra et al., 2006a; Mohapatra et al., 2006b; Sattar et al., 2008). In addition, the TFR method is also applied for the detection of other pipe anomalies, such as side branches (Duan & Lee, 2016).

Characteristics of the TFR Method

Compared with time domain methods (e.g., ITA and TWR methods), the FRF-based TFR method needs less computational time because the pressure and discharge responses are obtained analytically in the frequency domain by the transfer matrix method (see Section 2.1.2) (Gong et al., 2014b).

The TFR method has a high tolerance to the random background noise (Lee et al., 2013). Because an anomaly within the pipe system has the same effect on each period of the transient signal. These key periodic effects are further reinforced by the analysis in the frequency domain; thus, the random background noise in the measured pressure data can be reduced (Lee et al., 2006a).

All the existing FRF-based TFR methods are developed based on the linear system theory. In practical applications, the nonlinearity of transient waves in pipe systems can be attributed to various factors (e.g., friction, pipe anomalies, and boundaries) (Gong et al., 2016). A systematical analysis of the influence of the nonlinear friction component on the FRF extraction under various system and flow conditions has been conducted by Duan et al. (2018).

The current TFR method has been derived mainly for single or simple pipe systems with well-defined boundaries. However, the real-life water distribution systems are consisted of complex pipe networks with various junctions. Therefore, it is important to extend the current TFR method to such pipe networks. Lee et al. (2005b) suggested that the practical pipe networks can be subdivided into individual single pipes by isolating valves, where the FRF of each separated pipe can be obtained and the current TFR method can be applied to determine the integrity of each pipe. This relies on the availability of a sufficient number of valves in the pipe network.

2.5 Transient-based Method for Extended Blockage Detection

As mentioned in Section 2.4.4, the presence of a discrete blockage in the pipe system, like a leak, induces a sinusoidal fluctuation pattern on the resonant peaks of the FRF (Lee et al., 2008b; Sattar et al., 2008), whose period and amplitude can be used to detect the location and size of the discrete blockage. Therefore, discrete blockages can be detected using a similar TFR approach to leaks (Lee & Vitkovsky, 2008; Lee et al., 2008b; Mohapatra & Chaudhry, 2011; Mohapatra et al., 2006a; Mohapatra et al., 2006b; Sattar et al., 2008).

Brunone et al. (2008a) observed that extended blockages, which is a common scenario in aging water pipes, have a totally different influence on transient responses from discrete blockages; thus, the TFR method used for discrete blockage detection may not be applicable to extended blockages.

It was found by Duan et al. (2012a) and Tuck et al. (2013) that the occurrence of an extended blockage in water pipe systems not only changes the amplitude of resonant peaks, but also induces evident frequency shifts on resonant peaks (termed as blockage-induced frequency shifts), which contain physical information about the location and size of the extended blockage. Based on the derived wave-blockage dispersion relationship in (Duan et al., 2012a), a genetic algorithm (GA) inverse optimization procedure was proposed to determine the physical properties (such as lengths, sizes and locations) of potential extended blockages. Afterwards, the derived dispersion relationship was further simplified to identify the key parameters governing the blockage-induced frequency shifts, which was first verified by laboratory experiments (Duan et al., 2013). This frequency domain method was further coupled with a time domain method (Meniconi et al., 2011a; Meniconi et al., 2011c) by Meniconi et al. (2013b) to further improve its computational accuracy and efficiency for blockage detection.

Although the physical properties of an extended blockage have be diagnosed based on the blockage-induced frequency shifts on resonant peaks, the physical mechanism of the

frequency shift is unclear. A series of theoretical, numerical, and experimental studies were conducted to investigate the physical mechanism of the frequency shift induced by blockages in water pipes (Louati & Ghidaoui, 2017a, 2018; Louati et al., 2018; Louati et al., 2017). The underlying physics of the frequency shift is clarified.

Although the transient-based method has demonstrated its potential for extended blockage detection, this method is developed based on blockages of uniform constriction along their lengths (termed as *uniform blockages*), which is equivalent to multiple pipelines with different diameters connected in series. Extended blockages in real urban water supply systems are usually formed from various complicated physical, chemical, and biological processes; thus, as shown in Figs. 1.4(a) and 1.4(b), these blockages usually constrict randomly and non-uniformly along their lengths (termed as *non-uniform blockages*). Inaccuracy and invalidity of the current transient-based method have been observed in laboratories for non-uniform blockage detection (Duan et al., 2017). This is because the current transient-based theory is unable to describe the interaction between transient waves and non-uniform blockages. Therefore, an understanding of the transient wave behavior in water pipes with non-uniform blockages is necessary to enhance the practical applications of the transient-based method for extended blockage detection.

CHAPTER 3 MODELS AND GOVERNING EQUATIONS

3.1 Introduction

This chapter presents the general derivation procedure of various forms of one-dimensional (1D) and 2D water hammer models, which are used in this thesis, from the 3D Navier-Stokes equations for a compressible fluid. In addition, the assumptions inherent in these models are illuminated.

3.2 Navier-Stokes Equations

3.2.1 3D Navier-Stokes Equations

The 3D Navier-Stokes equations for a compressible fluid, which are derived based on the conservation principles of mass and momentum, in cylindrical coordinates are (Ghidaoui, 2004)

$$\frac{\partial \rho}{\partial t}+\frac{\partial(\rho u)}{\partial x}+\frac{1}{r}\frac{\partial(r\rho v)}{\partial r}+\frac{1}{r}\frac{\partial(\rho w)}{\partial \theta}=0 \tag{3.1a}$$

$$\begin{aligned}&\frac{\partial(\rho u)}{\partial t}+\frac{\partial\left(\rho u^2\right)}{\partial x}+\frac{1}{r}\frac{\partial(r\rho uv)}{\partial r}+\frac{1}{r}\frac{\partial(r\rho uw)}{\partial \theta}=\\&-\frac{\partial p}{\partial r}-(\kappa+\mu/3)\frac{\partial}{\partial x}\left(\frac{1}{\rho}\frac{D\rho}{Dt}\right)+\mu\nabla^2 u+\rho f_x\end{aligned} \tag{3.1b}$$

$$\begin{aligned}&\frac{\partial(\rho v)}{\partial t}+\frac{\partial(\rho uv)}{\partial x}+\frac{1}{r}\frac{\partial\left(r\rho v^2\right)}{\partial r}+\frac{1}{r}\frac{\partial(\rho vw)}{\partial \theta}-\rho\frac{w^2}{r}=-\frac{\partial p}{\partial r}\\&-(\kappa+\mu/3)\frac{\partial}{\partial r}\left(\frac{1}{\rho}\frac{D\rho}{Dt}\right)+\mu\left(\nabla^2 v-\frac{v}{r^2}-\frac{2}{r^2}\frac{\partial w}{\partial \theta}\right)+\rho f_r\end{aligned} \tag{3.1c}$$

$$\begin{aligned}&\frac{\partial(\rho w)}{\partial t}+\frac{\partial(\rho uw)}{\partial x}+\frac{1}{r}\frac{\partial(r\rho vw)}{\partial r}+\frac{1}{r}\frac{\partial\left(\rho w^2\right)}{\partial \theta}+\rho\frac{vw}{r}=-\frac{\partial p}{r\partial \theta}\\&-(\kappa+\mu/3)\frac{\partial}{r\partial \theta}\left(\frac{1}{\rho}\frac{D\rho}{Dt}\right)+\mu\left(\nabla^2 w-\frac{w}{r^2}+\frac{2}{r^2}\frac{\partial v}{\partial \theta}\right)+\rho f_\theta\end{aligned} \tag{3.1d}$$

where x = axial distance along the pipe axis; r = radial distance from the pipe axis; θ = azimuth; t = time; f_x, f_r, and f_θ = body force along x, r, and θ, respectively; u, v, and w = axial, radial, and azimuthal velocity components along x, r, and θ, respectively; μ = dynamic viscosity of the fluid; κ = volume viscosity of the fluid; ρ = density of the fluid; p = pressure; g = gravitational acceleration; D/Dt = material derivative in cylindrical coordinates; and ∇^2 = Laplace operator in cylindrical coordinates.

3.2.2 2D Navier-Stokes Equations

Assuming that the flow field remains axisymmetric during transients (Ghidaoui, 2004), the 3D Navier-Stokes equations in Eq. (3.1) are simplified into

$$\frac{1}{\rho}\left(\frac{\partial \rho}{\partial t}+u\frac{\partial \rho}{\partial x}+v\frac{\partial \rho}{\partial r}\right)+\frac{\partial u}{\partial x}+\frac{1}{r}\frac{\partial (rv)}{\partial r}=0 \tag{3.2a}$$

$$\begin{aligned}\frac{\partial u}{\partial t}+u\frac{\partial u}{\partial x}+v\frac{\partial u}{\partial r}=&-\frac{1}{\rho}\frac{\partial p}{\partial x}+\frac{\kappa+\mu/3}{\rho}\frac{\partial}{\partial x}\left(\frac{\partial u}{\partial x}+\frac{1}{r}\frac{\partial (rv)}{\partial r}\right)\\&+\frac{\mu}{\rho}\left(\frac{\partial^2 u}{\partial x^2}+\frac{1}{r}\frac{\partial}{\partial r}\left(r\frac{\partial u}{\partial r}\right)\right)+f_x\end{aligned} \tag{3.2b}$$

$$\begin{aligned}\frac{\partial v}{\partial t}+u\frac{\partial v}{\partial x}+v\frac{\partial v}{\partial r}=&-\frac{1}{\rho}\frac{\partial p}{\partial r}+\frac{\kappa+\mu/3}{\rho}\frac{\partial}{\partial r}\left(\frac{\partial u}{\partial x}+\frac{1}{r}\frac{\partial (rv)}{\partial r}\right)\\&+\frac{\mu}{\rho}\left(\frac{\partial^2 v}{\partial x^2}+\frac{1}{r}\frac{\partial}{\partial r}\left(r\frac{\partial v}{\partial r}\right)-\frac{v}{r^2}\right)+f_r\end{aligned} \tag{3.2c}$$

3.3 Water Hammer Models

3.3.1 Full-2D Water Hammer Model

The derivation of the full-2D water hammer model from the 2D Navier-Stokes equations Eq. (3.2) are based on three assumptions as follows.

(1) The compressibility of the fluid is only considered in the continuity equation (Mitra & Rouleau, 1985). Because the fluid is slightly compressible and the pipe wall is elastic (i.e., relatively rigid), the variation of fluid density ρ in radial and axial momentum

equations due to the variation of internal pressure can be neglected. However, the small variation of fluid density ρ in the continuity equation should be indirectly taken into account, since the value of the transient wave speed a_0 is finite. Otherwise the transient wave speed a_0 would be infinite. The equation of state for a slightly compressible fluid is

$$\frac{dp}{d\rho} = \frac{k}{\rho} = a_0^2 \tag{3.3}$$

where a_0 = transient wave speed; and k = bulk modulus.

(2) The volume viscosity of the fluid in axial and radial momentum equations Eqs. (3.2b) and (3.2c) is negligible, because the compressibility of the fluid is not considered in these two equations.

(3) The body forces in radial and axial momentum equations are neglected due to the relatively small scales of pipe size and pipe gradient in urban water supply systems focused in this thesis.

According to these three assumptions, the following full-2D water hammer model in Eq. (3.4) can be obtained (Mitra & Rouleau, 1985).

$$\frac{\partial p}{\partial t} + u\frac{\partial p}{\partial x} + v\frac{\partial p}{\partial r} + k\left(\frac{\partial u}{\partial x} + \frac{1}{r}\frac{\partial (rv)}{\partial r}\right) = 0 \tag{3.4a}$$

$$\frac{\partial u}{\partial t} + u\frac{\partial u}{\partial x} + v\frac{\partial u}{\partial r} = -\frac{1}{\rho_0}\frac{\partial p}{\partial x} + \frac{\mu}{\rho_0}\left(\frac{4}{3}\frac{\partial^2 u}{\partial x^2} + \frac{1}{r}\frac{\partial}{\partial r}\left(r\frac{\partial u}{\partial r}\right) + \frac{1}{3}\frac{\partial}{\partial x}\left(\frac{1}{r}\frac{\partial (rv)}{\partial r}\right)\right) \tag{3.4b}$$

$$\frac{\partial v}{\partial t} + u\frac{\partial v}{\partial x} + v\frac{\partial v}{\partial r} = -\frac{1}{\rho_0}\frac{\partial p}{\partial r} + \frac{\mu}{\rho_0}\left(\frac{1}{3}\frac{\partial^2 u}{\partial x \partial r} + \frac{\partial^2 v}{\partial x^2} + \frac{4}{3}\frac{\partial}{\partial r}\left(\frac{1}{r}\frac{\partial}{\partial r}(rv)\right)\right) \tag{3.4c}$$

where ρ_0 = reference density of the fluid.

3.3.2 Quasi-2D Water Hammer Model

The derivation of the quasi-2D water hammer model from the full-2D model in Eq. (3.4) are based on three assumptions as follows.

(1) Plane wave assumption: the radial variation of pressure is neglected (i.e., $\partial p/\partial r = 0$), and the radial velocity v as well as its derivatives in axial and radial momentum equations Eqs. (3.4b) and (3.4c) are neglected because of the small compressibility of the fluid (Ghidaoui et al., 2005; Pezzinga, 1999).

(2) The nonlinear convective terms in continuity and momentum equations are neglected since, for the low Mach number flow (i.e., Mach number $\mathbf{M} << 1$), the axial velocity u and the radial velocity v of the fluid are much smaller than the wave speed a_0 (Ghidaoui, 2004; Ghidaoui et al., 2005; Pezzinga, 1999).

(3) Integrating the continuity equation Eq. (3.4a) across the pipe cross section, the radial velocity v related term would be eliminated. Because the boundary conditions of radial velocity v at the pipe axis and the pipe wall are both equal to zero (e.g., $v_0 = 0$ and $v_R = 0$) (Ghidaoui et al., 2005).

These assumptions result in the following quasi-2D water hammer model

$$\frac{\partial H}{\partial t} + \frac{a^2}{gA}\frac{\partial Q}{\partial x} = 0 \tag{3.5a}$$

$$\frac{\partial u}{\partial t} + g\frac{\partial H}{\partial x} = \frac{\mu}{\rho_0 r}\frac{\partial}{\partial r}\left(r\frac{\partial u}{\partial r}\right) \tag{3.5b}$$

$$Q(x,t) = \int_A u dA \tag{3.5c}$$

where H = pressure head; Q = discharge; and A = pipe cross-sectional area. Note that the pressure p in Eq. (3.4) is transformed into the pressure head H in Eq. (3.5), which is a common practice in hydraulic engineering.

3.3.3 1D Water Hammer Model

The 1D water hammer model has the same assumptions with the quasi-2D water hammer model in Eq. (3.5). It can be obtained by integrating the momentum equation Eq. (3.5b) across the pipe cross section and only considering the wall shear stress.

$$\frac{\partial H}{\partial t}+\frac{a^2}{gA}\frac{\partial Q}{\partial x}=0 \tag{3.6a}$$

$$\frac{\partial Q}{\partial t}+gA\frac{\partial H}{\partial x}+\frac{\pi D}{\rho_0}\tau_w=0 \tag{3.6b}$$

$$\tau_w=\tau_{ws}+\tau_{wu} \tag{3.6c}$$

where τ_w = wall shear stress; τ_{ws} = quasi-steady component of τ_w; and τ_{wu} = unsteady component of τ_w, which is commonly simulated by different unsteady friction models (Vardy & Hwang, 1991; Zielke, 1968).

CHAPTER 4 TRANSIENT FREQUENCY RESPONSES OF WATER PIPES WITH NON-UNIFORM BLOCKAGES[3]

4.1 Introduction

Despite the successful application of the transient-based method for extended blockage detection in many numerical and laboratory tests, as described in Chapter 2, blockages used for analysis in these previous studies are idealized and simplified to uniform shapes (Duan et al., 2014; Duan et al., 2012a; Lee et al., 2013; Louati et al., 2017; Meniconi et al., 2013b; Rubio Scola et al., 2017; Tuck et al., 2013), which are equivalent to multiple pipe sections with different diameters connected in series (see Fig. 1.4(c)). However, real world blockages, formed from complex sources and processes, are usually in highly random and non-uniform shapes as illustrated in Figs. 4.1(a) and 4.1(b). Recently, Duan et al. (2017) experimentally investigated the influence of non-uniform blockages on transient wave behavior and validity of current transient-based method for non-uniform blockage detection. It was observed that the blockage non-uniformity may have a great impact on both the amplitude and the phase shift of *transient frequency responses*, which makes the current transient-based method become inaccurate or even invalid when it is used to detect these non-uniform blockages. Therefore, a further and in-depth understanding of the *transient frequency responses of water pipes with non-uniform blockages* is the basis of extending the current transient-based method for non-uniform blockage detection in practical urban water supply systems.

In a previous study, to investigate the modification effect of non-uniform blockages on the system frequency response, Chaudhry (2014) replaced the actual non-uniform

[3] This chapter is adapted from the research paper of the author and his co-authors (Che et al., 2018b).

blockage (i.e., pipes with gradually varying diameters) by a number of substitute uniform blockages in series. This treatment discretized the non-uniform blockage into many pricewise constant elements. Individual matrixes for each element are multiplied in the order of their locations to produce the approximated overall transfer matrix for the whole non-uniform blockage. This approximation method only gives satisfactory predictions for the first few harmonics. It is computationally expensive to get relatively accurate results for higher harmonics. As a result, this approximation treatment may induce potential errors in transient modeling and utilization, such as blockage detection, especially for pipes with multiple blockages. Therefore, it is worthwhile to develop more reliable (i.e., accurate and efficient) methods to describe the transient frequency responses of water pipes with non-uniform blockages.

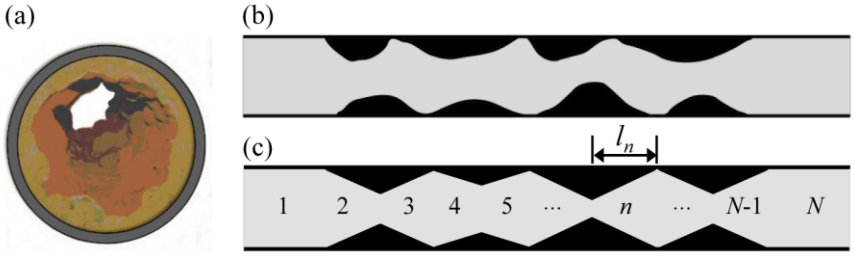

Fig. 4.1. (a) Random and non-uniform blockages in practical water pipes (adapted from James and Shahzad (2003)); (b) sketch of real pipe with non-uniform blockages; (c) sketch of pipe with linear non-uniform blockages used for analytical analysis.

As a preliminary study, to understand the fundamental physics and mechanism of the interaction between transient waves and non-uniform blockages, it is preferable and feasible to examine the realistic non-uniform blockages by starting with simple cases, such as blockages with linearly varying diameters (termed as *non-uniform blockages*) as shown in Fig. 4.1(c). Specifically, the transient wave behavior in various non-uniform blockages is obtained by analytically solving the one-dimensional (1D) wave equation under specific initial and boundary conditions. The obtained wave solutions are incorporated into the 1D overall transfer matrix of a reservoir-pipe-valve (RPV) system with non-uniform blockages. The derived overall transfer matrix is fully validated by the

traditional method of characteristics (MOC), which is used to systematically investigate the influences of non-uniform blockage shape, severity, and length on transient frequency responses. Finally, the findings and practical implications of this study are discussed.

4.2 Transfer Matrix of a Water Pipe with Non-uniform Blockages

4.2.1 Wave Equation for a Single Non-uniform Blockage

The 1D wave equation for non-uniform blockages with varying cross-sectional areas was derived as (Duan, 2017; Duan et al., 2011b) (more detailed procedures can be found in Appendix A1)

$$A\frac{\partial^2 P}{\partial t^2} = a^2 \frac{\partial}{\partial x}\left(A\frac{\partial P}{\partial x} \right) \tag{4.1}$$

where t = time; x = axial coordinate along the pipe; $A = A(x)$ = pipe cross-sectional area; P = instantaneous pressure in the time domain; $a = a(x)$ = acoustic wave speed, which represents the characteristics of pipe-wall deformation and properties of internal fluid (e.g., water).

Note that a frictionless pipe system with an elastic pipe wall is firstly considered in the analytical derivation to highlight the wave-blockage interaction (Duan et al., 2014). Pipe systems with linearized steady friction will be further discussed in Section 4.4.

Alternatively, Eq. (4.1) can be rewritten as

$$\frac{\partial^2 P}{\partial t^2} - a^2 \frac{\partial^2 P}{\partial x^2} = a^2 \frac{A'}{A}\frac{\partial P}{\partial x} \tag{4.2}$$

where A' = the derivative dA/dx. For transient pipe flows, the instantaneous pressure P can be expressed as (Chaudhry, 2014)

$$P = P_0 + p^* \tag{4.3}$$

where P_0 = mean pressure; p^* = pressure deviation from the mean. Because the pipe system is frictionless, P_0 is constant in terms of both x and t, then Eq. (4.2) becomes

$$\frac{\partial^2 p^*}{\partial t^2} - a^2 \frac{\partial^2 p^*}{\partial x^2} = a^2 \frac{A'}{A}\frac{\partial p^*}{\partial x} \tag{4.4}$$

which is a linear partial differential equation (PDE) and can be solved analytically under specific boundary and initial conditions.

4.2.2 Transient Wave Behavior in a Single Non-uniform Blockage

In above wave equation, it is assumed that the solution p^* has the following form (Chaudhry, 2014)

$$p^*(x,t) = p(x)e^{i\omega t} \tag{4.5}$$

where p = pressure in the frequency domain; ω = angular frequency; i = imaginary part.

Substituting Eq. (4.5) back into Eq. (4.4), the PDE becomes the following linear ordinary differential equation (ODE)

$$\frac{d^2p}{dx^2} + \frac{A'}{A}\frac{dp}{dx} + k^2 p = 0 \tag{4.6}$$

where $k = k(x) = \omega/a(x)$ = wave number. In fact, Eq. (4.6) is in the same form with the Webster's horn equation in acoustics (Webster, 1919). The variation of the wave speed within a shallow non-uniform blockage along the axial direction is relatively small compared with the wave speed a_0 in intact pipe sections. For example, the field tests by Lee et al. (2017) showed that the average percentage of wave speed variation in deteriorated field water pipes is around 8.25%. Thus, the wave speed $a_b(x)$ within the non-uniform blockage is represented by the average value (i.e., $\bar{a}_b$) throughout the blockage section, which is different from the original value of intact pipes (i.e., a_0) because of the blockage-induced changes in pipe properties (e.g., diameters, thicknesses and materials). As a result, the wave number k within the non-uniform blockage in Eq. (4.6) becomes $k_b = \omega/\bar{a}_b$. Sensitivity analysis will be conducted in Section 4.4.4 to examine the validity range (limitation) of this assumption (i.e., using the average wave speed within the blockage section).

Applying Eq. (4.6) in the n-th non-uniform blockage, as shown in Fig. 4.1(c), provides

$$\frac{d^2 p_n}{dx^2} + \frac{A_n^{'}}{A_n}\frac{dp_n}{dx} + k_b^2 p_n = 0 \tag{4.7}$$

For analytical analysis, the pipe radius of the *n*-th non-uniform blockage in Fig. 4.1(c) is defined as

$$r_n(x) = s_n x + R_{Ln} \tag{4.8}$$

where r_n = pipe radius of the *n*-th non-uniform blockage; R_{Ln} = pipe radius at the left boundary of the *n*-th non-uniform blockage; $s_n = (R–R_{Ln})/l_n$ = slope of the *n*-th non-uniform blockage, in which R = intact pipe radius and l_n = length of the *n*-th non-uniform blockage in Fig. 4.1(c).

Based on the expression of r_n in Eq. (4.8), the pipe cross-sectional area A_n and its derivative A_n' can be calculated, thus

$$\frac{A_n^{'}(x)}{A_n(x)} = \frac{2s_n}{s_n x + R_{Ln}} \tag{4.9}$$

Substituting Eq. (4.9) into Eq. (4.7), it becomes

$$\frac{d^2 p_n}{dx^2} + \frac{2s_n}{s_n x + R_{Ln}}\frac{dp_n}{dx} + k_b^2 p_n = 0 \tag{4.10}$$

It is assumed that the solution for the wave equation Eq. (4.10) is a plane wave solution in the following form (Munjal, 2014)

$$p_n = \frac{e^{\alpha x}}{r_n(x)} = \frac{e^{\alpha x}}{s_n x + R_{Ln}} \tag{4.11}$$

where α = coefficient that remains to be determined; note that the denominator is the pipe radius of the *n*-th non-uniform blockage in Eq. (4.8). Furthermore, substituting Eq. (4.11) into Eq. (4.10) results in the following characteristic equation for α

$$\alpha^2 + k_b^2 = 0 \tag{4.12}$$

As a result, α has two solutions

$$\alpha_1 = ik_b;\ \alpha_2 = -ik_b \tag{4.13}$$

Substituting above two solutions into Eq. (4.11), two special solutions for wave equation Eq. (4.10) can be obtained

$$(p_n)_1 = \frac{e^{ik_b x}}{s_n x + R_{Ln}};\ (p_n)_2 = \frac{e^{-ik_b x}}{s_n x + R_{Ln}} \tag{4.14}$$

In fact, these two plane wave solutions $(p_n)_1$ and $(p_n)_2$ are the incident and reflected waves propagating towards opposite directions. It can be observed from the numerator of Eq. (4.14) that transient waves distribute sinusoidally in space with a constant wave number k_b. In addition, the amplitude of these two waves is modified by the denominator, which is the pipe radius of the n-th non-uniform blockage. It means that the wave amplitude is inversely proportional to the radius of the n-th non-uniform blockage.

Because the wave equation Eq. (4.10) is a linear ODE, based on the superposition principle, the general solution for wave equation can be obtained

$$p_n = \frac{C_1 e^{ik_b x} + C_2 e^{-ik_b x}}{s_n x + R_{Ln}} \tag{4.15}$$

where C_1 and C_2 are two constants.

To have an intuitive sense of transient wave behavior in a single non-uniform blockage, the plane wave solutions in Eq. (4.14) are visualized in both uniform and non-uniform blockages. A localized incident wave is created at the right boundary of these two blocked pipes, and detailed parameters of these two systems are listed in Table 4.1. Note that these two pipes have the same blocked volume, which means that the average pipe diameters of these two blockages are the same. The left ends of these two pipes are reflection-free boundary conditions. The obtained results are plotted in Fig. 4.2, showing how the localized incident wave evolves as it propagates in the pipe from right to left. The spatial coordinate x is normalized by the intact pipe radius R and is expressed as x_D in the horizontal axis. The pressure is normalized by the pressure in the intact pipe section and is expressed as dimensionless pressure p_D.

Table 4.1. Parameter settings for illustrative systems with uniform and non-uniform blockages.

Type	l_n	s_n	R_{Ln}	k_b
Uniform blockage	100R	0	0.9R	$\pi/5$
Non-uniform blockage	100R	2e–3	0.8R	$\pi/5$

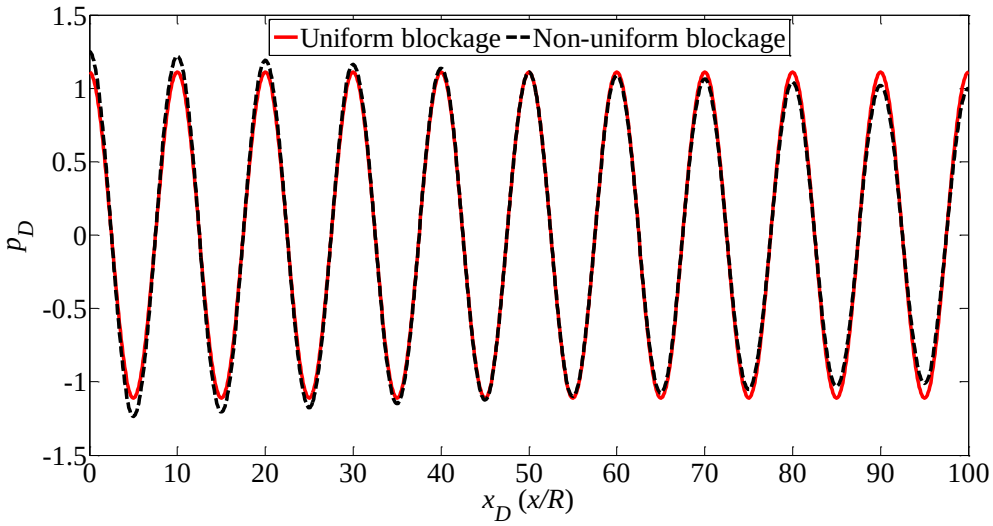

Fig. 4.2. Transient wave behavior in uniform and non-uniform blockages.

It can be observed from Fig. 4.2 that the wave amplitude in the uniform blockage keeps constant, while the wave amplitude in the non-uniform blockage gradually increases as the wave propagates to the left. This is consistent with the wave solution in Eq. (4.14), because the denominator of Eq. (4.14) for the non-uniform blockage gradually decreases from right to left. In fact, this result is consistent with the former study by the authors with regard to energy analysis of wave scattering in pipes with disordered diameters (Duan et al., 2011b). That is, the non-uniform blockages in pipe systems may cause energy re-distribution of pressure waves in both temporal and spatial domains.

4.2.3 Overall Transfer Matrix of Pipe Systems with a Single Non-uniform Blockage

To study the transient frequency responses of pipe systems with a single non-uniform blockage, the obtained wave solution in Eq. (4.15) is used to derive the transfer matrix. The transfer matrix is the linearized counterpart of mass and momentum equations in the frequency domain. It describes the wave behavior and connects state vectors at two boundaries of the pipe system without discretization of the pipe in space. Thus, it has the advantage of computational efficiency compared with some time domain methods, such as the MOC.

The derivation procedure of the transfer matrix of a single uniform blockage (i.e., a pipe) was provided in (Chaudhry, 2014). A similar procedure is adopted herein to derive the transfer matrix of a single non-uniform blockage, based on the wave solution in Eq. (4.15). Note that the pressure deviation p in Eq. (4.15) is transformed into the pressure head deviation h in this section, which is a common practice in hydraulic engineering.

The derived transfer matrix for a single non-uniform blockage (i.e., the n-th non-uniform blockage in Fig. 4.1(c)) is

$$\begin{pmatrix} q \\ h \end{pmatrix}_{n+1} = \begin{pmatrix} U_{11} & U_{12} \\ U_{21} & U_{22} \end{pmatrix} \begin{pmatrix} q \\ h \end{pmatrix}_{n} \tag{4.16}$$

where q = discharge deviation in the frequency domain; h = pressure head deviation in the frequency domain; subscript n and n+1 are upstream and downstream boundaries of the n-th non-uniform blockage, respectively; U_{ij} = elements of transfer matrix, with the following forms:

$$U_{11} = -\frac{iR_{Ln}}{2k_b\left(s_n l_n + R_{Ln}\right)^2}\frac{A_{n+1}}{A_n}\left\{\left[ik_b\left(s_n l_n + R_{Ln}\right) - s_n\right]e^{ik_b l_n} + \left[ik_b\left(s_n l_n + R_{Ln}\right) + s_n\right]e^{-ik_b l_n}\right\}$$

$$U_{12} = \frac{A_{n+1}g}{2\omega k_b\left(s_n l_n + R_{Ln}\right)^2}\left\{\left[ik_b\left(s_n l_n + R_{Ln}\right) - s_n\right]\left(ik_b R_{Ln} + s_n\right)e^{ik_b l_n} - \left[ik_b\left(s_n l_n + R_{Ln}\right) + s_n\right]\left(ik_b R_{Ln} - s_n\right)e^{-ik_b l_n}\right\}$$

$$U_{21} = \frac{\omega R_{Ln}}{2k_b\left(s_n l_n + R_{Ln}\right)A_n g}\left(e^{-ik_b l_n} - e^{ik_b l_n}\right)$$

$$U_{22} = \frac{1}{2ik_b\left(s_n l_n + R_{Ln}\right)}\left[\left(ik_b R_{Ln} + s_n\right)e^{ik_b l_n} + \left(ik_b R_{Ln} - s_n\right)e^{-ik_b l_n}\right]$$

Note that the uniform blockage is a special case of the non-uniform blockage when the slope s_n equals to zero ($s_n = 0$). As a result, Eq. (4.16) becomes

$$\begin{pmatrix} q \\ h \end{pmatrix}_{n+1} = \begin{pmatrix} \cos\left(k_0 l_n\right) & -i\dfrac{1}{M_{n+1}}\sin\left(k_0 l_n\right) \\ -iM_n \sin\left(k_0 l_n\right) & \cos\left(k_0 l_n\right) \end{pmatrix}\begin{pmatrix} q \\ h \end{pmatrix}_n \tag{4.17}$$

where k_0 = wave number for the uniform blockage; $M_n = a/A_n g$. This result is consistent with the transfer matrix of a uniform blockage in (Chaudhry, 2014).

To investigate the transient frequency responses, the derived transfer matrix is applied to an RPV system as shown in Fig. 4.3. The transfer matrix with external head and discharge perturbations should be expanded to a 3 × 3 matrix in the following form (Chaudhry, 2014; Duan et al., 2012a; Lee et al., 2008b)

$$\begin{pmatrix} q \\ h \\ 1 \end{pmatrix}_B = \begin{pmatrix} U_{11} & U_{12} & U_{13} \\ U_{21} & U_{22} & U_{23} \\ U_{31} & U_{32} & U_{33} \end{pmatrix}\begin{pmatrix} q \\ h \\ 1 \end{pmatrix}_A \tag{4.18}$$

where subscripts A and B are the upstream and downstream boundaries of the pipe system. Variables q_B and h_B at the downstream valve can be expressed as

$$q_B = U_{11}q_A + U_{12}h_A + U_{13} \tag{4.19}$$

$$h_B = U_{21}q_A + U_{22}h_A + U_{23} \tag{4.20}$$

For the RPV system in Fig. 4.3, it has the boundary conditions $h_A = q_B = 0$. Eqs. (4.19) and (4.20) result in

$$h_B = -\frac{U_{21}U_{13}}{U_{11}} + U_{13} \tag{4.21}$$

As a result, for a leak-free pipe system, Eq. (4.21) becomes (Lee et al., 2006b)

$$h_B = -\frac{U_{21}}{U_{11}} \tag{4.22}$$

The resonant frequency of head responses for RPV systems with a single non-uniform blockage can be obtained when the denominator of Eq. (4.22) (i.e., U_{11}) equals to zero.

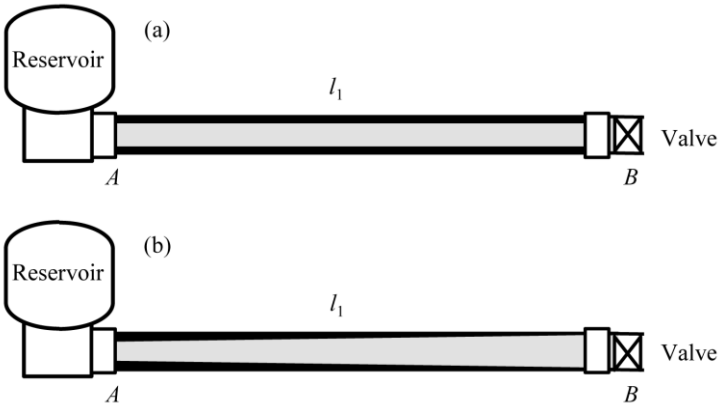

Fig. 4.3. Illustrative reservoir-pipe-valve (RPV) systems with a: (a) single uniform blockage; (b) single non-uniform blockage.

For RPV systems with a single uniform blockage, (n = 1 and s_1 = 0), the resonant frequency is

$$U_{11} = \cos(k_0 l_1) = 0 \tag{4.23}$$

which shows that the resonant peaks are uniformly distributed in the frequency domain.

Similarly, for RPV systems with a single non-uniform blockage, (n = 1 and $s_1 \neq 0$), let U_{11} = 0, resulting in the resonant frequency of this RPV system

$$k_b\left(s_1 l_1 + R_{L1}\right)\cos\left(k_b l_1\right) - s_1 \sin\left(k_b l_1\right) = 0 \tag{4.24}$$

Unlike the resonant frequency of the uniform blockage, Eq. (4.24) has an extra term $\sin(k_b l_1)$, which may result in resonant frequency shifts. If the slope of this non-uniform blockage equals to 0 (i.e., s_1 = 0), the non-uniform blockage becomes a uniform blockage and Eq. (4.24) becomes $\cos(k_b l_1) = 0$. This result indicates that resonant peaks of a uniform blockage are uniformly distributed regardless of the radius size, which is consistent with Eq. (4.23).

The transient frequency responses of an RPV system are studied for both uniform and non-uniform blockages. Note that the friction is neglected herein for highlighting the effect of blockage non-uniformity. As shown in Fig. 4.3, there is a single blockage (uniform or non-uniform) between the upstream reservoir and the downstream valve. Transients are caused by a fast and full closure of the downstream valve.

The frequency responses for both cases are plotted in Fig. 4.4. The frequency is normalized by the fundamental frequency of the pipe system $\omega_{th} = \bar{a}_b/4l_1$, and is expressed as non-dimensional frequency ω^*. Theoretically, the amplitude of transient frequency responses should go to infinity because friction is not included in the transfer matrix.

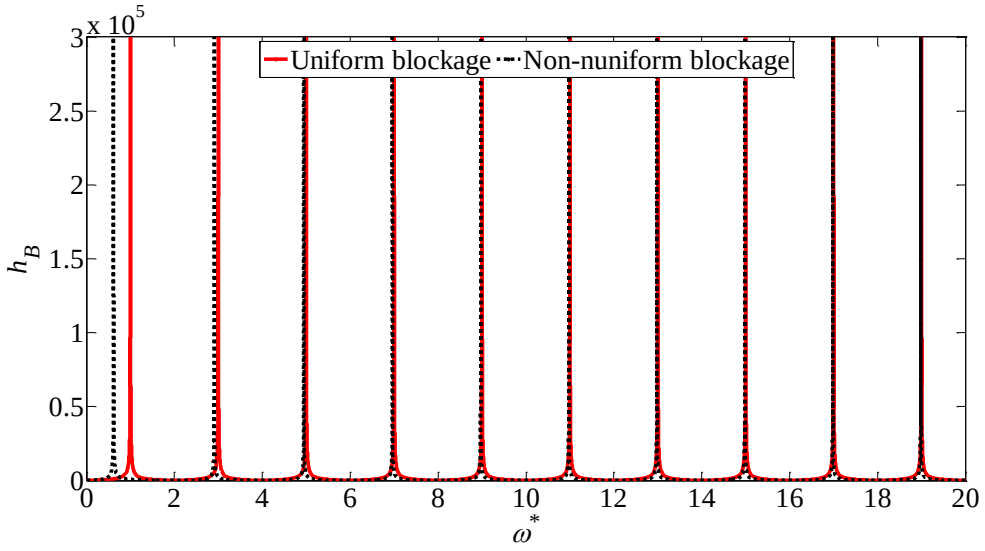

Fig. 4.4. Transient frequency responses for RPV systems with single uniform and non-uniform blockages (without friction effect).

It is shown in Fig. 4.4 that the resonant peaks of the uniform blockage are uniformly distributed, while that of the non-uniform blockage have evident frequency shifts, especially for the first resonant peak. Moreover, as the frequency increases, the induced frequency shift by the non-uniform blockage becomes less evident. This can be explained by the analytical resonant frequency in Eq. (4.24): as the frequency increases, the wave number k_b also increases, then the first term $\cos(k_b l_1)$ in Eq. (4.24) will become dominant.

Therefore, the frequency shift induced by the non-uniform blockage becomes less evident for higher harmonics.

4.2.4 Extended Transfer Matrix of Pipe Systems with Multiple Non-uniform Blockages

So far, the transfer matrixes of single uniform and non-uniform blockages have been obtained. For illustration and simplification, only the case of two joint non-uniform blockages, as shown in Fig. 4.5(b), is considered and investigated in this study, while similar analysis procedure presented herein can be applied to more complex cases. It is assumed there are no pressure head loss at pipe junctions (Duan et al., 2012a). The overall transfer matrix of this pipe system (made up of four pipe sections), which relates the state vectors at two boundaries *A* and *B*, can be obtained by multiplying individual matrixes for each pipe element in the order of their locations starting from the downstream end.

$$\begin{Bmatrix} q \\ h \end{Bmatrix}_B = \begin{bmatrix} \cos(k_0 l_4) & -i\frac{1}{M_4}\sin(k_0 l_4) \\ -iM_4 \sin(k_0 l_4) & \cos(k_0 l_4) \end{bmatrix} \times \begin{bmatrix} U_{11} & U_{12} \\ U_{21} & U_{22} \end{bmatrix}_3 \times \begin{bmatrix} U_{11} & U_{12} \\ U_{21} & U_{22} \end{bmatrix}_2 \times \begin{bmatrix} \cos(k_0 l_1) & -i\frac{1}{M_1}\sin(k_0 l_1) \\ -iM_1 \sin(k_0 l_1) & \cos(k_0 l_1) \end{bmatrix} \begin{Bmatrix} q \\ h \end{Bmatrix}_A \tag{4.25}$$

For clarity, Eq. (4.25) can be further derived and written as

$$\begin{Bmatrix} q \\ h \end{Bmatrix}_B = \begin{bmatrix} U_{11}^* & U_{12}^* \\ U_{21}^* & U_{22}^* \end{bmatrix} \begin{Bmatrix} q \\ h \end{Bmatrix}_A \tag{4.26}$$

where U_{ij}^* = elements of the overall transfer matrix for the four-pipe system.

Similar with Eqs. (4.23) and (4.24), the resonant frequency of the four-pipe system can be obtained by letting

$$U_{11}^* = 0 \tag{4.27}$$

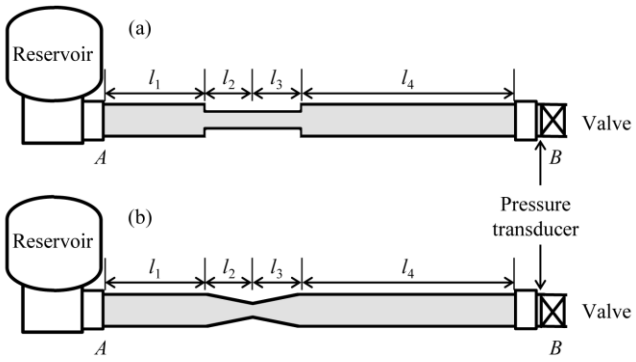

Fig. 4.5. Illustrative RPV systems with: (a) uniform blockages; (b) non-uniform blockages.

Note that the analytical result in Eq. (4.27) for resonant frequency of a four-pipe system becomes complicated in its mathematical expression, which can be obtained by solving the former Eqs. (4.16) and (4.25). Compared with the intact PRV system, the resonant frequency shift of Eq. (4.27) can be attributed to two sources: (i) the blockage non-uniformity $A(x)$; and (ii) the wave speed non-uniformity $a(x)$ along the axial direction of the PRV system. To highlight the influence of blockage non-uniformity (or to eliminate the influence of wave speed non-uniformity) on resonant frequency shifts and simplify the analytical derivation in Eq. (4.27), it is first assumed herein that: (i) the wave speed in the whole pipe system is constant; and (ii) the absolute values of non-uniform blockage slope $|s_2|$ (constriction section) and $|s_3|$ (expansion section) in Fig. 4.5(b) are equal ($|s_2| = |s_3| = s$). Then, Eq. (4.27) becomes

$$4R^2R_{L3}\omega^3\cos\left[k_b\left(l_1+l_2+l_3+l_4\right)\right]+\sum a^f s^f \omega^{3-f} F^{3-f}\left(R,R_{L3}\right)\sin\left[k_b\left(l_1\pm l_2\pm l_3\pm l_4\right)\right]=0 \qquad (4.28)$$

where the second term on the left-hand side contains a series of trigonometric terms; $F()$ = a linear function of R and R_{L3}; f = an integer ranges from 1 to 3. Three special cases are firstly verified as follows:

(1) $s = 0$ (i.e., blockage-free case): the pipe radius on the left boundary of second pipe in Fig. 4.5(b) R_{L2} is the same with the intact pipe radius R, $s = 0$ means that there is no blockage in the four-pipe system. All terms containing s equal zero, and only one term $4R^2R_{L3}\omega^3\cos[k_b(l_1 + l_2 + l_3 + l_4)] = 0$ does not contain s. Under this condition, Eq. (4.28) is simplified into

$$\cos[k_b(l_1 + l_2 + l_3 + l_4)] = 0$$

which implies that the resonant peaks of the intact four-pipe system in Fig. 4.5(b) are uniformly distributed in the frequency domain, which is consistent with previous studies (Chaudhry, 2014; Lee et al., 2013).

(2) $s \sim \infty$ ($(l_2 + l_3)/(l_1 + l_2 + l_3 + l_4) \sim 0$, i.e., discrete blockage case): if the slope of the non-uniform blockage tends to infinity, it means that the length of the non-uniform blockage is negligibly small compared with the total length of the pipe $(l_2 + l_3)/(l_1 + l_2 + l_3 + l_4) \sim 0$, and the non-uniform blockage can be regarded as a discrete blockage. Terms with s to the high order will become dominant, but the summation of all terms containing s^3 equals to zero. Therefore, all terms containing s^2 are further summed, and it turns out to be

$$\cos[k_b(l_1 + l_4)] = 0$$

Since the blockage length $l_2 + l_3$ is negligibly small compared with the total length of the pipe $l_1 + l_2 + l_3 + l_4$, the above equation can be approximated by $\cos[k_b(l_1 + l_2 + l_3 + l_4)] = 0$. This is equivalent to the former results for blockage-free case ($s = 0$), and indicates that discrete blockages do not induce frequency shifts, which is well verified by the known results from previous studies (Lee et al., 2013; Lee et al., 2008b).

(3) High frequency harmonic waves: the terms in the equation with the highest order of ω will play dominant roles. Only the term $4R^2R_{L3}\omega^3\cos[k_b(l_1 + l_2 + l_3 + l_4)] = 0$ contains ω^3, therefore Eq. (4.28) is simplified into

$$\cos[k_b(l_1 + l_2 + l_3 + l_4)] = 0$$

which is the same with the blockage-free case ($s = 0$). It means that the frequency shift induced by the blockage non-uniformity becomes less evident as the frequency increases. It is a reminder that this result and analysis here is obtained under the condition of constant wave speed in the whole pipe system, and the influence of wave speed variation from the blockage section is inspected in the following section.

4.3 Numerical Validation

To validate the analytical resonant frequency in Eq. (4.27), the classical frictionless 1D water hammer model coupling with the MOC is adopted herein for comparison. The RPV system with two joint non-uniform blockages is used for the numerical validation. In this study, non-uniform blockages are represented by stainless-steel pipes with linearly varying diameters as shown in Fig. 4.5(b). The original intact stainless-steel pipe (R = 0.25 m, L = 1000 m) is blocked by non-uniform blockages with minimum radius R_{L3} = 0.15 m and $l_2 = l_3$ = 105 m (detailed parameters can refer to Table 4.2). Wave speeds for intact and blocked pipe sections are calculated based on the wave speed formula given in Wylie et al. (1993) and Chaudhry (2014) as a_0 = 1206 m/s and $\bar{a}_b$ = 1249 m/s. For simplicity of numerical calculation, a_0 and $\bar{a}_b$ are taken to be 1000 m/s and 1050 m/s, respectively. In the numerical simulation, the non-uniform blockage is approximated by stepwise discretized grids, and the 1000-meter-long pipe is divided into 3,960 relatively small reaches (i.e., spatial grid size $\Delta x \sim 0.25$ m) to decrease the frequency shift caused by numerical errors. Transients are generated by a sudden and full closure of the downstream valve and the pressure head trace is measured at the upstream face of the valve. The measured pressure head trace is transformed into the frequency domain by a fast Fourier transform (FFT) algorithm.

The analytical and numerical transient frequency responses with the first 10 resonant peaks are plotted in Fig. 4.6(a). In addition, the resonant frequency difference between analytical and numerical results for the first 100 resonant peaks are extracted and plotted in Fig. 4.6(b). Fig. 4.6(a) shows that the resonant peaks of the non-uniform blockage system are not uniformly distributed, and this means the presence of the non-uniform blockages has changed the resonant frequencies of the original intact system. Moreover, both figures indicate good agreement between the analytical and numerical results in terms of resonant frequencies, which confirms the validity of the analytical result in Eq. (4.27).

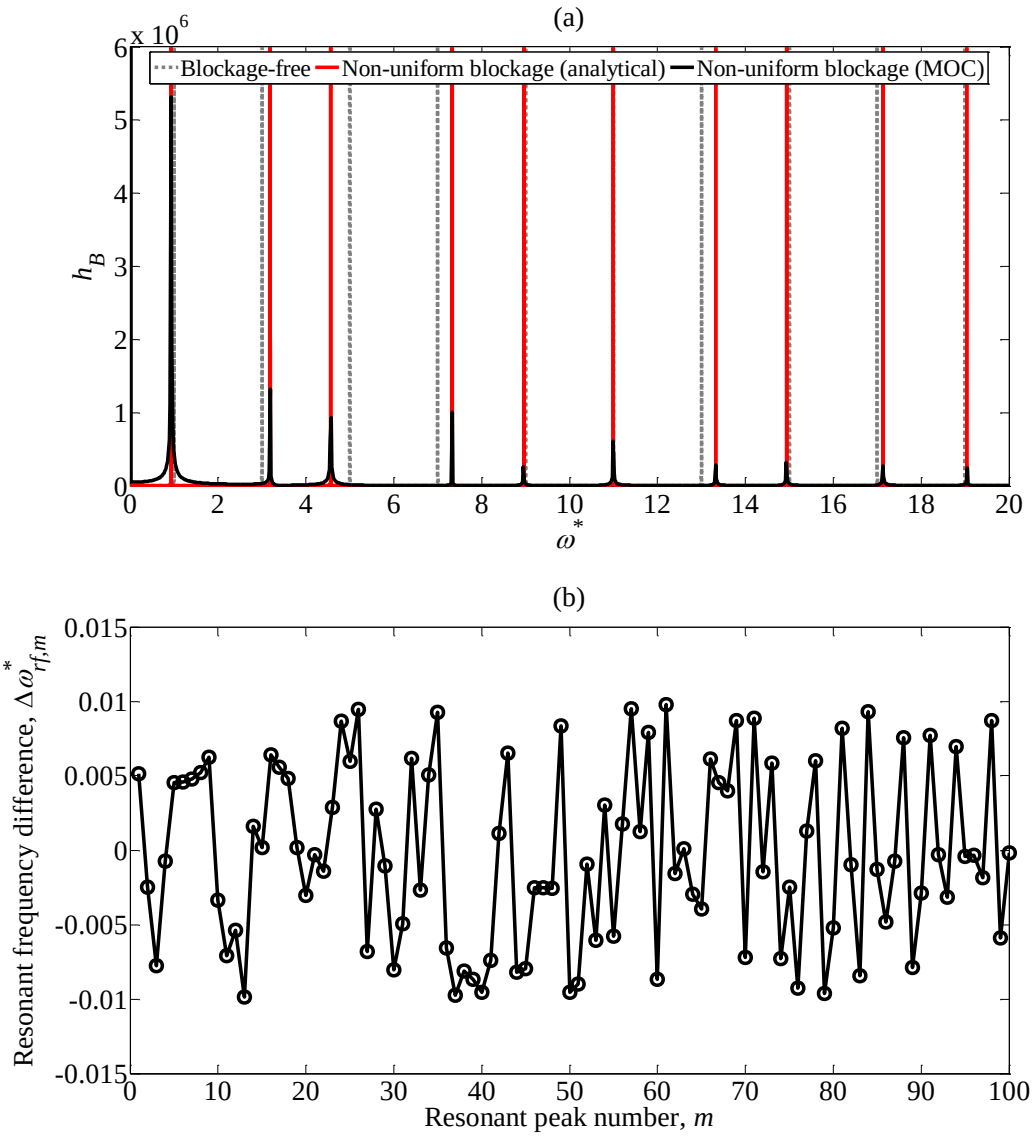

Fig. 4.6. Comparison of analytical and numerical results without friction effect: (a) transient frequency responses; (b) resonant frequency difference between analytical and numerical MOC results.

Table 4.2. Parameter settings for numerical validation.

Blockage type	l_1 (m)	l_2 (m)	l_3 (m)	l_4 (m)	R (m)	s	R_{L3} (m)	a_0 (m/s)	$\bar{a}_b$ (m/s)
non-uniform	295	105	105	495	0.25	0.1/105	0.15	1000	1050

4.4 Further Applications and Result Analysis

Based on the validated overall transfer matrix, the transient frequency responses for RPV systems with non-uniform blockages, as shown in Fig. 4.5(b), are investigated in this section. Duan et al. (2012a) demonstrated that friction effects (both steady and unsteady friction) induce decreases in the magnitude of resonant peaks but have little impact on the location of resonant peaks. The main purpose of this study is to investigate the influence of blockage non-uniformity on resonant frequency shifts; thus, only the linearized steady friction is included in the following numerical applications. The non-linear steady friction and unsteady friction (Meniconi et al., 2014) can be also included using a similar method as the one presented in Duan et al. (2018).

4.4.1 Uniform and Non-uniform Blockages with the Same Blocked Volume

To study the influence of blockage non-uniformity (e.g., blockage severity, length and slope) on transient frequency responses, seven test cases (Tests T1 ~ T7) with different parameters listed in Table 4.3 are investigated by the analytical results obtained in this study. In this section, the first three tests in Table 4.3 (i.e., T1 ~ T3) are used for comparison of the impacts of pipe blockage and its non-uniformity on transient frequency responses. Specifically, Tests T2 and T3 are the cases of uniform and non-uniform blockages with same blocked volume in the pipe, and Test T1 is the intact pipe system.

Table 4.3. Parameter settings for numerical test systems.

Test no.	Blockage type	l_1 (m)	l_2 (m)	l_3 (m)	l_4 (m)	R (m)	s	R_{L3} (m)	a_0 (m/s)	$\bar{a}_b$ (m/s)
T1	blockage-free	300	100	100	500	0.25	0	0.25	1206	1206
T2	uniform	300	100	100	500	0.25	0	0.20	1206	1249
T3	non-uniform	300	100	100	500	0.25	1e-3	0.15	1206	1249
T4	non-uniform	300	100	100	500	0.25	7.5e-4	0.175	1206	1238
T5	non-uniform	300	100	100	500	0.25	5e-4	0.20	1206	1227
T6	non-uniform	390	10	10	590	0.25	1e-2	0.15	1206	1249
T7	non-uniform	399	1	1	599	0.25	1e-1	0.15	1206	1249

The transient frequency responses of these three tests are plotted in Fig. 4.7. Fig. 4.7(a) is shown for the relatively low frequency domain, in which the dimensionless frequency ω^* ranges from 0 to 20.

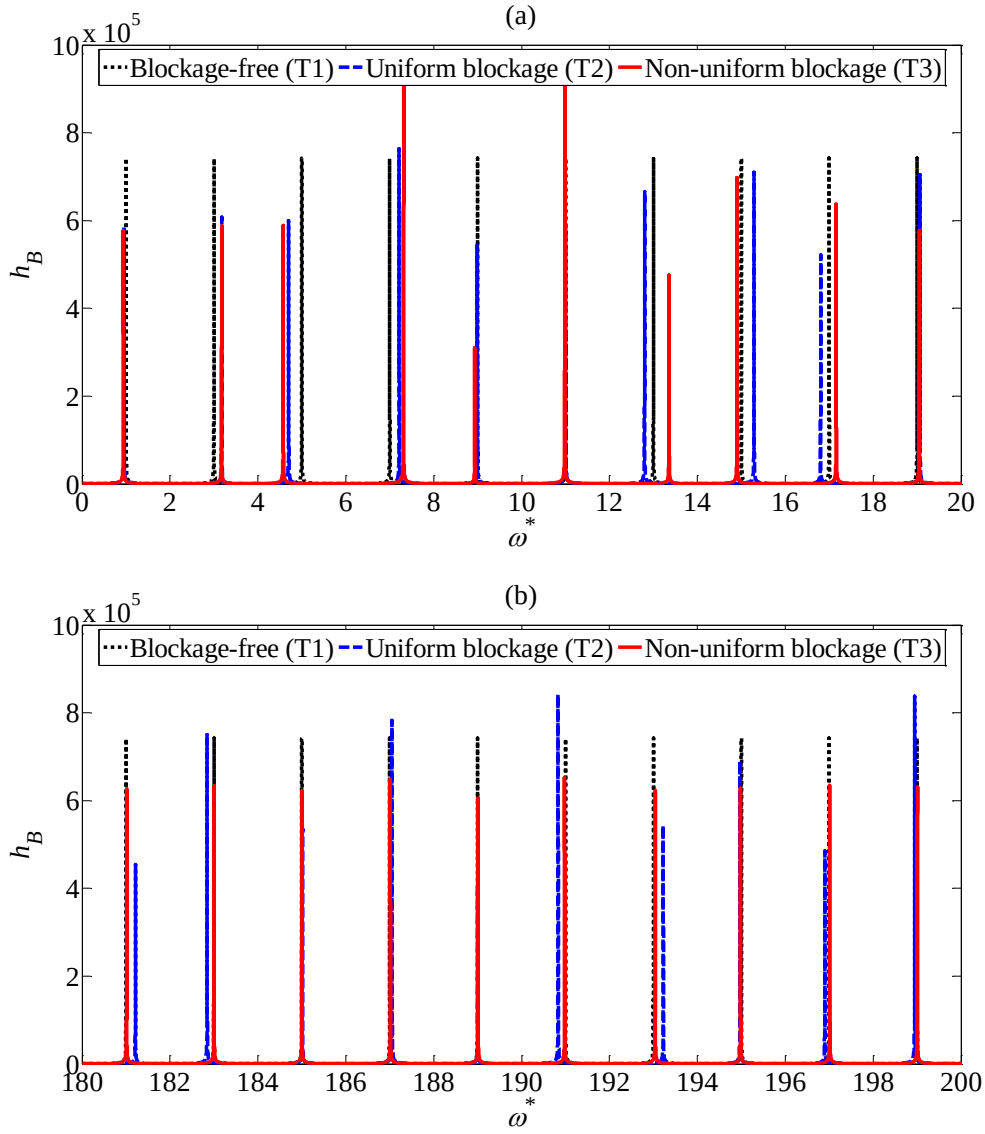

Fig. 4.7. Comparison of transient frequency responses of different pipe blockage situations with linearized steady friction effect: (a) low frequency harmonics; (b) higher frequency harmonics.

As shown in Fig. 4.7(a), the resonant peaks of the intact pipe system are uniformly distributed in the frequency domain, while the presence of uniform and non-uniform blockages within the pipe results in evident resonant frequency shifts and peak amplitude changes. Moreover, the resonant frequency shift and the peak amplitude change induced

by uniform and non-uniform blockages have significant differences, although the same blockage volume has been imposed for the two blockage situations. Fig. 4.7(b) is plotted for the relatively higher frequency domain, with the dimensionless frequency ω^* from 180 to 200. Similar with low frequency harmonics, both the resonant frequency shift and peak amplitude change caused by the non-uniform blockage are very different from that caused by the uniform blockage. Moreover, the resonant frequency of the non-uniform blockage system almost coincides with that of the blockage-free system. This can be explained by the Special Case (3) of Eq. (4.28): the frequency shift induced by non-uniform blockages becomes less evident for higher harmonics.

To gain an insight into the blockage induced frequency shift and amplitude change, the first 100 resonant peaks of the uniform and non-uniform blockage systems are further extracted and analyzed. The frequency shifts of uniform and non-uniform blockages are plotted in Fig. 4.8(a). Note that the blockage induced frequency shift for the *m*-th resonant peak is defined as $\delta\omega^*_m = \omega^*_{mb} - \omega^*_{mi}$, where ω^*_{mb} = frequency of *m*-th resonant peak for the blocked pipe system; and ω^*_{mi} = frequency of *m*-th resonant peak for the intact pipe system.

It can be observed from Fig. 4.8(a) that both the uniform and non-uniform blockages induced resonant frequency shifts that fluctuate with the peak number (equivalent to frequency). Specifically, the frequency shift fluctuation induced by the uniform blockage almost keeps the same order of magnitude as the peak number increases, while that induced by the non-uniform blockage is highly frequency dependent. In the results of non-uniform blockage, the frequency shift fluctuation becomes less evident (tends to zero) as frequency increases. Similarly, the blockage induced resonant peak amplitude change for the *m*-th resonant peak is defined as $\delta h_{B,m} = h_{B,mb} - h_{B,mi}$, where $h_{B,mb}$ = amplitude of *m*-th resonant peak for the blocked pipe system; and $h_{B,mi}$ = amplitude of *m*-th resonant peak for the intact pipe system. The resonant peak amplitude changes for uniform and non-uniform blockages are plotted in Fig. 4.8(b) for convenient comparison. Similar with frequency shift fluctuation, the resonant peak amplitude change fluctuation induced by

the uniform blockage almost keeps the same order of magnitude, while that induced by the non-uniform blockage gradually decreases with frequency.

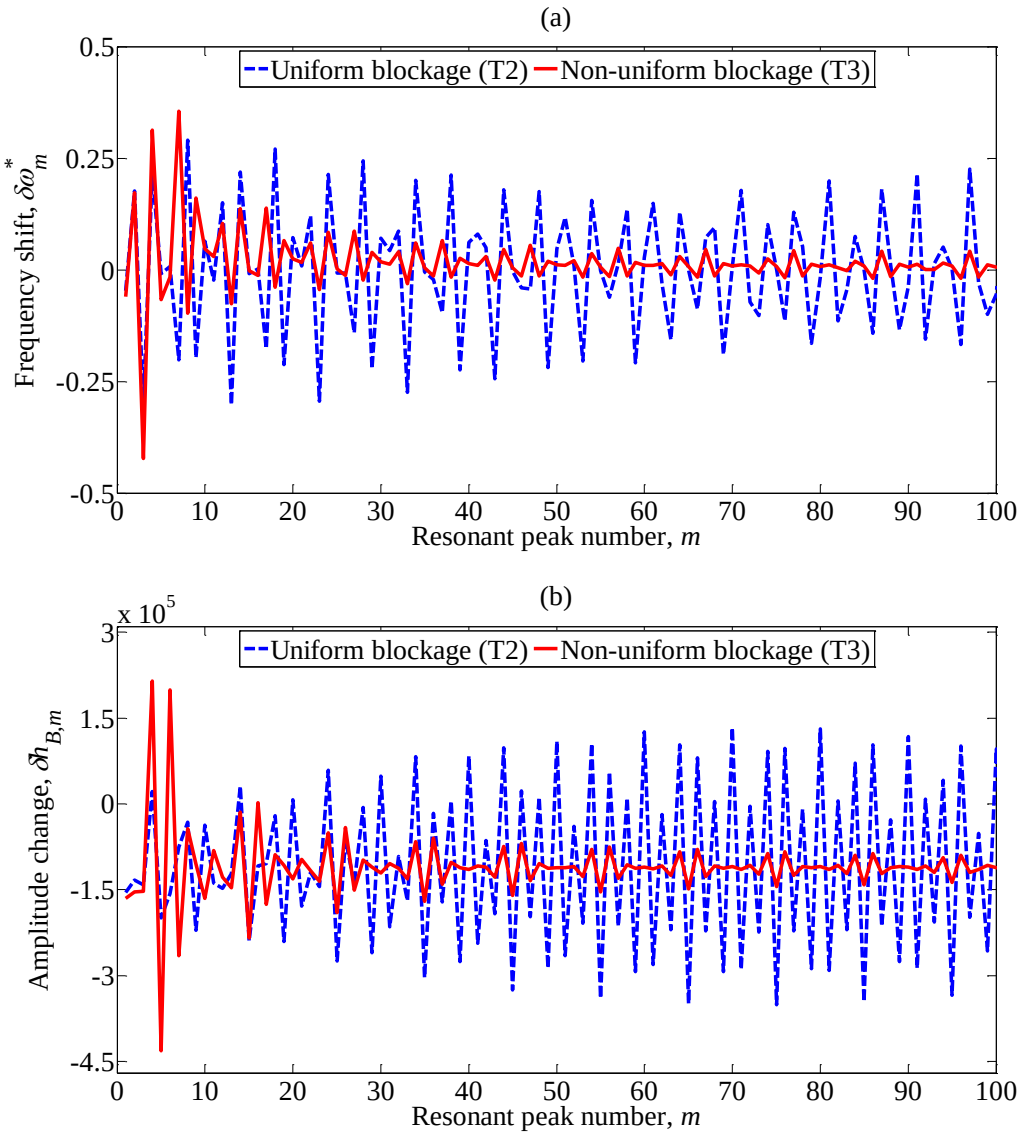

Fig. 4.8. Influence of uniform and non-uniform blockages on transient frequency responses: (a) relative resonant frequency shift; (b) relative resonant peak amplitude change.

4.4.2 Influence of Non-uniform Blockage Severity

In this section, the influence of non-uniform blockage severity on transient frequency responses is investigated. As shown in Fig. 4.5(b), the length of the non-uniform blockage (l_2 and l_3) is fixed. The blockage severity is defined as $S = (R - R_{L3})/R$, and it is proportional to the slope s of the non-uniform blockage $S \sim s = (R - R_{L3})/l_3$. For Tests T3 ~ T5 as shown in Table 4.3, R_{L3} gradually increases from 0.15 to 0.2 m, which means that the non-uniform blockage becomes less severe. The resonant frequency shift and peak amplitude change induced by non-uniform blockages are plotted in Fig. 4.9.

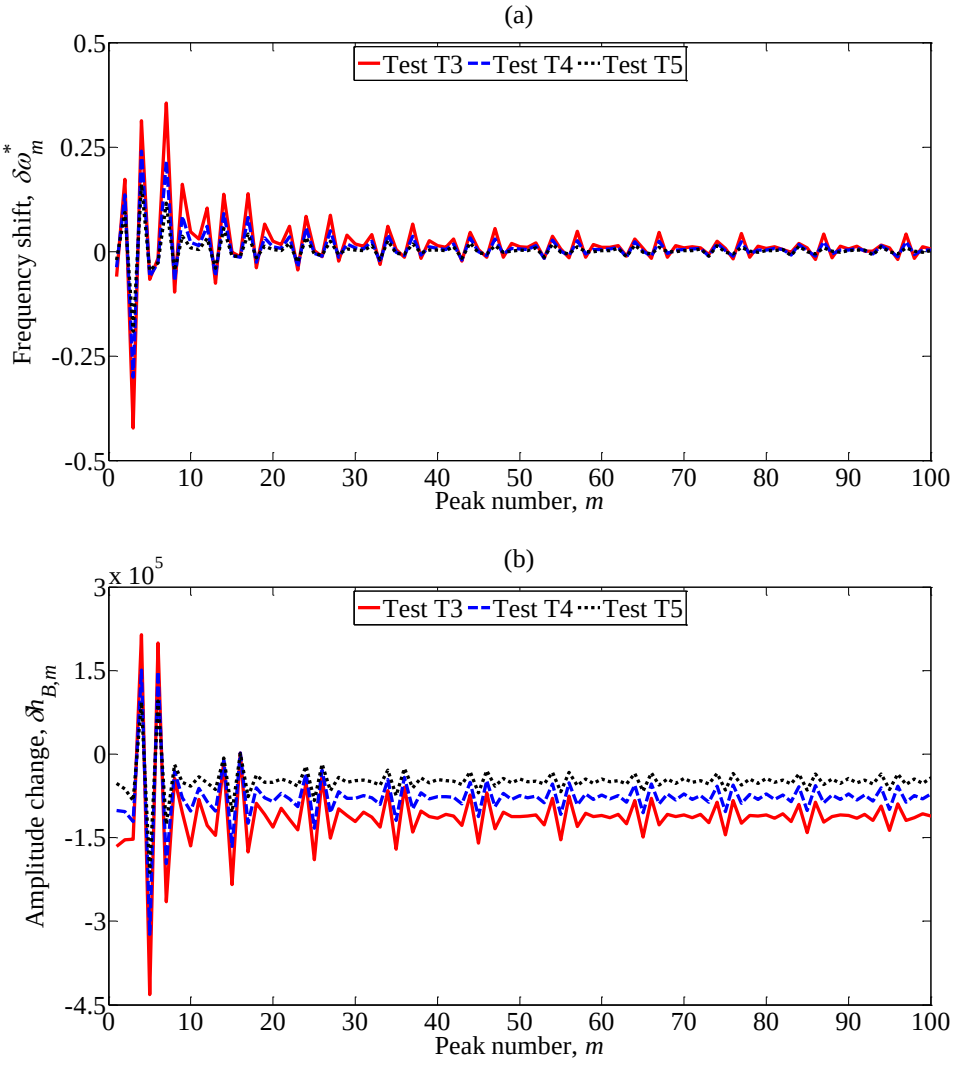

Fig. 4.9. Influence of non-uniform blockage with different blockage severities on transient frequency responses: (a) relative resonant frequency shift; (b) relative resonant peak amplitude change.

It is observed in Fig. 4.9(a) that the overall trend of frequency shift fluctuation for these cases is similar with Test T3 except for the extent of fluctuation. Specifically, the frequency shift fluctuation becomes less evident as the non-uniform blockage becomes less severe. Similarly, Fig. 4.9(b) indicates that the extent of amplitude change fluctuation decreases as the non-uniform blockage becomes less severe. These results are reasonable as severer non-uniform blockage should have more influences on the frequency and amplitude of transient frequency responses for original intact pipe system. In addition, the overall patterns (or trends) for frequency shift and amplitude change of these three cases are similar. This may indicate that the patterns of frequency shift and amplitude change are independent of the non-uniform blockage severity.

4.4.3 Influence of Non-uniform Blockage Lengths

The influence of non-uniform blockage length on transient frequency responses is examined herein by fixing other parameters. As is shown in Fig. 4.5(b), the location of non-uniform blockage center ($l_1 + l_2$) and the pipe radius at the left boundary of Pipe 3 (R_{L3}) are fixed. The non-uniform blockage length (l_2 and l_3) gradually decrease from 100 m to 1 m for Tests T3, T6 and T7 in Table 4.3. It is found that the frequency shift and amplitude change are in certain pattern, and the period of this pattern is inversely proportional to the length of the non-uniform blockage. For convenient observation, the peak number m is divided by the normalized parameter L/l_2 and is expressed as m^* in Fig. 4.10.

Fig. 4.10(a) shows that the frequency shift patterns for three cases are periodic and roughly the same, meanwhile the period of this induced pattern is in unit length of m^*. The overall extent of the frequency shift periodically decreases in terms of m^*. This frequency shift pattern can be explained by the former Special Case (3) of Eq. (4.28). As the m^*, which is proportional to ω, increases, the term $4R^2R_{L3}\omega^3\cos[k_b(l_1 + l_2 + l_3 + l_4)]$ containing ω^3 gradually becomes dominant and the frequency shift becomes less evident;

thus, the overall extent of periodic pattern gradually decreases. In addition, the periodic pattern can be attributed to the remaining trigonometric terms of Eq. (4.28). Similar behavior can be observed in Fig. 4.10(b) for the amplitude change induced by the non-uniform blockage. Besides, a longer non-uniform blockage causes more amplitude attenuation.

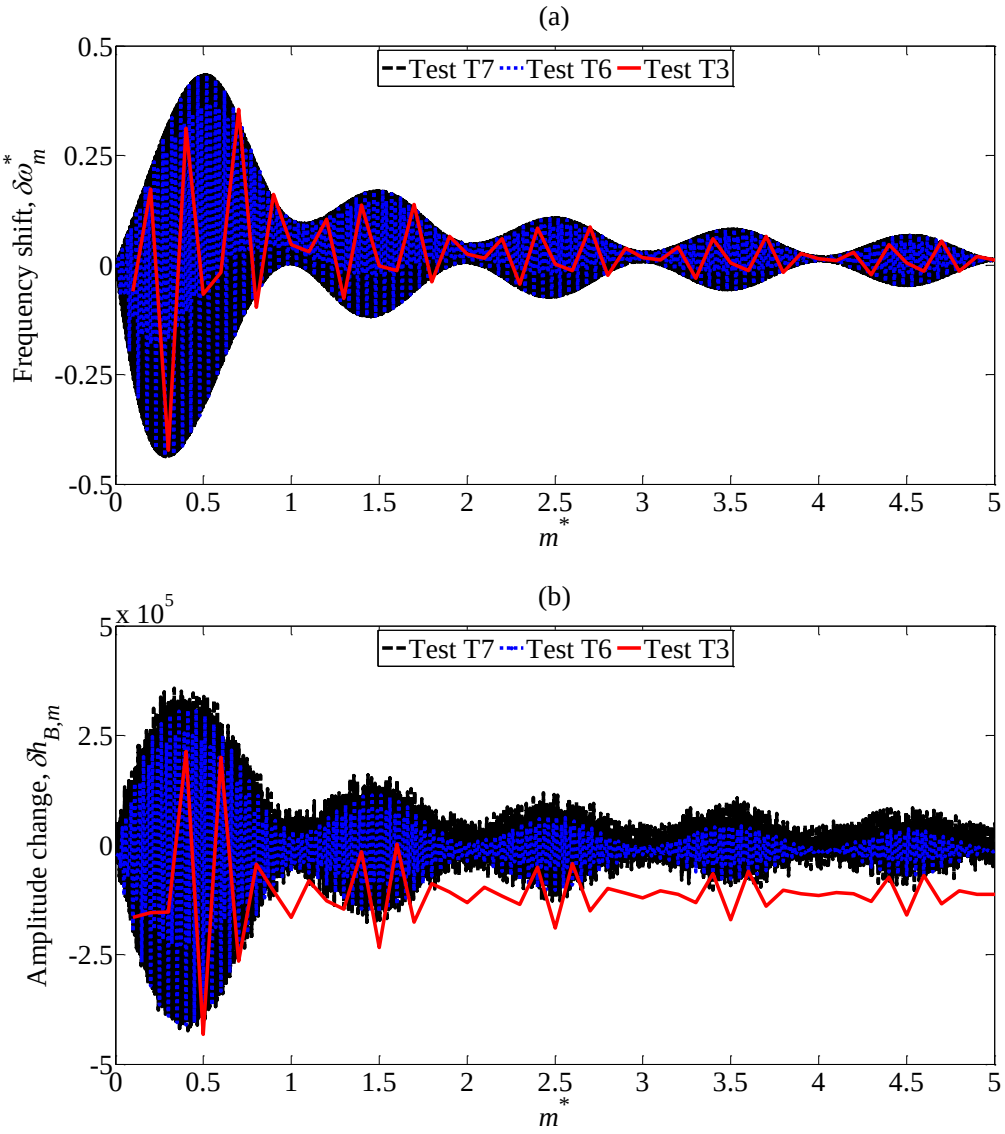

Fig. 4.10. Influence of non-uniform blockage with different blockage lengths on transient frequency responses: (a) relative resonant frequency shift; (b) relative resonant peak amplitude change.

4.4.4 Sensitivity Analysis of Resonant Frequency Shifts to the Transient Wave Speed

In realistic pipes as shown in Figs. 4.1(a) and 4.1(b), the wave speed $a_b(x)$ within the non-uniform blockage section would change along the axial direction due to the variation of pipe properties. In the above analytical derivations, the $a_b(x)$ is represented approximately by the average wave speed $\bar{a}_b$ under the same blocked volume condition. As a result, the observed resonant frequency shifts in Tests T3 ~ T7 are obtained based on this average wave speed $\bar{a}_b$. Therefore, it is necessary to examine the influence and validity range of this assumption for all tests in this study. For this purpose, the first-order second-moment (FOSM) method (Duan, 2016a) is adopted to theoretically investigate the sensitivity of the obtained resonant frequency shift patterns by the developed method in this study to the varying wave speed with average value of $\bar{a}_b$ in the non-uniform blockage section. Eq. (4.27) describes the relationship between the resonant frequency (ω_m) and system properties (e.g., average wave speed in the blocked section $\bar{a}_b$, wave speed in the intact section a_0, and slope of the non-uniform blockage s), which can be expressed as the following function

$$\omega_m = G(\bar{a}_b, a_0, s, R, R_{L3}, l_2, ...) = G(X_1, X_2, X_3, ..., X_j) \tag{4.29}$$

where $G()$ = function; $X_1 - X_j$ = uncertainty factors; j = number of uncertainty factors. The detailed procedures of FOSM for the sensitivity analysis may refer to the previous study of Duan (2016a).

For quantitative analysis, the sensitivity coefficient of resonant frequency shifts to the average wave speed $\bar{a}_b$ for the m-th resonant peak is defined as the variation (or variation percentage) of the transient response frequency shift to the variation (or variation percentage) of the wave speed

$$c_m = \frac{d(\delta\omega_m^*)}{da_b^*} = \frac{d(\delta\omega_m / \omega_{th})}{d(a_b / \bar{a}_b)} \tag{4.30}$$

Eq. (4.30) is evaluated at (μ_1, μ_2, μ_3, …, μ_j), in which $\mu_1 - \mu_j$ are mean values of variables $X_1 - X_j$.

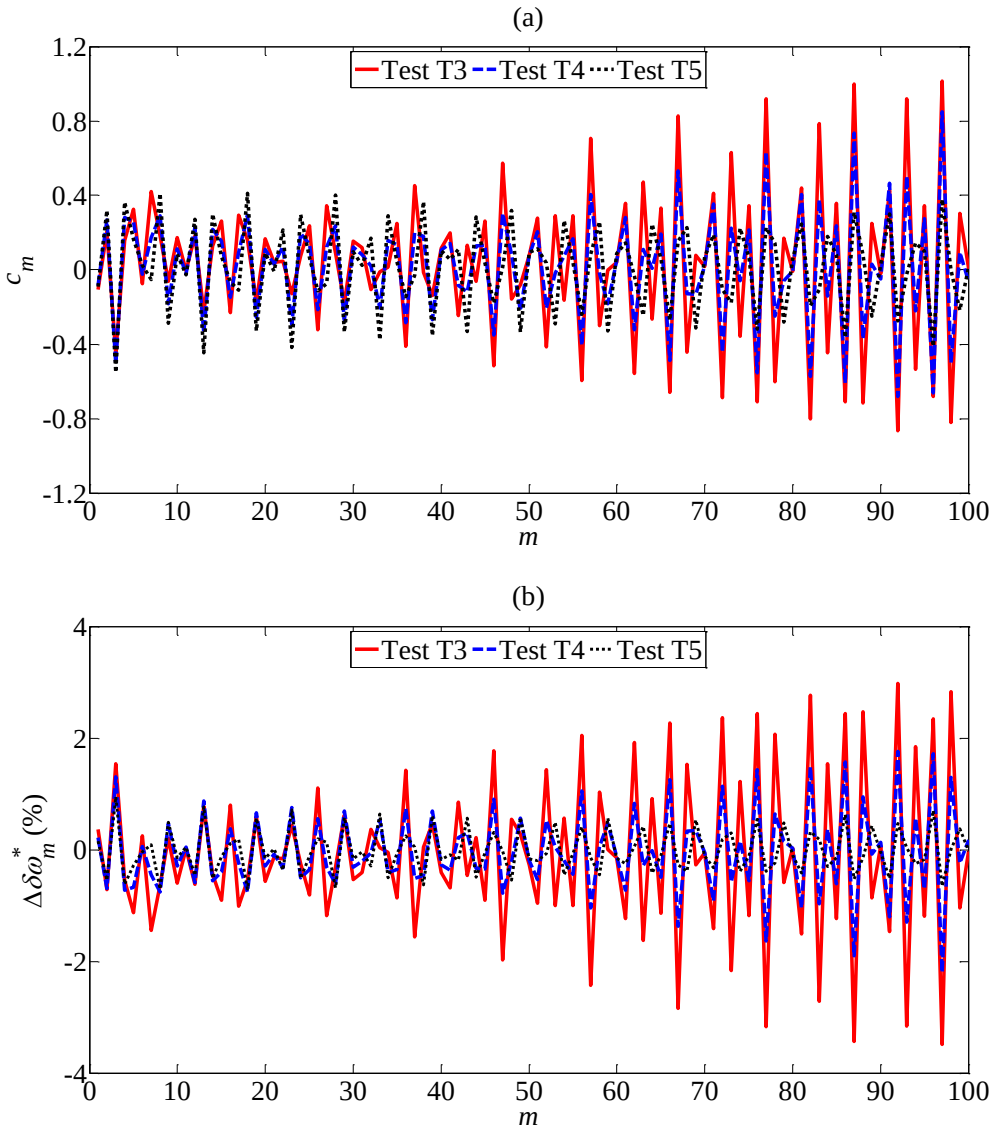

Fig. 4.11. (a) Sensitivity coefficients of resonant frequency shifts to the average wave speed within the blocked section; (b) errors of resonant frequency shifts for Tests T3, T4, and T5.

By combining the results of Eq. (4.27) through Eq. (4.30), the sensitivity coefficients (c_m) of Tests T3, T4, and T5 for the first 100 resonant peaks (representing for both low and relatively high frequency domains) are calculated and plotted in Fig. 4.11(a). It can be observed in Fig. 4.11(a) that the first 20 resonant peaks (i.e., relatively low frequency domain), which are usually of practical importance, is less sensitive to the wave speed variation compared with remaining resonant peaks in high frequency regions; and the

maximum value of sensitivity coefficient (i.e., 0.55) for the first 20 resonant peaks occurs at $m = 3$ for Test T5. Then, the sensitivity coefficients for two severer blockage cases (i.e., Tests T3 and T4) gradually increase with frequency. The maximum value of sensitivity coefficient (i.e., 1.01) occurs at $m = 97$ for Test T3, which means that the maximum error (or uncertainty) of resonant frequency shifts induced by the varying wave speed is in the same order as the variation of wave speed parameter. While the sensitivity coefficients for the shallow blockage case (i.e., Test T5) almost keep the same order of magnitude in the frequency domain, which is much less than 1.0. As a result, the percentage errors of frequency shifts $\Delta\delta\omega^*_m$ induced by the varying wave speed in the blockage section for Tests T3, T4, and T5 are calculated as $\Delta\delta\omega^*_m = c_m((a_0 - \bar{a}_b)/\bar{a}_b)\times 100\%$ and plotted in Fig. 4.11(b). The result clearly shows that the maximum frequency shift errors for Tests T3, T4, and T5 are within 3.5%, 2.2%, and 1.0%, respectively, which are acceptable for applications of blockage detection.

4.5 Discussion and Implications

The above results and analysis suggest that, unlike the uniform blockage, the frequency shift $\delta\omega^*_m$ induced by the non-uniform blockage is frequency dependent, $\delta\omega^*_m \sim 1/\omega^*_m$. As the frequency ω^*_m increases, the induced frequency shift $\delta\omega^*_m$ becomes less evident. This finding is useful to explain the inaccuracy of the current frequency domain transient-based method, which is based on the blockage induced frequency shift, for non-uniform blockage detection in Duan et al. (2017). Therefore, further improvement of such transient-based method is necessary for the non-uniform blockage detection.

The results comparison has also shown that, with fixed blockage length, the blockage induced frequency shift gets more evident as the non-uniform becomes severer (i.e., $\delta\omega^*_m \sim s$). Besides, the overall extent of frequency shifts for different blockage severities is decreased as frequency increases (i.e., $\delta\omega^*_m \sim 1/\omega^*_m$). Therefore, for non-uniform blockages with a fixed length, the blockage induced frequency shift $\delta\omega^*_m$ is proportional to the slope of the non-uniform blockage (s), and is inversely related to the frequency ω^*_m, that is $\delta\omega^*_m \sim s/\omega^*_m$. In addition, for non-uniform blockages with fixed severity, the frequency shift pattern for various blockage lengths is the same, and the period of this pattern $T_{pattern}$ is inversely proportional to the length of the blockage $T_{pattern} \sim 1/l_2$. This period may offer us a method to detect the length of the non-uniform blockage. Based on $m/(L/l_2) = T(m^*)$, where $T = 1$ is the period of the frequency shift pattern in terms of m^*, the blockage length l_2 can be determined.

The obtained dependence relationship between transient wave behavior and blockage non-uniformity may provide useful implications to the transient analysis and blockage detection in real world pipe systems. Specifically, the current transient-based method can be further extended to more general and realistic situations of pipe blockages. That is, it is necessary to include the characteristic parameters, i.e., the slope (s), severity (R_{L3}) and location (l_4) of non-uniform blockages, in the transient-based method, which can be inversely determined based on the derived results in Eq. (4.27) of this chapter.

Consequently, it is expected that, based on the results and findings of this chapter, the accuracy of current transient-based method can be improved and extended for realistic pipe diagnosis, which will be investigated through further theoretical analysis and experimental tests in future work.

4.6 Summary

This chapter investigates the transient frequency responses of pressurized water pipes with non-uniform blockages. The transient wave behavior is obtained by analytically solving the 1D wave equation for a single blockage with a linearly varying diameter. The wave solution is used to derive the overall transfer matrix of a pressurized water pipe system with non-uniform blockages, which is numerically validated by the traditional MOC.

With validated analytical results, the influences of the blockage shape (slope), severity and length on transient frequency responses are studied systematically for different cases. The results indicate the non-uniform blockage may induce very different modification patterns on the frequency shift and amplitude change of transient waves from the uniform blockage situation. Specifically, the resonant frequency shifts induced by non-uniform blockages become less evident for higher harmonics.

Although only the linear non-uniform blockages have been considered, this chapter may provide a framework for exploring the transient frequency responses of realistic pipes with non-uniform blockages. It is also noted that the physical mechanism of the non-uniform blockage induced frequency shift pattern is still unclear, which needs further investigations in the next chapter.

CHAPTER 5 ENERGY ANALYSIS OF THE RESONANT FREQUENCY SHIFT PATTERN INDUCED BY NON-UNIFORM BLOCKAGES IN WATER PIPES[4]

5.1 Introduction

In Chapter 4, the author studied the influence of *linear non-uniform blockages*, whose diameters vary linearly along their lengths (see Fig. 4.1(c)), on transient frequency responses (Che et al., 2018b). It was found that linear non-uniform blockages give rise to significantly different resonant frequency shift patterns from uniform blockages. Specifically, the resonant frequency shifts induced by linear non-uniform blockages become less evident for higher harmonics (termed as the *non-uniform blockage induced resonant frequency shift pattern*), but the physical mechanism of this pattern from analytical and numerical results is still unclear.

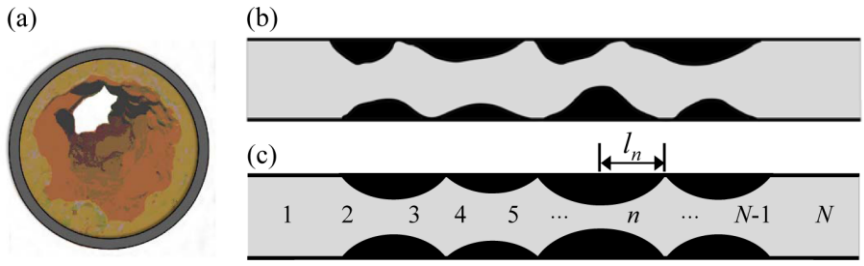

Fig. 5.1. (a) Random and non-uniform blockages in real water pipes (reprinted from (Che et al., 2018b), © ASCE); (b) sketch of a real pipe with random and non-uniform blockages; (c) sketch of a simplified pipe with exponential non-uniform blockages used for analytical analysis.

[4] This chapter is adapted from the research paper of the author and his co-authors (Che et al., 2019c).

As a continuation of the previous chapter on linear non-uniform blockages (Che et al., 2018b), this chapter intends to: (i) investigate the resonant frequency shift pattern induced by other non-linear non-uniform blockages, as shown in Fig. 5.1(c), whose diameters vary exponentially along their lengths (termed as *exponential non-uniform blockages*), to generalize further the conclusions drawn in the previous chapter (Che et al., 2018b); and (ii) qualitatively explain the *physical mechanism* of the non-uniform blockage induced frequency shift pattern from an *energy* perspective. To this end, the overall transfer matrixes of pipe systems with exponential non-uniform blockages are derived to realize Aim (i). To achieve Aim (ii), the energy transmission coefficients of blocked pipe systems are analytically derived based on the system overall transfer matrixes obtained in Aim (i). The results and findings of this study are expected to provide scientific basis for method development of blockage detection in urban water supply systems.

5.2 Energy Transmission Coefficient of an Unbounded Water Pipe with Blockages

5.2.1 Overall Transfer Matrix of a Pipe System with Exponential Non-uniform Blockages

To facilitate the analytical analysis, the real blockages in Figs. 5.1(a) and 5.1(b) are simplified into a series of exponential non-uniform blockages, as shown in Fig. 5.1(c), whose radiuses change exponentially along the axial direction. The one-dimensional (1D) wave equation in the frequency domain for the *n*-th exponential non-uniform blockage in Fig. 5.1(c) is (Che et al., 2017; Che et al., 2018b)

$$\frac{d^2 p_n}{dx^2} + \frac{A_n'}{A_n}\frac{dp_n}{dx} + k_0^2 p_n = 0 \tag{5.1}$$

where p = pressure deviation from the mean in the frequency domain; x = distance along the pipe; $A = A(x)$ = pipe cross-sectional area; A' = derivative of A; $k_0 = \omega/a_0$ = wave number in intact pipe sections, in which ω = angular frequency, a_0 = wave speed; subscript n = the n-th exponential non-uniform blockage in Fig. 5.1(c).

Note that a frictionless pipe system with an elastic pipe wall is firstly considered in the analytical analysis to highlight the interaction between transient waves and non-uniform blockages (Che et al., 2018b; Duan et al., 2014). The influence of friction on the derived analytical result will be further discussed in Section 5.4. In addition, it was found by the author in Chapter 4 (Che et al., 2018b) that the wave speed a_b within blockages has a limited influence on the overall resonant frequency shift pattern induced by non-uniform blockages. Therefore, to simplify the problem, the transient wave speed is assumed to be constant throughout the pipe (i.e., $a(x) = a_0$).

As shown in Fig. 5.1(c), the pipe radius of the *n*-th exponential non-uniform blockage is defined as

$$r_n(x) = R_{Ln} e^{s_n x} \tag{5.2}$$

where r_n = pipe radius of the n-th exponential non-uniform blockage; R_{Ln} = pipe radius at the left boundary of the n-th exponential non-uniform blockage; s_n = a coefficient that determines the radius changing rate of the n-th exponential non-uniform blockage, which is defined as $s_n = \ln(R_{Rn}/R_{Ln})/l_n$, where R_{Rn} = pipe radius at the right boundary of the n-th exponential non-uniform blockage, l_n = length of the n-th exponential non-uniform blockage.

Then, the cross-sectional area of the n-th exponential non-uniform blockage A_n and its derivative A_n' in Eq. (5.1) can be determined. Substituting A_n and A_n' into Eq. (5.1), the 1D wave equation for the n-th exponential non-uniform blockage becomes

$$\frac{d^2 p_n}{dx^2} + 2s_n \frac{dp_n}{dx} + k_0^2 p_n = 0 \tag{5.3}$$

Using the plane wave solution $p_n = e^{-ikx}$ as a trial solution of Eq. (5.3), results in the following dispersion relation

$$k^2 + 2is_n k - k_0^2 = 0 \tag{5.4}$$

where i = imaginary number; k = wave number. The solutions of Eq. (5.4) are (Che et al., 2017)

$$k = \pm\sqrt{k_0^2 - s_n^2} - is_n \tag{5.5}$$

Thus, the following general solutions for the n-th exponential non-uniform blockage can be obtained

$$p_n = \frac{C_1 e^{ik'x} + C_2 e^{-ik'x}}{R_{Ln} e^{s_n x}} \tag{5.6}$$

where $k' = (k_0^2 - s_n^2)^{1/2}$ = the group wave number of transient waves in the exponential non-uniform blockage; C_1 and C_2 are two constants.

The general solutions in Eq. (5.6) are a linear superposition of the incident and reflected waves propagating towards opposite directions. Moreover, in the case of exponential non-

uniform blockages, $|s_n|$ represents the cutoff wave number. At wave numbers lower than $|s_n|$ (i.e., $k_0 < |s_n|$), k' is imaginary. The general solutions in Eq. (5.6) become evanescent waves, which decay along the pipe and do not propagate as true transient pressure waves (Blackstock, 2000).

Based on the general solutions in Eq. (5.6), the transfer matrix of the n-th exponential non-uniform blockage in Eq. (5.7) connecting two state vectors at two boundaries is obtained (Che et al., 2017; Che et al., 2018b). Note that the pressure deviation p is transformed into the pressure head deviation h, which is a common practice in hydraulic engineering.

$$\begin{pmatrix} q \\ h \end{pmatrix}_{n+1} = \begin{pmatrix} U_{11} & U_{12} \\ U_{21} & U_{22} \end{pmatrix} \begin{pmatrix} q \\ h \end{pmatrix}_{n} \tag{5.7}$$

where subscripts n and n+1 are the upstream and downstream boundaries of the n-th exponential non-uniform blockage, respectively; q = discharge deviation in the frequency domain; h = pressure head deviation in the frequency domain; U_{ij} = transfer matrix elements, which are as follows:

$$U_{11} = \frac{S_{n+1}}{S_n} \frac{\left(ik' - s_n\right)e^{ik'l_n} + \left(ik' + s_n\right)e^{-ik'l_n}}{2ik'e^{s_n l_n}}$$

$$U_{12} = \frac{S_{n+1} g \left(ik' - s_n\right)\left(ik' + s_n\right)}{\omega} \frac{e^{ik'l_n} - e^{-ik'l_n}}{2k'e^{s_n l_n}}$$

$$U_{21} = \frac{\omega}{S_n g} \frac{-e^{ik'l_n} + e^{-ik'l_n}}{2k'e^{s_n l_n}}$$

$$U_{22} = \frac{\left(ik' + s_n\right)e^{ik'l_n} + \left(ik' - s_n\right)e^{-ik'l_n}}{2ik'e^{s_n l_n}}$$

where g = gravitational acceleration; S_n and S_{n+1} = pipe cross-sectional areas at the upstream and downstream boundaries of the n-th exponential non-uniform blockage, respectively.

Note that the uniform pipe is one special case of the exponential non-uniform blockage. Let $s_n = 0$, which is equivalent to a single uniform pipe, Eq. (5.7) becomes

$$\begin{pmatrix} q \\ h \end{pmatrix}_{n+1} = \begin{pmatrix} \cos(k_0 l_n) & -i\dfrac{S_{n+1} g}{a_0}\sin(k_0 l_n) \\ -i\dfrac{a_0}{S_n g}\sin(k_0 l_n) & \cos(k_0 l_n) \end{pmatrix} \begin{pmatrix} q \\ h \end{pmatrix}_n \tag{5.8}$$

which is consistent with previous studies on transfer matrixes of uniform pipes (Chaudhry, 2014; Wylie et al., 1993). The overall transfer matrix of a blocked pipe system, as shown in Fig. 5.1(c), can be produced by multiplying individual matrixes of each pipe component in the order of their locations (Chaudhry, 2014; Duan et al., 2012a; Lee et al., 2006b; Wylie et al., 1993).

$$\begin{aligned} \begin{pmatrix} q \\ h \end{pmatrix}_1 = & \begin{pmatrix} \cos(k_0 l_1) & -i\dfrac{S_2 g}{a_0}\sin(k_0 l_1) \\ -i\dfrac{a_0}{S_1 g}\sin(k_0 l_1) & \cos(k_0 l_1) \end{pmatrix} \times \cdots \times \begin{pmatrix} (U_{11})_n & (U_{12})_n \\ (U_{21})_n & (U_{22})_n \end{pmatrix} \times \cdots \\ & \times \begin{pmatrix} \cos(k_0 l_N) & -i\dfrac{S_{N+1} g}{a_0}\sin(k_0 l_N) \\ -i\dfrac{a_0}{S_N g}\sin(k_0 l_N) & \cos(k_0 l_N) \end{pmatrix} \begin{pmatrix} q \\ h \end{pmatrix}_{N+1} \end{aligned} \tag{5.9}$$

where subscripts "1" and "N+1" are locations of upstream and downstream boundaries of a blocked pipe system, as shown in Fig. 5.1(c), respectively.

Rewrite Eq. (5.9) in the following simplified form

$$\begin{pmatrix} q \\ h \end{pmatrix}_1 = \begin{pmatrix} U_{11}^* & U_{12}^* \\ U_{21}^* & U_{22}^* \end{pmatrix} \begin{pmatrix} q \\ h \end{pmatrix}_{N+1} \tag{5.10}$$

where U_{ij}^* = elements of the system overall transfer matrix.

5.2.2 Energy Transmission Coefficient of an Unbounded Blocked Pipe System

Based on the above overall transfer matrix in Eq. (5.10), the energy transmission coefficient of an unbounded blocked pipe system is derived in this section. To simplify the problem, a pipe system with two symmetrical exponential non-uniform blockages (i.e.,

$l_2 = l_3$), as shown in Fig. 5.2, is selected for investigation. Note that the derived energy transmission coefficient can be also applied to pipe systems with multiple non-uniform blockages (see Fig. 5.1(c)) as long as the system overall transfer matrixes are determined.

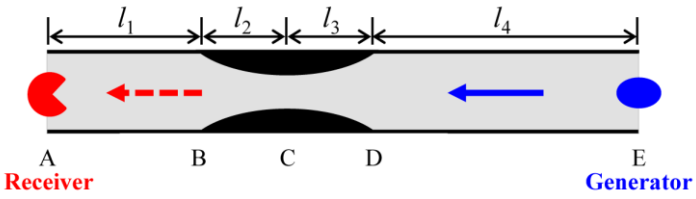

Fig. 5.2. An unbounded pipe system containing two symmetrical exponential non-uniform blockages (with a wave generator and a wave receiver).

In physics, a transient wave is a pressure disturbance that travels through fluids, accompanied by a transfer of energy. The energy transmission coefficient of a blocked pipe system with anechoic boundaries (i.e., located at A and E), as shown in Fig. 5.2, is defined as the ratio between the energy flow (i.e., power) transmitted through the non-uniform blockages (W_{tr}) and that incident on the non-uniform blockages (W_{in}).

$$T_C = \frac{W_{tr}}{W_{in}} \tag{5.11}$$

where T_C = energy transmission coefficient.

By applying the above-defined energy transmission coefficient T_C in Eq. (5.11) to the classical water hammer theory (note that the detailed derivation procedure is provided in Appendix A2), finally the T_C can be represented by the overall transfer matrix elements U_{ij}^* in Eq. (5.10).

$$T_C = \left| \frac{2}{\frac{gS_0U_{21}^*}{a_0} + U_{22}^* + U_{11}^* + \frac{a_0U_{12}^*}{gS_0}} \right|^2 \tag{5.12}$$

where S_0 = cross-sectional areas at two boundaries A and E in Fig. 5.2.

5.3 Energy Transmission Coefficient Pattern and Its Physical Mechanisms

5.3.1 Energy Transmission Coefficient Patterns of Pipe Systems with Various Blockages

Based on the derived energy transmission coefficient T_C in Eq. (5.12), the T_C patterns of pipe systems with various blockages are visualized in this section. Because the following results involve the Bragg's law, there is a need to review related fundamental theory herein. The Bragg's law was firstly proposed by Bragg and Bragg (1913) in the process of investigating the composition of X-rays. It relates the wavelength of the X-ray and the distance between crystal atomic sheets to the angles at which an impinging X-ray beam would be reflected. Recently, the Bragg resonance phenomena of transient waves in a pressurized water pipe containing a single uniform blockage were studied by Louati et al. (2018). As shown in Fig. 5.3(a), an incident wave with a certain wavelength (λ) impinges on the uniform blockage from the right end (i.e., Location E). From Location E to Location A, this incident wave first encounters a sudden constriction at Junction D and then a sudden expansion at Junction B. The incident wave is partially reflected at these junctions. According to the Joukowsky's equation (Joukowsky, 1898), the sign of the reflected wave from Junction D keeps the same with the incident wave. In contrast, the reflected wave from Junction B is opposite in sign to the incident wave. In addition, the reflected wave from Junction B travels a distance $2(l_2 + l_3)$ more than the wave reflected by Junction D. Because these two reflected waves from Junctions B and D are opposite in sign, they experience destructive interference at Junction D when $j\lambda = 2(l_2 + l_3)$, where j = 1, 2, 3…. On this occasion, the incident wave has the maximum transmission. Conversely, these two reflected waves experience constructive interference at Junction D when $(2j + 1)\lambda/2 = 2(l_2 + l_3)$, then the incident wave has the minimum transmission.

Whereas the Bragg resonance condition of non-uniform blockages in this thesis is different from that of uniform blockages investigated in the previous study of Louati et al. (2018). As shown in Figs. 5.3(b) and 5.3(c), from Location E to Location A, the

incident wave first encounters a continuous constriction between Junctions C and D and then a continuous expansion between Junctions B and C. On average, the waves reflected by the continuous expansion only travel a distance $2l_3$ (note that $l_2 = l_3$ in this study) more than the reflected waves from the continuous constriction. Therefore, these two regional waves reflected by the continuous constriction and expansion have destructive interference when $j\lambda = 2l_3$ and constructive interference when $(2j + 1)\lambda/2 = 2l_3$.

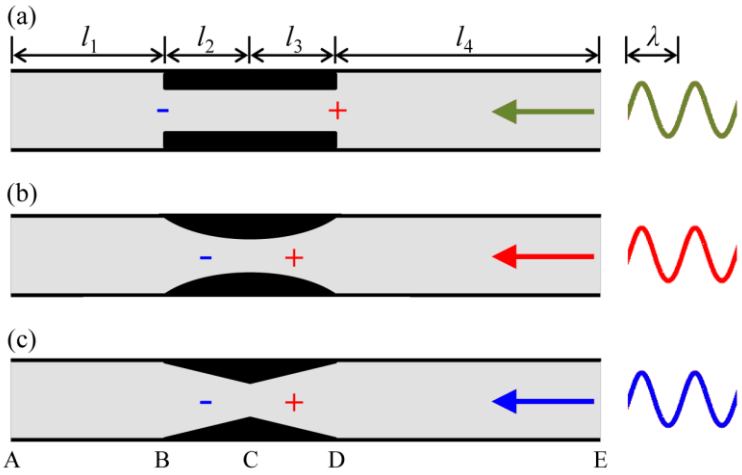

Fig. 5.3. Unbounded pipe systems with (a) uniform blockages; (b) exponential non-uniform blockages; and (c) linear non-uniform blockages.

Table 5.1. Detailed pipe system parameters for energy transmission coefficient T_C calculations.

Blockage type	l_1 (m)	l_2 (m)	l_3 (m)	l_4 (m)	R (m)	$\|s\|$	R_C (m)
intact	300	100	100	500	0.25	0	0.25
uniform	300	100	100	500	0.25	0	0.2
exp non-uniform	300	100	100	500	0.25	4.64E-03	0.1572
linear non-uniform	300	100	100	500	0.25	1.00E-03	0.15

The derived energy transmission coefficients T_C in Eq. (5.12) of unbounded pipe systems containing uniform or non-uniform (including linear and exponential) blockages are visualized in Fig. 5.4. Note that these blockages have the same blocked volume. The T_C curve of an intact pipe system is also plotted in Fig. 5.4 for convenient comparison. The detailed parameters of these 4 cases are listed in Table 5.1, in which R = radius of an

intact pipe; R_C = pipe radius at Junction C in Fig. 5.3; $|s|$ = the radius changing rate of non-uniform blockages; "exp" = is short for "exponential".

As shown in Fig. 5.4, the incident wave frequency is normalized by the minimum destructive interference frequency of the blockages, which is $2\pi(a_0/(2(l_2 + l_3)))$ for uniform blockages and $2\pi(a_0/(2l_3))$ for non-uniform blockages, and is expressed as ω^*. According to Fig. 5.4, the energy transmission coefficient T_C of the intact pipe system keeps the constant value of 1, which is physically reasonable since the incident wave should be entirely transmitted through an intact pipe without any reflection. However, the T_C curves of three blocked pipe systems are highly frequency dependent. Specifically, the T_C curve of the uniform blocked pipe system fluctuates periodically with constant extent. This is consistent with previous studies on uniform blockages (Duan et al., 2014; Louati et al., 2018). Although the T_C curves of these two pipe systems with non-uniform blockages also fluctuate periodically, their extent gradually becomes less evident for higher frequency incident waves. This means that the higher the incident wave frequency, the more energy is transmitted through these two non-uniform blockages. The physical mechanisms that govern these T_C patterns in Fig. 5.4 will be further explained in the following section (note that the following discussion mainly focuses on exponential non-uniform blockages, and more detailed information about the energy analysis of linear non-uniform blockages can be found in the conference paper (Che et al., 2018c)).

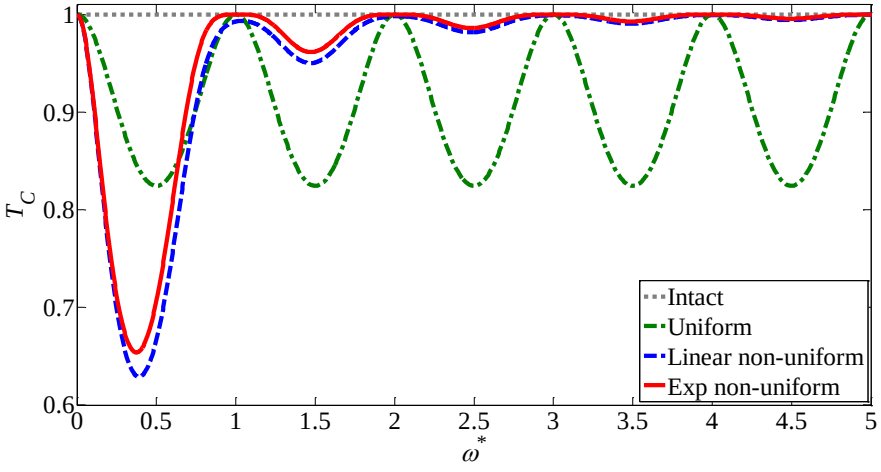

Fig. 5.4. Energy transmission coefficients T_C of intact and blocked pipe systems.

5.3.2 Physical Mechanisms of Energy Transmission Coefficient Patterns

Based on Eq. (A.9) in Appendix A2 and the frictionless 1D water hammer model, the impedance of a blocked pipe system can be written as

$$Z = \frac{p}{q} = \frac{Z_{sp}}{A} = \frac{\rho_0 \omega}{kA} \tag{5.13}$$

where Z = impedance; Z_{sp} = specific impedance; ρ_0 = fluid density. Substituting the forward propagating wave in Eq. (5.5) (i.e., keep the "+" sign) into Eq. (5.13), gives

$$\begin{aligned} Z_n &= \frac{\rho_0 \omega}{A\left(\sqrt{k_0^2 - s_n^2} - i s_n\right)} = \frac{\rho_0 a_0}{A\left(\sqrt{1 - \left(\frac{s_n}{k_0}\right)^2} - i\frac{s_n}{k_0}\right)} \\ &= \frac{\rho_0 a_0}{A}\left(\sqrt{1 - \left(\frac{s_n}{k_0}\right)^2} + i\frac{s_n}{k_0}\right) = \frac{\rho_0 a_0}{A}\left(\sqrt{1 - \left(\frac{\omega_{cut}}{\omega}\right)^2} + i\frac{\omega_{cut}}{\omega}\right) \end{aligned} \tag{5.14}$$

where $\omega_{cut} = s_n a_0$ is the cutoff frequency of the n-th exponential non-uniform blockage.

Two physical mechanisms that govern the overall patterns of T_C in Fig. 5.4 are: (1) the Bragg's law; and (2) the impedance mismatch between the intact and blocked pipe sections:

(1) Specifically, the fluctuation of energy transmission coefficient T_C curves in Fig. 5.4 is due to the Bragg's law. Take the uniform blockage in Fig. 5.3(a) for instance, the reflected waves (from Junctions B and D) of the incident wave at most frequencies would not experience constructive interference at Junction D, because these reflected waves would be out of phase (i.e., phase shift ranges from 0 to π), cancelling part of the reflected energy out. However, when the incident wave frequency is an integral multiple of the minimum destructive interference frequency of the blockage (i.e., ω^* = 1, 2, 3, 4, 5 in Fig. 5.4) the reflected waves (from Junctions B and D) would be completely out of phase (i.e., phase shift is π), cancelling each other out. In such situations, the incident wave has the maximum transmission. Therefore, the fluctuation period of T_C curves in Fig. 5.4 is one unit of the minimum destructive interference frequency of the blockages.

(2) The fluctuating extent of energy transmission coefficient T_C curves in Fig. 5.4 is governed by the impedance mismatch (ΔZ) at Junction D between the intact (e.g., Pipe 4 in Fig. 5.3) and blocked (e.g., Pipe 3 in Fig. 5.3) pipe sections. For the pipe with uniform blockages in Fig. 5.3(a), the impedance mismatch at Junction D is $\Delta Z = \rho_0 a_0(1/A_3 - 1/A_4)$, which is constant for the incident wave of various frequencies, therefore its T_C curve would fluctuate with constant extent. While for the pipe system with exponential non-uniform blockages in Fig. 5.3(b), the impedance of the blocked pipe section (i.e., Eq. (5.14)) is frequency dependent. In particular, the impedance of exponential non-uniform blockages gradually decreases as the increase of the incident wave frequency. This means the higher the incident wave frequency, the smaller is the impedance mismatch at Junction D (i.e., ΔZ tends to 0). On this occasion, higher frequency incident waves would feel a less blocking effect from the exponential non-uniform blockages; thus, more energy is transmitted through the non-uniform blockages, and the fluctuation of the T_C curve becomes less evident.

5.4 Numerical Validation

5.4.1 Energy Transmission Coefficient of a Frictionless Unbounded Pipe System

To validate the derived analytical result in Eq. (5.12), the classical frictionless 1D water hammer model is solved by the method of characteristics (MOC) (Chaudhry, 2014; Wylie et al., 1993). As shown in Fig. 5.2, an unbounded pipe system with two anechoic boundaries (i.e., upstream and downstream) is used for the numerical validation. The original intact pipe is blocked by exponential non-uniform blockages. The detailed parameters of this pipe system are listed in Table 5.2. In the numerical experiment, exponential non-uniform blockages are approximated by stepwise discretized grids. The 1000-m-long pipe is divided into 10000 small computational reaches (i.e., spatial grid size $\Delta x \sim 0.1$ m) to reduce the reflection caused by numerical errors. The incident wave generated at the downstream generator is given by the formula in Eq. (5.15) (i.e., a Gaussian-modulated sinusoidal pulse) (Louati et al., 2018), and the pressure trace is measured by the wave receiver located at the upstream end.

$$P_{in} = P_0 + P_0 \exp\left(-4\left(\frac{\omega_c}{\beta}\right)^2 \log(10)\left(t - \left(\frac{\beta}{\omega_c}\right)^2\right)\right)\sin\left(\omega_c\left(t - \frac{\beta}{\omega_c}\right)\right) \tag{5.15}$$

where P_{in} = the incident wave pressure at the generator; P_0 = the initial pressure in the pipe; ω_c = the angular central frequency of the incident wave; β = a coefficient that determines the frequency bandwidth of the incident wave; t = time; $0 < t \leq \beta/\omega_c$.

Table 5.2. Detailed system parameters for numerical validation.

Blockage type	l_1 (m)	l_2 (m)	l_3 (m)	l_4 (m)	R (m)	$\|s\|$	R_C (m)	a_0 (m/s)
exp non-uniform	300	100	100	500	0.25	4.64E-03	0.1572	1000

Two features of the Gaussian-modulated sinusoidal pulse in Eq. (5.15) are that: (i) most of the energy is distributed at its central frequency ω_c; and (ii) the frequency bandwidth of this pulse can be determined by appropriately adjusting the value of β.

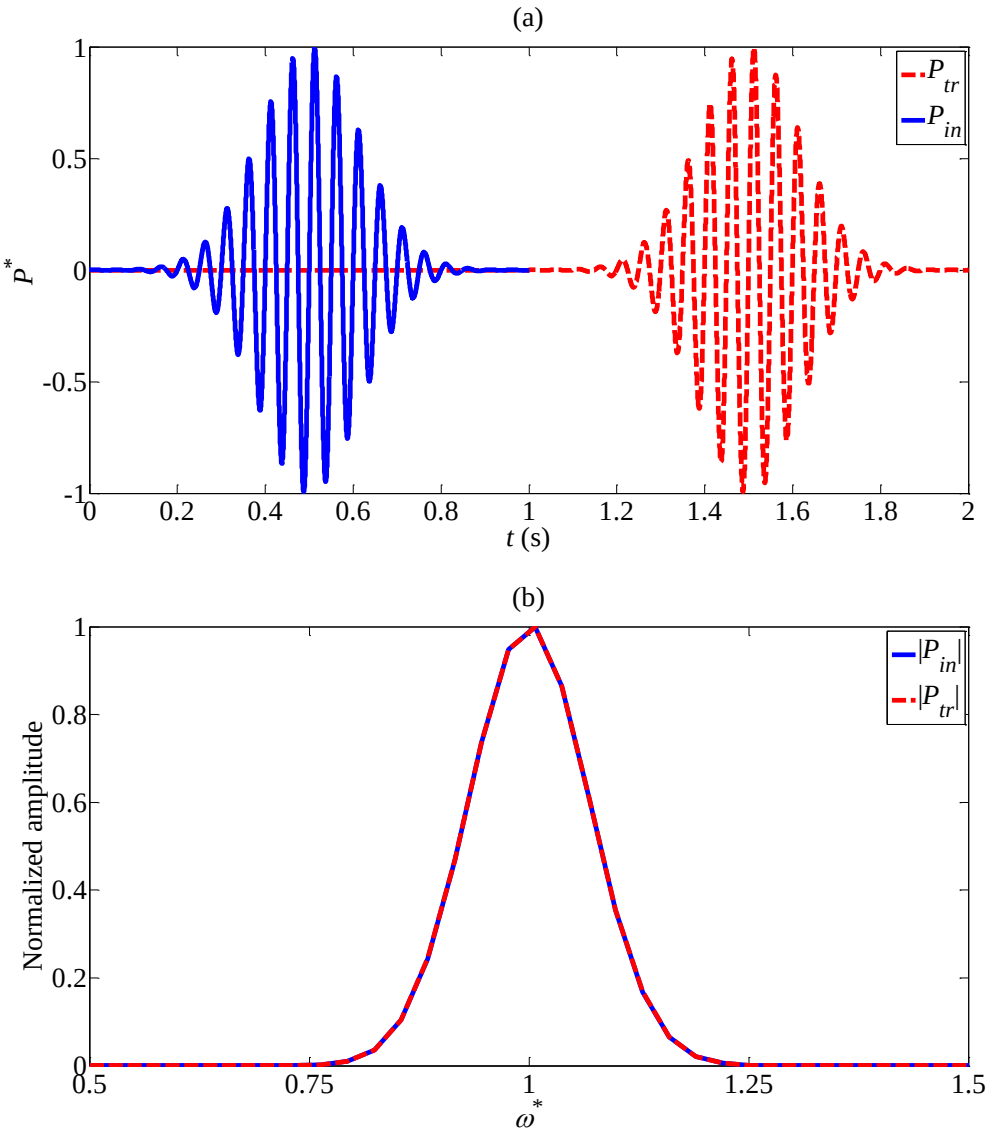

Fig. 5.5. (a) Measured pressure signals in the time domain ($\omega_c^* = 1$); (b) corresponding pressure signals in the frequency domain ($\omega_c^* = 1$).

The incident wave generated by the downstream generator and the transmitted wave measured by the upstream receiver are plotted in Fig. 5.5(a). The pressure P is normalized according to $(P - P_0)/P_0$ and plotted as P^*. Fig. 5.5(a) indicates that the amplitude of the transmitted wave is almost identical to that of the incident wave. To explain this

phenomenon, these time domain signals in Fig. 5.5(a) are transformed into the frequency domain in Fig. 5.5(b). It turns out that the central frequency of the incident wave is ω_c^* = 1.0, as shown in Fig. 5.7, at which the energy transmission coefficient T_C has a local maximum value 1.00. This means reflected waves from the non-uniform blockages experience destructive interference (i.e., condition of minimum reflection or maximum transmission). On this condition, all the energy carried by this incident wave should be transmitted through the non-uniform blockages.

As shown in Fig. 5.7, three more points on the energy transmission coefficient T_C curve (i.e., at ω_c^* = 0.5, 1.5, and 2.5) are further validated and discussed in detail herein. In Figs. 5.6(a) and 5.6(b), the amplitude of the transmitted wave is significantly less than that of the incident wave because of the low T_C value at the central frequency of the incident wave ω_c^* = 0.5 (at which point T_C = 0.71, this means only 71 percent of the energy carried by the incident wave is transmitted through the non-uniform blockages). Although ω_c^* = 1.5 and 2.5 are two local minimum points on the T_C curve in Fig. 5.7, compared with the ω_c^* = 0.5 case, the amplitude of these transmitted waves gradually increases as the increase of the incident wave frequency. This is because the exponential non-uniform blockages have a less blocking effect on the propagation of higher frequency waves. According to Eq. (A.17) in the Appendix A2 and the normalized amplitudes in Figs. 5.6(b), 5.6(d), and 5.6(f), the T_C values of these three points are calculated as 0.71, 0.96, and 0.99, respectively, which agree well with the analytical T_C values 0.71, 0.96, and 0.99 in Fig. 5.7.

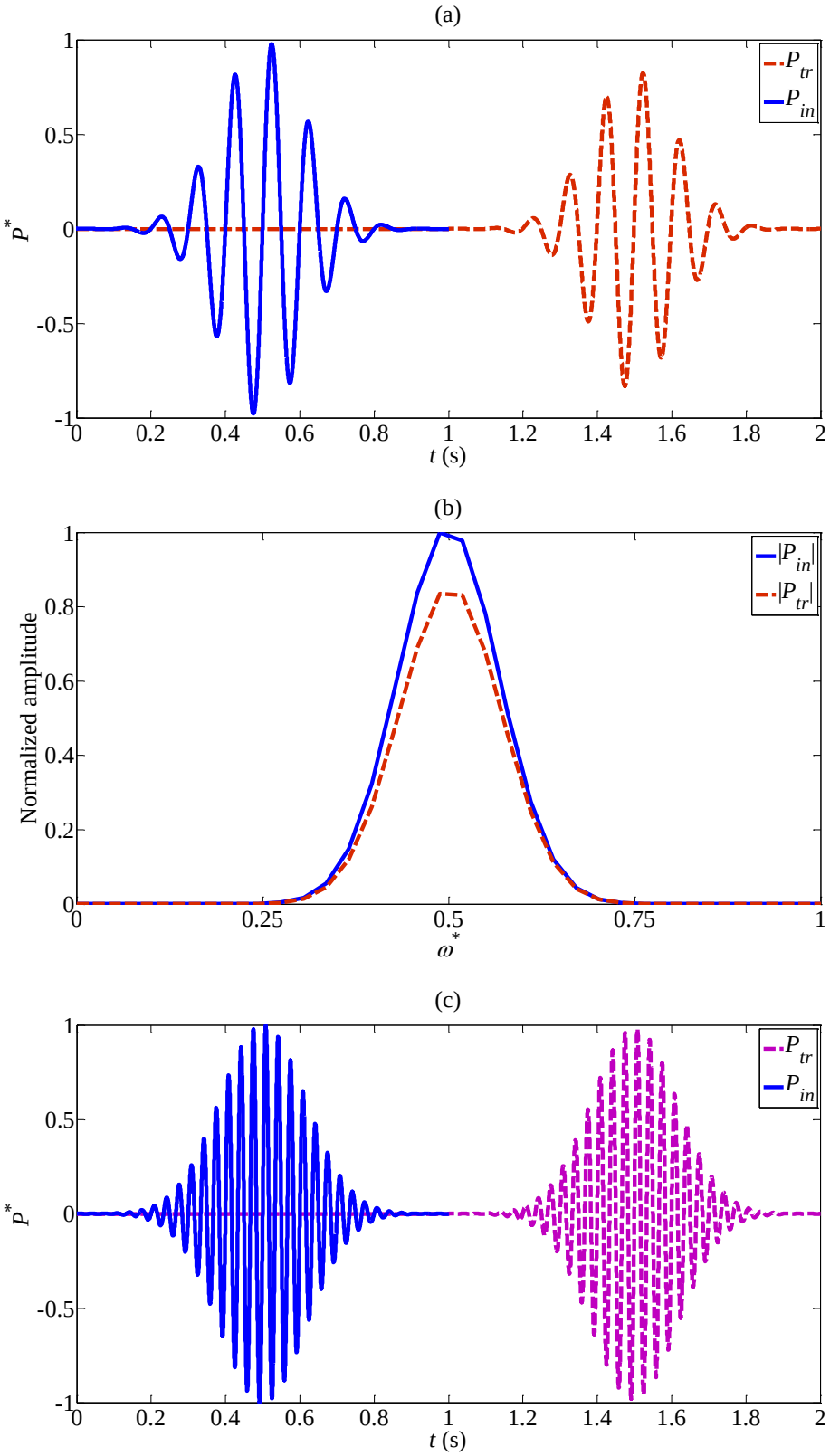

Fig. 5.6. (Part 1) Measured pressure signals in the time domain (a) ω_c^* = 0.5, (c) ω_c^* = 1.5, (e) ω_c^* = 2.5; corresponding pressure signals in the frequency domain (b) ω_c^* = 0.5, (d) ω_c^* = 1.5, (f) ω_c^* = 2.5.

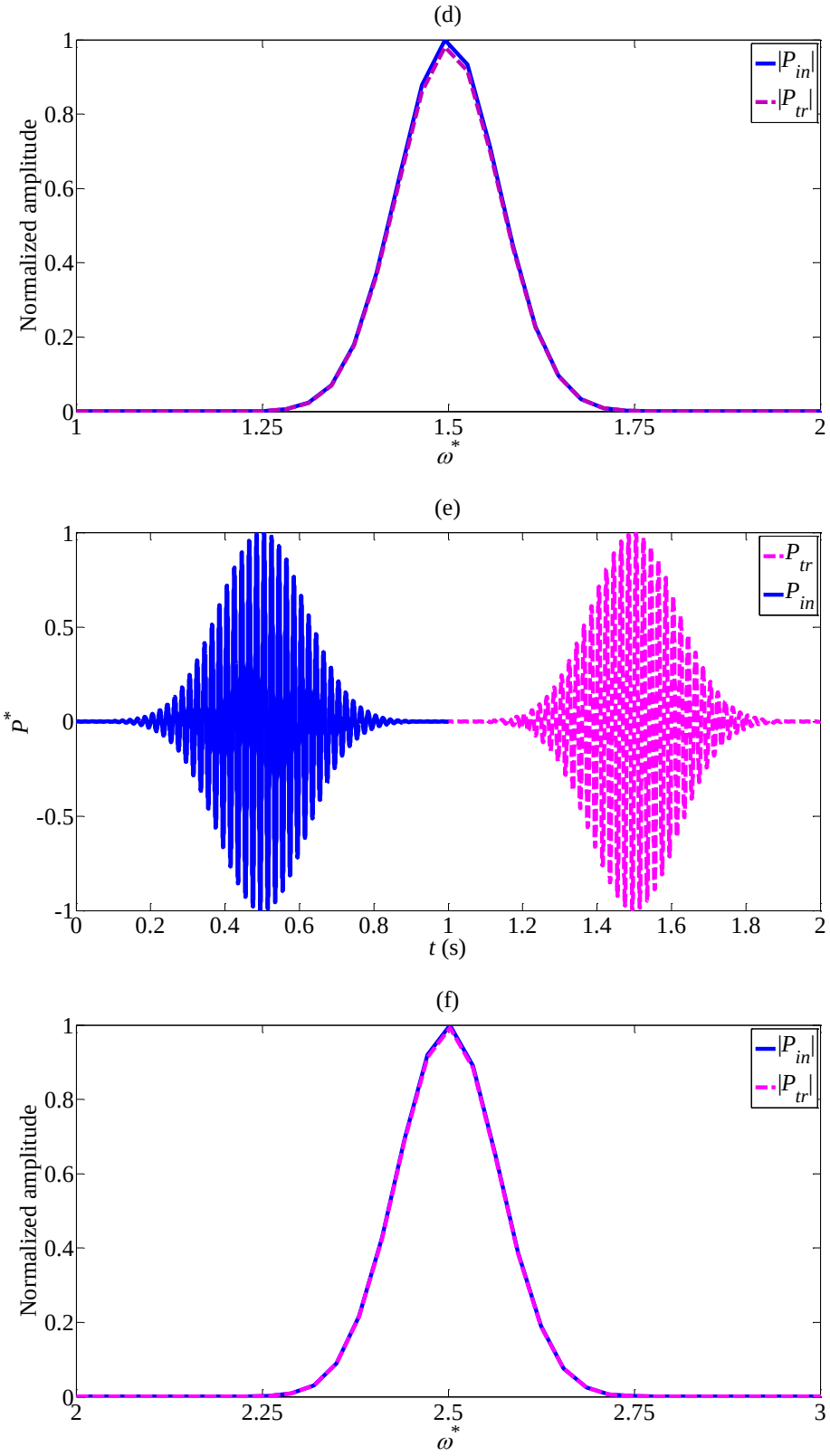

Fig. 5.6. (Part 2) Measured pressure signals in the time domain (a) $\omega_c^* = 0.5$, (c) $\omega_c^* = 1.5$, (e) $\omega_c^* = 2.5$; corresponding pressure signals in the frequency domain (b) $\omega_c^* = 0.5$, (d) $\omega_c^* = 1.5$, (f) $\omega_c^* = 2.5$.

In addition, more points on the energy transmission coefficient T_C curve are numerically obtained and plotted in Fig. 5.7. It shows good agreement between the numerical and analytical results, which confirms the validity of the derived result in Eq. (5.12) as well as the analytical method in this study.

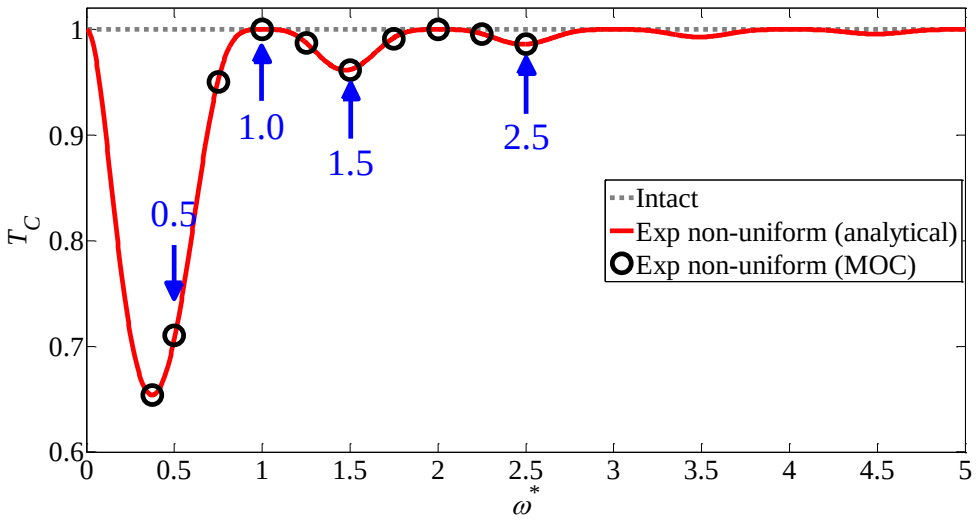

Fig. 5.7. Numerical validation of the derived energy transmission coefficient T_C.

5.4.2 Influence of a Frictional Bounded Pipe System on the Derived Energy Transmission Coefficient

The analytical result derived in Eq. (5.12) is based on an unbounded pipe system without any friction. However, in real urban water supply systems, the pipe systems are commonly bounded by various of boundaries (e.g., reservoirs and valves). In addition, the friction would change the amplitude of a transient wave propagating along an intact pipe section. Therefore, it is necessary to further investigate the influences of system boundaries and friction on the analytical result in Eq. (5.12). As shown in Fig. 5.8, a pipe system with an upstream reservoir and a downstream valve is adopted. Both steady and unsteady friction (Vardy & Brown, 1995) are considered in this bounded system. Detailed system parameters of bounded and unbounded pipe systems are listed in Table 5.3, where f = friction factor.

Table 5.3. Detailed pipe system parameters.

Pipe system	l_1 (m)	l_2 (m)	l_3 (m)	l_4 (m)	R (m)	R_C (m)	$\|s\|$	f
bounded	399	1	1	599	0.25	0.15	5.11E-01	0.02
unbounded	399	1	1	599	0.25	0.15	5.11E-01	0

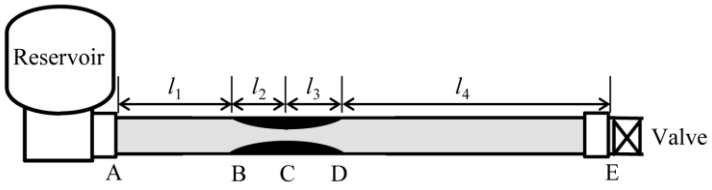

Fig. 5.8. A bounded reservoir-pipe-valve (RPV) system.

First, as shown in Fig. 5.9, the transient frequency responses of the bounded pipe system with friction are numerically obtained based on the transfer matrix method (Che et al., 2018b). The energy transmission coefficients T_C of the bounded pipe system are estimated by (Kinsler et al., 1999)

$$T_C = 1 - \frac{\delta h_m^2}{h_{mi}^2} = 1 - \frac{\left(h_{mb} - h_{mi}\right)^2}{h_{mi}^2} \tag{5.16}$$

where δh_m = the blockage induced amplitude change for the m-th resonant peak; h_{mi} = amplitude of the m-th resonant peak for the intact pipe system; h_{mb} = amplitude of the m-th resonant peak for the pipe system with non-uniform blockages.

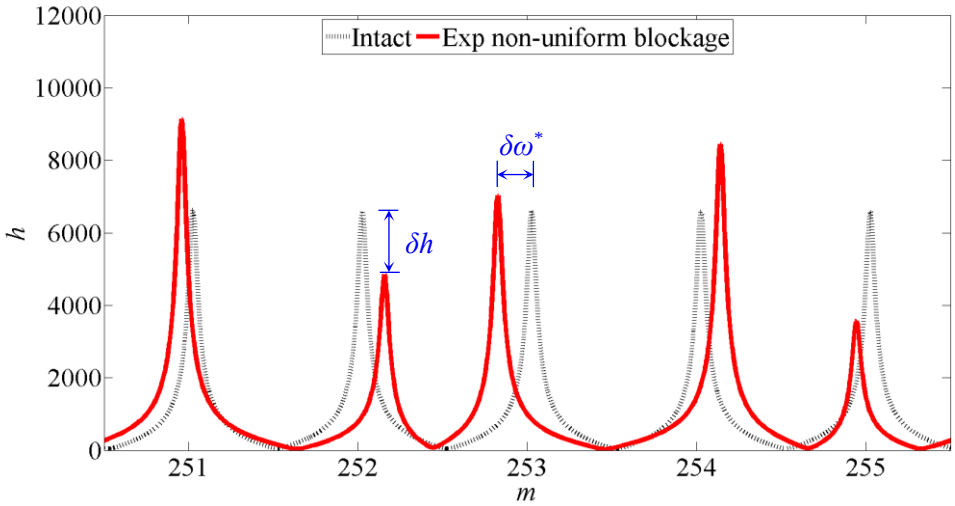

Fig. 5.9. Transient frequency responses of bounded pipe systems with both steady and unsteady friction.

The energy transmission coefficient T_C curves of bounded (based on Eq. (5.16)) and unbounded (based on Eq. (5.12)) pipe systems are plotted in Fig. 5.10. According to Fig. 5.10, the overall phase and fluctuation trend of these two curves for two systems show good agreement. This means that the overall pattern of T_C curve for the bounded pipe system with friction is also governed by two physical mechanisms: (1) the Bragg's law; (2) the impedance mismatch between the intact and blocked pipe sections. In addition, Fig. 5.10 indicates that the analytical result in Eq. (5.12) may underestimate the amount of energy transmitted through non-uniform blockages in a frictional bounded pipe system, especially for relative low frequency incident waves (e.g., $\omega^* < 1$). One reason for this is that the energy transmission coefficient of the frictional bounded system is calculated based on the amplitude of resonant peaks, as shown in Eq. (5.16), which could be further reinforced by system boundaries.

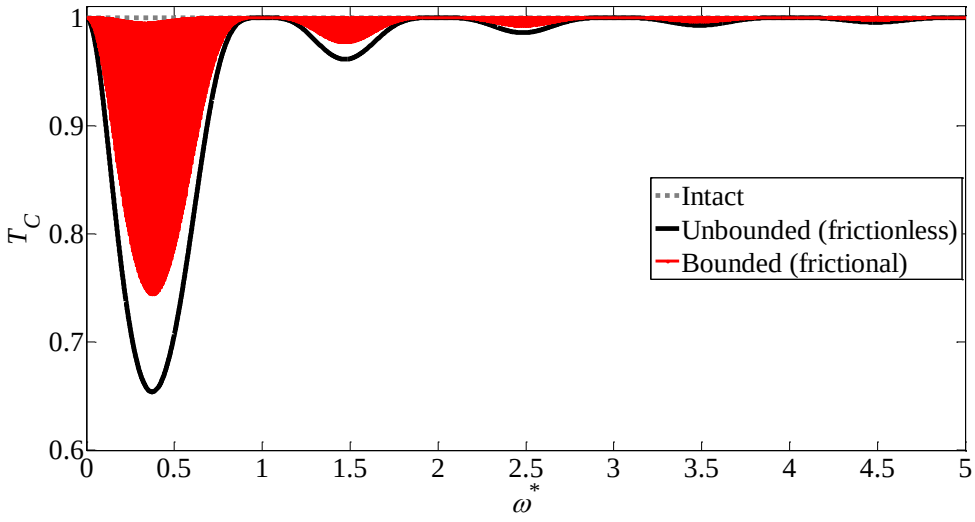

Fig. 5.10. Energy transmission coefficients T_C of bounded and unbounded pipe systems.

5.5 Further Applications and Result Analysis

5.5.1 Energy Explanation of the Non-uniform Blockage Induced Resonant Frequency Shift Pattern

Based on the validated analytical result in Eq. (5.12), the influences of non-uniform blockage properties (i.e., length and severity) on the energy transmission coefficient T_C of unbounded pipe systems are systematically investigated in this section. Detailed system parameters can refer to Table 5.4. At the same time, to explain the non-uniform blockage induced resonant frequency shift patterns from an energy perspective, the transient frequency responses of bounded pipe systems (like Fig. 5.9), with the same system parameters (i.e., Table 5.4) as the unbounded systems, are also obtained.

First, the influence of non-uniform blockage severity on the energy transmission coefficient T_C of unbounded pipe systems is studied. According to Table 5.4, the blockage lengths (i.e., l_2 and l_3) of Tests T1, T2, and T3 are fixed. From Test T1 to T3, the minimum radius R_C of the blockage gradually increase from 0.15 m to 0.20 m, which means the blockage becomes less severe. The T_C curves of these three tests are plotted in Fig. 5.11(a). It shows that the overall trend of these three curves is the same except for the T_C values at a specific frequency. Specifically, for a fixed incident wave frequency, more energy is transmitted through the non-uniform blockages as the blockages become less severe. This is obvious since less severe blockages should have a less blocking effect on the propagation of transient waves.

Table 5.4. Detailed pipe system parameters of bounded and unbounded pipe systems.

Test no.	l_1 (m)	l_2 (m)	l_3 (m)	l_4 (m)	R (m)	R_C (m)	$\|s\|$
T1	300	100	100	500	0.25	0.15	5.11E-03
T2	300	100	100	500	0.25	0.175	3.57E-03
T3	300	100	100	500	0.25	0.20	2.23E-03
T4	390	10	10	590	0.25	0.15	5.11E-02
T5	399	1	1	599	0.25	0.15	5.11E-01

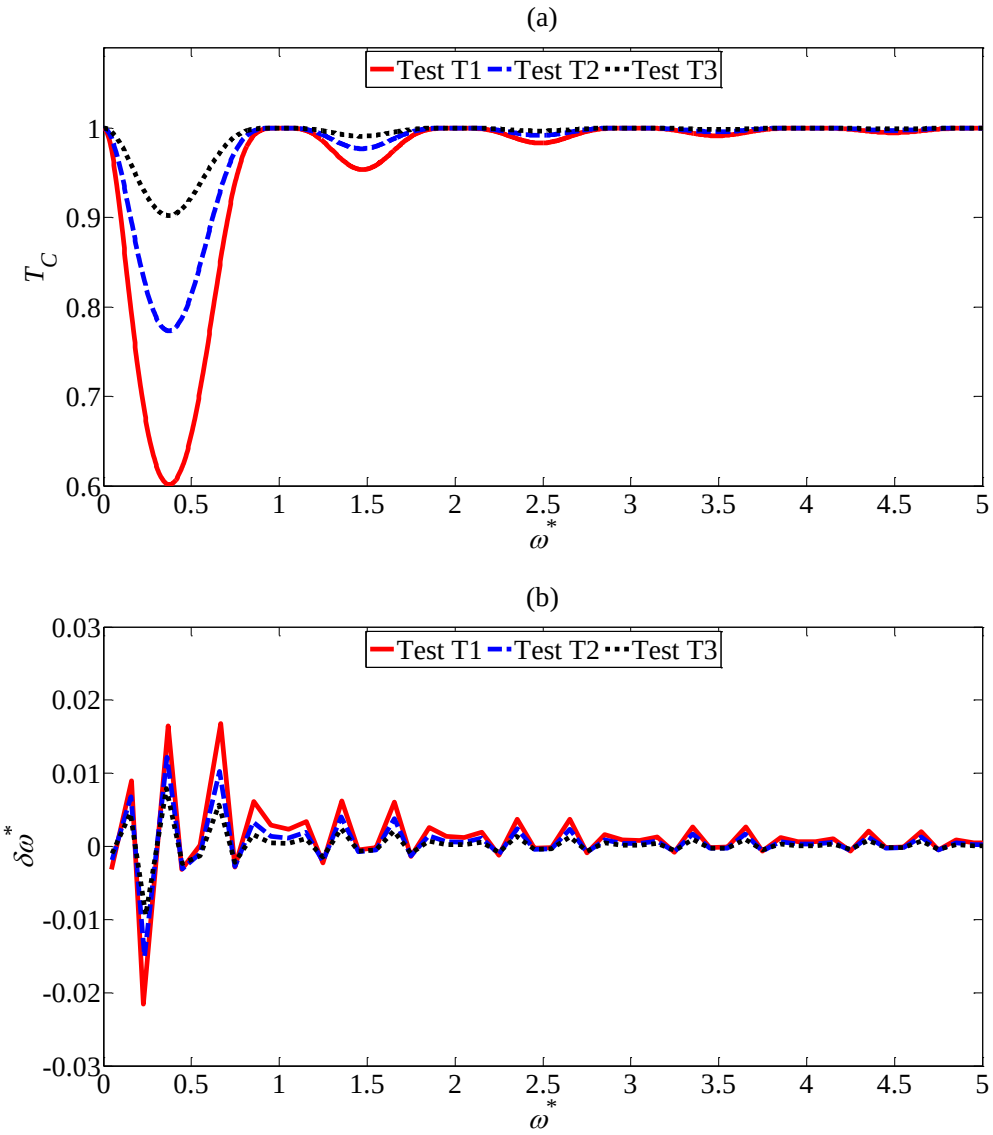

Fig. 5.11. (a) Energy transmission coefficients T_C of unbounded non-uniform blocked pipe systems; (b) resonant frequency shifts of bounded systems induced by non-uniform blockages.

The resonant frequency shift patterns of bounded pipe systems, with the same system parameters as Tests T1, T2, and T3, adapted from Chapter 4 (Che et al., 2018b) are plotted in Fig. 5.11(b). The normalized resonant frequency shift of the *m*-th resonant peak is defined as $\delta\omega_m^* = \omega_{mb}^* - \omega_{mi}^*$ (like Fig. 5.9), where ω_{mi}^* = the *m*-th normalized resonant frequency of the intact pipe system; ω_{mb}^* = the *m*-th normalized resonant frequency of the pipe system with non-uniform blockages. As shown in Fig. 5.11(b), the fluctuation of resonant frequency shift patterns induced by non-uniform blockages becomes less evident

as the incident wave frequency increases. A reasonable explanation for this is that non-uniform blockages, as shown in Fig. 5.11(a), have a less blocking effect on the propagation of higher frequency waves, thus the resonant frequency shifts in Fig. 5.11(b) induced by non-uniform blockages become less evident.

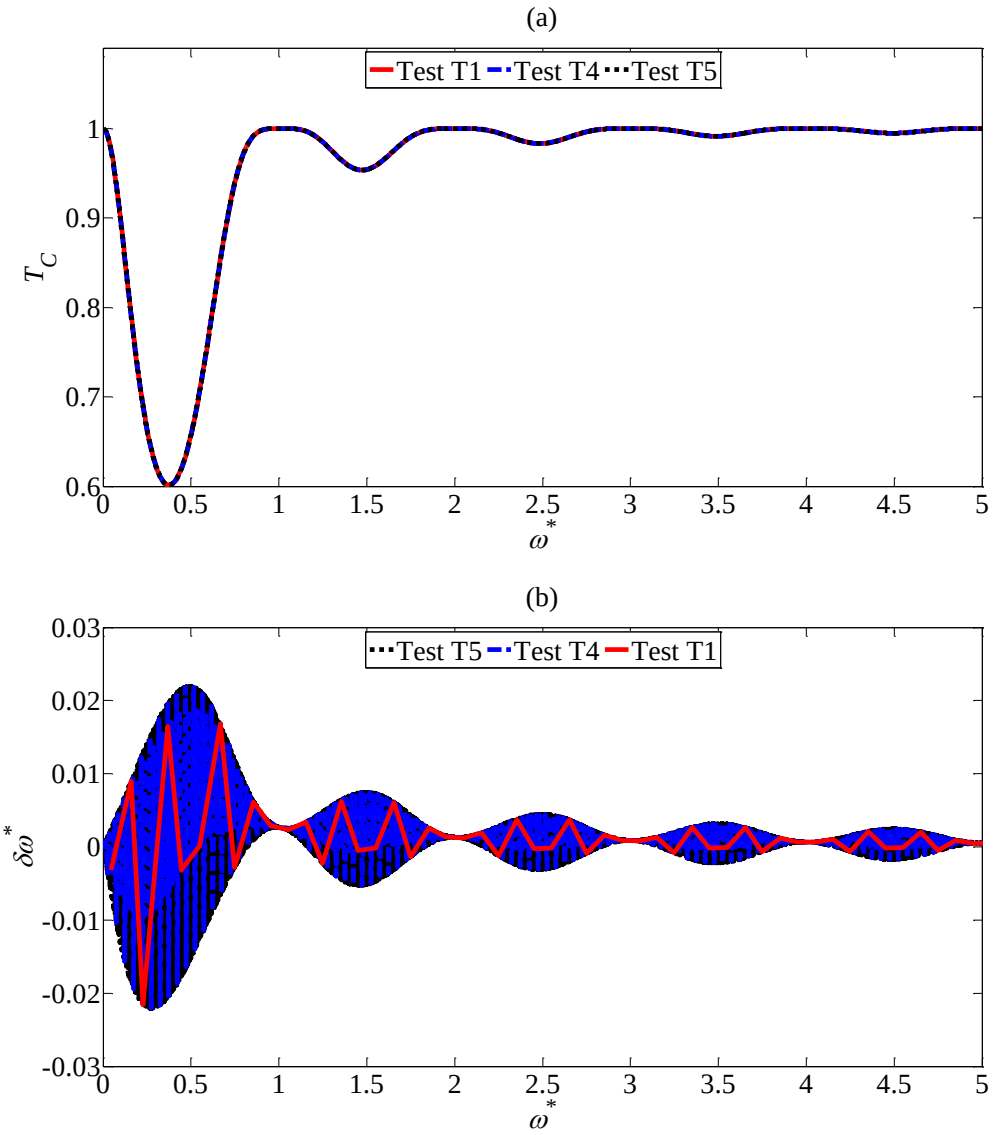

Fig. 5.12. (a) Energy transmission coefficients T_C of unbounded non-uniform blocked pipe systems; (b) resonant frequency shifts of bounded systems induced by non-uniform blockages.

The influence of non-uniform blockage length on the energy transmission coefficient T_C of unbounded pipe systems is also investigated. As shown in Table 5.4, the minimum radius R_C (i.e., severity) of the blockages in Tests T1, T4, and T5 is fixed. The length of

the non-uniform blockages gradually decreases from 100 m to 1 m. As shown in Figs. 5.12(a) and 5.12(b), the obtained T_C curves (for unbounded system) and resonant frequency shift patterns (for bounded system) are similar with previous tests. Moreover, both T_C curves and resonant frequency shift patterns of these three tests almost coincide with each other. This means that the non-uniform blockage length has a limited influence on the amount of energy transmitted through non-uniform blockages. Thus, these three tests with various blockage lengths have the same blocking effect on the propagation of transient waves.

5.5.2 Preliminary Applications to Interpreting Laboratory Data

As shown in Fig. 5.13, two types of irregular blockages, made of aggregate or coir, have been investigated in the laboratory by the author and his co-investigators for their influences on transient wave behavior (Duan et al., 2017). But the influence of exponential non-uniform blockages has not yet well verified due to the difficulty of constructing perfectly exponential non-uniform blockages in laboratories. Therefore, as a preliminary application, the irregular blockage made of coir (with a mean roughness height of 3 mm) used in Duan et al. (2017) is selected and approximated by uniform and exponential non-uniform blockages (see Fig. 5.13). Then, the validity of two blockage approximation methods for transmission coefficient estimations is studied and discussed. Note that these two approximated uniform and non-uniform blockages have the same blocked volume. The experiment system consists of an upstream reservoir, a pipe with irregular blockages (like A to E in Fig. 5.8), and a downstream discharge tank. Detailed system parameters are listed in Table 5.5, where l_b, $\bar{R}_b$, and $\bar{a}_b$ are the length, average radius, and average wave speed of the blocked section, respectively. More detailed experimental settings and operations are reported in Duan et al. (2017).

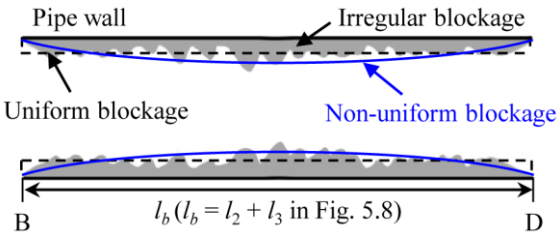

Fig. 5.13. Sketches of the irregular blockage and its uniform and exponential non-uniform approximations.

Table 5.5. Settings of the experimental test system (Duan et al., 2017).

Blockage type	l_1 (m)	$l_b = l_2 + l_3$ (m)	l_4 (m)	R (mm)	a_0 (m/s)	$\bar{R}_b$ (mm)	$\bar{a}_b$ (m/s)
rough coir	15.58	5.54	20.41	36.6	1180	29.8	1010

Because the experimental data in the frequency domain become relatively noisy for higher harmonics, only the first ten peaks are selected to calculate the energy transmission coefficient T_C based on Eq. (5.16). The T_C curves of the bounded pipe system with irregular blockages (Eq. (5.16)) as well as corresponding unbounded pipe systems with two approximated blockages (Eq. (5.12)) are plotted in Fig. 5.14. As shown in Fig. 5.14(a), when the irregular blockage is simplified into a uniform blockage, the periods (i.e., 1.00 and 1.16) of two T_C curves agrees well, but the energy transmission estimation is quite inaccurate. In contrast, according to Fig. 5.14(b), the approximation in exponential non-uniform blockages has a relatively good estimation of energy transmission, but the period agreement is relatively poor (i.e., 0.58 and 1.00). This can be attributed to the simplicity of current approximations, and detailed physical mechanisms of the interaction between transient waves and irregular blockages cannot be wholly represented by these two simplified blockages.

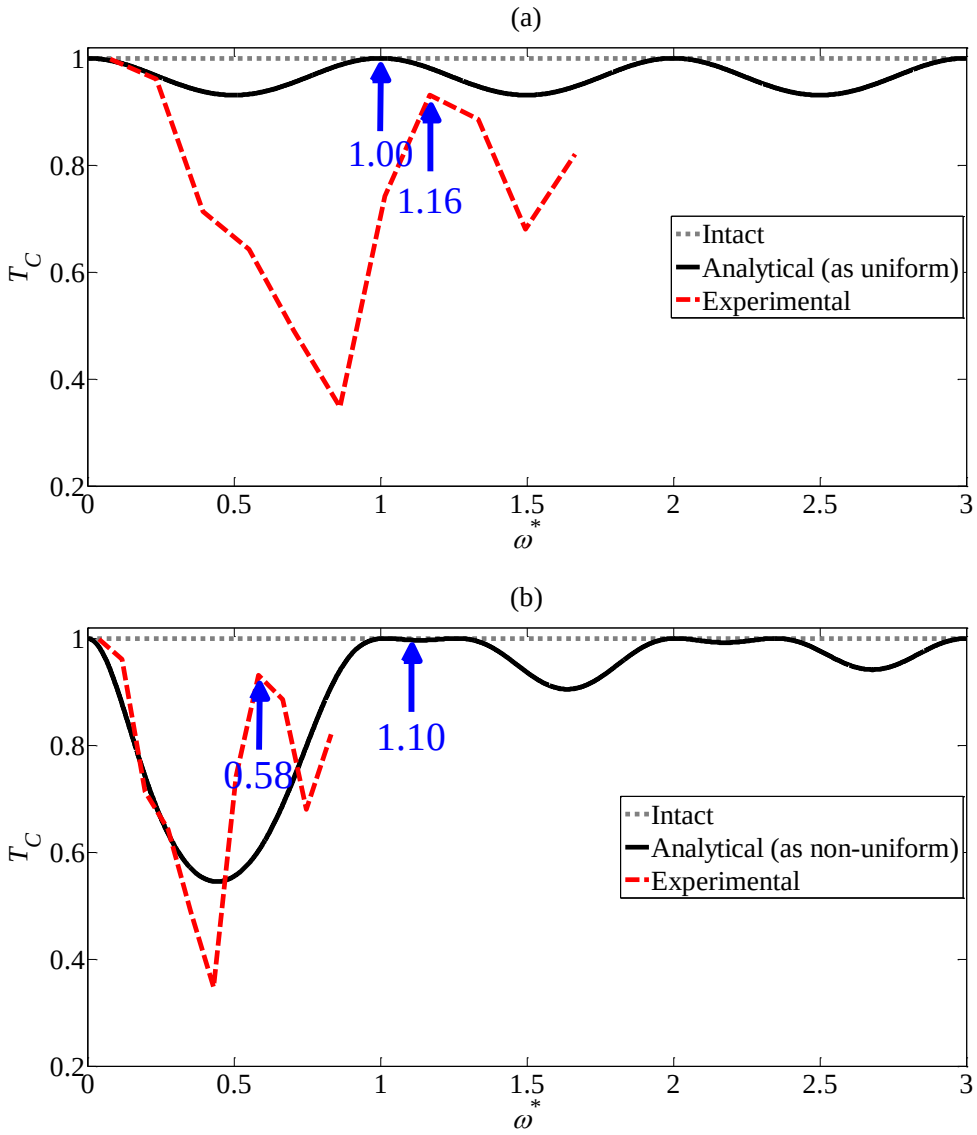

Fig. 5.14. The irregular blockage is approximated as (a) uniform blockage; (b) exponential non-uniform blockages.

5.6 Implications and Recommendations

In previous studies (Duan et al., 2014; Louati et al., 2018), the amplitude (equivalent to energy) of transmitted and reflected waves of a uniform blockage in an unbounded pipe system, as shown in Fig. 5.3(a), was obtained by applying the mass and momentum conservation at pipe junctions (i.e., Junctions B and D in Fig. 5.3(a)). However, the cross area of a pipe system with non-uniform blockages, as shown in Figs. 5.3(b) and 5.3(c), changes continuously along its axial direction. This means that the cross areas of intact and blocked pipe sections are the same at pipe junctions. Therefore, the previous method (Duan et al., 2014; Louati et al., 2018) cannot be used for calculating the energy transmission coefficients T_C of a pipe system containing non-uniform blockages. Based on the overall transfer matrix in Eq. (5.10), this paper proposes a new approach that is suitable for calculating the energy transmitted through non-uniform blockages in an unbounded pipe system. In addition, the derived result in Eq. (5.12) can be also applied to unbounded pipe systems with multiple blockages, which are more practical, once the system overall transfer matrixes are determined.

The results and findings above demonstrate that two physical mechanisms govern the overall pattern of energy transmission coefficient T_C in Fig. 5.4: (i) the Bragg's law; and (ii) the impedance mismatch between intact and blocked pipe sections. The fluctuation of these T_C curves is due to the Bragg's law, and the fluctuation extent is determined by the impedance mismatch between intact and blocked pipe sections. The impedance of exponential non-uniform blockages is frequency dependent, which becomes smaller for higher frequency waves. This means that the higher the incident wave frequency, the smaller the impedance mismatch between intact and blocked pipe sections. On this occasion, higher frequency waves would feel a less blocking effect from exponential non-uniform blockages. Therefore, more energy of higher frequency waves is transmitted through the non-uniform blockages, and the induced resonant frequency shifts become less evident.

In practical applications of non-uniform blockage detection, it is a preferable and labour-saving way to place the transient wave receiver at the same accessible point with the generator. Understanding the energy transmission coefficient T_C curve of incident waves with various frequencies provide valuable insights into the blocking effect of non-uniform blockages on transient waves. It is useful for the selection of appropriate incident wave frequency and bandwidth to ensure that the reflected waves contain enough energy for the pressure transducer (i.e., receiver) to measure. Otherwise, the reflected waves, which have limited energy, may be buried by the background noises. In this case, the useful resonant frequency shifts of this measured signal may be less evident that cannot be used to detect non-uniform blockages accurately.

The preliminary application of the derived result in the laboratory indicates that approximations of the irregular blockage into a single uniform or exponential non-uniform blockage only have a reasonable estimation in either the phase or the amplitude of the real energy transmission coefficients. This is due to the relatively simple geometry of two approximated blockages, which is unable to capture the complex interaction between transient waves and irregular blockages. Therefore, it is necessary to further investigate the transient wave behavior in a series of jointed non-uniform blockages (i.e., irregular blockage) and its influence on energy transmission coefficients. In this regard, the derived transmission coefficient in Eq. (5.12) is also applicable to an appropriate combination of multiple and different non-uniform blockages, which may form as a more realistic irregular blockage (like Fig. 5.1(c)), once the overall transfer matrix of this combination is determined.

5.7 Summary

This chapter explains the resonant frequency shift pattern induced by non-uniform blockages in pressurised water pipes from an energy perspective. First, the overall transfer matrix of a pipe system containing exponential non-uniform blockages is analytically derived based on the 1D plane wave solutions. The overall transfer matrix is then used to derive the energy transmission coefficient of the unbounded pipe system, which is numerically validated by the MOC. Finally, the resonant frequency shift pattern of bounded pipe systems with non-uniform blockages is explained by energy transmission curves of unbounded pipe systems.

The results indicate that the exponential non-uniform blockages have a less blocking effect on the propagation of higher frequency waves. This is because the impedance of non-uniform blockages is frequency dependent, which becomes smaller for higher frequency incident waves. Therefore, the non-uniform blockage induced resonant frequency shifts become less evident for higher harmonics. In practical applications of non-uniform blockage detection, the frequency and bandwidth of the incident wave should be selected carefully according to the energy transmission coefficient T_C curve to ensure that the reflected wave contains enough energy for pressure transducers to measure.

The preliminary applications to interpreting laboratory data indicates that further experimental and numerical verification of the derived result, as well as further investigation on the influence of irregular blockages on transient wave behavior are needed in the future work.

It is also noted that the results and physical interpretations in Chapters 4 and 5 are based on the 1D water hammer model, where the plane wave assumption is imposed. However, as the increase of the incident wave frequency, radial pressure waves will be generated; thus, the plane wave assumption in the current 1D model may be violated. Therefore, the validity range of the developed theory needs further investigations in the next chapter.

CHAPTER 6 RANGE OF VALIDITY OF THE DEVELOPED THEORY AND RADIAL PRESSURE WAVE BEHAVIOR IN WATER PIPES[5]

6.1 Introduction

The traditional application of transient analysis is mainly for the prediction of pressure history in pipe systems to assist the design and evaluation of pipe strength and the installation of transient control devices (Chaudhry, 2014; Duan et al., 2010b; Wylie et al., 1993). For many years, one-dimensional (1D) and quasi-2D water hammer models are commonly adopted for predicting such pressure history. In these models, radial inertia and viscous terms are neglected (see Chapter 3) due to the slight compressibility of the water and the small expansion of the pipe wall (termed as the *plane wave assumption*) (Ghidaoui, 2004). Many applications have demonstrated that both 1D and quasi-2D models, based on the plane wave assumption, give satisfactory results in the prediction of pressure history for the design purpose (Pezzinga, 1999; Vardy & Hwang, 1991; Zielke, 1968).

It is worth noting that the 1D wave equation (see Appendix A1), used in Chapters 4 and 5, is derived from the classic 1D water hammer model, where the plane wave assumption has been imposed (Chaudhry, 2014). However, as the incident wavelength approaches the pipe diameter (i.e., relatively high frequency waves), the radial pressure stats to distort and radial pressure waves are generated, which may violate the plane wave assumption in the current 1D wave equation. As a result, the *validity frequency range* of the obtained

[5] This chapter is adapted from the research paper of the author and his co-authors (Che et al., 2018a).

results and physical interpretations in Chapters 4 and 5 should be governed by the plane wave theory.

The full-2D water hammer model, including all terms neglected in 1D and quasi-2D models, is a potential tool for: (i) investigating the *range of validity of the developed theory* in Chapters 4 and 5; and (ii) observing the *radial pressure wave behavior* in water pipes. The full-2D model was proposed by Mitra and Rouleau (1985) to observe the radial and axial variations of transient pressure waves caused by valve closures. The full-2D model is solved numerically by an implicit matrix factorization method; in this way, the 2D problem is decomposed into two 1D problems, saving significant computational effort. Despite this improvement, the numerical method in (Mitra & Rouleau, 1985) still contains inefficiencies due to: (i) the complexity of coefficient matrixes; and (ii) the application of uniform grids in the radial direction, because very fine grids are needed to capture the detailed physical phenomena in the boundary layer near the pipe wall. Recently, a high-order finite volume scheme for the full-2D model was developed (Louati & Ghidaoui, 2017b, 2017c) to investigate the properties of high frequency waves in a pressurized water pipe. However, this previous study is limited to relatively idealized flow situations (i.e., inviscid and initially stagnant flows); thus, their results mainly provides a basic understanding of acoustic wave propagation in a water-filled pipe.

In urban water supply systems, the flows always have non-uniform (i.e., non-plane) velocity profiles due to the existence of viscosity; and transients are commonly generated by a change in flowrate due to hydraulic device operations (e.g., valves and pumps). Such practical flow situations may have an influence on the generation and propagation of radial pressure waves. For example, radial pressure waves were observed by Mitra and Rouleau (1985) after stopping a laminar flow by valve closures. Therefore, it is important to: (i) investigate the validity range of the developed theory in Chapters 4 and 5; and (ii) observe the radial pressure wave behavior in viscous and initially non-static flows under various valve operations, which is the main scope of this chapter.

This chapter first addresses the inefficiency problem of the original Mitra-Rouleau scheme by: (i) transforming the original scheme into tridiagonal systems; and (ii) implementing non-uniform computational grids along the radial direction. The modified efficient scheme is extended into a typical reservoir-pipe-valve (RPV) system to simulate a water hammer event. The efficient model is validated by numerical data from the Zielke's 1D analytical model, which has been extensively confirmed by lab experiments (Adamkowski & Lewandowski, 2006; Bergant et al., 2001; Zielke, 1968). Afterwards, the modified and validated numerical scheme is used to investigate systematically: (i) the validity frequency range of the plane wave assumption; and (ii) the radial pressure wave behavior in transient laminar pipe flows under different flow perturbations. Particularly, the generation mechanism and detailed components of radial pressure waves are studied and examined in this chapter. Finally, the findings and practical implications are discussed.

6.2 Original and Modified Mitra-Rouleau Schemes

6.2.1 Derivation of the Full-2D Water Hammer Model

The 2D non-conservative form Navier-Stokes equations for a compressible Newtonian fluid in an axis symmetric flow field, written in a cylindrical coordinate system (Ghidaoui, 2004), are as follows

$$\frac{\partial \rho}{\partial t} + u' \frac{\partial \rho}{\partial x} + v' \frac{\partial \rho}{\partial r} + \rho \left(\frac{\partial u'}{\partial x} + \frac{\partial v'}{\partial r} + \frac{v'}{r} \right) = 0 \tag{6.1a}$$

$$\rho \left(\frac{\partial u'}{\partial t} + u' \frac{\partial u'}{\partial x} + v' \frac{\partial u'}{\partial r} \right) = -\frac{\partial p'}{\partial x} + (\kappa + \mu/3) \frac{\partial}{\partial x} \left(\frac{\partial u'}{\partial x} + \frac{1}{r} \frac{\partial (r v')}{\partial r} \right) + \mu \left(\frac{\partial^2 u'}{\partial x^2} + \frac{1}{r} \frac{\partial}{\partial r} \left(r \frac{\partial u'}{\partial r} \right) \right) + \rho F_x \tag{6.1b}$$

$$\rho \left(\frac{\partial v'}{\partial t} + u' \frac{\partial v'}{\partial x} + v' \frac{\partial v'}{\partial r} \right) = -\frac{\partial p'}{\partial r} + (\kappa + \mu/3) \frac{\partial}{\partial r} \left(\frac{\partial u'}{\partial x} + \frac{1}{r} \frac{\partial (r v')}{\partial r} \right) + \mu \left(\frac{\partial^2 v'}{\partial x^2} + \frac{1}{r} \frac{\partial}{\partial r} \left(r \frac{\partial v'}{\partial r} \right) - \frac{v'}{r^2} \right) + \rho F_r \tag{6.1c}$$

where t = time; x = axial coordinate along pipe axis; r = radial coordinate from pipe axis; ρ = fluid density; u' = axial velocity; v' = radial velocity; p' = pressure; μ = dynamic viscosity; κ = volume viscosity; F_x = body force along x; and F_r = body force along r.

To derive the full-2D water hammer model from Eqs. (6.1), two assumptions are made here:

(1) In classic water hammer problems, the compressibility of the fluid (i.e., water) is only considered in the continuity equation Eq. (6.1a). Since water is slightly compressible and the pipe wall is elastic (i.e., relatively rigid) in this study, the spatial variation of fluid density ρ in radial and axial momentum equations due to the spatial variation of internal pressure can be neglected. Meanwhile, the volume viscosity can be also neglected due to the slight compressibility of the fluid in this investigation. However, the small spatial variation of fluid density ρ in the continuity equation should be included since the wave

speed a_0 is finite. The equation of state for a slightly compressible fluid is (Mitra & Rouleau, 1985)

$$\frac{dp'}{d\rho} = \frac{k}{\rho} = a_0^2 \tag{6.2}$$

where a_0 = wave speed; and k = bulk modulus.

(2) The body forces F_x and F_r are negligible due to the relatively small scales of pipe size and pipe gradient in urban water supply systems focused in this study (Chaudhry, 2014; Ghidaoui, 2004; Ghidaoui et al., 2005; Mitra & Rouleau, 1985).

These two assumptions reduce Eqs. (6.1) to

$$\frac{\partial p'}{\partial t} + u'\frac{\partial p'}{\partial x} + v'\frac{\partial p'}{\partial r} + k\left(\frac{\partial u'}{\partial x} + \frac{\partial v'}{\partial r} + \frac{v'}{r}\right) = 0 \tag{6.3a}$$

$$\frac{\partial u'}{\partial t} + u'\frac{\partial u'}{\partial x} + v'\frac{\partial u'}{\partial r} = -\frac{1}{\rho_0}\frac{\partial p'}{\partial x} + \frac{\mu}{\rho_0}\left(\frac{4}{3}\frac{\partial^2 u'}{\partial x^2} + \frac{1}{r}\frac{\partial}{\partial r}\left(r\frac{\partial u'}{\partial r}\right) + \frac{1}{3}\frac{\partial}{\partial x}\left(\frac{1}{r}\frac{\partial\left(rv'\right)}{\partial r}\right)\right) \tag{6.3b}$$

$$\frac{\partial v'}{\partial t} + u'\frac{\partial v'}{\partial x} + v'\frac{\partial v'}{\partial r} = -\frac{1}{\rho_0}\frac{\partial p'}{\partial r} + \frac{\mu}{\rho_0}\left(\frac{1}{3}\frac{\partial^2 u'}{\partial x \partial r} + \frac{\partial^2 v'}{\partial x^2} + \frac{4}{3}\frac{\partial}{\partial r}\left(\frac{1}{r}\frac{\partial\left(rv'\right)}{\partial r}\right)\right) \tag{6.3c}$$

where ρ_0 = mean density of the fluid.

In this chapter, the above full-2D model is further expressed in the dimensionless form so as to inspect the principle and physics behind the problem with more general results. The chosen dimensionless variables are as follows (Mitra & Rouleau, 1985): $u = u'/u_0$, where u_0 is the initial average axial velocity; $v = v'/u_0$; $p = (p' - p_e')/\rho_0 u_0 a_0$, where p_e' = pressure at $x = 0$; $\tau = a_0 t/R$, where R = pipe radius; and $\xi = x/R$; $\eta = r/R$. This results in the following dimensionless full-2D model

$$\frac{\partial p}{\partial \tau} + \frac{\partial u}{\partial \xi} + \frac{\partial v}{\partial \eta} + \frac{v}{\eta} = -\mathbf{M}\left(u\frac{\partial p}{\partial \xi} + v\frac{\partial p}{\partial \eta}\right) \tag{6.4a}$$

$$\frac{\partial u}{\partial \tau} + \frac{\partial p}{\partial \xi} = -\mathbf{M}\left(u\frac{\partial u}{\partial \xi} + v\frac{\partial u}{\partial \eta}\right) + \mathbf{K}\left[\frac{4}{3}\frac{\partial^2 u}{\partial \xi^2} + \frac{1}{\eta}\frac{\partial}{\partial \eta}\left(\eta\frac{\partial u}{\partial \eta}\right) + \frac{1}{3}\frac{\partial}{\partial \xi}\left(\frac{1}{\eta}\frac{\partial}{\partial \eta}(\eta v)\right)\right] \tag{6.4b}$$

$$\frac{\partial v}{\partial \tau}+\frac{\partial p}{\partial \eta}=-\mathbf{M}\left(u\frac{\partial v}{\partial \xi}+v\frac{\partial v}{\partial \eta}\right)+\mathbf{K}\left[\frac{1}{3}\frac{\partial^2 u}{\partial \xi \partial \eta}+\frac{\partial^2 v}{\partial \xi^2}+\frac{4}{3}\frac{\partial}{\partial \eta}\left(\frac{1}{\eta}\frac{\partial}{\partial \eta}(\eta v)\right)\right] \tag{6.4c}$$

where $\mathbf{M} = u_0/a_0$ is the Mach number; and $\mathbf{K} = \mu/R\rho_0 a_0$.

6.2.2 Original Mitra-Rouleau Scheme

Mitra and Rouleau (1985) numerically solved the full-2D model in Eqs. (6.4) by an implicit matrix factorization method. In water hammer applications, the values of factors **M** and **K** on the right-hand side of Eqs. (6.4) are negligibly small compared with one unit (i.e., $\mathbf{M} << 1$ and $\mathbf{K} << 1$); thus, terms on the right-hand side of Eqs. (6.4) are handled explicitly and terms on the left-hand side are handled implicitly. The time derivatives on the left-hand side of Eqs. (6.4) are discretized by the three-point backward difference given by $(\partial Z/\partial \tau)^{n+1} = (3Z^{n+1} - 4Z^n + Z^{n-1})/2\Delta\tau$, where $Z = p$, u or v; $\Delta\tau$ = size of the time step; n = n-th time step; and $Z(\tau, \xi, \eta) = Z(n\Delta\tau, \xi, \eta) = Z^n(\xi, \eta)$. By expressing the right-hand side of Eqs. (6.4) as R_1, R_2 and R_3, Eqs. (6.4) are written in a matrix form **ax** = **b** as

$$\begin{bmatrix} 1 & \frac{2}{3}\Delta\tau\frac{\partial}{\partial \xi} & \frac{2}{3}\Delta\tau\left(\frac{\partial}{\partial \eta}+\frac{1}{\eta}\right) \\ \frac{2}{3}\Delta\tau\frac{\partial}{\partial \xi} & 1 & 0 \\ \frac{2}{3}\Delta\tau\frac{\partial}{\partial \eta} & 0 & 1 \end{bmatrix}\begin{bmatrix} p^{n+1} \\ u^{n+1} \\ v^{n+1} \end{bmatrix}=\begin{bmatrix} \frac{4}{3}p^n-\frac{1}{3}p^{n-1}+\frac{2}{3}\Delta\tau R_1^n \\ \frac{4}{3}u^n-\frac{1}{3}u^{n-1}+\frac{2}{3}\Delta\tau R_2^n \\ \frac{4}{3}v^n-\frac{1}{3}v^{n-1}+\frac{2}{3}\Delta\tau R_3^n \end{bmatrix} \tag{6.5}$$

where **a** = coefficient matrix; **x** = unknown vector consisting of variables at time step n+1; and **b** = known vector consisting of variables at time steps n and n–1. Then the coefficient matrix **a** in Eq. (6.5) is approximately split into two individual coefficient matrixes

$$\mathbf{a} \approx \mathbf{a}_\xi \mathbf{a}_\eta \tag{6.6}$$

where $\mathbf{a}_\xi$ = coefficient matrix in the ξ-direction; $\mathbf{a}_\eta$ = coefficient matrix in the η-direction. $\mathbf{a}_\xi$ and $\mathbf{a}_\eta$ are in the following forms (Mitra & Rouleau, 1985)

$$\mathbf{a}_\xi = \begin{bmatrix} 1 & \frac{2}{3}\Delta\tau\frac{\partial}{\partial\xi} & 0 \\ \frac{2}{3}\Delta\tau\frac{\partial}{\partial\xi} & 1 & 0 \\ 0 & 0 & 1 \end{bmatrix}; \quad \mathbf{a}_\eta = \begin{bmatrix} 1 & 0 & \frac{2}{3}\Delta\tau\left(\frac{\partial}{\partial\eta}+\frac{1}{\eta}\right) \\ 0 & 1 & 0 \\ \frac{2}{3}\Delta\tau\frac{\partial}{\partial\eta} & 0 & 1 \end{bmatrix}.$$

Substituting Eq. (6.6) into Eq. (6.5), it becomes

$$\mathbf{a}_\xi \mathbf{a}_\eta \mathbf{x} = \mathbf{b} \tag{6.7}$$

A two-step algorithm is used to determine the unknown variables p^{n+1}, u^{n+1} and v^{n+1} in the vector **x**. Firstly, they swept in the ξ-direction and solved Eq. (6.8) to get $\mathbf{x}^*$.

$$\mathbf{a}_\xi \mathbf{x}^* = \mathbf{b} \tag{6.8}$$

where $\mathbf{x}^* = (p^{*\,n+1}, u^{*\,n+1}, v^{*\,n+1})^{\mathrm{T}}$ is an intermediate vector, in which $p^{*\,n+1}$, $u^{*\,n+1}$ and $v^{*\,n+1}$ are intermediate variables. Secondly, they swept in the η-direction and solved Eq. (6.9) to get the unknown vector $\mathbf{x} = (p^{n+1}, u^{n+1}, v^{n+1})^{\mathrm{T}}$.

$$\mathbf{a}_\eta \mathbf{x} = \mathbf{x}^* \tag{6.9}$$

In this way, the 2D problem is decomposed into two 1D problems, which reduces the computational burden. The spatial derivatives in $\mathbf{a}_\xi$ and $\mathbf{a}_\eta$ of Eqs. (6.8) and (6.9) are approximated by the upwind scheme.

The whole flow field is spatially discretized into *I* and *J* uniform sections in the ξ- and η-directions, respectively. Donating the known vector **b** on the right-hand side of Eq. (6.5) as $\mathbf{b} = (T_1^n, T_2^n, T_3^n)^{\mathrm{T}}$, for an arbitrary cross in the flow field $(\xi, \eta) = (i\Delta\xi, j\Delta\eta)$, Eq. (6.8) could be expressed as

$$-\frac{1}{3}\frac{\Delta\tau}{\Delta\xi}u_{i-1,j}^{*n+1} - \frac{1}{3}\frac{\Delta\tau}{\Delta\xi}p_{i-1,j}^{*n+1} + 0u_{i,j}^{*n+1} + \left(1+\frac{2}{3}\frac{\Delta\tau}{\Delta\xi}\right)p_{i,j}^{*n+1} + \frac{1}{3}\frac{\Delta\tau}{\Delta\xi}u_{i+1,j}^{*n+1} - \frac{1}{3}\frac{\Delta\tau}{\Delta\xi}p_{i+1,j}^{*n+1} = \left(T_1^n\right)_{i,j} \tag{6.10a}$$

$$-\frac{1}{3}\frac{\Delta\tau}{\Delta\xi}u_{i-1,j}^{*n+1} - \frac{1}{3}\frac{\Delta\tau}{\Delta\xi}p_{i-1,j}^{*n+1} + \left(1+\frac{2}{3}\frac{\Delta\tau}{\Delta\xi}\right)u_{i,j}^{*n+1} + 0p_{i,j}^{*n+1} - \frac{1}{3}\frac{\Delta\tau}{\Delta\xi}u_{i+1,j}^{*n+1} + \frac{1}{3}\frac{\Delta\tau}{\Delta\xi}p_{i+1,j}^{*n+1} = \left(T_2^n\right)_{i,j} \tag{6.10b}$$

$$v_{i,j}^{*n+1} = \left(T_3^n\right)_{i,j} \tag{6.10c}$$

where $\Delta\xi$ = spatial step in the ξ-direction; $\Delta\eta$ = spatial step in the η-direction; i = i-th spatial step in the ξ-direction; and j = j-th spatial step in the η-direction.

Similarly, for the cross located at ($i\Delta\xi$, $j\Delta\eta$), Eq. (6.9) could be written as

$$-\frac{1}{3}\frac{\Delta\tau}{\Delta\eta}v_{i,j-1}^{n+1}-\frac{1}{3}\frac{\Delta\tau}{\Delta\eta}p_{i,j-1}^{n+1}+\frac{2}{3}\frac{\Delta\tau}{(j-1)\Delta\eta}v_{i,j}^{n+1}+\left(1+\frac{2}{3}\frac{\Delta\tau}{\Delta\eta}\right)p_{i,j}^{n+1}+\frac{1}{3}\frac{\Delta\tau}{\Delta\eta}v_{i,j+1}^{n+1}-\frac{1}{3}\frac{\Delta\tau}{\Delta\eta}p_{i,j+1}^{n+1}=p_{i,j}^{*n+1} \quad (6.11a)$$

$$u_{i,j}^{n+1}=u_{i,j}^{*n+1} \quad (6.11b)$$

$$-\frac{1}{3}\frac{\Delta\tau}{\Delta\eta}v_{i,j-1}^{n+1}-\frac{1}{3}\frac{\Delta\tau}{\Delta\eta}p_{i,j-1}^{n+1}+\left(1+\frac{2}{3}\frac{\Delta\tau}{\Delta\eta}\right)v_{i,j}^{n+1}+0\,p_{i,j}^{n+1}-\frac{1}{3}\frac{\Delta\tau}{\Delta\eta}v_{i,j+1}^{n+1}+\frac{1}{3}\frac{\Delta\tau}{\Delta\eta}p_{i,j+1}^{n+1}=v_{i,j}^{*n+1} \quad (6.11c)$$

Therefore, the governing equations at fixed (j, n+1) for all inner points along the ξ-direction (i.e., i ranges from 2 to I–1) could be written in matrix form as $\mathbf{A}_\xi\mathbf{X}^*=\mathbf{B}$, where $\mathbf{X}^*=[(u^{*n+1})_{1,j}, (p^{*n+1})_{1,j}, \ldots, (u^{*n+1})_{i,j}, (p^{*n+1})_{i,j}, \ldots, (u^{*n+1})_{I,j}, (p^{*n+1})_{I,j}]^{\mathrm{T}}$ = unknown vector; $\mathbf{B}=[(T_1{}^n)_{2,j}, (T_2{}^n)_{2,j}, \ldots, (T_1{}^n)_{i,j}, (T_2{}^n)_{i,j}, \ldots, (T_1{}^n)_{I\text{-}1,j}, (T_2{}^n)_{I\text{-}1,j}]^{\mathrm{T}}$ = known vector; and $\mathbf{A}_\xi$ is a coefficient matrix in the following form

$$\begin{pmatrix}
-\frac{E}{2} & -\frac{E}{2} & 0 & F & \frac{E}{2} & -\frac{E}{2} & & & & & \cdots & & & & 0 \\
-\frac{E}{2} & -\frac{E}{2} & F & 0 & -\frac{E}{2} & \frac{E}{2} & & & & & & & & & \\
 & & -\frac{E}{2} & -\frac{E}{2} & 0 & F & \frac{E}{2} & -\frac{E}{2} & & & & & & & \\
 & & -\frac{E}{2} & -\frac{E}{2} & F & 0 & -\frac{E}{2} & \frac{E}{2} & & & & & & & \\
0 & & & & \cdots & \cdots & \cdots & \cdots & & & & & & & \\
 & & & & & & & & \cdots & \cdots & \cdots & \cdots & & & 0 \\
 & & & & & & & & -\frac{E}{2} & -\frac{E}{2} & 0 & F & \frac{E}{2} & -\frac{E}{2} & \\
 & & & & & & & & -\frac{E}{2} & -\frac{E}{2} & F & 0 & -\frac{E}{2} & \frac{E}{2} & \\
 & & & & & & & & & & -\frac{E}{2} & -\frac{E}{2} & 0 & F & \frac{E}{2} & -\frac{E}{2} \\
0 & & & & \cdots & & & & & & -\frac{E}{2} & -\frac{E}{2} & F & 0 & -\frac{M}{2} & \frac{E}{2}
\end{pmatrix} \quad (6.12)$$

where $E = 2/3(\Delta\tau/\Delta\xi)$; and $F = 1 + 2/3(\Delta\tau/\Delta\xi)$.

Similarly, the governing equations at fixed (i, n+1) for all inner points along the η-direction (i.e., j ranges from 2 to J–1) could be written in matrix form as $\mathbf{A}_\eta\mathbf{X}=\mathbf{X}^*$, where $\mathbf{X}=[(v^{n+1})_{i,1}, (p^{n+1})_{i,1}, \ldots, (v^{n+1})_{i,j}, (p^{n+1})_{i,j}, \ldots, (v^{n+1})_{i,J}, (p^{n+1})_{i,J}]^{\mathrm{T}}$ = unknown vector; $\mathbf{A}_\eta$ is a coefficient matrix in the following form

$$\begin{pmatrix}
-\frac{Z}{2} & -\frac{Z}{2} & V_2 & Y & \frac{Z}{2} & -\frac{Z}{2} & & & & \cdots & & & & 0 \\
-\frac{Z}{2} & -\frac{Z}{2} & Y & 0 & -\frac{Z}{2} & \frac{Z}{2} & & & & & & & & \\
 & & -\frac{Z}{2} & -\frac{Z}{2} & V_3 & Y & \frac{Z}{2} & -\frac{Z}{2} & & & & & & \\
 & & -\frac{Z}{2} & -\frac{Z}{2} & Y & 0 & -\frac{Z}{2} & \frac{Z}{2} & & & & & & \\
0 & & & & \cdots & \cdots & \cdots & \cdots & & & & & & \\
 & & & & & & & & \cdots & \cdots & \cdots & \cdots & & & 0 \\
 & & & & & & & & -\frac{Z}{2} & -\frac{Z}{2} & V_{J-2} & Y & \frac{Z}{2} & -\frac{Z}{2} & \\
 & & & & & & & & -\frac{Z}{2} & -\frac{Z}{2} & Y & 0 & -\frac{Z}{2} & \frac{Z}{2} & \\
 & & & & & & & & & & -\frac{Z}{2} & -\frac{Z}{2} & V_{J-1} & Y & \frac{Z}{2} & -\frac{Z}{2} \\
0 & & & & \cdots & & & & & & -\frac{Z}{2} & -\frac{Z}{2} & Y & 0 & -\frac{Z}{2} & \frac{Z}{2}
\end{pmatrix} \tag{6.13}$$

where $Z = 2/3(\Delta\tau/\Delta\eta)$; $Y = 1 + 2/3(\Delta\tau/\Delta\eta)$; and $V_j = 2/3(\Delta\tau/(j-1)\Delta\eta)$.

Although the 2D problem has been decomposed into two 1D problems, the original Mitra-Rouleau scheme is still computationally intensive due to the complexity of the two coefficient matrixes in Eqs. (6.12) and (6.13). Moreover, it is not convenient and practical to capture detailed physics in the boundary layer near the pipe wall by uniform grids along the radial direction (i.e., from the pipe axis to the pipe wall) implemented in the original Mitra-Rouleau scheme.

6.2.3 Modified Mitra-Rouleau Scheme

Inspired by the previous work of Zhao and Ghidaoui (2003), the efficiency of the existing scheme for the full-2D model can be enhanced by transforming the original matrixes in Eqs. (6.12) and (6.13) to two tridiagonal matrixes in Eqs. (6.14) and (6.15), which can be solved by the lower-upper (LU) factorization method efficiently. Meanwhile, the non-uniform computational grid (the grid size expressed as $\Delta\eta_j$) is also implemented along the radial direction to enhance the efficiency and reliability of the numerical scheme. In general, the application cases in this chapter demonstrate that, for the same expected accuracy and computer environment, compared with the original scheme, only about 1/6 of the CPU time and 1/2 of the computer memory are needed for the modified scheme.

$$\begin{pmatrix} \frac{2EF}{E^2-F^2} & 1 & \frac{F^2+E^2}{F^2-E^2} & & & & \cdots & & & 0 \\ & \frac{F^2+E^2}{E^2-F^2} & 1 & \frac{2EF}{F^2-E^2} & & & & & & \\ & & \frac{2EF}{E^2-F^2} & 1 & \frac{F^2+E^2}{F^2-E^2} & & & & & \\ & & & \frac{F^2+E^2}{E^2-F^2} & 1 & \frac{2EF}{F^2-E^2} & & & & \\ 0 & & & & \cdots & \cdots & \cdots & & & \\ & & & & & \cdots & \cdots & \cdots & & 0 \\ & & & & & & \frac{2EF}{E^2-F^2} & 1 & \frac{F^2+E^2}{F^2-E^2} & \\ & & & & & & & \frac{F^2+E^2}{E^2-F^2} & 1 & \frac{2EF}{F^2-E^2} \\ & & & & & & & \frac{2EF}{E^2-F^2} & 1 & \frac{F^2+E^2}{F^2-E^2} \\ 0 & & & & \cdots & & & & \frac{F^2+E^2}{E^2-F^2} & 1 & \frac{2EF}{F^2-E^2} \end{pmatrix} \tag{6.14}$$

$$\begin{pmatrix} \frac{YZ-W_1Z}{W_1X_2+Z^2} & 1 & \frac{W_1Y-Z^2}{W_1X_2+Z^2} & & & & \cdots & & & 0 \\ & \frac{W_2Y-Z^2}{Y^2-Z^2} & 1 & \frac{YZ+X_3Z}{Y^2-Z^2} & & & & & & \\ & & \frac{YZ-W_2Z}{W_2X_3+Z^2} & 1 & \frac{W_2Y-Z^2}{W_2X_3+Z^2} & & & & & \\ & & & \frac{W_3Y-Z^2}{Y^2-Z^2} & 1 & \frac{YZ+X_4Z}{Y^2-Z^2} & & & & \\ 0 & & & & \cdots & \cdots & \cdots & & & \\ & & & & & \cdots & \cdots & \cdots & & 0 \\ & & & & & & \frac{YZ-W_{J-3}Z}{W_{J-3}X_{J-2}+Z^2} & 1 & \frac{W_{J-3}Y-Z^2}{W_{J-3}X_{J-2}+Z^2} & \\ & & & & & & & \frac{W_{J-2}Y-Z^2}{Y^2-Z^2} & 1 & \frac{YZ+X_{J-1}Z}{Y^2-Z^2} \\ & & & & & & & \frac{YZ-W_{J-2}Z}{W_{J-2}X_{J-1}+Z^2} & 1 & \frac{W_{J-2}Y-Z^2}{W_{J-2}X_{J-1}+Z^2} \\ 0 & & & & \cdots & & & & \frac{W_{J-1}Y-Z^2}{Y^2-Z^2} & 1 & \frac{YZ+X_JZ}{Y^2-Z^2} \end{pmatrix} \tag{6.15}$$

where $W_j = 2/3(\Delta\tau/\eta_j) - 1 - 2/3(\Delta\tau/\Delta\eta_j)$; and $X_j = 1 + 2/3(\Delta\tau/\Delta\eta_j) + 2/3(\Delta\tau/\eta_j)$.

6.2.4 Initial and Boundary Conditions

Then the modified Mitra-Rouleau scheme is extended into a RPV experimental system (Fig. 6.1), with following initial and boundary conditions:

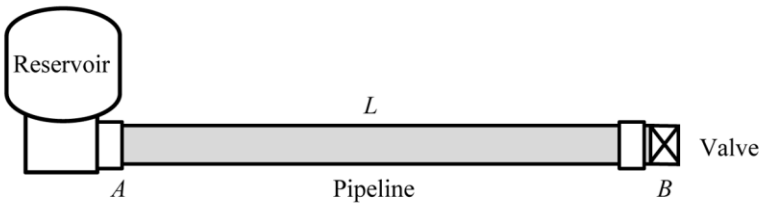

Fig. 6.1. A reservoir-pipe-valve (RPV) experimental system.

Initial Conditions

The initial flow ($\tau = 0$) in the pipe is a Poiseuille laminar flow. The initial values for the axial velocity u, radial velocity v and pressure p are given below

$$u = 2\left(\eta^2 - 1\right);\ v = 0;\ p = 8\mathbf{K}\xi \tag{6.16}$$

The initial axial velocity profile along the pipe radius and the area-averaged velocity is plotted in Fig. 6.2.

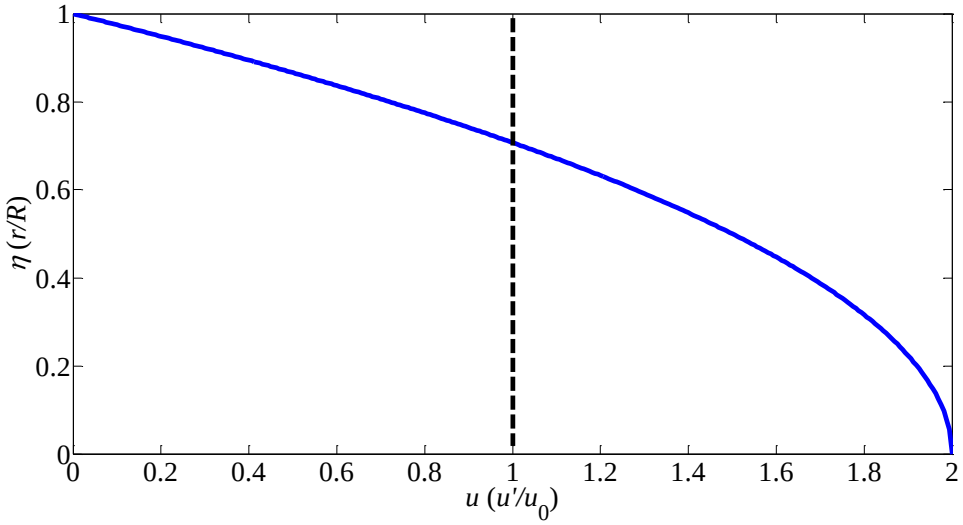

Fig. 6.2. The initial velocity profile (solid line) and area-averaged velocity (dashed line) for laminar pipe flows.

Boundary Conditions

The no-slip condition at the pipe wall ($\eta = 1$) is

$$u = 0;\ v = 0;\ \frac{\partial p}{\partial \eta} = R_3 \tag{6.17}$$

The symmetry condition at the pipe axis ($\eta = 0$) is

$$\frac{\partial u}{\partial \eta} = 0;\ v = 0;\ \frac{\partial p}{\partial \eta} = 0 \tag{6.18}$$

The upstream reservoir ($\xi = I\Delta\xi$) with constant pressure

$$\frac{\partial u}{\partial \xi} = R_1;\ v = 0;\ p = 8\mathbf{K}\xi \tag{6.19}$$

Different Operations on the Downstream Valve

To generate transients, the downstream valve is mainly operated in the following two patterns:

(1) Sudden valve closure

$$u = 2\left(\eta^2 - 1\right) \text{ when } \tau = 0;\ u = 0 \text{ when } \tau > 0;\ \frac{\partial p}{\partial \xi} = -\frac{\partial u}{\partial \tau} + R_2 \tag{6.20}$$

(2) Valve oscillation with frequency f_{in}

$$u = 0.5\left[2\left(\eta^2 - 1\right)\right]\left[\cos\left(2\pi f_{in}\tau\right) + 1\right] \text{ when } \tau < \tau_0;\ u = 0 \text{ when } \tau > \tau_0;\ \frac{\partial p}{\partial \xi} = -\frac{\partial u}{\partial \tau} + R_2 \tag{6.21}$$

where τ_0 = time duration of the valve oscillation.

6.3 Numerical Validation

The validity of the present code is firstly examined by numerical data from Mitra and Rouleau (1985). Detailed system parameters of this numerical experiment are listed in Table 6.1. Note that the reflection-free condition is applied to the upstream boundary. An initial Poiseuille laminar flow in the pipe is stopped by a downstream valve (located at $\xi = 0$) closure with closing time $\tau_0 = 0.4$. The pressure history at the valve for three different radial points is plotted in Fig. 6.3. A good agreement can be observed between numerical data from the present code and Mitra and Rouleau (1985).

Table 6.1. System parameters of the numerical experiment conducted by Mitra and Rouleau (1985).

a_0 (m/s)	R (m)	μ/ρ_0 (m^2/s)	Re	τ_0	$\Delta\tau = \Delta\xi = \Delta\eta$
1325	1.25e-02	3.97e-05	100	0.4	0.05

The modified scheme is further extended into a classical RPV water hammer experimental system (Fig. 6.1). Initially, keeping the downstream valve fully open, a steady laminar flow with average axial velocity u_0 is formed in the pipe. As mentioned, transients are caused by various operations on the downstream valve.

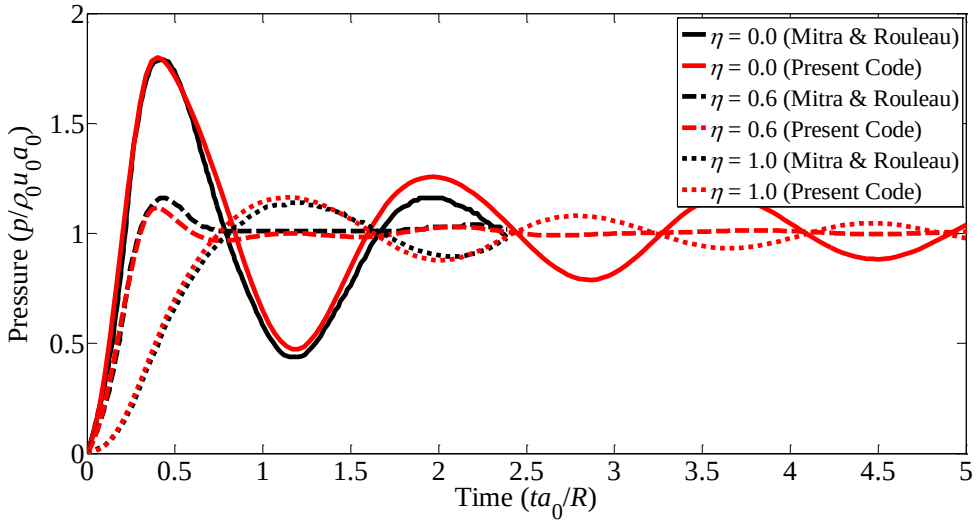

Fig. 6.3. Pressure time-history at the downstream valve for three different radial points.

6.3.1 Grid Independence Tests

In the modified Mitra-Rouleau scheme, uniform and non-uniform spatial grids are adopted in the ξ- and η- directions, respectively. In transient pipe flows, the high-resolution grid is essential for the finite difference scheme to accurately calculate hydraulic variables. For this purpose, three different grid sizes, as shown in Table 6.2, are tested to verify the modified full-2D model, in which N_r is the number of non-uniform grid along the radial direction. The upstream boundary is a reservoir with constant pressure (i.e., Eq. (6.19)).

Table 6.2. System parameters of numerical experiments for grid independent tests (Re = 100).

a_0 (m/s)	R (m)	L (m)	μ/ρ_0 (m^2/s)	τ_0	N_r
1325	0.2	10	3.97e-05	0	50
1325	0.2	10	3.97e-05	0	80
1325	0.2	10	3.97e-05	0	100

As shown in Fig. 6.1, transients are caused by a typical operation of sudden downstream valve closure. Pressure along the pipe radius (termed as radial pressure) is measured at the valve and the mid-length of the pipe. The area-averaged pressure traces are calculated and plotted in Fig. 6.4. As shown in Fig. 6.4, the pressure is normalized by the steady state pressure head at the downstream valve and the time is normalized by the system theoretical period $T_{th} = 4L/a_0$. The pressure gets convergence as the mesh becomes finer. The result of $N_r = 80$ demonstrates sufficient accuracy; thus, it will be chosen as the computational grid in the numerical validation.

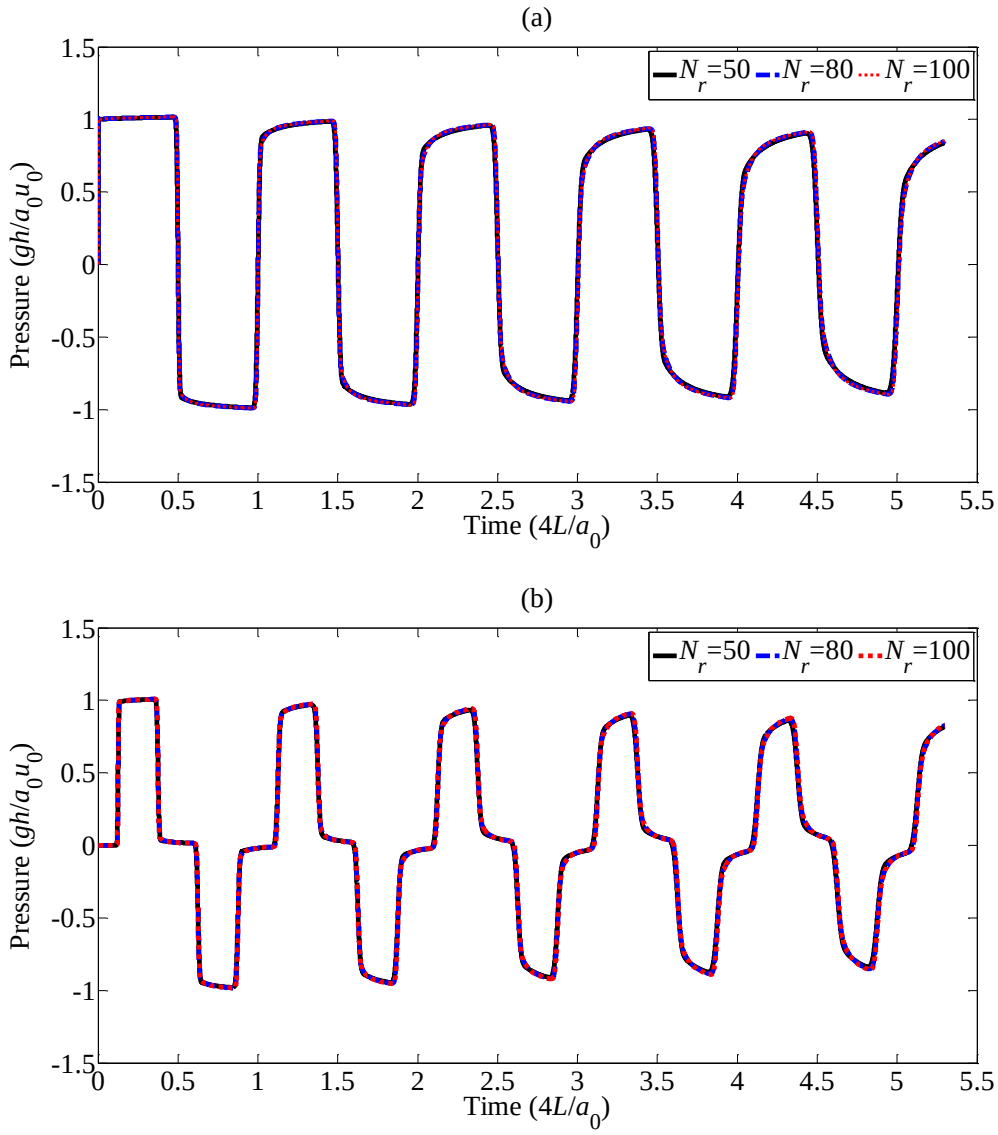

Fig. 6.4. Pressure time-history for various grid density at (a) the downstream valve; (b) the mid-length of the pipe.

6.3.2 Numerical Validation

The Zielke's 1D analytical and quasi-2D models for transient laminar flows have been widely validated by experimental tests in the literature, for their capability of capturing area-averaged pressure head traces (Pezzinga, 1999; Vardy & Hwang, 1991; Zielke, 1968). But the two-dimensionality of transient pipe flows has not yet well verified due to the difficulty of measuring two-dimensional data in experimental tests. Therefore, the modified full-2D model of this chapter is validated herein by the Zielke's 1D model for modeling the area-averaged transient pressure head. Afterwards, the radial pressure

waves in transient laminar pipe flows are analyzed based on the validated full-2D model in the numerical applications.

Transients are caused by a sudden and complete downstream valve closure. Radial pressure is measured at the valve and the mid-length of the pipe to calculate the area-averaged pressure. The area-averaged pressure trace of the full-2D model is plotted in Fig. 6.5. Good agreement between the full-2D model and the Zielke's 1D model in both pressure amplitude and pressure phase can be observed in Fig. 6.5. This demonstrates the validity of the present full-2D model for modeling transient laminar pipe flows.

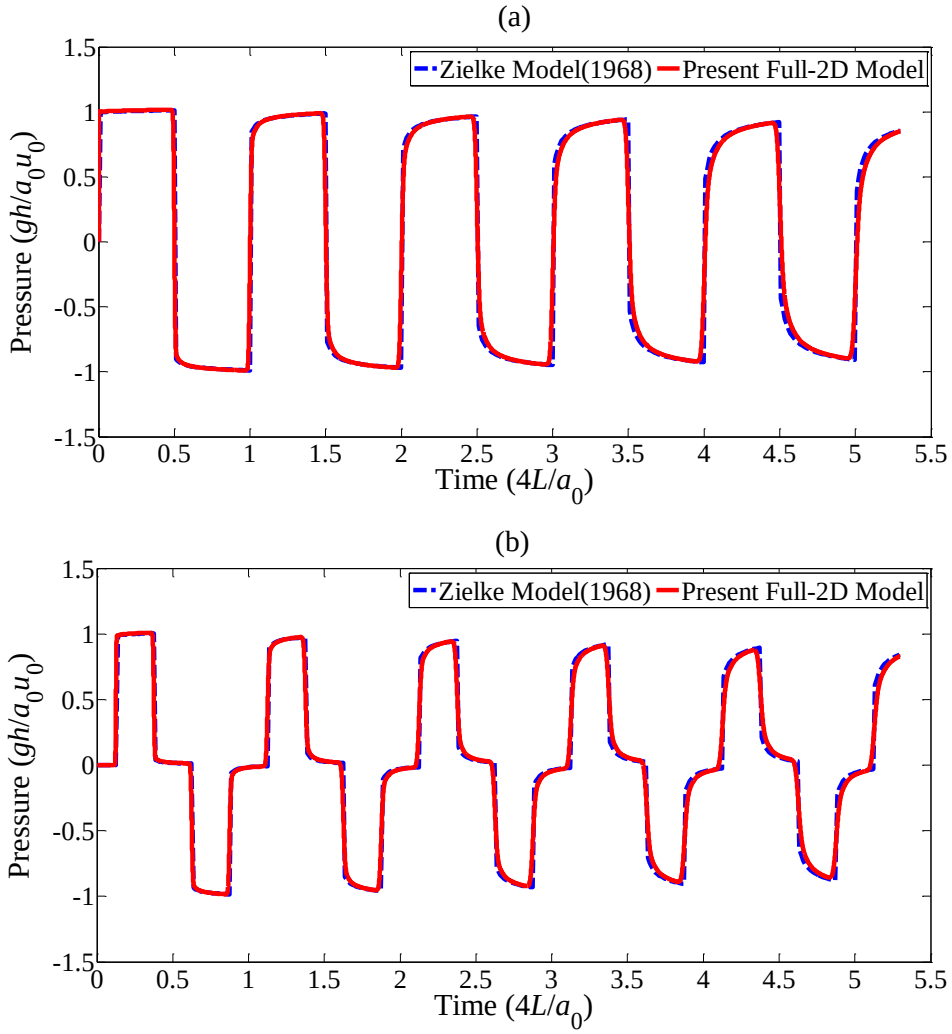

Fig. 6.5. Pressure time-history at (a) the downstream valve; (b) the mid-length of the pipe.

6.4 Generation Mechanism and Components of Radial Pressure Waves

The validated full-2D model is applied to an RPV system (Fig. 6.1) to investigate the generation mechanism and components of radial pressure waves. Three tests are conducted, in which transients are caused by different operations on the downstream valve (specifically, sudden closure for Test 1, low frequency perturbation for Test 2, and high frequency perturbation for Test 3). The definitions of low frequency flow perturbation and high frequency flow perturbation are system dependent, which will be clarified later in the case study. For the study of urban water supply systems, the fluid used is water and the wave speed a_0 is assumed to be 1485 m/s for relatively rigid pipes (Chaudhry, 2014). The initial condition in the pipe is a Poiseuille flow with Re = 100 (Eq. (6.16) and Fig. 6.2).

However, as the increase of the incident wave frequency, the transient wavelength would be in the same order with (or even smaller than) the pipe radius. Therefore, the transient wave may propagate along the pipe radius, which means radial pressure profile becomes curved and radial pressure waves are generated.

Because the following results involve high radial modes, there is a need to review related fundamental theory herein. Louati and Ghidaoui (2017b) showed that the radial wave number k_{rm} for a water-filled pipe can be determined by the no-flux boundary condition at the pipe wall $J_1(\alpha_{rm}) = 0$, where $\alpha_{rm} = k_{rm}R$; J_1 is the Bessel function of first kind of order 1. $J_1(\alpha_{rm}) = 0$ gives α_{rm} = 0, 3.83171, 7.01559, 10.17347, …, etc, then the radial wave number k_{rm} ($k_{rm} = \alpha_{rm}/R$) and cut-off frequency f_m ($f_m = a_0 k_{rm}/2\pi$) of the m-th radial mode can be calculated accordingly. The group velocity V_{gm} of m-th radial mode is given by Eq. (6.22) and the result for the test system in Table 6.3 is plotted in Fig. 6.6 (Louati & Ghidaoui, 2017b). For simplicity of illustration, these high radial modes are defined as mode 1 (M1), mode 2 (M2), etc., in the following study.

$$V_{gm} = \frac{a\sqrt{(\omega/a)^2 - k_{rm}^2}}{\omega/a} \tag{6.22}$$

Table 6.3. System parameters of three numerical applications (Re = 100).

Test No.	L/R	a_0 (m/s)	μ/ρ_0 (m^2/s)	τ_0	Valve operation
1	50	1485	1e-6	0	Sudden closure
2	50	1485	1e-6	$0.125T_{th}$	oscillation $f_{in1} = 0.2f_r$
3	50	1485	1e-6	$0.125T_{th}$	oscillation $f_{in2} = 1.0f_r$

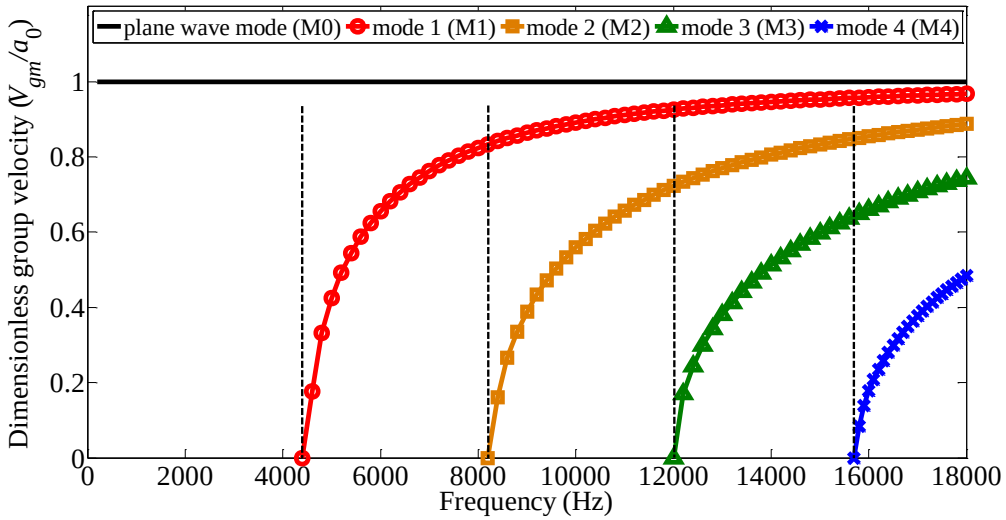

Fig. 6.6. Cut-off frequency (dashed line) and group velocity for each mode.

6.4.1 Flow Perturbation by a Sudden Valve Closure

For Test 1 in Table 6.3, transients are caused by a sudden and complete downstream valve (at $\xi = 0$) closure at time 0. The temporal variations of pressure at the valve for two radial locations, at the pipe axis p_{axis} (at $\eta = 0$) and pipe wall p_{wall} (at $\eta = 1$), are plotted in Fig. 6.7. Note that the area-averaged pressure p_{avg} at the valve is plotted for convenient comparison. To intuitively observe the spatial variation of pressure in the radial direction (validity of the plane wave assumption), the pressure difference Δp between the pipe axis and the pipe wall (Eq. (6.23)) is also plotted in Fig. 6.7.

$$\Delta p = p_{axis} - p_{wall} \tag{6.23}$$

Fig. 6.7 shows that the worst-case moment for the plane wave assumption (i.e., largest value of radial pressure difference Δp) is observed at time 0 when the valve is suddenly closed. The pressure at the pipe wall p_{wall} remains 0.0 and the pressure at the pipe axis p_{axis} leaps to its peak value of 2.0, which is twice the area-averaged pressure p_{avg}. This is

due to the velocity profile of the initial Poiseuille laminar flow. As shown in Fig. 6.2, velocities at the pipe axis and the pipe wall as well as area-averaged velocity are 2, 0 and 1, respectively. When the valve is closed at time 0, all the three velocities are reduced to 0. Based on the normalized Joukowsky's equation (Joukowsky, 1898), $\Delta p = -\Delta u/u_0$, the p_{axis}, p_{wall} and p_{avg} should become 2, 0 and 1, respectively. Because of the existence of the relatively large pressure variation within the pipe cross section, the radial flux (or radial velocity) is formed, so is the radial pressure waves. Afterwards, both pressure curves (p_{axis} and p_{wall}) fluctuate with decreasing amplitude due to the existence of the viscosity.

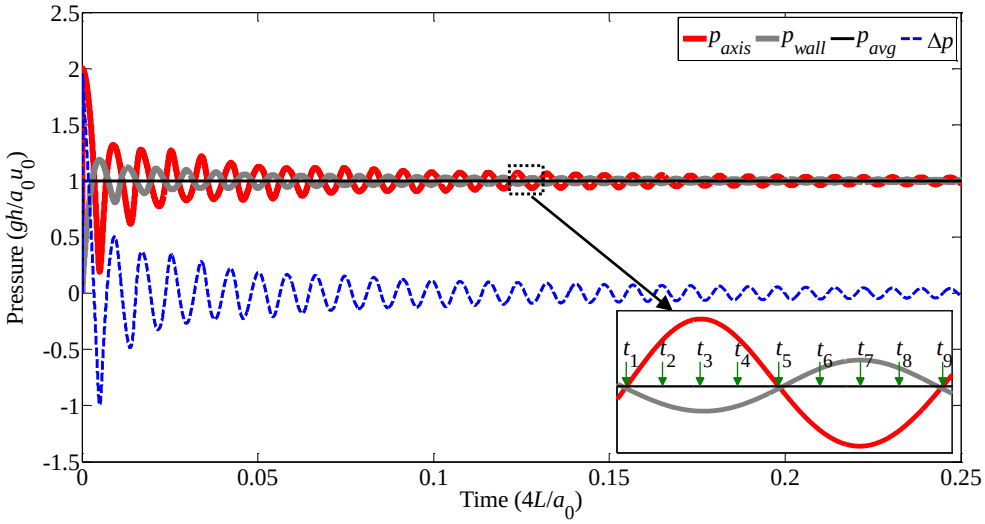

Fig. 6.7. The temporal variations of pressure at the downstream valve.

It is also noticed that no matter how the radial pressure changes at the valve, the area-averaged pressure (black curve in Fig. 6.7) maintains the constant value of 1.0, which is exactly the equivalent pressure information that 1D and quasi-2D models can only obtain. The radial pressure profiles at nine time points (i.e., denoted as $t_1 \sim t_9$) within one period of the pressure fluctuation, as shown in the enlarged view of Fig. 6.7, are selected and plotted in Fig. 6.8(a). Fig. 6.8(a) shows that there are two pressure antinodes, where the radial pressure fluctuation has the maximum amplitude, locating at the pipe axis (at η = 0.0) and pipe wall (at η = 1.0). Moreover, a pressure node is observed at η = 0.625, which agrees well with the theoretical result of the node location $\eta \approx 0.627$ of M1 for this studied case (Louati & Ghidaoui, 2017b, 2017c).

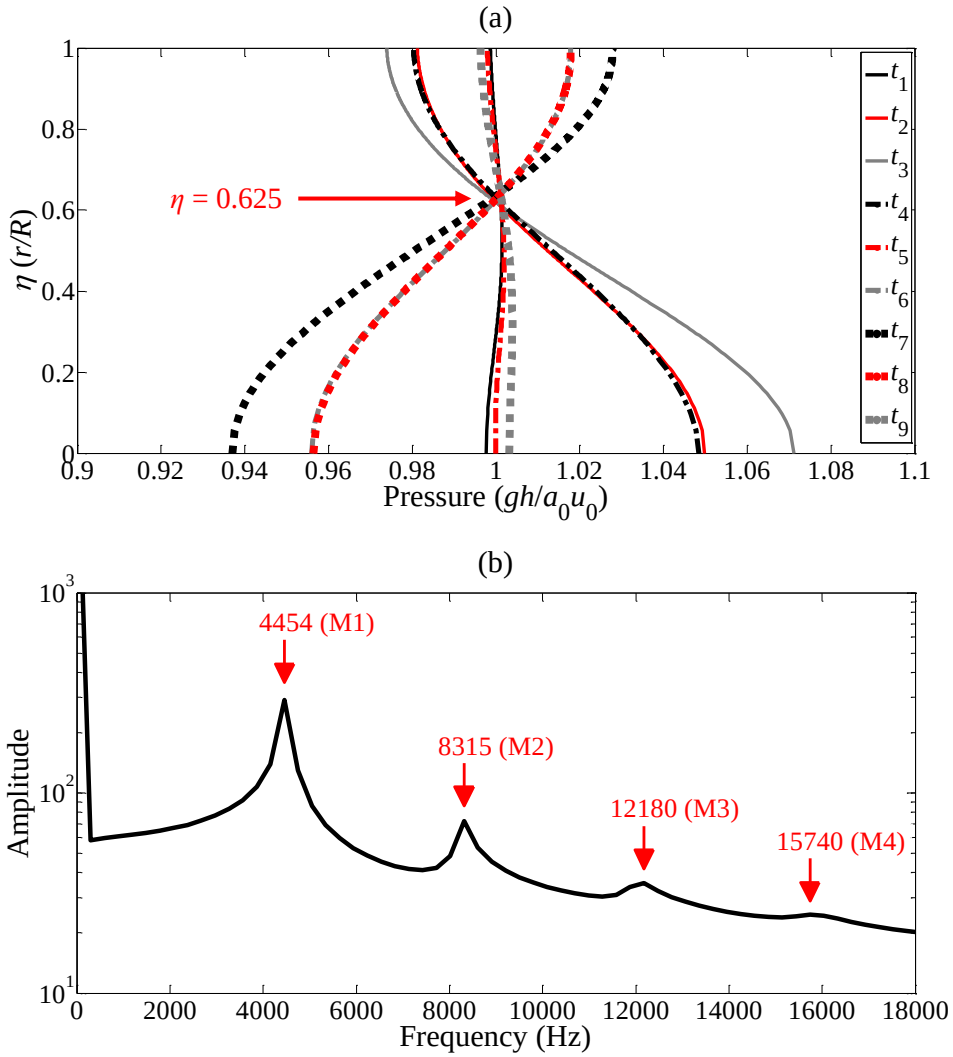

Fig. 6.8. (a) Radial pressure profiles at nine time points within one period of the pressure fluctuation; (b) the pressure signal after valve closure in the frequency domain.

To gain an insight into the components of radial pressure waves caused by a sudden valve closure, the time domain signal in Fig. 6.7 is transformed into the frequency domain by a fast Fourier transform (FFT) algorithm shown in Fig. 6.8(b). For clarity, the amplitude in Fig. 6.8(b) is plotted in a logarithmic coordinate. Fig. 6.8(b) shows that the first four frequency peaks of radial pressure waves are 4454, 8315, 12180 and 15740, which are consistent with the theoretical cut-off frequency of first four high radial modes in Fig. 6.6 (i.e., 4528, 8291, 12022 and 15745 by Eq. (6.22)) (Louati & Ghidaoui, 2017b, 2017c). Note that the group velocities of radial pressure waves in cut-off frequency should be 0 (Fig. 6.6). This means that the pressure signals (Fig. 6.7) measured at the valve would be

the superposition of several radial standing waves. According to Fig. 6.8(b), most of the energy is distributed in the frequency mode of 4454 (i.e., M1), which also results in the pressure node location at $\eta = 0.625$.

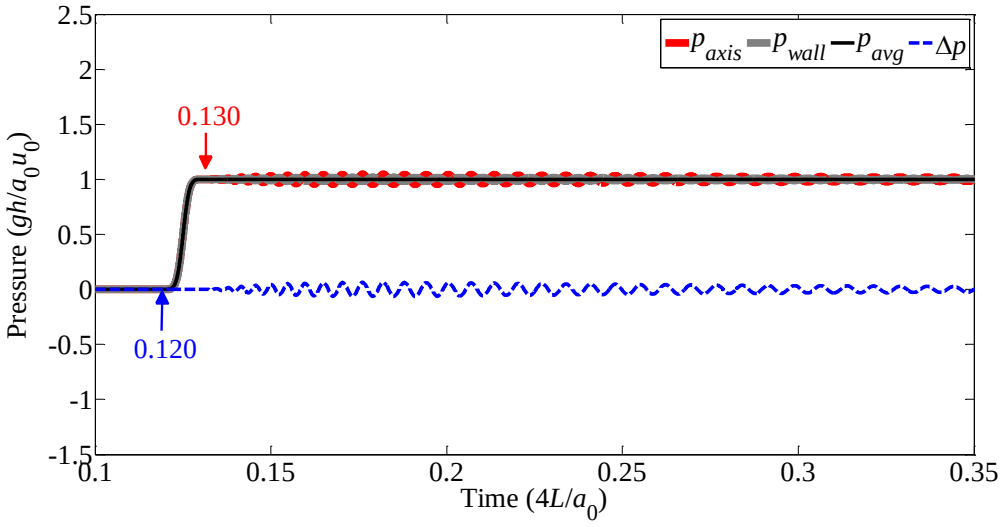

Fig. 6.9. The temporal variations of pressure at mid-length of the pipe.

Furthermore, the temporal variations of pressure at mid-length of the pipe (i.e., at $\xi = 25$) are plotted in Fig. 6.9. According to Fig. 6.9, the wave front arrives at the mid-length at time $0.125T_{th}$. Shortly after the wave front, the pressure difference between the pipe axis and pipe wall (i.e., Δp) is approximately equals to 0. To explain this, the velocity profiles at the mid-length before (i.e., at $0.120T_{th}$) and after (i.e., at $0.130T_{th}$) the wave front are plotted in Fig. 6.10. The result clearly shows that the passage of the wave front almost induces a uniform shift in velocity profile across the pipe radius (Riasi et al., 2009). Based on the Joukowsky's equation (Joukowsky, 1898), the pressure along the pipe radius should uniformly jump to 1; thus, the wave shortly after the wave front is a plane wave and no localized high radial modes are excited. As shown in Fig. 6.9, this plane wave is followed by high radial modes (i.e., waves after $0.130T_{th}$). These high radial modes propagating from the downstream valve, with group velocity $V_{gn} < a_0$ (Fig. 6.6), should arrive later than the wave front (i.e., wave dispersion).

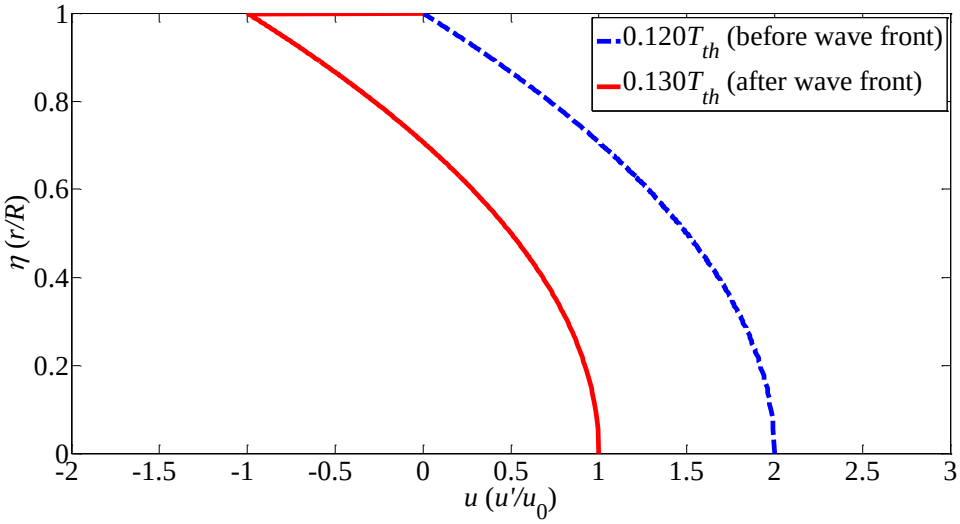

Fig. 6.10. The change of velocity profile (before and after the wave front) at mid-length of the pipe.

6.4.2 Low Frequency Flow Perturbation by Valve Oscillations

For Test 2 in Table 6.3, transients are generated by periodically oscillating the downstream valve (at $\xi = 0$). During this valve oscillation process, the axial velocity profile at the valve is given as $u_1 = 0.5\cdot[2(\eta^2-1)]\cdot[\cos(2\pi f_{in1}\tau)+1]$ (i.e., Eq. (6.21)), where f_{in1} is the induced flow perturbation (i.e., valve oscillation) frequency. The ratio of f_{in1} to f_r is 0.2, i.e., $f_{in1}/f_r = 0.2 < 1$, which is defined as *low frequency flow perturbation* in this study. The duration of this perturbation process is $0.125T_{th}$.

To inspect, the temporal variations of pressure at the valve are plotted in Fig. 6.11, which reveals that the pressure difference between the pipe axis and the pipe wall (Δp) changes periodically during the valve oscillation. The radial pressure profiles for nine time points (i.e., $t_1 \sim t_9$) within one period of the valve oscillation, as shown in the left enlarged view of Fig. 6.11, is plotted in Fig. 6.12(a). As is shown in Fig. 6.12(a), the pressure variation along the radial direction is quite evident. The pressure signal during the valve oscillation is transformed into the frequency domain in Fig. 6.12(b) by an FFT algorithm. The largest frequency peak with the value of 1485, which contains the most energy, is the frequency of the periodic valve oscillation ($f_{in1} = 0.2f_r = 1485$ Hz). In addition, the radial modes M1,

M2 and M3 are also excited, but the energy carried by these high radial modes is relatively limited.

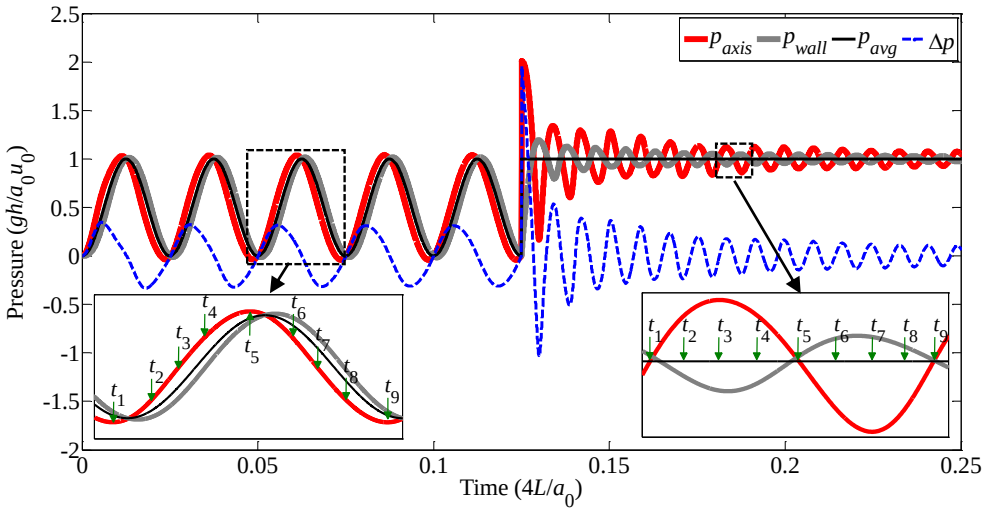

Fig. 6.11. The temporal variations of pressure at the downstream valve.

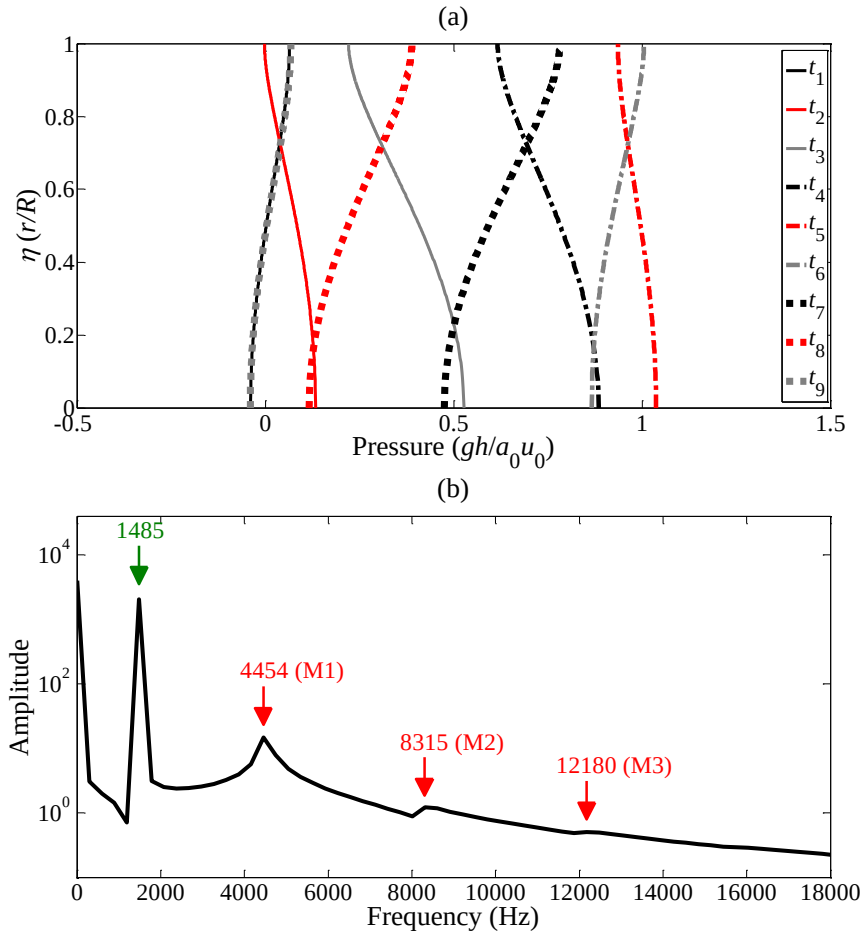

Fig. 6.12. (a) Radial pressure profiles at nine time points within one period of the valve oscillation; (b) the pressure signal during the valve oscillation in the frequency domain.

Similar to Test 1, according to Fig. 6.11, the plane wave assumption experiences the worst-case moment at time $0.125T_{th}$ when the valve is completely closed. The pressure at the pipe axis p_{axis} reaches its maximum value of 2.0, which is twice the area-averaged pressure p_{avg}. Afterwards, both local pressure curves (i.e., p_{axis} and p_{wall}) fluctuate periodically with amplitude damping. The pressure profiles for nine time points (i.e., t_1 ~ t_9) within one general fluctuation, as shown in the right enlarged view of Fig. 6.11, are selected and plotted in Fig. 6.13(a). It can be seen from Fig. 6.13(a) that the pressure node locates approximatively at $\eta = 0.625$. As is shown in Fig. 6.13(b), the pressure signal after the valve closure is also transformed into the frequency domain. Several high radial modes (i.e., M1, M2, M3 and M4) are motivated, but most of the energy is trapped in the M1, which can explain the location of the pressure node at $\eta = 0.625$ in Fig. 6.13(a).

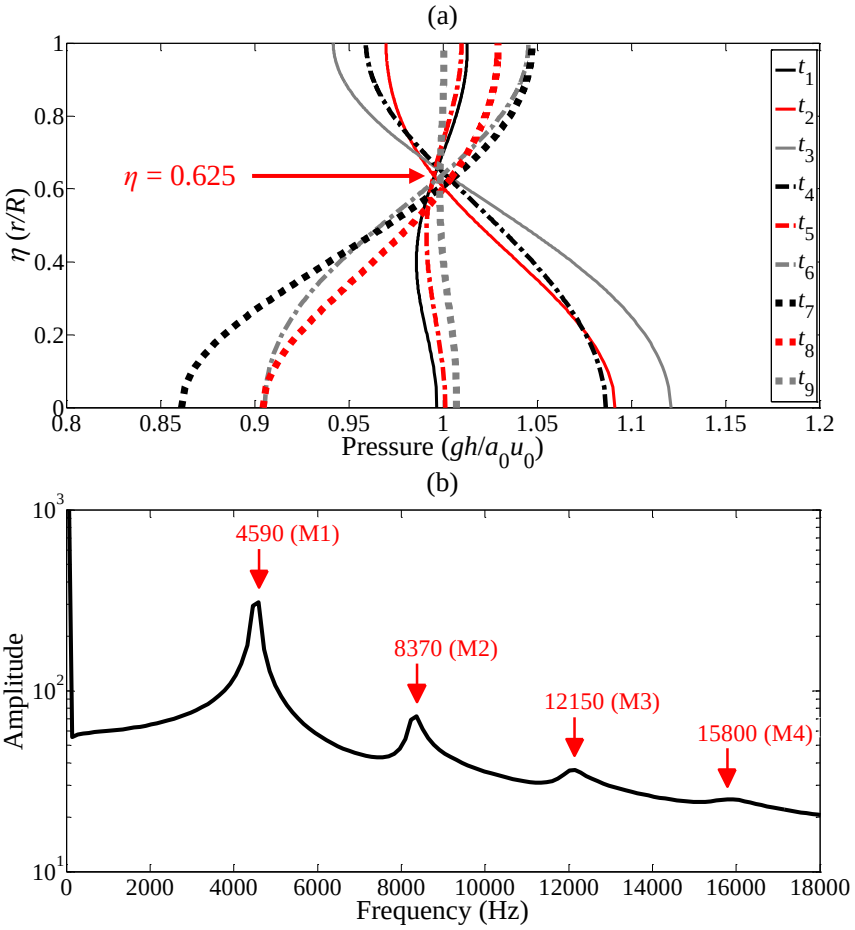

Fig. 6.13. (a) Radial pressure profiles at nine time points within one period of the pressure fluctuation after the valve closure; (b) the pressure signal after the valve closure in the frequency domain.

Fig. 6.14 shows the temporal variations of pressure at the mid-length (i.e., $\xi = 25$) of the pipe. Similar with Test 1, no localized high radial modes are excited because the passage of the wave front uniformly changes the velocity profile along the pipe radius (like Fig. 6.10). According to Fig. 6.14, the signal, ranging from $0.125T_{th}$ to $0.25T_{th}$, corresponding to valve-induced flow perturbation becomes a plane wave. This could be attributed to the relatively limited energy carried by the high radial modes, with an order of 10^0 in comparison with the case of valve oscillation with an order of 10^3 (see Fig. 6.12(b)).

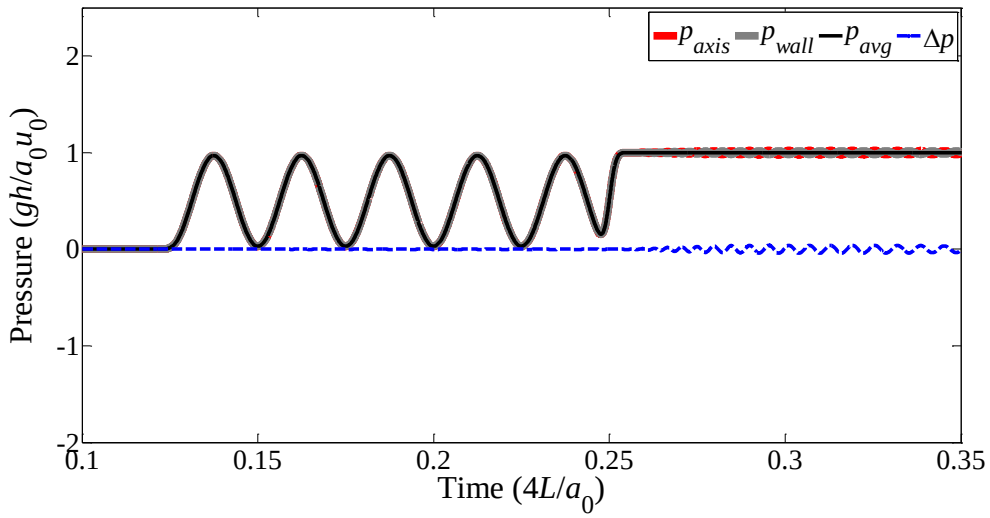

Fig. 6.14. The temporal variations of pressure at mid-length of the pipe.

6.4.3 High Frequency Flow Perturbation by Valve Oscillations

For Test 3 in Table 6.3, the generation mechanism of transients is the same as Test 2 (i.e., periodic oscillation of the downstream valve), but with a relatively high frequency. The axial velocity profile at the valve is given by $u_2 = 0.5\cdot[2(\eta^2-1)]\cdot[\cos(2\pi f_{in2}\tau)+1]$, where f_{in2} is the valve oscillation frequency. In Test 3, f_{in2} equals to the radial wave frequency f_r, i.e., $f_{in1}/f_r = 1$, which is defined as *high frequency flow perturbation* in this study. The time duration of the valve operation is $0.125T_{th}$.

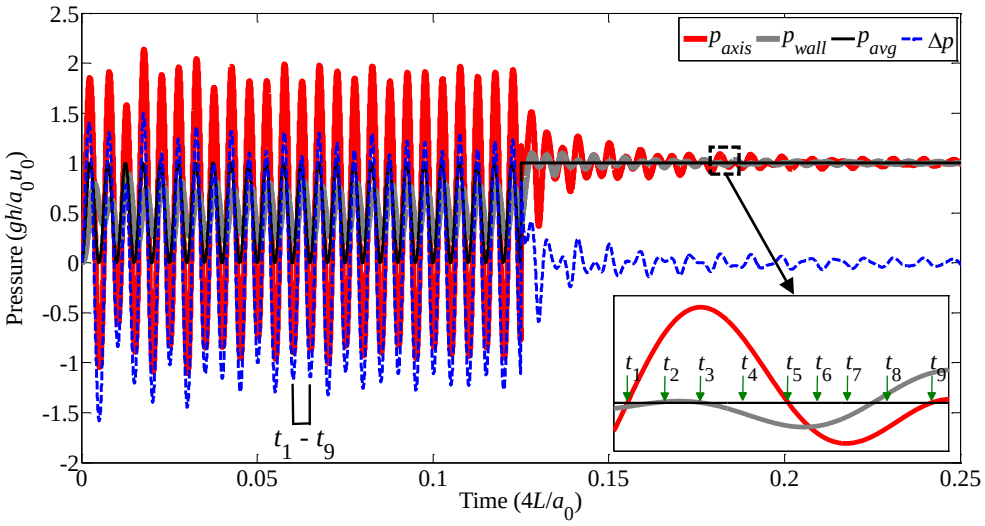

Fig. 6.15. The temporal variations of pressure at the downstream valve.

The variations of pressure with time at the valve are plotted in Fig. 6.15. According to Fig. 6.15, the pressure difference (Δp) between the pipe axis and the pipe wall is much larger than that of Test 2. One reason for this is that the valve oscillation frequency (f_{in2}) is comparable to the radial wave frequency (f_r). Within one period of valve oscillation, there is no enough time for the radial wave to influence the whole pressure profile across the pipe cross section. Again, the radial pressure profiles for nine time points (i.e., $t_1 \sim t_9$), within one general period of valve oscillation, as shown in Fig. 6.15, are plotted in Fig. 6.16(a). This result shows that the pressure node and antinode locate at the pipe wall (η = 1.0) and pipe axis (η = 0.0), respectively. This can also be attributed to the relative high frequency of valve oscillation compared with the radial wave frequency (f_r). The pressure signal during the valve oscillation is transformed into the frequency domain (Fig. 6.16(b)) by an FFT algorithm. It is shown in Fig. 6.16(b) that most of the energy is distributed in the frequency of valve oscillation (i.e., 7425 Hz). Although the energy trapped in high frequency modes is still relatively limited, the value is now much larger than that of the Test 2.

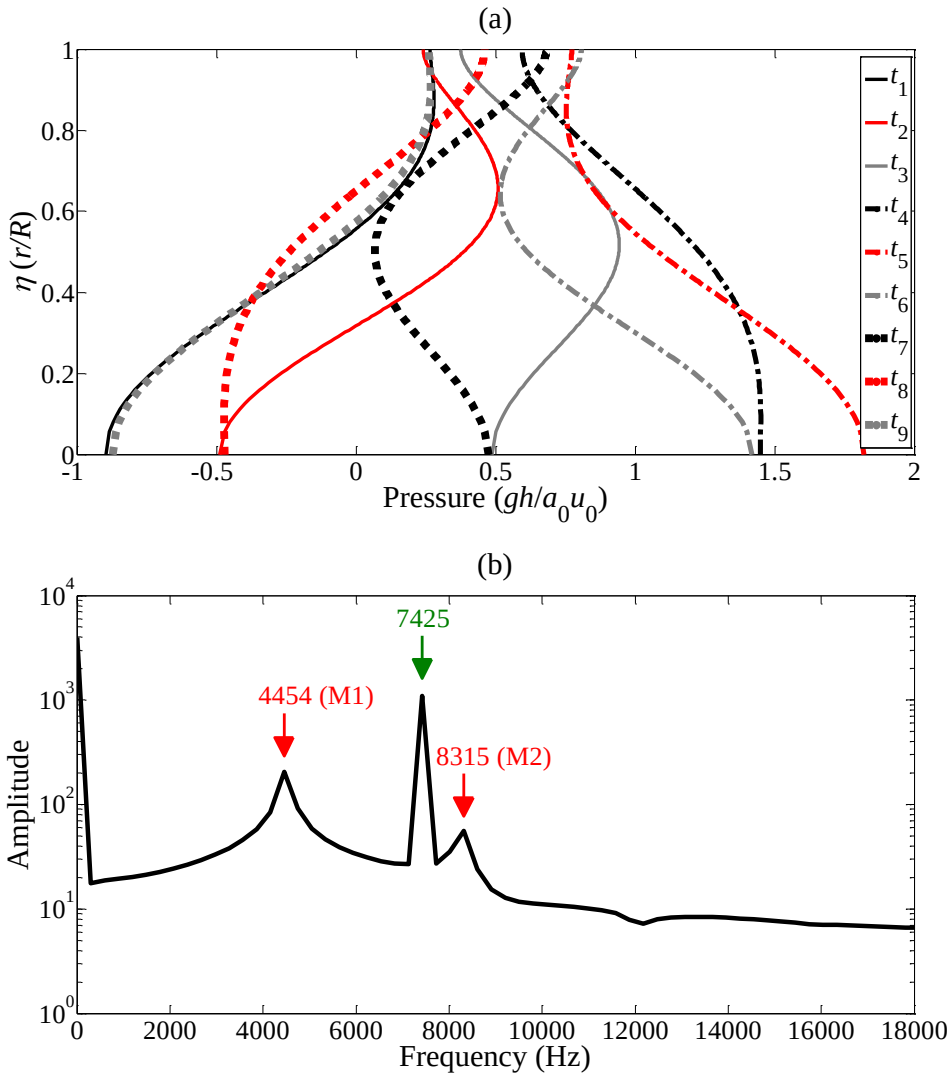

Fig. 6.16. (a) Radial pressure profiles at nine time points within one period of the valve oscillation; (b) the pressure signal during the valve oscillation in the frequency domain.

In this test case, the valve is completely closed at time $0.125T_{th}$. Unlike Test 1 and Test 2, both pressure curves (p_{aixs} and p_{wall}) fluctuate disorderly after the complete valve closure as shown in Fig. 6.15. The pressure profiles for nine time points within one general period, as shown in the enlarged view of Fig. 6.15, after the valve closure are plotted in Fig. 6.17(a). According to Fig. 6.17(a), it indicates that two pressure nodes (i.e., around η = 0.35 and 0.80) exist along the radial direction, which are close to the theoretical pressure node locations of M2 (i.e., $\eta \approx 0.343$ and 0.787) (Louati & Ghidaoui, 2017b). To explore the components of radial pressure waves in Fig. 6.17(a), the pressure signal after the valve closure is transformed into the frequency domain and plotted in Fig. 6.17(b). The obtained

result reveals that several high radial modes (i.e., M1, M2, M3 and M4) are excited. Moreover, the amplitude of M2 is comparable to the amplitude of M1. In other words, the energy almost trapped equally in M1 and M2. Therefore, both M1 and M2 are dominant among high radial modes. This can explain the disorder of both pressure curves (p_{axis} and p_{wall}) in Fig. 6.15 after the complete valve closure under the condition of high frequency valve oscillation.

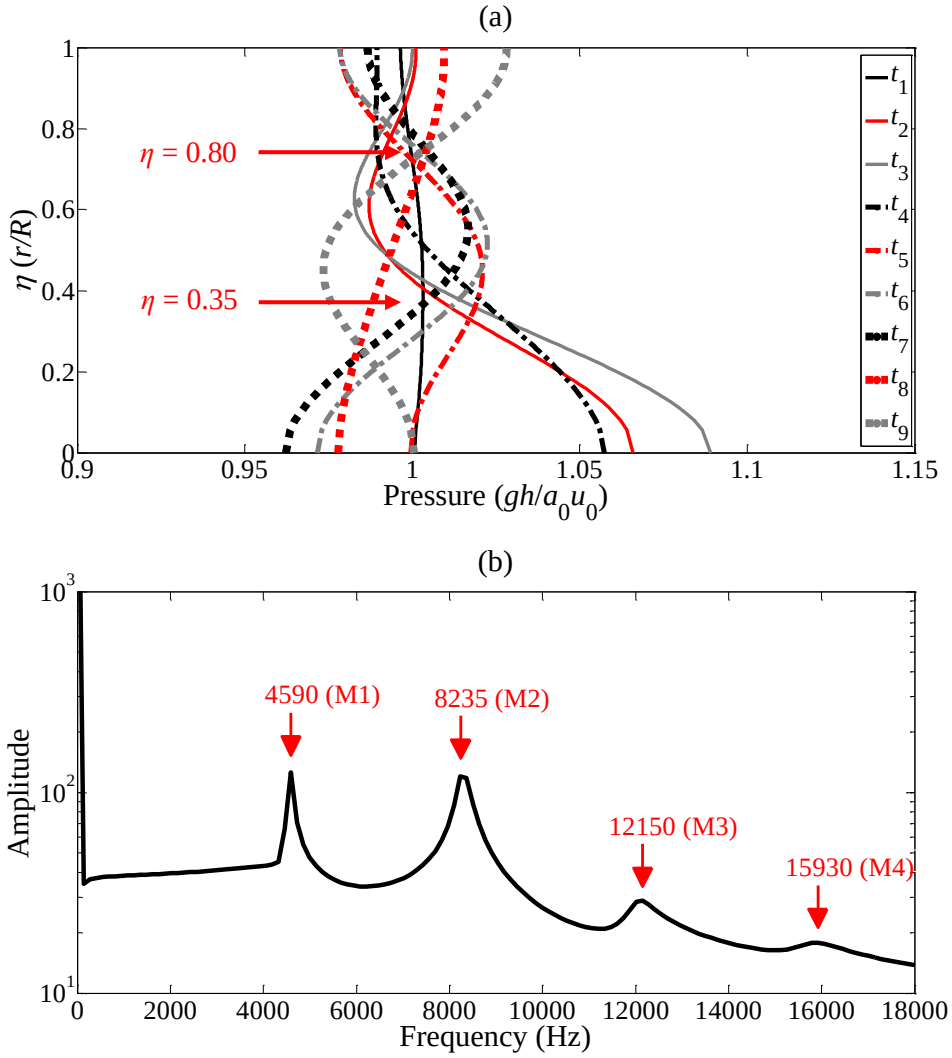

Fig. 6.17. (a) Radial pressure profiles at nine time points within one period of the pressure fluctuation after valve closure; (b) the pressure signal after the valve closure in the frequency domain.

The temporal variations of pressure at mid-length of the pipe (i.e., at $\xi = 25$) are plotted in Fig. 6.18. Similar with Test 1 and Test 2, no localized high radial modes are excited.

However, the amplitude of the radial pressure waves, coming from the downstream valve, is larger than that of the Test 1 and Test 2. This is because more energy is distributed into the high radial modes, which are now in an order of 10^1 or 10^2 for Test 3 in Fig. 6.16(b), during the valve oscillation.

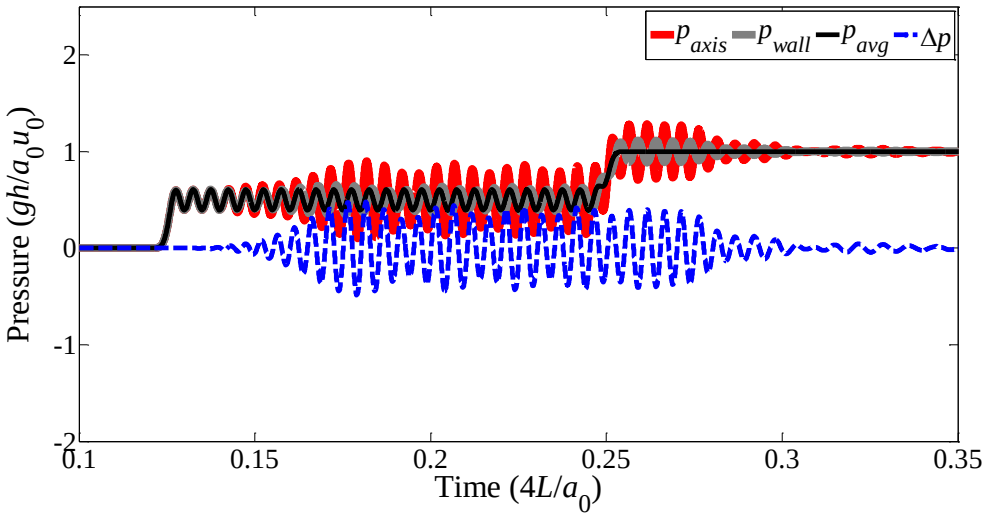

Fig. 6.18. The temporal variations of pressure at mid-length of the pipe.

6.5 Discussion and Implications

The results and findings above demonstrate that radial pressure waves can be excited by different operations on the downstream valve. A recent research conducted by Louati and Ghidaoui (2017b) has observed that radial pressure waves cannot be excited if the wave generator has the same size with the pipe diameter. This is due to the inviscid and initially stagnant flows considered in (Louati & Ghidaoui, 2017b). Under such idealized flow conditions, if the transient source size equals to the pipe diameter, the generated transient pressure will be independent of the pipe radius and propagate as a plane wave (M0). However, another generating mechanism of radial pressure waves has been identified for viscous and initially non-static flows in the present chapter, even though the downstream valve, having the same size with the pipe diameter, is used as the transient generator. That is, the non-uniform change in the initial velocity profile forms pressure gradients along the radial direction, which thereafter becomes the driving force of the formation of radial flux and radial pressure waves during a transient flow process. In practical urban water supply systems, flows usually distribute with certain axial velocity profiles along the radial direction; thus, radial pressure waves caused by the non-uniform change in initial velocity profiles could occur and should also be considered in applications.

Furthermore, it has also shown that radial pressure waves may have different behavior under different transient generation conditions (i.e., valve operations). Specifically, for Test 1 with the typical operation of a sudden and complete valve closure, high radial modes can be excited and most of the energy is carried by M1. As a result, a pressure node exists at $\eta = 0.625$ along the radial direction, which is useful to the better selection of pressure measurement locations during practical transient applications. For Test 2, during the relatively low frequency flow perturbation, the dominant energy is carried exactly by the valve oscillation (flow perturbation) frequency. After the complete valve closure at time $0.125T_{th}$, the amplitude of each excited high radial mode stays almost the same with Test 1. This implies that the valve oscillation with a low frequency of f_{in1} (e.g., $f_{in1} = 0.2f_r$ in this chapter) has a limited influence on the energy distribution among high

radial modes. In Test 3, which is used for investigating the relatively high frequency flow perturbation, most of the energy is carried by the perturbation frequency during the valve oscillation. This is similar with Test 2. However, after the complete valve closure at time $0.125T_{th}$, the amplitude of M2 is almost identical to the M1 (see Fig. 6.17(b)), which indicates that the valve oscillation with the frequency of f_{in2} (i.e., $f_{in2} = 1.0f_r$) redistributes the energy among different high radial modes. Moreover, the pressure amplitude measured at the mid-length of the pipe is larger than that of Test 1 and Test 2.

The obtained results have also demonstrated that the maximum pressure (especially the local pressure at the pipe axis), caused by the fast valve closure or high frequency valve oscillation, can be much larger than the maximum pressure predicted by the 1D and quasi-2D models where a plane wave assumption is imposed. For viscous laminar pipe flows, the axial velocity is distributed parabolically along the radial direction (i.e., Fig. 6.2) because of the no-slip boundary condition. The maximum velocity occurs at the pipe axis and it is twice the area-averaged velocity. The present full-2D model can give the true localized pressure variation along the radial direction. However, the pressure in the 1D and quasi-2D models can only be obtained from a perspective of the area-averaged quantity. Therefore, the traditional 1D and quasi-2D models might underestimate the destructive effects of the water hammer due to neglecting the influence of radial pressure waves during the complex transient process.

Consequently, the development and results of the efficient full-2D model in this chapter are useful to: (i) investigate the validity frequency range of the plane wave assumption; (ii) observe the radial pressure wave behavior in water pipes; and (iii) design qualified pipes and related accessories for pipe system safety with regard to the pressure prediction.

6.6 Summary

This chapter investigates systematically: (i) the validity frequency range of the plane wave assumption; and (ii) the radial pressure wave behavior in transient laminar flows under different flow perturbations. First, the inefficiency problem of the current full-2D model has been addressed by proposing a more efficient numerical scheme. The modified efficient full-2D model is extended into an RPV system to simulate a whole water hammer process, which is validated by the Zielke's 1D analytical model. With the efficient full-2D model, the generation mechanism and components of radial pressure waves excited by different valve operations are investigated systematically.

The obtained results demonstrate that the plane wave assumption is valid if the incident wave frequency is lower than the cut-off frequency of M1 (i.e., radial mode 1). Radial pressure waves can be induced from the non-uniform change in the initial velocity profile under valve operations, which forms pressure gradients along the radial direction. After transient generation, the existence of radial pressure gradients becomes the driving force of the formation of radial flux and radial pressure waves. This formation mechanism and results should be considered and included in the practical transient analysis, since the flows in practical water piping systems are usually viscous and non-static. The results analysis also reveals that the generated radial pressure waves are composed of different high radial modes. Moreover, the valve-induced flow perturbations (with different frequencies) may influence the energy distribution among different high radial modes. Specifically, the results of this chapter indicate that most of the energy is carried by M1 for cases of flow perturbations by sudden valve closure and low frequency valve oscillation, while for high frequency flow perturbation, the energy is almost entrapped equally in M1 and M2.

From the results and findings of this chapter, it is demonstrated that the developed efficient full-2D model has made it possible to understand: (i) the validity range of the plane wave assumption; and (ii) the radial pressure wave behavior in transient laminar

pipe flows. It is also noted that only initial laminar flows and valve-based transient excitation techniques are considered in this chapter; thus, further investigations will be required for turbulent flows and other complex transients in future work.

CHAPTER 7 CFD VALIDATION OF THE DEVELOPED THEORY[6]

7.1 Introduction

In previous chapters (Che et al., 2018b; Che et al., 2019c), the author investigated the influence of various non-uniform blockages in water pipes on transient frequency responses. It was found that the resonant frequency shifts induced by non-uniform blockages have totally different patterns from that of uniform blockages. Specifically, the frequency shifts induced by non-uniform blockages become less evident for higher harmonics. Afterwards, the physical mechanism of this pattern is interpreted from an energy perspective (Che et al., 2019c). It turns out that the impedance of non-uniform blockages is frequency dependent, which becomes smaller for higher frequency incident waves. This means non-uniform blockages have a less blocking effect on the propagation of high frequency waves; thus, the frequency shifts induced by non-uniform blockages become less evident.

However, these studies are only numerically validated by the one-dimensional (1D) water hammer model, which is mainly solved by the fixed-grid method of characteristics (MOC) (Chaudhry, 2014; Wylie et al., 1993). As discussed in Chapter 3, several assumptions are inherent in the 1D water hammer model. In addition, the pipe radius of the non-uniform blockage section varies along the axial direction, so does the transient wave speed (Chaudhry, 2014; Ghidaoui et al., 2005). In previous chapters (Che et al., 2018b; Che et al., 2019c), to use the fixed-grid MOC, the varying wave speed is assumed to be the average wave speed within the non-uniform blockage section. These assumptions may

[6] This chapter is adapted from the research paper of the author and his co-authors (Che et al., 2019b).

deviate the numerical results from the real situations. The sole criterion of the validity of the developed theory in previous chapters (Che et al., 2018b; Che et al., 2019c) is the experiment. But the developed theory has not yet well verified experimentally due to the difficulty of constructing perfectly exponential (or linear) non-uniform blockages in laboratories. As an alternative, the computational fluid dynamics (CFD) model coupled with user-defined functions (UDFs) relaxes these assumptions and makes it possible to validate the developed theory under more realistic and complex conditions.

This chapter aims to further validate the theory developed in previous chapters (Che et al., 2018b; Che et al., 2019c) by the CFD model coupled with UDFs. The 2D axisymmetric Navier-Stokes equations are first applied into a reservoir-pipe-valve (RPV) system (i.e., a bounded system) to simulate the whole process of a water hammer event, which is validated by the well-established Zielke's 1D analytical model (Zielke, 1968). Afterwards, the 2D CFD model is applied to different pipe systems with non-uniform blockages to validate: (i) the theoretical resonant frequency shifts induced by non-uniform blockages in bounded pipe systems; and (ii) the theoretical energy transmission coefficient through non-uniform blockages in unbounded pipe systems. Transients are introduced into different pipe systems by different transient excitation techniques at the downstream boundary.

7.2 CFD Setup and Numerical Procedure

7.2.1 Governing Equations

2D Navier-Stokes Equations

In ANSYS Fluent, the governing equations for all flows are derived from the fundamental conservation principles of mass, momentum, and energy. The temperature variation during transients is assumed to be negligible due to the high specific heat capacity of water (Saemi et al., 2018). Therefore, the 2D conservative form Navier-Stokes equations for a Newtonian fluid (e.g., water) in an axisymmetric non-rotating flow field, expressed in a cylindrical coordinate system, are

$$\frac{\partial \rho}{\partial t}+\frac{\partial}{\partial x}(\rho u)+\frac{\partial}{\partial r}(\rho v)+\frac{\rho v}{r}=0 \tag{7.1a}$$

$$\begin{aligned}&\frac{\partial}{\partial t}(\rho u)+\frac{1}{r}\frac{\partial}{\partial x}(r\rho uu)+\frac{1}{r}\frac{\partial}{\partial r}(r\rho vu)=-\frac{\partial p}{\partial x}+\frac{1}{r}\frac{\partial}{\partial x}\left[r\mu\left(2\frac{\partial u}{\partial x}-\frac{2}{3}(\nabla\cdot\mathbf{u})\right)\right]\\&+\frac{1}{r}\frac{\partial}{\partial r}\left[r\mu\left(\frac{\partial u}{\partial r}+\frac{\partial v}{\partial x}\right)\right]+F_x\end{aligned} \tag{7.1b}$$

$$\begin{aligned}&\frac{\partial}{\partial t}(\rho v)+\frac{1}{r}\frac{\partial}{\partial x}(r\rho uv)+\frac{1}{r}\frac{\partial}{\partial r}(r\rho vv)=-\frac{\partial p}{\partial r}+\frac{1}{r}\frac{\partial}{\partial x}\left[r\mu\left(\frac{\partial v}{\partial x}+\frac{\partial u}{\partial r}\right)\right]\\&+\frac{1}{r}\frac{\partial}{\partial r}\left[r\mu\left(2\frac{\partial v}{\partial r}-\frac{2}{3}(\nabla\cdot\mathbf{u})\right)\right]-2\mu\frac{v}{r^2}+\frac{2}{3}\frac{\mu}{r}(\nabla\cdot\mathbf{u})+F_r\end{aligned} \tag{7.1c}$$

where Eqs. (7.1a), (7.1b), and (7.1c) are the conservation equations of mass, axial momentum, and radial momentum, respectively; t = time; x = axial coordinate along the pipe axis; r = radial coordinate from the pipe axis; ρ = density of water; u = axial velocity; v = radial velocity; p = pressure; μ = dynamic viscosity; F_x = body force along x; F_r = body force along r; and $\nabla\cdot\mathbf{u} = \partial u/\partial x + \partial v/\partial r + v/r$.

Modification of Water Bulk Modulus

In pressurized elastic water pipes, the general expression of the transient wave speed is (Ghidaoui, 2004; Ghidaoui et al., 2005)

$$\frac{1}{a^2} = \frac{d\rho}{dp} + \frac{\rho}{A}\frac{dS}{dp} \tag{7.2}$$

where a = transient wave speed; and S = pipe cross-sectional area.

It is observed in Eq. (7.2) that two main factors contribute to the transient wave speed: (i) the first term on the right-hand side represents the water compressibility; and (ii) the second term represents the effect of pipe wall deformability. By relating these two terms on the right-hand side of Eq. (7.2) to the material properties of water and to the material and geometrical properties of pipes, which are anchored against longitudinal movement throughout their lengths, Eq. (7.2) becomes (Chaudhry, 2014; Ghidaoui et al., 2005)

$$a = \sqrt{\frac{K}{\rho\left[1+\left(K/E\right)\left(D/e\right)\left(1-\nu^2\right)\right]}} \tag{7.3}$$

where K = bulk modulus of elasticity of water; E = Young's modulus of elasticity of the pipe wall; D = pipe diameter, which depends on x (i.e., $D(x)$) for pipes with non-uniform blockages; e = pipe wall thickness; and ν = Poisson ratio.

In ANSYS Fluent, the 2D model in Eq. (7.1) considers the water compressibility as $K = dp/(d\rho/\rho)$. However, it does not take account of the effect of material (e.g., pipe wall deformability along r) and geometrical (e.g., pipe diameter variation along x) properties of pipes on the transient wave speed, which means the pipe wall is considered as a rigid boundary (i.e., $E = \infty$) (Martins et al., 2016). Therefore, the transient wave speed in Eq. (7.3) is simplified into $a = (K/\rho)^{1/2}$.

To include the effect of pipe wall elasticity and pipe diameter variation on the transient wave speed, the bulk modulus of water is artificially modified in UDFs of density and wave speed, as shown in Eq. (7.4) (Saemi et al., 2018, 2019).

$$K' = a_{th}^2 \rho = \frac{K}{1+\left(K/E\right)\left(D/e\right)\left(1-\nu^2\right)} \tag{7.4}$$

where K' = modified bulk modulus of water; and a_{th} = theoretical transient wave speed in elastic pipes.

In this way, the obtained modified transient wave speed in Eq. (7.5) is equivalent to the one considering physical properties of both water and pipe walls.

$$a = \sqrt{\frac{K'}{\rho}} \tag{7.5}$$

7.2.2 Numerical Settings

As shown in Fig. 7.1, the simulation of transient pipe flows using ANSYS Fluent is an interactive step-by-step process, which includes three main stages: (i) pre-processing; (ii) simulation; and (iii) post-processing (Martins et al., 2014). By taking the example of an intact RPV system, as shown in Fig. 7.2, the main procedures in the pre-processing stage are described in this section (i.e., Section 7.2.2).

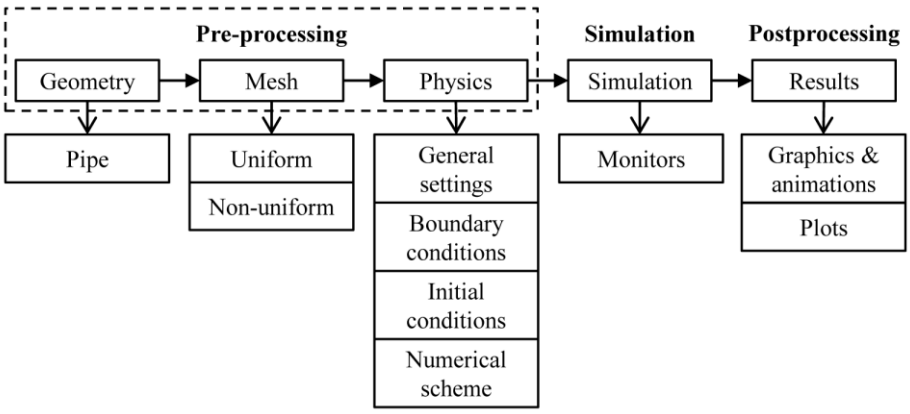

Fig. 7.1. An interactive step-by-step process for simulating transient pipe flows.

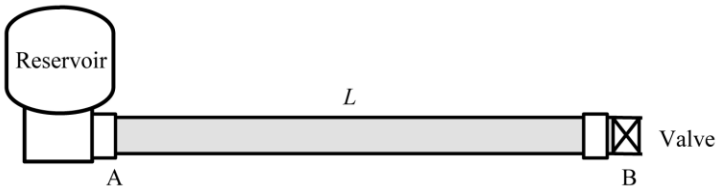

Fig. 7.2. An intact reservoir-pipe-valve (RPV) system.

Geometry Creation and Mesh Generation

Detailed parameters of the intact RPV system in Fig. 7.2 are listed in Table 7.1, where a_0 = transient wave speed in intact pipes; Re = Reynolds number. ANSYS Design Modeler is used to draw a 2D axisymmetric pipe with a total length L = 42 m and an inner radius R = 0.0362 m. To solve the governing equations (i.e., Eq. (7.1)), which are a set of partial differential equations (PDEs), the interior geometric domain of the 2D pipe needs to be spatially discretized into a number of small simple shapes, resulting in meshes. These meshes are generated by ANSYS Fluent Meshing. As shown in Fig. 7.3, to capture more detailed physical phenomena near the pipe wall (e.g., wall shear stress), non-uniform meshes are adopted in the radial direction. The growth rate of the mesh size Δr along the radial direction ranges from 1.05 to 1.10 for different tests in the intact pipe system. In addition, meshes are uniformly distributed along the axial direction with different mesh size Δx in different tests. The propagation of transient wave in the radial direction can be neglected due to the plane wave assumption. Therefore, the time step Δt in the simulation of transient pipe flows can be determined by the Courant-Friedrichs-Lewy (CFL) condition, which mainly depends on the axial grid size Δx and the maximum transient wave speed a_{max}. Therefore, the original form PDEs are transformed into their discretized form in the space-time field with certain grid and time steps, respectively.

Table 7.1. System parameters of the intact reservoir-pipe-valve (RPV) system.

a_0 (m/s)	R (m)	L (m)	μ/ρ (m^2/s)	Re
1218.86	0.0362	42	1e-6	1670

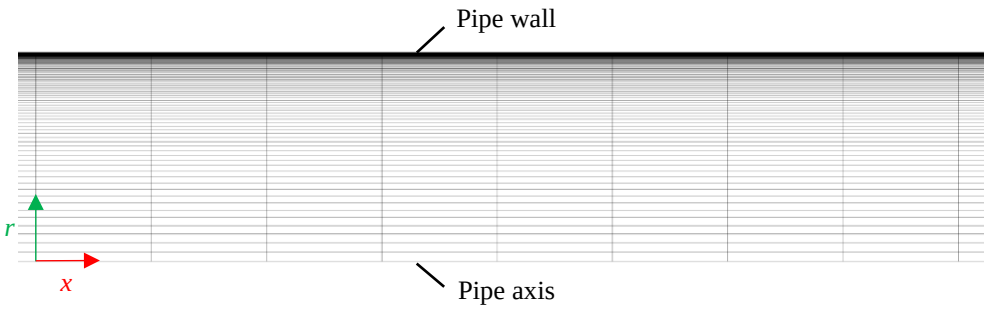

Fig. 7.3. Uniform and non-uniform meshes along the axial and radial directions.

Initial and Boundary Conditions

For each mesh point in 2D transient pipe flows, three unknowns (e.g., p, u, and v) need to be solved. To close the discretized form PDEs in the whole space-time field, appropriate initial and boundaries conditions should be specified. As shown in Fig. 7.2, a classical RPV water hammer experimental systems is adopted in this study to simulate transient pipe flows. The pipe used in this RPV system is made of stainless steel. The boundary condition at the wall is described by the "no-slip condition" and the flow field in the pipe is assumed to be axisymmetric. A reservoir, whose pressure head remains constant during transient events, is installed at the upstream end of the pipe. The downstream end of the pipe is bounded by an inline valve, which can be appropriately adjusted to form an initial steady flow (i.e., Poiseuille laminar flow) in the RPV system.

To induce transients into the RPV system, various operations on the downstream valve can be taken, such as: (i) a sudden and complete closure of the downstream valve (Al-Khomairi, 2008; Ferrante et al., 2009a; Kim, 2005; Meniconi et al., 2011c); (ii) a "closure-open-closure" operation on the downstream valve (Duan et al., 2011a, 2012a); and (iii) a specific oscillation pattern of the downstream valve (e.g., a Gaussian-modulated sinusoidal pulse) (Che et al., 2019c; Louati & Ghidaoui, 2017b). More detailed information about these operations will be discussed in the following sections.

Numerical Scheme

The discretization method used in ANSYS Fluent is the finite volume method (FVM), which solves the governing equations in a conservative form and guarantees the conservation of fluxes through a specific control volume. Due to the relative low Mach number of transient flows in the RPV system, the pressure field is determined by the Semi-Implicit Method for Pressure Linked Equations (SIMPLE) algorithm, which is a pressure-based segregated algorithm (Ferziger & Peric, 2001; Patankar, 1980). The non-linear governing equations Eq. (7.1) are solved iteratively and the convergence criterion (i.e., the residual error) is chosen as 10^{-6}.

7.3 Model Validation

7.3.1 Steady State Velocity Profile

As shown in Fig. 7.2, initially, the downstream valve is kept fully open to form a steady laminar pipe flow in the RPV system. In the fully developed region of the laminar pipe flow, the axial velocity profile $u(r)$ keeps the same along the flow direction (i.e., the axial direction). The theoretical velocity profile of this fully developed laminar flow is given in Eq. (7.6) (Çengel & Cimbala, 2006), which is a parabolic profile (i.e., Hagen-Poiseuille flow), with the maximum velocity (i.e., $2u_0$) at the pipe axis and minimum velocity (i.e., 0) at the pipe wall.

$$u(r) = 2u_0\left(1-\frac{r^2}{R^2}\right) \tag{7.6}$$

where u_0 = initial average axial velocity.

Velocity profiles from both full-2D numerical simulation and the exact solution in Eq. (7.6) are compared and plotted in Fig. 7.4. The axial velocity u is normalized by u_0 and plotted as u^* in the x-axis. The distance from the pipe axis r is normalized by R and plotted as r^* in the y-axis. A good agreement between the numerical and analytical results can be observed in Fig. 7.4, which confirms the validity of the obtained numerical results and related CFD settings.

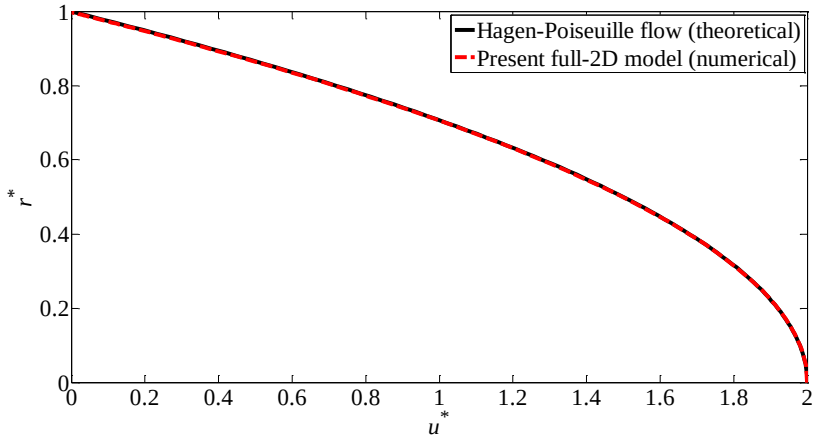

Fig. 7.4. Comparison between the simulated and the exact velocity profiles.

7.3.2 Mesh Independence Tests

In the numerical simulation, as shown in Fig. 7.3, uniform and non-uniform meshes are adopted in the *x*- and *r*-directions, respectively. In transient pipe flows, the accuracy of the calculated hydraulic variables greatly depends on the mesh density within the fluid domain. Fine meshes generally result in more accurate results but need more computational resources (i.e., low efficiency) (Martins et al., 2016); thus, there should be a trade-off between computational accuracy and efficiency. For this purpose, three tests with different mesh density, as shown in Table 7.2, are conducted to select the relatively optimal mesh density, which is used to conduct further numerical experiments. Table 7.2 indicates that the numbers of spatial mesh node of the coarse, medium, and fine tests are 0.21e5, 0.67e5, and 2.1e5, respectively.

Table 7.2. Various mesh density used in mesh independence tests.

	N_r	Δx (m)	Δt (s)
Coarse mesh	50	0.10	6.70e-5
Medium mesh	80	0.05	3.35e-5
Fine mesh	100	0.02	1.34e-5

As shown in Fig. 7.2, transients are caused by a sudden and complete closure of the downstream valve. Two pressure transducers are installed at the valve and the mid-length of the pipe to measure the pressure near the pipe wall (i.e., at $r = R$). The obtained pressure-time histories are plotted in Fig. 7.5. The time t is normalized by the fundamental period of the RPV system (i.e., $4L/a_0$) and plotted as t^* in the x-axis. The pressure p is normalized according to $(p - p_0)/(\rho a_0 u_0)$, where p_0 = initial pressure in the pipe, and plotted as p^* in the y-axis. It is observed in Fig. 7.5 that the result gradually converges as the increase of the mesh density. In addition, there is no visible difference between the pressure-time histories calculated by medium and fine meshes; thus, the medium mesh is chosen in the numerical validation.

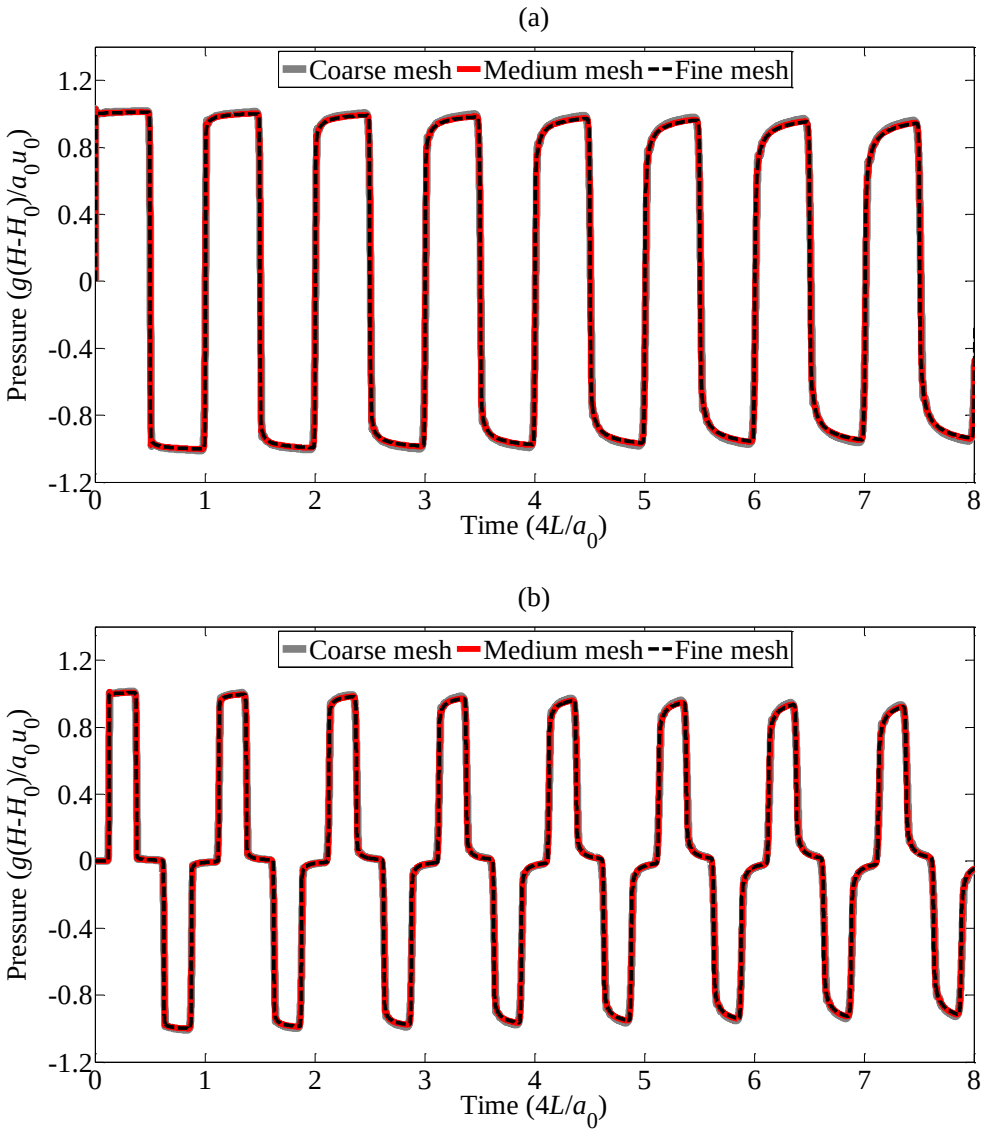

Fig. 7.5. Pressure time histories of various mesh density at (a) the downstream valve; and (b) the mid-length of the pipe.

7.3.3 1D Numerical Validation

The present full-2D model is validated by the well-established Zielke's 1D analytical model, which has been widely validated by experimental tests in the literature (Zielke, 1968). As shown in Fig. 7.2, transients are caused by a sudden downstream valve closure. The pressure is measured at both the valve and mid-length of the pipe, which is plotted in Fig. 7.6. Fig. 7.6 indicates good agreement between the present full-2D model and the Zielke's 1D analytical model in terms of both pressure amplitude and phase. This

confirms the validity of the full-2D model and numerical settings for modeling transient pipe flows.

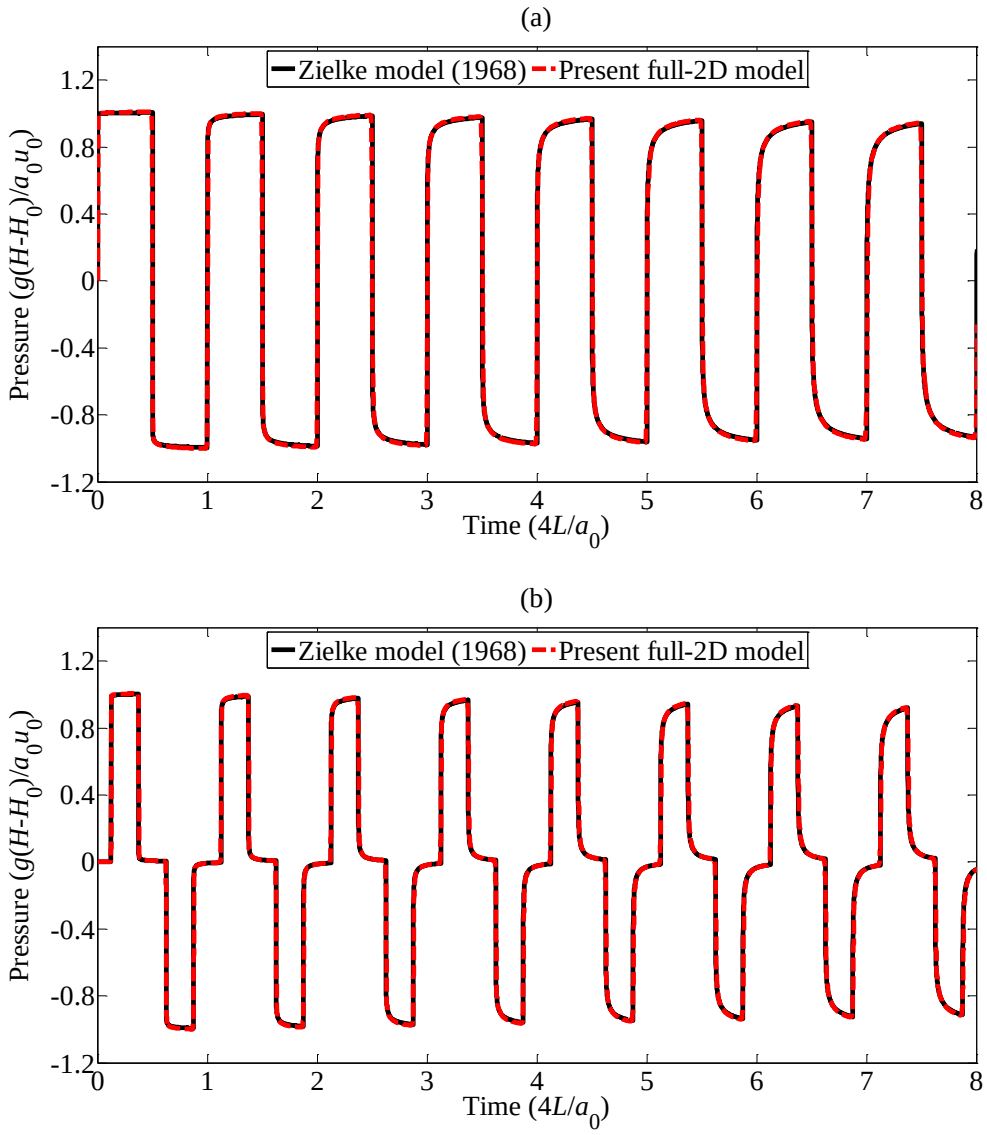

Fig. 7.6. Validation of pressure time histories at (a) the downstream valve; and (b) the mid-length of the pipe.

7.4 Validation of the Developed Theory by Numerical CFD Experiments

7.4.1 Energy Transmission Coefficients of Transient Waves through Non-uniform Blockages

To validate the energy transmission coefficient of transient waves through non-uniform blockages in Eq. (7.7), which is derived in Chapter 5 (Che et al., 2019c), the CFD model in Section 7.3 is applied to an unbounded pipe system with non-uniform blockages. As shown in Fig. 7.7, the unbounded pipe system has two anechoic boundaries (i.e., the upstream and downstream boundaries) and is blocked by non-uniform blockages. The incident wave is generated by the downstream generator and the transmitted wave through non-uniform blockages is measured by the wave receiver located at the upstream end. The transient wave speed varies along the axial direction of the pipe due to the change of the pipe diameter, which is calculated by Eq. (7.5) and plotted in Fig. 7.8. More detailed parameters of the pipe system are listed in Table 7.3, where R_C = pipe radius at Junction C; and $\bar{a}_b$ = average wave speed within the blockage section.

$$T_C = \frac{W_{tr}}{W_{in}} = \left| \frac{2}{\frac{gS_0U_{21}^*}{a_0} + U_{22}^* + U_{11}^* + \frac{a_0U_{12}^*}{gS_0}} \right|^2 \tag{7.7}$$

where T_C = energy transmission coefficient; W_{tr} = energy flow (i.e., power) transmitted through the non-uniform blockages; W_{in} = energy flow incident on the non-uniform blockages; g = gravitational acceleration; S_0 = cross-sectional areas at two boundaries A and E in Fig. 7.7; and U_{ij}^* = elements of the system overall transfer matrix in Eq. (7.8). The transfer matrix is the linearized counterpart of the 1D water hammer model in the frequency domain. It describes the wave behavior and connects state vectors at two boundaries of the pipe system without discretization of the pipe in space (Che et al., 2018b).

$$\begin{pmatrix} q \\ h \end{pmatrix}_E = \begin{pmatrix} U_{11}^* & U_{12}^* \\ U_{21}^* & U_{22}^* \end{pmatrix} \begin{pmatrix} q \\ h \end{pmatrix}_A \tag{7.8}$$

where subscripts A and E = locations of the upstream and downstream boundaries; q = discharge deviation in the frequency domain; and h = pressure head deviation in the frequency domain.

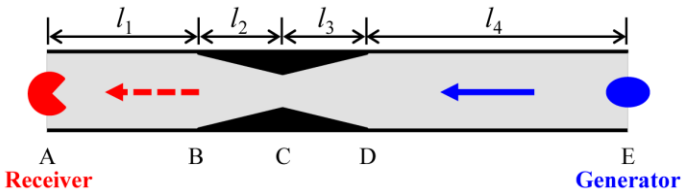

Fig. 7.7. An unbounded pipe system containing a symmetrical linear non-uniform blockage (with a wave generator and a wave receiver).

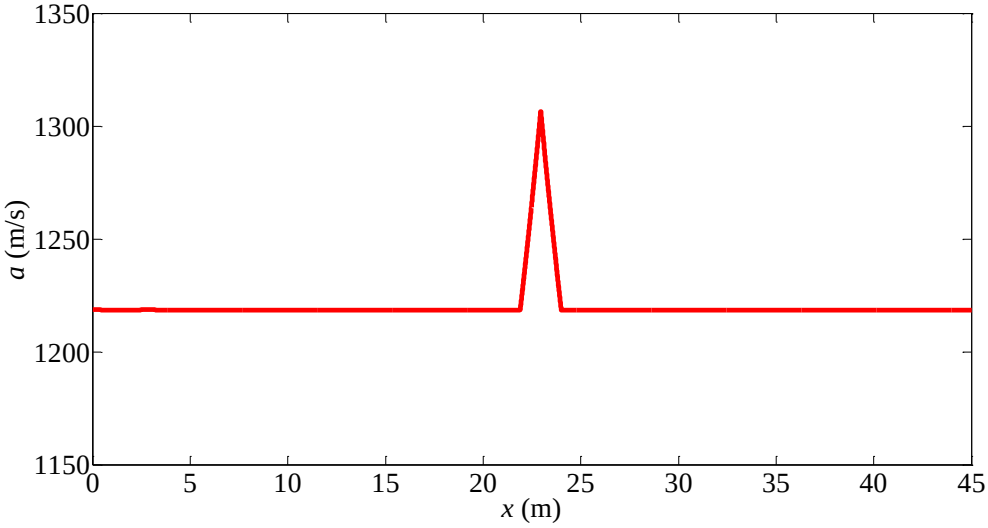

Fig. 7.8. Distribution of the transient wave speed along the axial direction of the pipe.

Table 7.3. Parameters of the unbounded pipe system.

Blockage type	l_1 (m)	l_2 (m)	l_3 (m)	l_4 (m)	R (m)	R_C (m)	a_0 (m/s)	$\bar{a}_b$ (m/s)
linear non-uniform	21.9	1.05	1.05	21	0.0362	0.02172	1218.86	1262.95

The incident wave generated at the downstream end is a Gaussian-modulated sinusoidal pulse (UDFs) governed by Eq. (7.9). Fig. 7.9 illustrates the input pulse in both time and frequency domains. As introduced in Chapter 5 (Che et al., 2019c), this pulse has two main features: (i) most energy of this pulse is distributed at its central frequency ω_c; and (ii) the frequency bandwidth of the incident wave can be easily determined by adjusting the value of β.

$$p_{in} = p_0 + \alpha p_0 \exp\left(-4\left(\frac{\omega_c}{\beta}\right)^2 \log(10)\left(t - \frac{\beta}{\omega_c}\right)^2\right)\sin\left(\omega_c\left(t - \frac{\beta}{\omega_c}\right)\right) \tag{7.9}$$

where p_{in} = incident wave pressure at the generator; ω_c = angular central frequency of the incident wave; α = a coefficient that determines the amplitude of the incident wave; and β = a coefficient that determines the frequency bandwidth of the incident wave.

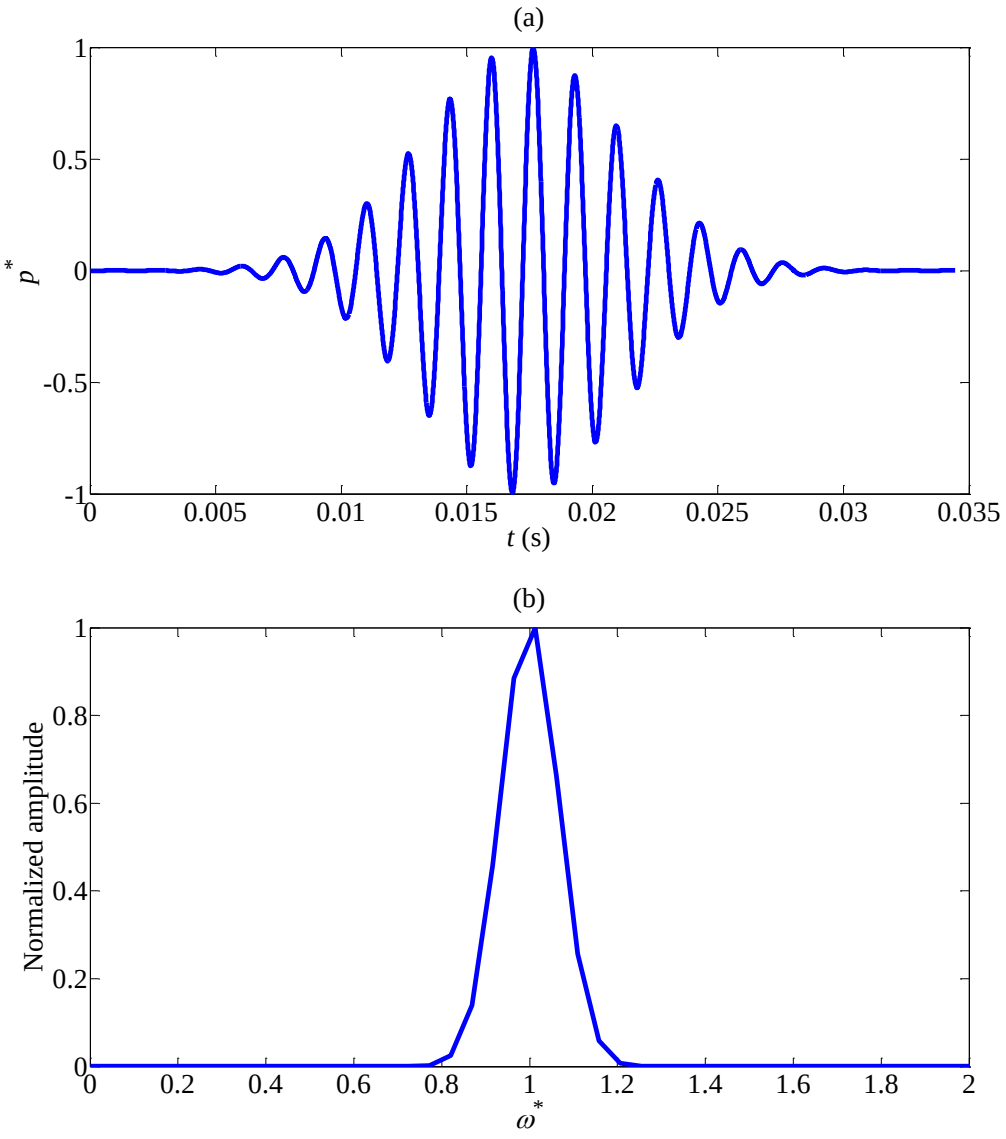

Fig. 7.9. Input pulse in the (a) time domain; and (b) frequency domain.

The incident wave generated at the downstream end and the transmitted wave measured by the upstream wave receiver are plotted in Fig. 7.10. The pressure p is normalized according to $(p - p_0)/\alpha p_0$ and plotted as p^* in the y-axis.

As shown in Fig. 7.10(a), a considerable portion of the energy carried by the incident wave cannot be transmitted to the upstream wave receiver. The energy losses can be attributed to two main sources: (i) the friction occur in the pipe; and (ii) the reflection from the non-uniform blockage. The time domain signals in Fig. 7.10(a) are further transformed into the frequency domain in Fig. 7.10(b). The frequency is normalized by the fundamental frequency of the non-uniform blockage $2\pi\left(\bar{a}_b / 2l_3\right)$ (Che et al., 2019c) and plotted as ω^*. Fig. 7.10(b) indicates that the normalized central frequency $\omega_c{}^*$ of the incident wave is 0.5. According to the theoretical energy transmission coefficient T_C curve (i.e., the solid curve) in Fig. 7.11, at ω^* = 0.5, the percentage of the energy transmitted through the non-uniform blockage is relatively low. This is one reason for the considerable portion of energy losses observed in the time domain. Based on Eq. 7.10 (Che et al., 2019c), the transmission coefficient of the numerical CFD results equals to 0.60, which means only 60% of the energy carried by the incident wave is transmitted to the upstream receiver.

$$T_C = \left| \frac{M_{tr}}{M_{in}} \right|^2 \tag{7.10}$$

where M_{tr} = amplitude of the transmitted wave in the frequency domain; and M_{in} = amplitude of the incident wave in the frequency domain.

As shown in Fig. 7.11, two more points (i.e., at $\omega_c{}^*$ = 0.8, and 1.0) on the energy transmission coefficient T_C curve are further illustrated and analyzed in detail. Fig. 7.10 indicates that as the central frequency of the incident wave $\omega_c{}^*$ grows from 0.5 to 1.0, the amplitude of the transmitted wave gradually increases, which means more energy carried by the incident wave is transmitted through the non-uniform blockages. This growing trend can be explained by Bragg's law in Chapter 5 (Che et al., 2019c). As shown in Fig. 7.7, at most incident frequencies, the reflected waves from the continuous constriction (i.e., between Junctions C and D) and the continuous expansion (i.e., between Junctions B and C) would not experience constructive interference, because these reflected waves

would be out of phase, cancelling part of the energy out. However, when the incident wave frequency equals to the minimum destructive interference frequency of the non-uniform blockages (i.e., at $\omega_c^* = 1.0$), the reflected waves would be completely out of phase, cancelling each other out (i.e., minimum reflection). In this situation, the incident wave has the maximum transmission. Theoretically, at $\omega_c^* = 1$, all the energy carried by the incident wave should be transmitted to the wave receiver, but the calculated energy transmission coefficient T_C from the numerical CFD results is 0.91. This is because of the frictionless pipe system adopted in the derivation of the theoretical energy transmission coefficient in Eq. (7.7).

In addition, more points on the theoretical energy transmission coefficient T_C curve are tested by the CFD model and the calculated T_C is plotted in Fig. 7.11. It is observed in Fig. 7.11, the T_C at $\omega_c^* = 1.5$ is apparently higher than that at $\omega_c^* = 0.5$. This is because the impedance of non-uniform blockages is frequency dependent, which becomes smaller for higher frequency incident waves. This means non-uniform blockages have a less blocking effect on the propagation of high frequency incident waves (Che et al., 2019c). Fig. 7.11 also indicates that the theoretical T_C may overestimate the energy transmitted through the non-uniform blockages. These discrepancies between the theoretical and numerical T_C can be attributed to the energy dissipation caused by friction as the wave travels in the pipe system. However, the overall pattern of the numerical T_C agrees well with the theoretical T_C, which confirms the validity of the physical interpretations of the non-uniform blockage induced resonant frequency shift pattern in Chapter 5 (Che et al., 2019c).

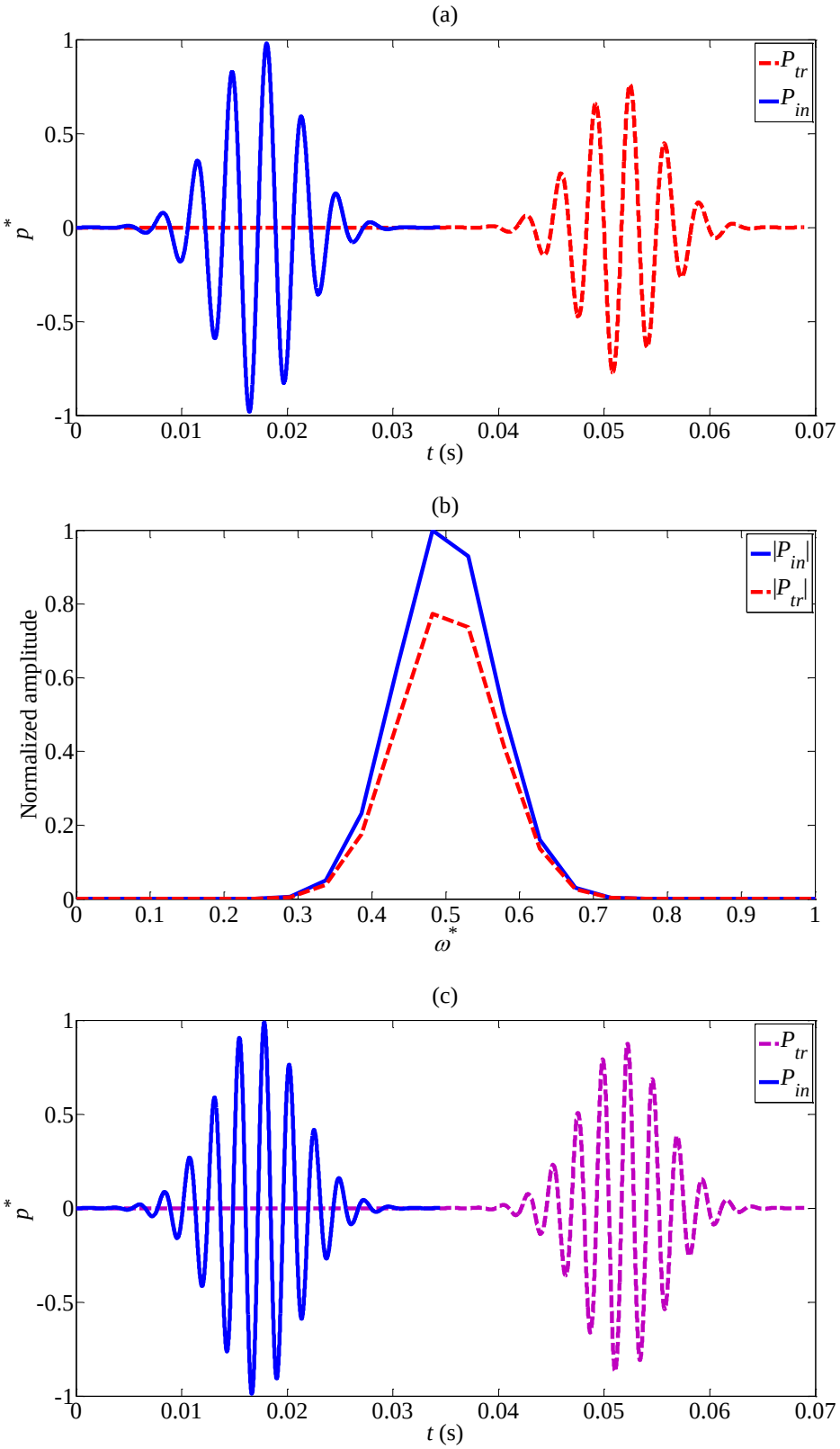

Fig. 7.10. (Part 1) Measured pressure signals in the time domain at (a) $\omega_c^* = 0.5$, (c) $\omega_c^* = 0.8$, (e) $\omega_c^* = 1.0$; and corresponding pressure signals in the frequency domain at (b) $\omega_c^* = 0.5$, (d) $\omega_c^* = 0.8$, (f) $\omega_c^* = 1.0$.

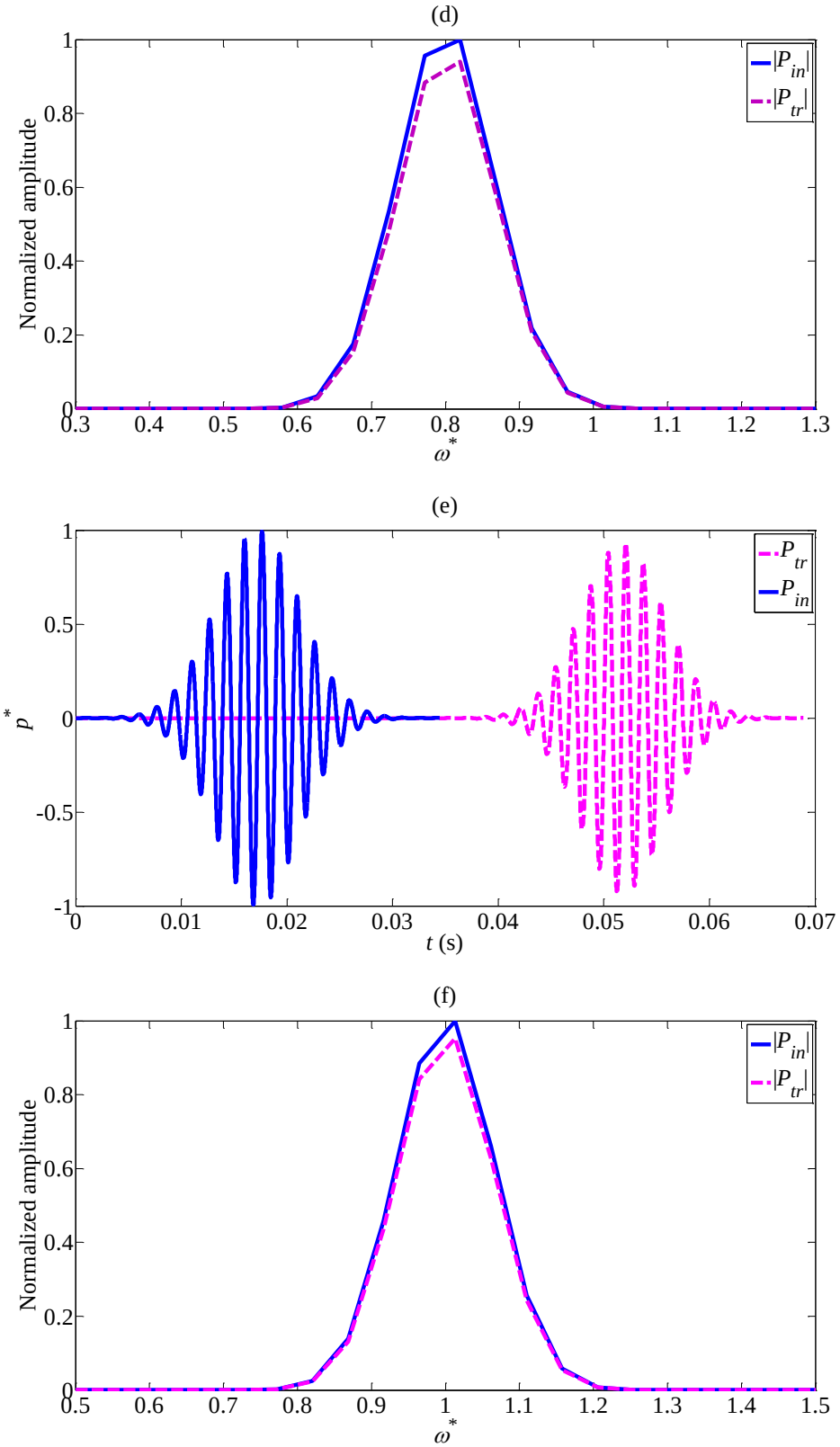

Fig. 7.10. (Part 2) Measured pressure signals in the time domain at (a) $\omega_c^* = 0.5$, (c) $\omega_c^* = 0.8$, (e) $\omega_c^* = 1.0$; and corresponding pressure signals in the frequency domain at (b) $\omega_c^* = 0.5$, (d) $\omega_c^* = 0.8$, (f) $\omega_c^* = 1.0$.

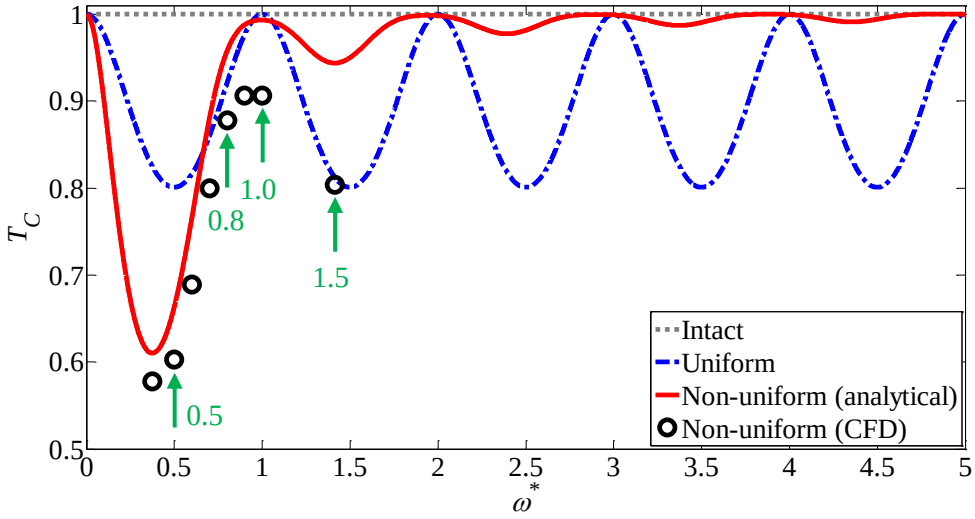

Fig. 7.11. Numerical validation of the theoretical energy transmission coefficient T_C.

7.4.2 Resonant Frequency Shift Pattern Induced by Non-uniform Blockages in Bounded Pipe Systems

To validate the derived resonant frequency shift induced by non-uniform blockages in a bounded pipe system, as shown in Fig. 7.12, the full-2D CFD model is applied into an RPV system. Non-uniform blockages in the RPV system is represented by stainless steel pipe sections with linearly varying diameters. More detailed parameters of the RPV pipe system are listed in Table 7.4.

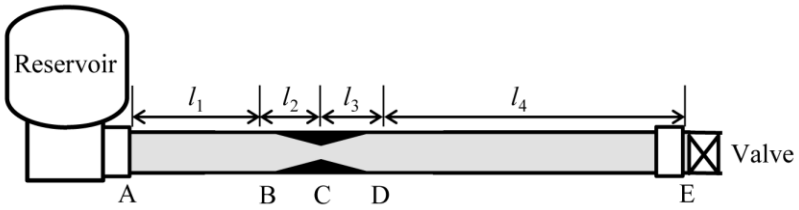

Fig. 7.12. Reservoir-pipe-valve (RPV) system with non-uniform blockages.

Table. 7.4. Parameters of the reservoir-pipe-valve (RPV) system.

Pipe system	l_1 (m)	l_2 (m)	l_3 (m)	l_4 (m)	R (m)	R_C (m)	a_0 (m/s)	$\bar{a}_b$ (m/s)
bounded	12.6	4.2	4.2	21	0.0362	0.02172	1218.86	1262.95

Initially, the downstream valve is kept fully closed to form a static flow in the pipe. Transients are introduced into the pipe system by a “closure-open-closure” operation

(UDFs) on the downstream valve (i.e., a discharge pulse) as illustrated in Fig. 7.13. The time domain pressure response is measured at the downstream valve and plotted in Fig. 7.14.

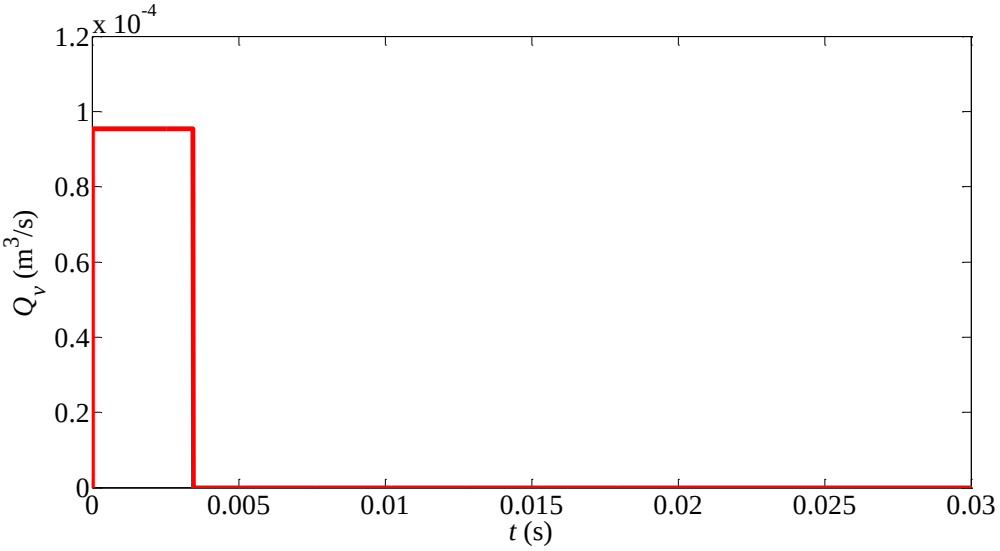

Fig. 7.13. Discharge variation given at the downstream valve.

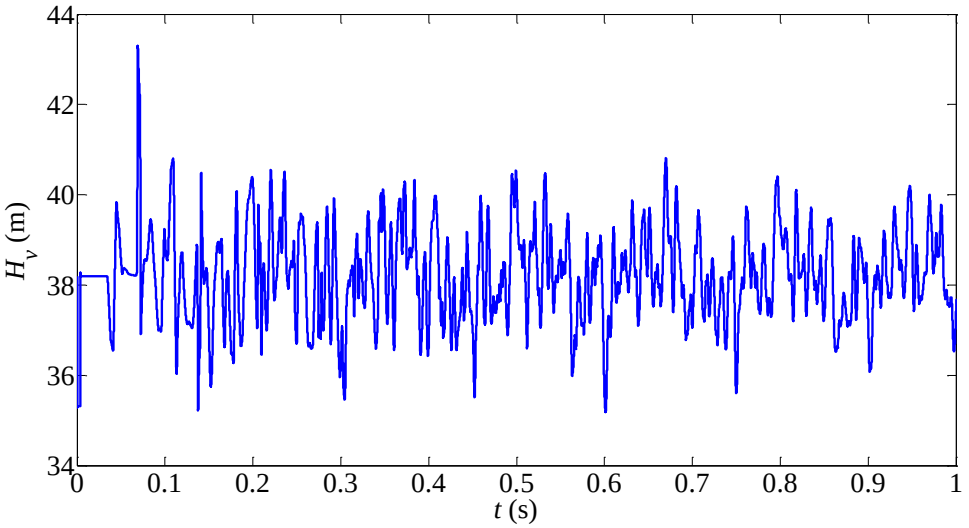

Fig. 7.14. Pressure time history measured at the downstream valve.

Based on the measured discharge (i.e., input) and pressure (i.e., output) variations at the downstream valve, the frequency response function (FRF) (see Section 2.3.2) of the pipe system is calculated according to Eq. (7.11) (Lee et al., 2006b) and plotted in Fig. 7.15.

$$FRF(\omega) = \frac{S_{xy}(\omega)}{S_{xx}(\omega)} \tag{7.11}$$

where $FRF(\omega)$ = frequency response function; $S_{xy}(\omega)$ = Fourier transform of the cross-correlation between the input (x) and the output (y); and $S_{xx}(\omega)$ = Fourier transform of the autocorrelation of the input.

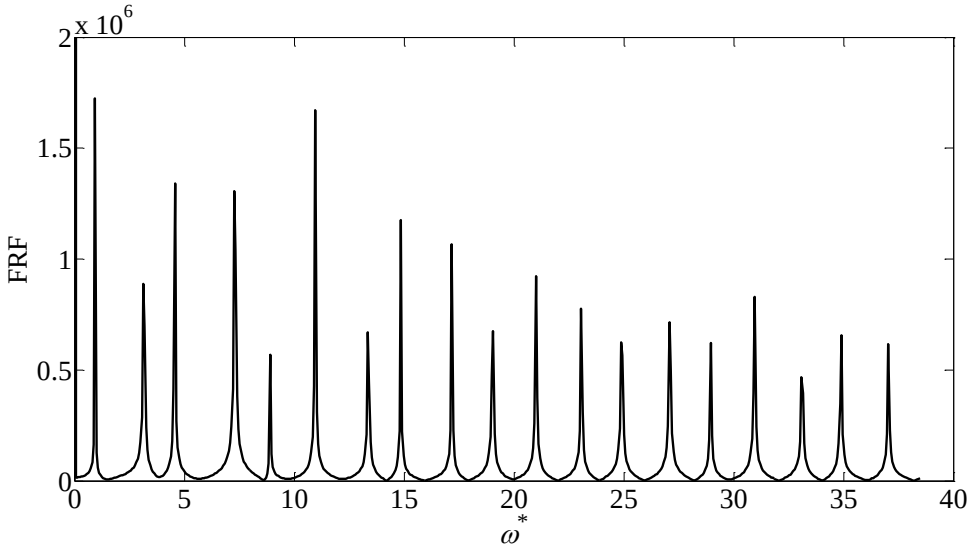

Fig. 7.15. Frequency response function of the blocked pipe system.

As shown in Fig. 7.15, the presence of non-uniform blockages induces evident frequency shifts on the resonant peaks of the FRF. To confirm the validity of the derived resonant frequency shift induced by non-uniform blockages in Chapter 4 (Che et al., 2018b), the frequency shifts $\Delta\omega_m^*$ (see Eq. (7.12)) of the first 20 resonant peaks from both analytical and numerical CFD results are extracted and plotted in Fig. 7.16. The theoretical frequency shifts are obtained by the transfer matrix method (Che et al., 2018b), in which the transient wave speed used in the non-uniform blockage equals to its average wave speed $\bar{a}_b$.

$$\Delta\omega_m^* = \omega_{mb}^* - \omega_{mi}^* \tag{7.12}$$

where $\Delta\omega_m^*$ = frequency shift of the m-th resonant peak; ω_{mb}^* = frequency of the m-th resonant peak in the blocked pipe system; and ω_{mi}^* = frequency of the m-th resonant peak in the intact pipe system.

It is observed in Fig. 7.16 that the frequency shift induced by non-uniform blockages in water pipes becomes less evident for higher harmonics. This is because the impedance of the non-uniform blockage is frequency dependent, which becomes smaller for higher frequency incident waves (Che et al., 2019c). That means non-uniform blockages have a less blocking effect on the propagation of higher frequency incident waves; thus, the frequency shifts induced by non-uniform blockages become less evident. In addition, the resonant frequency shifts from both analytical and numerical CFD results show good agreement. This confirms the validity of the theoretical resonant frequency shifts induced by non-uniform blockages in bounded pipe systems in Chapter 4 (Che et al., 2018b).

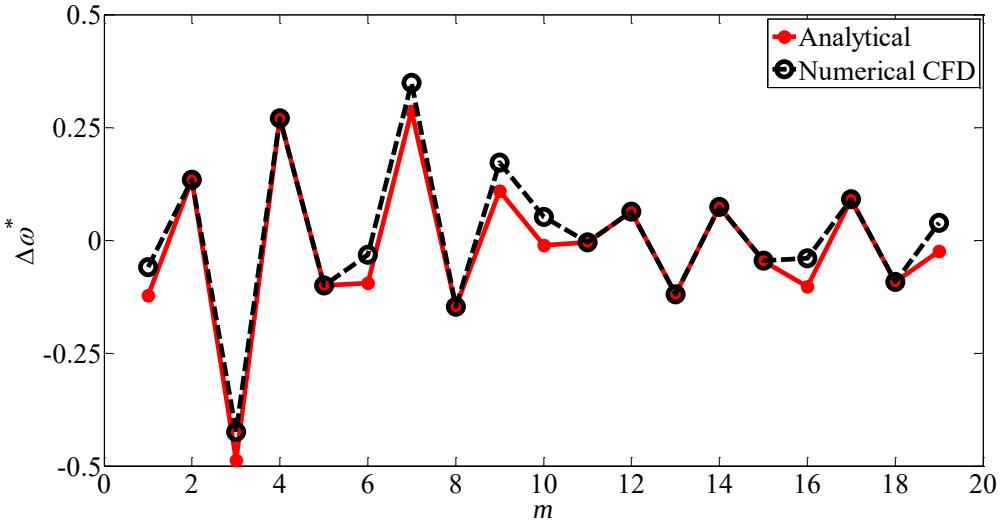

Fig. 7.16. Frequency shifts of analytical and numerical CFD results.

7.5 Summary

This chapter validates the theory developed in Chapters 4 and 5 by a 2D CFD model. First, transients are introduced into the bounded pipe system (i.e., an RPV system) by suddenly and completely closing the downstream valve to stop the initial steady flow. The pressure responses are measured at both the downstream valve and the mid-length of the pipe, which are used to validate the CFD model by comparing with the results obtained from the well-established Zielke's 1D analytical model. Afterwards, the 2D CFD model is applied to bounded and unbounded pipe systems to confirm the validity of the theory developed in Chapters 4 and 5, where various transient excitation techniques are adopted, such as a square pulse in the bounded pipe system and a Gaussian-modulated sinusoidal pulse in the unbounded pipe system.

The obtained results indicate that (i) the agreement of the frequency shifts induced by non-uniform blockages in bounded pipe systems between theoretical and numerical CFD results is good; and (ii) although discrepancies in the energy transmission coefficient T_C exist between theoretical and numerical results because of friction, the overall pattern of the T_C calculated from the numerical CFD results agrees well with the theoretical T_C pattern, which confirms of the validity of two physical mechanisms govern the overall pattern of T_C curve.

CHAPTER 8 CONCLUSIONS AND RECOMMENDATIONS FOR FUTURE WORK

8.1 Conclusions

The major aim of this thesis is to deepen an understanding of transient wave behavior in water pipes with non-uniform blockages, which is necessary to enhance the practical applications of the transient-based method for real blockage detection. The transient wave behavior in water pipes with non-uniform blockages is investigated in both the time and frequency domains by the combined methodology of theoretical analysis and numerical simulation.

First, to understand the fundamental physics and mechanism of the interaction between transient waves and non-uniform blockages, the transient wave behavior in various (e.g., linear and exponential) non-uniform blockages is obtained by analytically solving the one-dimensional (1D) wave equation under specific initial and boundary conditions. The obtained wave solutions are incorporated into the 1D overall transfer matrix of a reservoir-pipe-valve (RPV) system (i.e., a bounded pipe system) with non-uniform blockages, which is used to systematically investigate the influences of non-uniform blockage shape, severity, and length on transient frequency responses. It is found that the resonant frequency shifts induced by non-uniform blockages have very different patterns from that of uniform blockages. Specifically, the resonant frequency shifts induced by non-uniform blockages become less evident for higher harmonics (termed as the non-uniform blockage induced frequency shift pattern).

Second, the physical mechanism of this observed non-uniform blockage induced frequency shift pattern is clarified from an energy perspective. For this purpose, the

energy transmission coefficient through various blockages in an unbounded pipe system is analytically derived based on the overall transfer matrix of the pipe system. With this derived result, the influences of non-uniform blockage properties on the energy transmission are investigated systematically. The results indicate that the impedance of non-uniform blockages is highly frequency dependent, which becomes smaller for higher frequency incident waves. This means non-uniform blockages have a less blocking effect on the propagation of higher frequency incident waves; thus, the frequency shifts induced by non-uniform blockages become less evident.

Afterwards, the frequency range of validity of the developed theory in previous chapters is investigated numerically by the full-2D water hammer model. The inefficiency of the current numerical scheme for the full-2D model is first addressed. The modified efficient scheme is used to study the generation mechanism and components of the radial pressure waves, caused by different valve operations, in transient laminar pipe flows. The results indicate that the existence of radial pressure gradients is the driving force of the formation of radial flux and radial pressure waves. In addition, to satisfy the developed theory in previous chapters, the incident wave frequency must be lower than the cut-off frequency of the radial mode 1 (M1).

Finally, a 2D computational fluid dynamics (CFD) model is used to numerically validate the theory developed in previous chapters under more realistic and complex conditions. The 2D axisymmetric Navier-Stokes equations in a cylindrical coordinate system are solved by the semi-implicit method for pressure linked equations (SIMPLE) algorithm. Various boundary conditions (e.g., pipe wall elasticity and different transient excitation operations) are included into the CFD model by user-defined functions (UDFs). The CFD results confirm: (i) the theoretical resonant frequency shifts induced by non-uniform blockages in bounded pipe systems; and (ii) the theoretical energy transmission coefficient through non-uniform blockages in unbounded pipe systems and the physical mechanisms behind it.

The physical understanding gained in this thesis may contribute to narrow the gap between transient-based theory and practical applications of non-uniform blockage detection, which is crucial and necessary for developing smart urban water supply systems.

8.2 Recommendations for Future Work

Several potential research directions recommended for future work are listed as follows.

1. This thesis mainly focuses on the transient wave behavior in water pipes with a single non-uniform blockage, but multiple non-uniform blockages may exist in real water pipes. Therefore, further studies of the transient wave behavior in water pipes with multiple non-uniform blockages are needed.

2. Due to the difficulty of constructing perfectly linear/exponential non-uniform blockages in laboratories, the validation of the theory developed in this thesis is mainly based on numerical experiments. In future work, laboratory experiments are needed to further confirm the validity of the developed theory.

3. Currently, nearly all of transient-based techniques for pipe anomaly detection are based on the plane wave theory. In this thesis, the behavior of radial pressure waves is only investigated in the intact section of water pipes. The behavior of radial pressure waves in non-uniform blockages needs further research.

4. The 1D/2D numerical simulation in this thesis only considers inviscid or viscous but laminar pipe flows. But turbulent flows often exist in real water pipes, where the influence of turbulence on the transient wave behavior need to be investigated.

5. Although this thesis takes a step towards understanding the transient wave behavior in water pipes with real blockages, the shape of the investigated blockages is relatively simple and regular (i.e., symmetric in both the radial and axial directions). The influence

of more complicated and irregular blockages (e.g., asymmetric blockages in both the axial and radial directions) on the transient wave behavior should be further investigated.

6. Based on the physical understanding gained in this thesis, it is important and necessary to extend the current transient-based method for non-uniform blockage detection in future work.

APPENDICES

Appendix A1 - Detailed Derivation Procedure of the Wave Equation for a Pipe with a Slowly Varying Cross-sectional Area

The classical one-dimensional (1D) water hammer model for a pipe with slowly varying cross-sectional area excluding frictional and viscoelastic effects

$$\frac{\partial(\rho A)}{\partial t}+\frac{\partial(\rho UA)}{\partial x}=0 \tag{A.1}$$

$$\frac{\partial(\rho UA)}{\partial t}+A\frac{\partial P}{\partial x}=0 \tag{A.2}$$

where ρ = density of water; U = average velocity; P = pressure; A = varying pipe cross-sectional area; x = distance along axial direction; and t = time.

The equation of state

$$\frac{1}{a^2}=\frac{1}{A}\frac{d(\rho A)}{dP} \tag{A.3}$$

where a = wave speed.

Substitute Eq. (A.3) into Eq. (A.1), then Eqs. (A.1) and (A.2) become (note that the compressibility of water and pipe wall has been put into the wave speed a, thus density ρ can be written as ρ_0)

$$\frac{A}{a^2}\frac{\partial P}{\partial t}+\rho_0\frac{\partial Q}{\partial x}=0 \tag{A.4}$$

$$\rho_0\frac{\partial Q}{\partial t}+A\frac{\partial P}{\partial x}=0 \tag{A.5}$$

where ρ_0 = average density of water; and Q = flowrate.

Differentiate Eq. (A.4) by t and Eq. (A.5) by x, and add them together, resulting the wave equation for a pipe with slowly varying cross-sectional area

$$A\frac{\partial^2 P}{\partial t^2} = a^2 \frac{\partial}{\partial x}\left(A\frac{\partial P}{\partial x} \right) \tag{A.6}$$

Appendix A2 - Detailed Derivation Procedure of the Energy Transmission Coefficient

As shown in Fig. 5.2, at the upstream and downstream boundaries of the pipe system (i.e., locations A and E), the energy flow (i.e., power) passing through a unit cross-sectional area (termed as power intensity) is defined as (Blackstock, 2000)

$$I = \frac{1}{T}\int_0^T p^* u^* dt \tag{A.7}$$

where I = power intensity; $T = 2\pi/\omega$ for time-harmonic waves; p^* = pressure deviation from the mean in the time domain; u^* = axial velocity deviation from the mean in the time domain; and t = time.

In classical acoustics, including water hammer problems focused on herein, it is often assumed that p^* and u^* are time-harmonic waves (Chaudhry, 2014; Che et al., 2018b)

$$p^* = pe^{i\omega t},\ u^* = ue^{i\omega t} \tag{A.8}$$

where p and u are complex amplitude. Specifically, let $u = |u|e^{i\theta}$, where $|u|$ = amplitude; and θ = phase.

In the transient pipe flow analysis, the specific impedance is usually used for describing the transient wave propagation characteristics in specified pipes, which is defined as

$$Z_{\mathrm{sp}} = \frac{p^*}{u^*} = \frac{p}{u} = \mathrm{Re}\left(Z_{\mathrm{sp}}\right) + i\,\mathrm{Im}\left(Z_{\mathrm{sp}}\right) = \left|Z_{\mathrm{sp}}\right| e^{i\phi} \tag{A.9}$$

where Z_{sp} = specific impedance; "Re" = real part; "Im" = imaginary part; Re(Z_{sp}) = resistance; Im(Z_{sp}) = reactance; and ϕ = phase angle between p^* and u^*. Substituting Eq. (A.9) into Eq. (A.7), it becomes

$$\begin{aligned} I &= \frac{\omega}{2\pi}\int_0^{2\pi/\omega} \mathrm{Re}\left(Z_{sp}u^*\right)\mathrm{Re}\left(u^*\right)dt \\ &= \frac{\omega}{2\pi}\int_0^{2\pi/\omega} \left|Z_{sp}\right|\left|u\right|^2 \cos\left(\omega t+\theta+\phi\right)\cos\left(\omega t+\theta\right)dt \\ &= \frac{1}{2}\left|u\right|^2\left|Z_{sp}\right|\cos\phi \\ &= \frac{1}{2}\left|u\right|^2 \mathrm{Re}\left(Z_{sp}\right) \end{aligned} \tag{A.10}$$

As shown in Fig. 5.2, for the upstream (i.e., location A) and downstream (i.e., location E) boundaries with a cross-sectional area S_0, the energy flow passing through this area is

$$W = IS_0 = \frac{1}{2}\left|u\right|^2 \mathrm{Re}\left(Z_{sp}\right)S_0 \tag{A.11}$$

where W = energy flow; and S_0 = the pipe cross-sectional area of intact junctions.

The energy transmission coefficient T_C of a blocked pipe system with anechoic boundaries (i.e., located at A and E), as shown in Fig. 5.2, is defined as the ratio between the energy flow transmitted through the non-uniform blockage (W_{tr}) and that incident on the blockage (W_{in}).

$$T_C = \frac{W_{tr}}{W_{in}} \tag{A.12}$$

The general solutions of p for the one-dimensional (1D) wave equation in intact Pipe 1 and Pipe 4, as shown in Fig. 5.2, are (Duan et al., 2014)

$$p = Me^{-ik_0x} + Ne^{ik_0x} \tag{A.13}$$

where M and N are amplitude of the incident and reflected waves, respectively.

Substituting Eq. (A.13) into the frictionless 1D water hammer model, the following general solutions of u can be obtained

$$u = \frac{1}{\rho_0 a_0}\left(Me^{-ik_0 x} - Ne^{ik_0 x}\right) \tag{A.14}$$

where ρ_0 = fluid density. The energy flow generated at the downstream boundary (i.e., located at E) is

$$W_{in} = \frac{1}{2\rho_0 a_0}\left|M_{\mathrm{E}}\right|^2 \mathrm{Re}\left(Z_{\mathrm{sp}}\right) S_0 = \frac{\left|M_{\mathrm{E}}\right|^2}{2} S_0 \tag{A.15}$$

where M_{E} = amplitude of the incident wave generated at the downstream boundary (i.e., located at E).

Similarly, the energy flow transmitted through the non-uniform blockages (i.e., measured at A) is

$$W_{tr} = \frac{1}{2\rho_0 a_0}\left|M_{\mathrm{A}}\right|^2 \mathrm{Re}\left(Z_{\mathrm{sp}}\right) S_0 = \frac{\left|M_{\mathrm{A}}\right|^2}{2} S_0 \tag{A.16}$$

where M_{A} = amplitude of the transmitted wave received at the upstream boundary (i.e., located at A).

Therefore, the energy transmission coefficient T_C of the unbounded blocked system in Fig. 5.2 is

$$T_C = \frac{W_{tr}}{W_{in}} = \left|\frac{M_{\mathrm{A}}}{M_{\mathrm{E}}}\right|^2 \tag{A.17}$$

The amplitude of a progressive wave keeps constant as it travels along a uniform pipe section (Munjal, 2014). Therefore, as shown in Fig. 5.2, M_{A} and M_{E} can be measured at any point along Pipe 1 and Pipe 4, respectively. To simplify the calculation, pipe lengths l_1 and l_4 can be taken as zero if necessary.

The overall transfer matrix (in terms of u and p) of a blocked pipe system, as shown in Fig. 5.2, is

$$\begin{Bmatrix} u \\ p \end{Bmatrix}_{\mathrm{D}} = \begin{bmatrix} V_{11}^* & V_{12}^* \\ V_{21}^* & V_{22}^* \end{bmatrix} \begin{Bmatrix} u \\ p \end{Bmatrix}_{\mathrm{A}} \tag{A.18}$$

where V_{ij}^* = elements of the overall transfer matrix (in terms of u and p).

Based on the general solutions in Eqs. (A.13) and (A.14), the p and u at two locations A and D can be expressed as (note that $N_A = 0$)

$$p_A = M_A + N_A = M_A \tag{A.19a}$$

$$u_A = \frac{1}{\rho_0 a_0}\left(M_A - N_A\right) = \frac{M_A}{\rho_0 a_0} \tag{A.19b}$$

$$p_D = M_E + N_E \tag{A.19c}$$

$$u_D = \frac{1}{\rho_0 a_0}\left(M_E - N_E\right) \tag{A.19d}$$

From Eqs. (A.19a) to (A.19d)

$$\begin{aligned} M_E &= \frac{p_D + \rho_0 a_0 u_D}{2} = \frac{\left(V_{21}^* u_A + V_{22}^* p_A\right) + \rho_0 a_0 \left(V_{11}^* u_A + V_{12}^* p_A\right)}{2} \\ &= \frac{\left(V_{21}^* \dfrac{M_A}{\rho_0 a_0} + V_{22}^* M_A\right) + \rho_0 a_0 \left(V_{11}^* \dfrac{M_A}{\rho_0 a_0} + V_{12}^* M_A\right)}{2} \end{aligned} \tag{A.20}$$

The ratio between M_A and M_E is

$$\frac{M_A}{M_E} = \frac{2}{\dfrac{V_{21}^*}{\rho_0 a_0} + V_{22}^* + V_{11}^* + \rho_0 a_0 V_{12}^*} \tag{A.21}$$

Therefore, the energy transmission coefficient T_C can be represented by the overall transfer matrix elements V_{ij}^* (in terms of u and p)

$$T_C = \left|\frac{M_A}{M_E}\right|^2 = \left|\frac{2}{\dfrac{V_{21}^*}{\rho_0 a_0} + V_{22}^* + V_{11}^* + \rho_0 a_0 V_{12}^*}\right|^2 \tag{A.22}$$

In terms of discharge q and pressure head h, the overall transfer matrix of the unbounded pipe system in Fig. 5.2 is

$$\begin{Bmatrix} q \\ h \end{Bmatrix}_D = \begin{bmatrix} U_{11}^* & U_{12}^* \\ U_{21}^* & U_{22}^* \end{bmatrix} \begin{Bmatrix} q \\ h \end{Bmatrix}_A \tag{A.23}$$

Writing Eq. (A.23) in the equation form

$$S_{\mathrm{D}}u_{\mathrm{D}} = U_{11}^{*}S_{\mathrm{A}}u_{\mathrm{A}} + U_{12}^{*}\frac{p_{\mathrm{A}}}{\rho_0 g} \tag{A.24a}$$

$$\frac{p_{\mathrm{D}}}{\rho_0 g} = U_{21}^{*}S_{\mathrm{A}}u_{\mathrm{A}} + U_{22}^{*}\frac{p_{\mathrm{A}}}{\rho_0 g} \tag{A.24b}$$

where S_{A} and S_{D} are the pipe cross-sectional areas at two boundaries A and D in Fig. 5.2, respectively.

Rewrite Eqs. (A.24) as

$$u_{\mathrm{D}} = \underbrace{\frac{S_{\mathrm{A}}}{S_{\mathrm{D}}}U_{11}^{*}}_{V_{11}^{*}}u_{\mathrm{A}} + \underbrace{\frac{U_{12}^{*}}{\rho_0 g S_{\mathrm{D}}}}_{V_{12}^{*}}p_{\mathrm{A}} \tag{A.25a}$$

$$p_{\mathrm{D}} = \underbrace{\rho_0 g S_{\mathrm{A}}U_{21}^{*}}_{V_{21}^{*}}u_{\mathrm{A}} + \underbrace{U_{22}^{*}}_{V_{22}^{*}}p_{\mathrm{A}} \tag{A.25b}$$

in which $S_{\mathrm{A}} = S_{\mathrm{D}} = S_0$. Therefore, the energy transmission coefficient T_C can be represented by overall transfer matrix elements U_{ij}^{*} (in terms of q and h)

$$T_C = \left| \frac{2}{\frac{gS_0U_{21}^{*}}{a_0} + U_{22}^{*} + U_{11}^{*} + \frac{a_0U_{12}^{*}}{gS_0}} \right|^2 \tag{A.26}$$

REFERENCES

Adamkowski, A., & Lewandowski, M. (2006). Experimental examination of unsteady friction models for transient pipe flow simulation. *Journal of Fluids Engineering, 128*(6), 1351-1363. doi:10.1115/1.2354521

Al-Khomairi, A. (2008). Leak detection in long pipelines using the least squares method. *Journal of Hydraulic Research, 46*(3), 392-401. doi:10.3826/jhr.2008.3191

AWWA. (1979). Leak detection: a money-saving expense. *Journal - American Water Works Association, 71*(2), 51. doi:10.1002/j.1551-8833.1979.tb04297.x

AWWA. (2001). *Dawn of the replacement era: reinvesting in drinking water infrastructure*. Retrieved from

AWWA. (2012). *Buried no longer: confronting America's water infrastructure challenge*. Retrieved from

Beck, S. B. M., Curren, M. D., Sims, N. D., & Stanway, R. (2005). Pipeline network features and leak detection by cross-correlation analysis of reflected waves. *Journal of Hydraulic Engineering, 131*(8), 715-723. doi:10.1061/(ASCE)0733-9429(2005)131:8(715)

Bergant, A., Simpson, A. R., & Vítkovský, J. P. (2001). Developments in unsteady pipe flow friction modelling. *Journal of Hydraulic Research, 39*(3), 249-257. doi:10.1080/00221680109499828

Blackstock, D. T. (2000). *Fundamentals of physical acoustics*: John Wiley & Sons.

Bragg, W. H., & Bragg, W. L. (1913). The reflection of X-rays by crystals. *Proceedings of the Royal Society A, 88*(605), 428-438. doi:10.1098/rspa.1913.0040

Brunone, B. (1999). Transient test-based technique for leak detection in outfall pipes. *Journal of Water Resources Planning and Management, 125*(5), 302-306. doi:10.1061/(ASCE)0733-9496(1999)125:5(302)

Brunone, B., & Ferrante, M. (2004). Pressure waves as a tool for leak detection in closed conduits. *Urban Water Journal, 1*(2), 145-155. doi:10.1080/1573062042000271073

Brunone, B., Ferrante, M., & Meniconi, S. (2008a). Discussion of "Detection of partial blockage in single pipelines" by P. K. Mohapatra, M. H. Chaudhry, A. A. Kassem, and J. Moloo. *Journal of Hydraulic Engineering, 134*(6), 872-874. doi:10.1061/(ASCE)0733-9429(2008)134:6(872)

Brunone, B., Ferrante, M., & Meniconi, S. (2008b). Portable pressure wave‐maker for leak detection and pipe system characterization. *Journal‐American Water Works Association, 100*(4), 108-116. doi:10.1002/j.1551-8833.2008.tb09607.x

Cao, X. Q., & Ruan, C. M. (2017). Compilation of investigation on water loss rate of water supply pipelines in global major cities. *Water Purification Technology, 36*(4), 6-14. doi:10.15890/j.cnki.jsjs.2017.04.002

Capponi, C., & Ferrante, M. (2017). Numerical investigation of pipe length determination in branched systems by transient tests. *Water Science and Technology: Water Supply*, *18*(3), 1062-1071. doi:10.2166/ws.2017.180

Capponi, C., Ferrante, M., Zecchin, A. C., & Gong, J. (2017). Leak detection in a branched system by inverse transient analysis with the admittance matrix method. *Water Resources Management, 31*(13), 4075-4089. doi:10.1007/s11269-017-1730-6

Çengel, Y. A., & Cimbala, J. M. (2006). *Fluid mechanics: fundamentals and applications*. Boston: McGraw-Hill Higher Education.

Chaudhry, M. H. (2014). *Applied hydraulic transients*. New York: Springer-Verlag.

Che, T. C., Duan, H. F., Lee, P. J., & Ghidaoui, M. S. (2017). *Theoretical analysis of the influence of blockage irregularities on transient waves in water supply pipelines*. Paper presented at the 37th IAHR World Congress, Kuala Lumpur, Malaysia.

Che, T. C., Duan, H. F., Lee, P. J., & Karney, B. W. (2019a). Transient-based methods for anomaly detection in pressurized water pipes: a review. *Applied Mechanics Reviews*, to be submitted.

Che, T. C., Duan, H. F., Lee, P. J., Meniconi, S., Pan, B., & Brunone, B. (2018a). Radial pressure wave behavior in transient laminar pipe flows under different flow perturbations. *Journal of Fluids Engineering, 140*(10), 101203. doi:10.1115/1.4039711

Che, T. C., Duan, H. F., Lee, P. J., Pan, B., & Ghidaoui, M. S. (2018b). Transient frequency responses for pressurized water pipelines containing blockages with linearly varying diameters. *Journal of Hydraulic Engineering, 144*(8), 04018054. doi:10.1061/(ASCE)HY.1943-7900.0001499

Che, T. C., Duan, H. F., Pan, B., Lee, P. J., & Ghidaoui, M. S. (2019b). 2D numerical study of the non-uniform blockage effect on transient waves in pressurized water pipes. *Computers & Fluids*, to be submitted.

Che, T. C., Duan, H. F., Pan, B., Lee, P. J., & Ghidaoui, M. S. (2019c). Energy analysis of the resonant frequency shift pattern induced by non-uniform blockages in pressurized water pipes. *Journal of Hydraulic Engineering, 145*(7), 04019027. doi:10.1061/(ASCE)HY.1943-7900.0001607

Che, T. C., Duan, H. F., Zheng, F., Pan, B., & Lee, P. J. (2018c). *Energy analysis of transient frequency shift pattern induced by non-uniform blockages in water pipelines*. Paper presented at the 1st International WDSA/CCWI Joint Conference, Kingston, Ontario, Canada.

Covas, D., & Ramos, H. (2010). Case studies of leak detection and location in water pipe systems by inverse transient analysis. *Journal of Water Resources Planning and Management, 136*(2), 248-257. doi:10.1061/(ASCE)0733-9496(2010)136:2(248)

Covas, D., Ramos, H., & De Almeida, A. B. (2004). Discussion of "Detecting leaks in pressurised pipes by means of transients" by Bruno Brunone and Marco

Ferrante. *Journal of Hydraulic Research, 42*(1), 105-109. doi:10.1080/00221686.2004.9641189

Covas, D., Ramos, H., & De Almeida, A. B. (2005a). Standing wave difference method for leak detection in pipeline systems. *Journal of Hydraulic Engineering, 131*(12), 1106-1116. doi:10.1061/(ASCE)0733-9429(2005)131:12(1106)

Covas, D., Stoianov, I., Mano, J. F., Ramos, H., Graham, N., & Maksimovic, C. (2005b). The dynamic effect of pipe-wall viscoelasticity in hydraulic transients. Part II—Model development, calibration and verification. *Journal of Hydraulic Research, 43*(1), 56-70. doi:10.1080/00221680509500111

Datta, S., & Sarkar, S. (2016). A review on different pipeline fault detection methods. *Journal of Loss Prevention in the Process Industries, 41*(2016), 97-106. doi:10.1016/j.jlp.2016.03.010

Duan, H. F. (2016a). Sensitivity analysis of a transient-based frequency domain method for extended blockage detection in water pipeline systems. *Journal of Water Resources Planning and Management, 142*(4), 04015073. doi:10.1061/(ASCE)WR.1943-5452.0000625

Duan, H. F. (2016b). Transient frequency response based leak detection in water supply pipeline systems with branched and looped junctions. *Journal of Hydroinformatics, 19*(1), 17-30. doi:10.2166/hydro.2016.008

Duan, H. F. (2017). Transient wave scattering and its influence on transient analysis and leak detection in urban water supply systems: theoretical analysis and numerical validation. *Water, 9*(10), 789. doi:10.3390/w9100789

Duan, H. F., Che, T. C., Lee, P. J., & Ghidaoui, M. S. (2018). Influence of nonlinear turbulent friction on the system frequency response in transient pipe flow modelling and analysis. *Journal of Hydraulic Research, 56*(4), 451-463. doi:10.1080/00221686.2017.1399936

Duan, H. F., & Lee, P. J. (2016). Transient-based frequency domain method for dead-end side branch detection in reservoir pipeline-valve systems. *Journal of*

Hydraulic Engineering, 142(2), 04015042. doi:10.1061/(ASCE)HY.1943-7900.0001070

Duan, H. F., Lee, P. J., Che, T. C., Ghidaoui, M. S., Karney, B. W., & Kolyshkin, A. A. (2017). The influence of non-uniform blockages on transient wave behavior and blockage detection in pressurized water pipelines. *Journal of Hydro-environment Research, 17*(2017), 1-7. doi:10.1016/j.jher.2017.08.002

Duan, H. F., Lee, P. J., Ghidaoui, M. S., & Tuck, J. (2014). Transient wave-blockage interaction and extended blockage detection in elastic water pipelines. *Journal of fluids and structures, 46*(2014), 2-16. doi:10.1016/j.jfluidstructs.2013.12.002

Duan, H. F., Lee, P. J., Ghidaoui, M. S., & Tung, Y. K. (2010a). Essential system response information for transient-based leak detection methods. *Journal of Hydraulic Research, 48*(5), 650-657. doi:10.1080/00221686.2010.507014

Duan, H. F., Lee, P. J., Ghidaoui, M. S., & Tung, Y. K. (2011a). Leak detection in complex series pipelines by using the system frequency response method. *Journal of Hydraulic Research, 49*(2), 213-221. doi:10.1080/00221686.2011.553486

Duan, H. F., Lee, P. J., Ghidaoui, M. S., & Tung, Y. K. (2012a). Extended blockage detection in pipelines by using the system frequency response analysis. *Journal of Water Resources Planning and Management, 138*(1), 55-62. doi:10.1061/(ASCE)WR.1943-5452.0000145

Duan, H. F., Lee, P. J., Ghidaoui, M. S., & Tung, Y. K. (2012b). System response function–based leak detection in viscoelastic pipelines. *Journal of Hydraulic Engineering, 138*(2), 143-153. doi:10.1061/(ASCE)HY.1943-7900.0000495

Duan, H. F., Lee, P. J., Kashima, A., Lu, J. L., Ghidaoui, M. S., & Tung, Y. K. (2013). Extended blockage detection in pipes using the system frequency response: analytical analysis and experimental verification. *Journal of Hydraulic Engineering, 139*(7), 763-771. doi:10.1061/(ASCE)HY.1943-7900.0000736

Duan, H. F., Lu, J. L., Kolyshkin, A. A., & Ghidaoui, M. S. (2011b). *The effect of random inhomogeneities of pipe cross-sectional area on wave propagation.* Paper presented at the 34th IAHR Congress, Brisbane, Australia.

Duan, H. F., Tung, Y. K., & Ghidaoui, M. S. (2010b). Probabilistic analysis of transient design for water supply systems. *Journal of Water Resources Planning and Management, 136*(6), 678-687. doi:10.1061/(ASCE)WR.1943-5452.0000074

Evangelista, S., Leopardi, A., Pignatelli, R., & De Marinis, G. (2015). Hydraulic transients in viscoelastic branched pipelines. *Journal of Hydraulic Engineering, 141*(8), 04015016. doi:10.1061/(ASCE)HY.1943-7900.0001030

Ferrante, M., & Brunone, B. (2003a). Pipe system diagnosis and leak detection by unsteady-state tests. 1. Harmonic analysis. *Advances in Water Resources, 26*(1), 95-105. doi:10.1016/S0309-1708(02)00101-X

Ferrante, M., & Brunone, B. (2003b). Pipe system diagnosis and leak detection by unsteady-state tests. 2. Wavelet analysis. *Advances in Water Resources, 26*(1), 107-116. doi:10.1016/S0309-1708(02)00102-1

Ferrante, M., Brunone, B., & Meniconi, S. (2007). Wavelets for the analysis of transient pressure signals for leak detection. *Journal of Hydraulic Engineering, 133*(11), 1274-1282. doi:10.1061/(ASCE)0733-9429(2007)133:11(1274)

Ferrante, M., Brunone, B., & Meniconi, S. (2009a). Leak-edge detection. *Journal of Hydraulic Research, 47*(2), 233-241. doi:10.3826/jhr.2009.3220

Ferrante, M., Brunone, B., & Meniconi, S. (2009b). Leak detection in branched pipe systems coupling wavelet analysis and a Lagrangian model. *Journal of Water Supply: Research and Technology-AQUA, 58*(2), 95-106. doi:10.2166/aqua.2009.022

Ferrante, M., Brunone, B., Meniconi, S., Karney, B. W., & Massari, C. (2014). Leak size, detectability and test conditions in pressurized pipe systems. *Water Resources Management, 28*(13), 4583-4598. doi:10.1007/s11269-014-0752-6

Ferziger, J. H., & Peric, M. (2001). *Computational methods for fluid dynamics*: Springer.

Ghidaoui, M. S. (2004). On the fundamental equations of water hammer. *Urban Water Journal, 1*(2), 71-83. doi:10.1080/15730620412331290001

Ghidaoui, M. S., Zhao, M., McInnis, D. A., & Axworthy, D. H. (2005). A review of water hammer theory and practice. *Applied Mechanics Reviews, 58*(1), 49-76. doi:10.1115/1.1828050

Gong, J., Lambert, M. F., Nguyen, S. T. N., Zecchin, A. C., & Simpson, A. R. (2018). Detecting thinner-walled pipe sections using a spark transient pressure wave generator. *Journal of Hydraulic Engineering, 144*(2), 06017027. doi:10.1061/(ASCE)HY.1943-7900.0001409

Gong, J., Lambert, M. F., Simpson, A. R., & Zecchin, A. C. (2013a). Single-event leak detection in pipeline using first three resonant responses. *Journal of Hydraulic Engineering, 139*(6), 645-655. doi:10.1061/(ASCE)HY.1943-7900.0000720

Gong, J., Lambert, M. F., Simpson, A. R., & Zecchin, A. C. (2014a). Detection of localized deterioration distributed along single pipelines by reconstructive MOC analysis. *Journal of Hydraulic Engineering, 140*(2), 190-198. doi:10.1061/(ASCE)HY.1943-7900.0000806

Gong, J., Lambert, M. F., Zecchin, A. C., & Simpson, A. R. (2016). Experimental verification of pipeline frequency response extraction and leak detection using the inverse repeat signal. *Journal of Hydraulic Research, 54*(2), 210-219. doi:10.1080/00221686.2015.1116115

Gong, J., Simpson, A. R., Lambert, M. F., Zecchin, A. C., Kim, Y. I., & Tijsseling, A. S. (2013b). Detection of distributed deterioration in single pipes using transient reflections. *Journal of Pipeline Systems Engineering and Practice, 4*(1), 32-40. doi:10.1061/(ASCE)PS.1949-1204.0000111

Gong, J., Stephens, M. L., Arbon, N. S., Zecchin, A. C., Lambert, M. F., & Simpson, A. R. (2015). On-site non-invasive condition assessment for cement mortar–lined metallic pipelines by time-domain fluid transient analysis. *Structural Health Monitoring, 14*(5), 426-438. doi:10.1177/1475921715591875

Gong, J., Zecchin, A. C., Simpson, A. R., & Lambert, M. F. (2014b). Frequency response diagram for pipeline leak detection: comparing the odd and even harmonics. *Journal of Water Resources Planning and Management, 140*(1), 65-74. doi:10.1061/(ASCE)WR.1943-5452.0000298

Hachem, F. E., & Schleiss, A. J. (2012a). Detection of local wall stiffness drop in steel-lined pressure tunnels and shafts of hydroelectric power plants using steep pressure wave excitation and wavelet decomposition. *Journal of Hydraulic Engineering, 138*(1), 35-45. doi:10.1061/(ASCE)HY.1943-7900.0000478

Hachem, F. E., & Schleiss, A. J. (2012b). Effect of drop in pipe wall stiffness on water-hammer speed and attenuation. *Journal of Hydraulic Research, 50*(2), 218-227. doi:10.1080/00221686.2012.656838

Haghighi, A., Covas, D., & Ramos, H. (2012). Direct backward transient analysis for leak detection in pressurized pipelines: from theory to real application. *Journal of Water Supply: Research and Technology-AQUA, 61*(3), 189-200. doi:10.2166/aqua.2012.032

Haghighi, A., & Ramos, H. M. (2012). Detection of leakage freshwater and friction factor calibration in drinking networks using central force optimization. *Water Resources Management, 26*(8), 2347-2363. doi:10.1007/s11269-012-0020-6

Haghighi, A., & Shamloo, H. (2011). Transient generation in pipe networks for leak detection. *Proceedings of the Institution of Civil Engineers - Water Management, 164*(6), 311-318. doi:10.1680/wama.2011.164.6.311

Hamilton, S., & Charalambous, B. (2013). *Leak detection technology and implementation*: IWA Publishing.

Henry, R., & Luxmoore, A. R. (1996). A pipe-profiling adapter for CCTV inspection cameras: development of a pipe-profiling instrument. *Measurement Science and Technology, 7*(4), 495-504. doi:10.1088/0957-0233/7/4/005

HK-WSD. (2019). Replacement and rehabilitation programme of water mains. Retrieved from https://www.wsd.gov.hk/en/core-businesses/major-infrastructure-projects/r-r-projects/index.html

James, W., & Shahzad, A. (2003). *Water distribution losses caused by encrustation and biofouling: theoretical study applied to Walkerton, ON.* Paper presented at the World Water & Environmental Resources Congress 2003.

Jönsson, L., & Larson, M. (1992). Leak detection through hydraulic transient analysis *Pipeline systems* (Vol. 7, pp. 273-286): Springer, Dordrecht.

Joukowsky, N. E. (1898). Memoirs of the Imperial Academy Society of St. Petersburg. *Proceedings of the American Water Works Association, 24*, 341-424.

Kapelan, Z. S., Savic, D. A., & Walters, G. A. (2003). A hybrid inverse transient model for leakage detection and roughness calibration in pipe networks. *Journal of Hydraulic Research, 41*(5), 481-492. doi:10.1080/00221680309499993

Kapelan, Z. S., Savic, D. A., & Walters, G. A. (2004). Incorporation of prior information on parameters in inverse transient analysis for leak detection and roughness calibration. *Urban Water Journal, 1*(2), 129-143. doi:10.1080/15730620412331290029

Kim, S. H. (2005). Extensive development of leak detection algorithm by impulse response method. *Journal of Hydraulic Engineering, 131*(3), 201-208. doi:10.1061/(ASCE)0733-9429(2005)131:3(201)

Kim, S. H. (2016). Impedance method for abnormality detection of a branched pipeline system. *Water Resources Management, 30*(3), 1101-1115. doi:10.1007/s11269-015-1213-6

Kim, S. H., Zecchin, A., & Choi, L. (2014). Diagnosis of a pipeline system for transient flow in low reynolds number with impedance method. *Journal of Hydraulic Engineering, 140*(12), 04014063. doi:10.1061/(ASCE)HY.1943-7900.0000945

Kinsler, L. E., Frey, A. R., Coppens, A. B., & Sanders, J. V. (1999). *Fundamentals of acoustics*. New York: John Wiley & Sons.

Lee, P. J. (2005). *Using system response functions of liquid pipelines for leak and blockage detection.* (Doctor of Philosophy), University of Adelaide, Adelaide, Australia.

Lee, P. J., Duan, H. F., Ghidaoui, M. S., & Karney, B. W. (2013). Frequency domain analysis of pipe fluid transient behaviour. *Journal of Hydraulic Research, 51*(6), 609-622. doi:10.1080/00221686.2013.814597

Lee, P. J., Duan, H. F., Tuck, J., & Ghidaoui, M. (2015). Numerical and experimental study on the effect of signal bandwidth on pipe assessment using fluid transients. *Journal of Hydraulic Engineering, 141*(2), 04014074. doi:10.1061/(ASCE)HY.1943-7900.0000961

Lee, P. J., Lambert, M. F., Simpson, A. R., Vítkovský, J. P., & Liggett, J. (2006a). Experimental verification of the frequency response method for pipeline leak detection. *Journal of Hydraulic Research, 44*(5), 693-707. doi:10.1080/00221686.2006.9521718

Lee, P. J., Lambert, M. F., Simpson, A. R., Vítkovský, J. P., & Liggett, J. A. (2006b). Experimental verification of the frequency response method for pipeline leak detection. *Journal of Hydraulic Research, 44*(5), 693-707. doi:10.1080/00221686.2006.9521718

Lee, P. J., Tuck, J., Davidson, M., & May, R. (2017). Piezoelectric wave generation system for condition assessment of field water pipelines. *Journal of Hydraulic Research, 55*(5), 721-730. doi:10.1080/00221686.2017.1323805

Lee, P. J., & Vitkovsky, J. P. (2008). Discussion of "Detection of partial blockage in single pipelines" by P. K. Mohapatra, M. H. Chaudhry, A. A. Kassem, and J. Moloo. *Journal of Hydraulic Engineering, 134*(6), 874-876. doi:10.1061/(ASCE)0733-9429(2008)134:6(874)

Lee, P. J., Vítkovský, J. P., Lambert, M. F., & Simpson, A. R. (2008a). Valve design for extracting response functions from hydraulic systems using pseudorandom binary signals. *Journal of Hydraulic Engineering, 134*(6), 858-864. doi:10.1061/(ASCE)0733-9429(2008)134:6(858)

Lee, P. J., Vítkovský, J. P., Lambert, M. F., Simpson, A. R., & Liggett, J. (2007). Leak location in pipelines using the impulse response function. *Journal of Hydraulic Research, 45*(5), 643-652. doi:10.1080/00221686.2007.9521800

Lee, P. J., Vitkovsky, J. P., Lambert, M. F., Simpson, A. R., & Liggett, J. A. (2008b). Discrete blockage detection in pipelines using the frequency response diagram: Numerical study. *Journal of Hydraulic Engineering, 134*(5), 658-663. doi:10.1061/(ASCE)0733-9429(2008)134:5(658)

Lee, P. J., Vítkovský, J. P., Lambert, M. F., Simpson, A. R., & Liggett, J. A. (2005a). Frequency domain analysis for detecting pipeline leaks. *Journal of Hydraulic Engineering, 131*(7), 596-604. doi:10.1061/(ASCE)0733-9429(2005)131:7(596)

Lee, P. J., Vítkovský, J. P., Lambert, M. F., Simpson, A. R., & Liggett, J. A. (2005b). Leak location using the pattern of the frequency response diagram in pipelines: a numerical study. *Journal of Sound and Vibration, 284*(3-5), 1051-1073. doi:10.1016/j.jsv.2004.07.023

Li, R., Huang, H., Xin, K., & Tao, T. (2014). A review of methods for burst/leakage detection and location in water distribution systems. *Water Science and Technology: Water Supply, 15*(3), 429-441. doi:10.2166/ws.2014.131

Liemberger, R., & Wyatt, A. (2019). Quantifying the global non-revenue water problem. *Water Science and Technology: Water Supply, 19*(3), 831-837. doi:10.2166/ws.2018.129

Liggett, J. A., & Chen, L. C. (1994). Inverse transient analysis in pipe networks. *Journal of Hydraulic Engineering, 120*(8), 934-955. doi:10.1061/(ASCE)0733-9429(1994)120:8(934)

Liou, C. P. (1998). Pipeline leak detection by impulse response extraction. *Journal of Fluids Engineering, 120*(4), 833-838. doi:10.1115/1.2820746

Liu, Z., & Kleiner, Y. (2013). State of the art review of inspection technologies for condition assessment of water pipes. *Measurement, 46*(1), 1-15. doi:10.1016/j.measurement.2012.05.032

Liu, Z., & Kleiner, Y. (2014). Computational intelligence for urban infrastructure condition assessment: Water transmission and distribution systems. *Ieee Sensors Journal, 14*(12), 4122-4133. doi:10.1109/JSEN.2014.2336240

Louati, M., & Ghidaoui, M. S. (2017a). Eigenfrequency shift mechanism due to variation in the cross sectional area of a conduit. *Journal of Hydraulic Research, 55*(6), 829-846. doi:10.1080/00221686.2017.1394373

Louati, M., & Ghidaoui, M. S. (2017b). High-frequency acoustic wave properties in a water-filled pipe. Part 1: dispersion and multi-path behaviour. *Journal of Hydraulic Research, 55*(5), 613–631. doi:10.1080/00221686.2017.1354931

Louati, M., & Ghidaoui, M. S. (2017c). High-frequency acoustic wave properties in a water-filled pipe. Part 2: range of propagation. *Journal of Hydraulic Research, 55*(5), 632-646. doi:10.1080/00221686.2017.1354934

Louati, M., & Ghidaoui, M. S. (2018). Eigenfrequency shift mechanism due to an interior blockage in a pipe. *Journal of Hydraulic Engineering, 144*(1), 04017055. doi:10.1061/(ASCE)HY.1943-7900.0001380

Louati, M., Ghidaoui, M. S., Meniconi, S., & Brunone, B. (2018). Bragg-type resonance in blocked pipe system and its effect on the eigenfrequency shift. *Journal of Hydraulic Engineering, 144*(1), 04017056. doi:10.1061/(ASCE)HY.1943-7900.0001383

Louati, M., Meniconi, S., Ghidaoui, M. S., & Brunone, B. (2017). Experimental study of the eigenfrequency shift mechanism in a blocked pipe system. *Journal of Hydraulic Engineering, 143*(10), 04017044. doi:10.1061/(ASCE)HY.1943-7900.0001347

Malekpour, A., & She, Y. (2018). *Air pocket detection in water and wastewater conveyance pipelines using inverse transient analysis*. Paper presented at the Pipelines 2018, Toronto, Ontario, Canada.

Martins, N. M. C., Carrico, N. J. G., Ramos, H. M., & Covas, D. I. C. (2014). Velocity-distribution in pressurized pipe flow using CFD: accuracy and mesh analysis. *Computers & Fluids, 105*(2014), 218-230. doi:10.1016/j.compfluid.2014.09.031

Martins, N. M. C., Soares, A. K., Ramos, H. M., & Covas, D. I. C. (2016). CFD modeling of transient flow in pressurized pipes. *Computers & Fluids, 126*(2016), 129-140. doi:10.1016/j.compfluid.2015.12.002

Mazzocchi, E., Pachoud, A. J., Farhat, M., Hachem, F. E., De Cesare, G., & Schleiss, A. J. (2016). Signal analysis of an actively generated cavitation bubble in pressurized pipes for detection of wall stiffness drops. *Journal of fluids and structures, 65*(2016), 60-75. doi:10.1016/j.jfluidstructs.2016.05.009

Meniconi, S., Brunone, B., & Ferrante, M. (2011a). In-line pipe device checking by short-period analysis of transient tests. *Journal of Hydraulic Engineering, 137*(7), 713-722. doi:10.1061/(ASCE)HY.1943-7900.0000309

Meniconi, S., Brunone, B., Ferrante, M., & Massari, C. (2011b). Potential of transient tests to diagnose real supply pipe systems: what can be done with a single extemporary test. *Journal of Water Resources Planning and Management, 137*(2), 238-241. doi:10.1061/(ASCE)WR.1943-5452.0000098

Meniconi, S., Brunone, B., Ferrante, M., & Massari, C. (2011c). Small amplitude sharp pressure waves to diagnose pipe systems. *Water Resources Management, 25*(1), 79-96. doi:10.1007/s11269-010-9688-7

Meniconi, S., Brunone, B., Ferrante, M., & Massari, C. (2011d). Transient tests for locating and sizing illegal branches in pipe systems. *Journal of Hydroinformatics, 13*(3), 334-345. doi:10.2166/hydro.2011.012

Meniconi, S., Duan, H. F., Brunone, B., Ghidaoui, M. S., Lee, P. J., & Ferrante, M. (2014). Further developments in rapidly decelerating turbulent pipe flow modeling. *Journal of Hydraulic Engineering, 140*(7), 04014028. doi:10.1061/(ASCE)HY.1943-7900.0000880

Meniconi, S., Duan, H. F., Lee, P. J., Brunone, B., Ghidaoui, M. S., & Ferrante, M. (2013a). Experimental investigation of coupled frequency and time-domain transient test-based techniques for partial blockage detection in pipelines. *Journal of Hydraulic Engineering, 139*(10), 1033-1040. doi:10.1061/(ASCE)HY.1943-7900.0000768

Meniconi, S., Duan, H. F., Lee, P. J., Brunone, B., Ghidaoui, M. S., & Ferrante, M. (2013b). Experimental investigation of coupled frequency and time-domain transient test–based techniques for partial blockage detection in pipelines.

Journal of Hydraulic Engineering, 139(10), 1033-1040. doi:10.1061/(ASCE)HY.1943-7900.0000768

Misiunas, D., Lambert, M., Simpson, A., & Olsson, G. (2007). Assessing water mains condition using hydraulic transients. *Proceedings of the Institution of Civil Engineers-Water Management, 160*(2), 89-94. doi:10.1680/wama.2007.160.2.89

Mitra, A. K., & Rouleau, W. T. (1985). Radial and axial variations in transient pressure waves transmitted through liquid transmission lines. *Journal of Fluids Engineering, 107*(1), 105-111. doi:10.1115/1.3242423

Mohapatra, P. K., & Chaudhry, M. H. (2011). Frequency responses of single and multiple partial pipeline blockages. *Journal of Hydraulic Research, 49*(2), 263-266. doi:10.1080/00221686.2010.544887

Mohapatra, P. K., Chaudhry, M. H., Kassem, A., & Moloo, J. (2006a). Detection of partial blockages in a branched piping system by the frequency response method. *Journal of Fluids Engineering, 128*(5), 1106-1114. doi:10.1115/1.2238880

Mohapatra, P. K., Chaudhry, M. H., Kassem, A. A., & Moloo, J. (2006b). Detection of partial blockage in single pipelines. *Journal of Hydraulic Engineering, 132*(2), 200-206. doi:10.1061/(ASCE)0733-9429(2006)132:2(200)

Munjal, M. L. (2014). *Acoustics of ducts and mufflers*: John Wiley & Sons.

Nguyen, S. T. N., Gong, J., Lambert, M. F., Zecchin, A. C., & Simpson, A. R. (2018). Least squares deconvolution for leak detection with a pseudo random binary sequence excitation. *Mechanical Systems and Signal Processing, 99*(2018), 846-858. doi:10.1016/j.ymssp.2017.07.003

Nixon, W., Ghidaoui, M. S., & Kolyshkin, A. A. (2006). Range of validity of the transient damping leakage detection method. *Journal of Hydraulic Engineering, 132*(9), 944-957. doi:10.1061/(ASCE)0733-9429(2006)132:9(944)

Patankar, S. V. (1980). *Numerical heat transfer and fluid flow*: CRC press.

Pezzinga, G. (1999). Quasi-2D model for unsteady flow in pipe networks. *Journal of Hydraulic Engineering, 125*(7), 676-685. doi:10.1061/(ASCE)0733-9429(1999)125:7(676)

Riasi, A., Nourbakhsh, A., & Raisee, M. (2009). Unsteady velocity profiles in laminar and turbulent water hammer flows. *Journal of Fluids Engineering, 131*(12), 121202. doi:10.1115/1.4000557

Rubio Scola, I., Besançon, G., & Georges, D. (2017). Blockage and leak detection and location in pipelines using frequency response optimization. *Journal of Hydraulic Engineering, 143*(1), 04016074. doi:10.1061/(ASCE)HY.1943-7900.0001222

Saemi, S., Raisee, M., Cervantes, M. J., & Nourbakhsh, A. (2018). Numerical investigation of the pressure-time method considering pipe with variable cross section. *Journal of Fluids Engineering, 140*(10), 101401. doi:10.1115/1.4040718

SaemI, S., Raisee, M., Cervantes, M. J., & Nourbakhsh, A. (2019). Computation of two- and three-dimensional water hammer flows. *Journal of Hydraulic Research, 57*(3), 386-404. doi:10.1080/00221686.2018.1459892

Sarkamaryan, S., Haghighi, A., & Adib, A. (2018). Leakage detection and calibration of pipe networks by the inverse transient analysis modified by Gaussian functions for leakage simulation. *Journal of Water Supply: Research and Technology-AQUA, 64*(4), 404-413. doi:10.2166/aqua.2018.176

Sattar, A. M., & Chaudhry, M. H. (2008). Leak detection in pipelines by frequency response method. *Journal of Hydraulic Research, 46*(sup1), 138-151. doi:10.1080/00221686.2008.9521948

Sattar, A. M., Chaudhry, M. H., & Kassem, A. A. (2008). Partial blockage detection in pipelines by frequency response method. *Journal of Hydraulic Engineering, 134*(1), 76-89. doi:10.1061/(ASCE)0733-9429(2008)134:1(76)

Shamloo, H., & Haghighi, A. (2009). Leak detection in pipelines by inverse backward transient analysis. *Journal of Hydraulic Research, 47*(3), 311-318. doi:10.1080/00221686.2009.9522002

Shamloo, H., & Haghighi, A. (2010). Optimum leak detection and calibration of pipe networks by inverse transient analysis. *Journal of Hydraulic Research, 48*(3), 371-376. doi:10.1080/00221681003726304

Shi, H., Gong, J., Zecchin, A. C., Lambert, M. F., & Simpson, A. R. (2017). Hydraulic transient wave separation algorithm using a dual-sensor with applications to pipeline condition assessment. *Journal of Hydroinformatics, 19*(5), 752-765. doi:10.2166/hydro.2017.146

Shucksmith, J. D., Boxall, J. B., Staszewski, W. J., Seth, A., & Beck, S. B. M. (2012). Onsite leak location in a pipe network by cepstrum analysis of pressure transients. *Journal - American Water Works Association, 104*(8), E457-E465. doi:10.5942/jawwa.2012.104.0108

Silva, R. A., Buiatti, C. M., Cruz, S. L., & Pereira, J. A. F. R. (1996). Pressure wave behaviour and leak detection in pipelines. *Computers & chemical engineering, 20*(sup1), S491-S496. doi:10.1016/0098-1354(96)00091-9

Soares, A. K., Covas, D. I. C., & Reis, L. F. R. (2010). Leak detection by inverse transient analysis in an experimental PVC pipe system. *Journal of Hydroinformatics, 13*(2), 153-166. doi:10.2166/hydro.2010.012

Stephens, M. L., Lambert, M. F., & Simpson, A. R. (2013). Determining the internal wall condition of a water pipeline in the field using an inverse transient. *Journal of Hydraulic Engineering, 139*(3), 310-324. doi:10.1061/(ASCE)HY.1943-7900.0000665

Sun, J., Wang, R., & Duan, H. F. (2016). Multiple-fault detection in water pipelines using transient-based time-frequency analysis. *Journal of Hydroinformatics, 18*(6), 975-989. doi:10.2166/hydro.2016.232

Taghvaei, M., Beck, S. B. M., & Staszewski, W. J. (2006). Leak detection in pipelines using cepstrum analysis. *Measurement Science and Technology, 17*(2), 367. doi:10.1088/0957-0233/17/2/018

Tuck, J., & Lee, P. (2013). Inverse transient analysis for classification of wall thickness variations in pipelines. *Sensors, 13*(12), 17057-17066. doi:10.3390/s131217057

Tuck, J., Lee, P. J., Davidson, M., & Ghidaoui, M. S. (2013). Analysis of transient signals in simple pipeline systems with an extended blockage. *Journal of Hydraulic Research, 51*(6), 623-633. doi:10.1080/00221686.2013.814599

Vardy, A. E., & Brown, J. M. B. (1995). Transient, turbulent, smooth pipe friction. *Journal of Hydraulic Research, 33*(4), 435-456. doi:10.1080/00221689509498654

Vardy, A. E., & Hwang, K. L. (1991). A characteristics model of transient friction in pipes. *Journal of Hydraulic Research, 29*(5), 669-684. doi:10.1080/00221689109498983

Vítkovský, J. P., Lambert, M. F., Simpson, A. R., & Liggett, J. A. (2007). Experimental observation and analysis of inverse transients for pipeline leak detection. *Journal of Water Resources Planning and Management, 133*(6), 519-530. doi:10.1061/(ASCE)0733-9496(2007)133:6(519)

Vítkovský, J. P., Simpson, A. R., & Lambert, M. F. (2000). Leak detection and calibration using transients and genetic algorithms. *Journal of Water Resources Planning and Management, 126*(4), 262-265. doi:10.1061/(ASCE)0733-9496(2000)126:4(262)

Wang, X., & Ghidaoui, M. S. (2018). Pipeline leak detection using the matched-field processing method. *Journal of Hydraulic Engineering, 144*(6), 04018030. doi:10.1061/(ASCE)HY.1943-7900.0001476

Wang, X. J., Lambert, M. F., & Simpson, A. R. (2005). Detection and location of a partial blockage in a pipeline using damping of fluid transients. *Journal of Water Resources Planning and Management, 131*(3), 244-249. doi:10.1061/(ASCE)0733-9496(2005)131:3(244)

Wang, X. J., Lambert, M. F., Simpson, A. R., Liggett, J. A., & Vítkovský, J. P. (2002). Leak detection in pipelines using the damping of fluid transients. *Journal of Hydraulic Engineering, 128*(7), 697-711. doi:10.1061/(ASCE)0733-9429(2002)128:7(697)

Webster, A. G. (1919). Acoustical impedance and the theory of horns and of the phonograph. *Proceedings of the National Academy of Sciences, 5*(7), 275-282. doi:10.1073/pnas.5.7.275

Wu, Z. Y., Sage, P., & Turtle, D. (2010). Pressure-dependent leak detection model and its application to a district water system. *Journal of Water Resources Planning and Management, 136*(1), 116-128. doi:10.1061/(ASCE)0733-9496(2010)136:1(116)

Wylie, E. B., Streeter, V. L., & Suo, L. S. (1993). *Fluid transients in systems*. Englewood Cliffs, New Jersey: Prentice-Hall.

Zecchin, A. C., Simpson, A. R., Lambert, M. F., White, L. B., & Vítkovský, J. P. (2009). Transient modeling of arbitrary pipe networks by a Laplace-domain admittance matrix. *Journal of Engineering Mechanics, 135*(6), 538-547. doi:10.1061/(ASCE)0733-9399(2009)135:6(538)

Zhang, C., Gong, J., Zecchin, A., Lambert, M., & Simpson, A. (2018a). Faster inverse transient analysis with a head-based method of characteristics and a flexible computational grid for pipeline condition assessment. *Journal of Hydraulic Engineering, 144*(4), 04018007. doi:10.1061/(ASCE)HY.1943-7900.0001438

Zhang, C., Zecchin, A. C., Lambert, M. F., Gong, J., & Simpson, A. R. (2018b). Multi-stage parameter-constraining inverse transient analysis for pipeline condition assessment. *Journal of Hydroinformatics, 20*(2), 281-300. doi:10.2166/hydro.2018.154

Zhao, M., & Ghidaoui, M. S. (2003). Efficient quasi-two-dimensional model for water hammer problems. *Journal of Hydraulic Engineering, 129*(12), 1007-1013. doi:10.1061/(ASCE)0733-9429(2003)129:12(1007)

Zielke, W. (1968). Frequency-dependent friction in transient pipe flow. *Journal of Basic Engineering, 90*(1), 109-115. doi:10.1115/1.3605049